MODELLING AND MONITORING OF PHOSPHORUS TRANSPORT AND SPECIATION IN SOIL

by

DARREN MICHAEL WILLIAM PEAT

A thesis submitted to the University of Plymouth

in partial fulfilment for the degree of

DOCTOR OF PHILOSOPHY

Department of Environmental Sciences

Faculty of Science

In collaboration with

The Institute of Grassland and Environmental Research,

North Wyke, Devon.

March 1998

ABSTRACT

MODELLING AND MONITORING OF PHOSPHORUS TRANSPORT AND SPECIATION IN SOIL

Darren Michael William Peat

Flow through soil into groundwater has been classically conceptualised as taking place through a set of aligned capillary tubes. In solute transport models these approximations are also present. Pore-Cor (a network model) has been used to model the void structure of soil by using water retention and mercury porosimetry curves. The model successfully predicts trends in saturated hydraulic conductivity.

The effect of the assumptions used in the Pore-Cor geometry have been investigated by comparing of two dimensional slices of the simulated networks with two dimensional image analysis data. The geometric limitations of the model cause packing inefficiencies which prevent the model from representing the size distribution of voids found in real samples.

The observation of environmental events is dependent upon the implementation of rapid and reliable analytical techniques. This work presents an adaptation of an FI method for the determination of dissolved reactive phosphorus (DRP) and a new method for the determination of total dissolved phosphorus (TDP). Both are ideally suited to the detection of phosphorus species in soil leachate and runoff waters over the concentration range 3 to 1000 $\mu g\ l^{-1}$.

The effect of compaction on solute transport is described and the experimental data have been modelled using a modified form of the convection dispersion equation (CDE). The parameters of the CDE have been given structural interpretation by the network model. The model was used to interpret a change in dispersivity and the behaviour of reactive phosphorus species on compaction.

LIST OF CONTENTS

LIST OF TABLES

CHAPTER 5

CHAPTER 6

LIST OF FIGURES

CHAPTER 1

CHAPTER 2

CHAPTER 3

CHAPTER 4

CHAPTER 5

CHAPTER 6

CHAPTER 7

ACKNOWLEDGEMENTS

I would like to thank my supervisors, Dr Peter Matthews and Professor Paul Worsfold for their endless enthusiasm, friendship and support.

I am grateful to Andrew Williams and John Dowd for their helpful discussions on soil modelling. Also to Paul Russell for showing me how to run the image analyser and to Anne Kelly for giving me practical advice on soil impregnation.

Thanks also go to Dr Ian McKelvie for letting me see some of the amazing work that is going on at the Water Studies Centre of Monash University in Melbourne.

I would like to say thank you to Cathy, Louise, Toby, Andy, Dave, Matt, Leslie, Richard and everyone else for helping make the last three years interesting and enjoyable.

Finally I would like to say thank you to Ange and my parents who have given me their support throughout.

AUTHOR'S DECLARATION

At no time during the registration for the degree of Doctor of Philosophy has the author been registered for any other University award.

This study was financed by an internal Q_r studentship plus additional support from IGER North Wyke.

Relevant scientific seminars and conference were regularly attended at which work was often presented; external institutions (particularly IGER North Wyke) were visited for consultation purposes, and several publications were prepared for publication.

PUBLICATIONS FROM THIS RESEARCH

Techniques for the Quantification and Speciation of Phosphorus in Natural Waters. McKelvie, I.D., D.M.W. Peat and P.J. Worsfold. *Analytical Proceedings*, **32**, (1995) p. 437.

Rapid Determination of Dissolved Organic Phosphorus in Soil Leachates and Runoff Waters by Flow Injection Analysis with On-line Photo-oxidation. Peat, D.M.W., I.D. McKelvie, G.P. Matthews, P.M. Haygarth and P.J. Worsfold. *Talanta*, **45**, (1997) p. 47.

Elimination of the Schlieren Effect in the Analysis of Reactive Phosphorus in Estuarine Waters by Flow Injection Analysis. McKelvie, I.D., D.M.W. Peat, G.P. Matthews and P.J. Worsfold. *Analytica Chimica Acta,* **351,** (1997), p.265.

Determination of Dissolved Reactive Phosphorus in Estuarine Waters Using a Reversed Flow Injection Manifold. Auflitsch, S., D.M.W. Peat, I.D. McKelvie and P.J. Worsfold. *Analyst,* **122,** (1997), p.1477.

Three-Dimensional Void Space Modelling of Soil Water Retention and Prediction of Saturated Hydraulic Conductivity. Peat, D.M.W., G.P. Matthews, P.J. Worsfold and S. Jarvis. *European Journal of Soil Science*, Submitted October 1997.

Application of a Soil Void Space Model to a range of Textural Classes. Peat, D.M.W., G.P. Matthews, P.J. Worsfold and S. Jarvis. *In preparation.*

CONFERENCES, PRESENTATIONS AND RESEARCH TRAINING

(A= attendance, P = poster presentation and L = lecture presentation)

Void Space Modelling of Homogeneous, Inhomogeneous and Compressible Porous Media, by G.P. Matthews. RSC Particle Characterisation Group Meeting. Burlington House, London. March 1995. (A)

Transport in Porous Media. Society of Chemical Industry International Conference. London. March 1995. (A)

Monitoring and Modelling of Phosphorus Speciation and Transport in Soils. Research and Development Topics Meeting. University of Hull. July 1995. (P)

Phosphorus Transport and Speciation in Soils. Unifying Themes in Environmental Chemistry and Toxicology, SETAC Europe 6th Annual Meeting. Plymouth Pavilions. September 1995. (P,L)

Pollutant Transport in Soils and Rocks. BBSRC/NERC Initiative in Pollutant Transport in Soils and Rocks. Institute of Civil Engineers (ICE). London. November 1995. (A)

Prediction and Measurement of Phosphorus Transport in a Sandy Loam Soil. Partnerships for the Environment : *Science, Education, and Policy* ; SETAC North America 17th Annual Meeting. Washington DC. November 1996. (P)

Methods for the Determination of Phosphorus Species in Soils, Sediments and Estuarine Waters. Analytical Science and Environment Meeting. Newcastle. June 1997.

Signed ....

Darren MW. Peat, December 1997

1 INTRODUCTION

1.1 PHOSPHORUS IN THE ENVIRONMENT

Phosphorus is an important nutrient for plant growth in terrestrial and aquatic ecosystems. Much of the world's phosphorus is stored in the earth's crust in igneous rocks containing apatite - complexes of phosphate with calcium and is released from the geological pool by weathering, a naturally occurring mechanism, which is also fundamental to the formation of soil itself. When phosphorus moves from apatite into clay minerals, it is both tightly bound to the clay lattice in place of hydroxyl ions and more reversibly bound by electrostatic attraction to aluminium or iron [1,2].

Phosphorus in soil occurs in both inorganic and organic forms, and the total concentration of phosphorus held in soil minerals is high, typically 200 mg kg^{-1} [3]. The dominant characteristics of soil phosphate are the very low solubility of phosphate minerals and strong binding to particle surfaces giving relatively small soil solution concentrations, typically 10 - 300 $\mu g\ l^{-1}$ PO_4-P [3]. As a result, phosphorus deficiencies which limit plant growth are common [4].

Modern agricultural practices have improved crop yields by widespread application of phosphate fertilisers. These applications improve crop yields by augmenting the natural supply of available phosphorus which alleviates potential deficiencies. This can be shown clearly in Figure 1.1 where the additional phosphate inputs (shown by the red lines), into the environment are as a result of human intervention. Most phosphorus extracted by mining is used for the production of fertilisers and application to soil. The rest is used to make consumer products such as detergents.

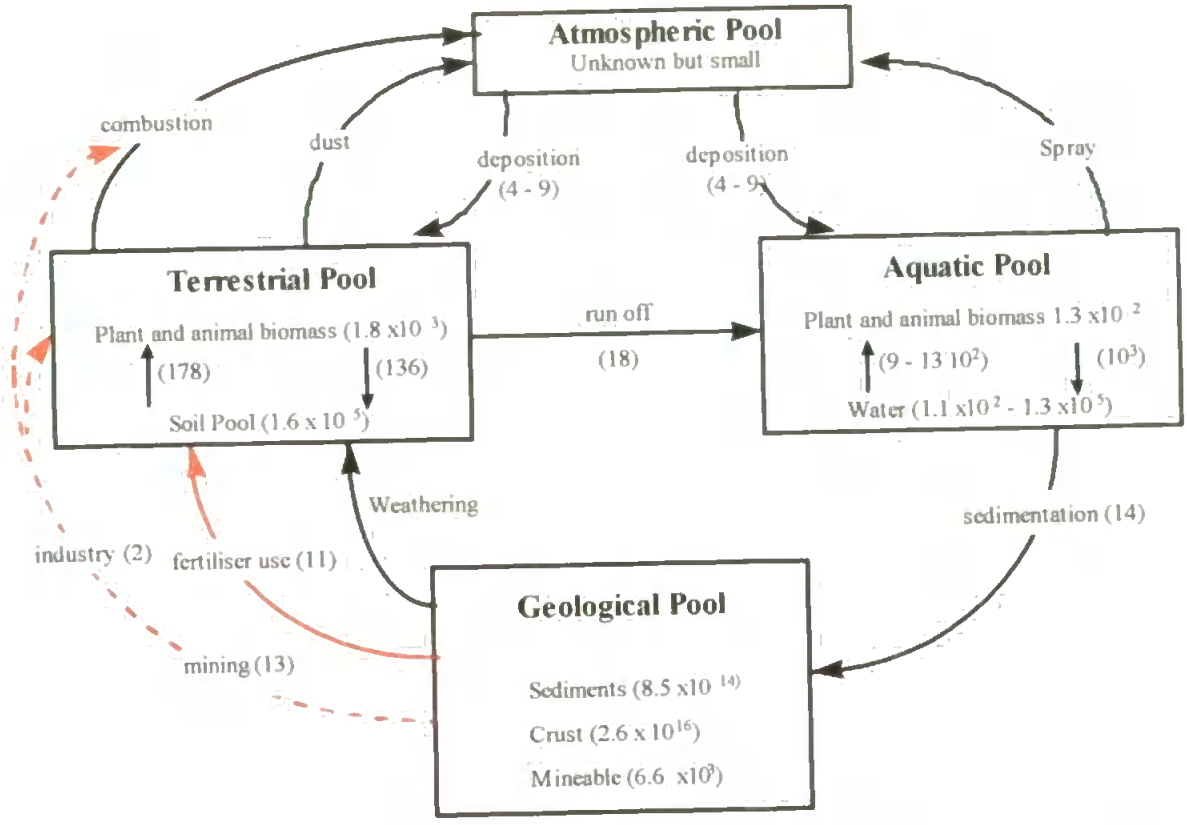

Figure 1.1: Global phosphorus cycle including both natural and human-enhanced pathways. Quantities taken from Pierrou [5], reservoirs in Tg (10^{12} g), fluxes in Tg $year^{-1}$.

1.1.1 Agricultural Application of Phosphorus

Phosphorus fertiliser is usually applied in a granular form to the soil's surface. Typically 37 kg ha^{-1} $year^{-1}$ of fertiliser is applied and is a sufficiently large amount for it to be visible in dairy paddocks as a white powder. In a rainfall or storm event, water dissolves the granular phosphorus fertiliser's active component, monocalcium phosphate (MCP) into a low pH orthophosphate solution. Calcium orthophosphates such as superphosphate and triple superphosphate are the most commonly used fertilisers and typically contain 7 - 9.5 % and 16 - 22 % by weight of P_2O_5 respectively. Iron, aluminium and manganese are dissolved at his low pH (around 1.5) and form phosphorus complexes. These metal-phosphate

complexes then reprecipitate as pH rises with further rainfall dilution. This is shown schematically in Figure 1.2.

Dissolved phosphorus may also be washed away as runoff and bypass the soil completely. This occurs when the soil is saturated and its pore network cannot conduct water away quickly enough. The extent of runoff is a function of soil's permeability, topology and the precipitation rate and a large amount of phosphorus can enter groundwater by this mechanism [4].

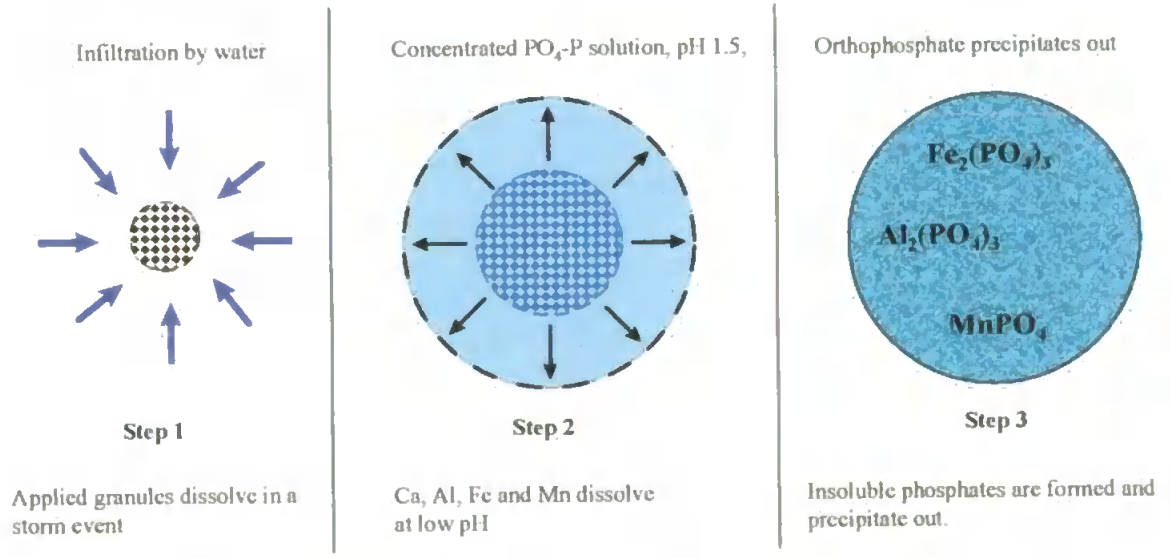

Figure 1.2: Process of MCP solvation and reprecipitation adapted from Tisdale et al. [6]

1.1.2 EUTROPHICATION

Large scale use of agrochemicals has disturbed the balance of ecosystems which have evolved over millions of years. The use of phosphorus fertiliser has undoubtedly improved crop yields [7], but because much of it can pass into aquatic ecosystems it can unintentionally contribute to eutrophication.

Increased nutrient concentrations due to human activities are now extremely common and some of the largest lakes in Europe and North America which have been studied since the

late nineteenth century provide clear demonstrations of nutrient enrichment [8,9]. In the Laurentien Great Lakes of North America, data sets running for over one hundred years are available from analyses of water supply intakes and fish catch records and provide indirect evidence for eutrophication.

Catastrophic disturbance of aquatic ecosystems can occur when nutrient concentrations build up to critical levels. For phosphorus, as little as 45 $\mu g\ l^{-1}$ PO_4-P has been found to be sufficient to support eutrophication [10]. The triggering of this process is very complex and depends upon a number of other factors which relate to the particular environmental system and external factors such as high temperature and sunlight intensity. During eutrophication, high nutrient concentrations allow excessive algal growth creating blooms which may deplete aquatic oxygen and cause the large scale wipe out of aquatic organisms [11]. Algal blooms of cyanobacteria (more commonly known as blue-green algae) are toxic. An outbreak of these blooms was observed in Britain and across Europe in 1989 caused by a mild winter in 1988/89, high 1989 summer temperatures and prolonged calm spells. About twenty-five different species of cyanobacteria produce toxins, of three kinds: neurotoxins, hepatotoxins and lipopolysacharides. Hepatotoxins are the most commonly occurring and are produced by *Microcystis*, *Oscllatoria* and *Anabaena cyanobacteria*. These toxins are poisonous to aquatic organisms, birds and terrestrial mammals including humans [10].

Nutrient enrichment of aquatic ecosystems is clearly of great concern because of its role in eutrophication. The aim of this thesis is to improve understanding of the way in which nutrients (in particular phosphorus) are transported through soil pore networks into groundwater.

1.2 THREE-DIMENSIONAL VOID SPACE MODELLING OF SOIL WATER RETENTION AND PREDICTION OF SATURATED HYDRAULIC CONDUCTIVITY

A wide range of effects depend on hydraulic conductivity, primarily hydraulic conductivity determines the rate of flow of water through soil, and consequently affects the rate of surface run-off. The ease of water flow through soil also profoundly affects the nature of groundwater via its influence on transport rates of labile species. Finally, hydraulic conductivity also affects a range of other biological and chemical processes within the soil.

Chapter 2 describes the use of a recently developed void structure network model called 'Pore-Cor' to model soil water retention curves, and from them predict trends in saturated hydraulic conductivities. However, saturated hydraulic conductivities are easier to measure than water retention curves, and thus the prediction itself is of limited value. Its importance lies in the fact that the prediction validates a network model which has interpolative and predictive capabilities for both these and a range of other properties. The scope of the present model is wider than that of other soil network models in the literature, which tend to focus only the prediction of unsaturated ('relative') hydraulic conductivity from saturated hydraulic conductivity measurements.

The study covers a range of soil transport properties, and begins by briefly reviewing other work in the area. Firstly, existing approaches to the prediction of saturated, and then unsaturated, hydraulic conductivity are discussed, and then the structural approximations within solute transport models. The review continues by describing three of the models which are available to explain the shapes of water retention curves, one of which is used to

extrapolate experimental data. Finally, network models which have been applied to soil, and also to other materials such as sandstone, are discussed.

Existing models for the prediction of saturated hydraulic conductivity have tended to focus on the application of pedo transfer functions. These transfer functions rely on empirical parameterisations to relate measurable soil properties such as particle size distribution to saturated hydraulic conductivity. No account is taken of the void space network of the soil, and predictions can sometimes be extremely inaccurate [12]. Other approaches to the estimation of soil hydraulic properties have included so-called two-domain estimators [13]. These models arbitrarily separate macro and matrix flow, and use empirical functions of soil water content to predict the hydraulic conductivity of each domain. The prediction of saturated hydraulic conductivity has also involved the use of fractals [14,15], based on Sierpinsky carpets [16]. The carpet takes the form of a simple, infinitely repeating pattern, which represents the cross-section of bundles of parallel tubes. The application of this approach to soils is reliant upon estimating the fractal dimension of the porosity from the application of power scaling laws [17,18]. However, it is possible that in some cases the power index of these functions may be a fractal dimension of the solid phase.

Soil usually exists in an unsaturated state, but the measurement of unsaturated hydraulic conductivity is much more difficult than that of saturated hydraulic conductivity. Most models of hydraulic conductivity in soil are therefore focused upon the prediction of unsaturated conductivity relative to an experimentally determined value under saturated conditions. Burdine [19] and Mualem [20] have proposed functions that have been used with water retention curve data for such purposes. These functions, though useful, involve empirical fitting parameters which do not explicitly relate to soil structure.

Solute transport models have also been developed within a similar framework of approximations, with a reliance on arbitrary fitting functions and over-simplification of soil structure. Water flow is still commonly conceptualised as being due to aligned cylindrical tubes passing through the soil [21], (Figure 1.3). Laminar flow increases as the fourth power of the tube radius, and because of this high size dependence, macropores are often assumed to be responsible for preferential flow [22]. However, preferential flow can only occur if these pores are well connected. Evidence of this is rarely presented when making the assumption that macropores are responsible for early breakthrough of solutes moving down soil profiles.

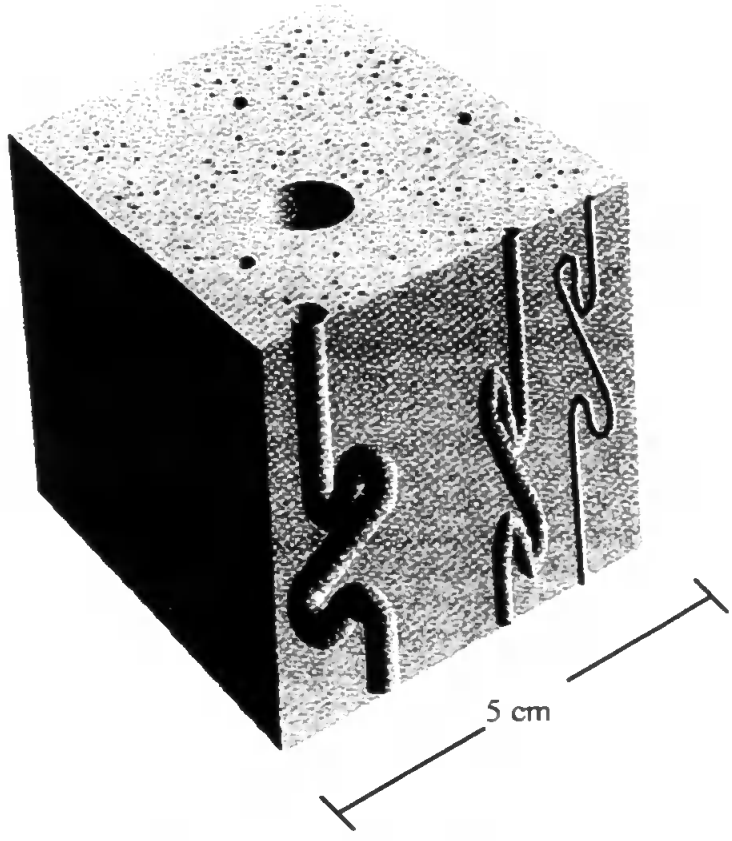

Figure 1.3 : Traditional 2D modelling approach in which all pores are accessible.

1.2.1 WATER RETENTION MODELS

All empirical water retention models use the Laplace / Washburn equation [23], to relate the capillary pressure p to the pore radius r_n of the n^{th} pore:

$$p_n = \frac{-2\gamma_n \cos\beta_n}{\rho_w g r_n} \tag{1.1}$$

Here γ is the interfacial tension between water and air, β is the contact angle where the water meniscus touches the solid surface, ρ_W is the density of water and g is the acceleration due to gravity.

Various approximations are implicit in the use of this equation. The first is that all pores are cylindrical, since this is the geometry to which Equation (1.1) applies. Although much work has been published on the capillary pressure in other shapes of pores [24-26], in a natural sample it is very difficult to measure three-dimensional shape distributions [27]. The pores are therefore represented as cylinders, the percolation and permeability characteristics of each pore being a mapping of the characteristics of a real pore of a possibly different shape and size [28]. Other approximations are that the contact angle and interfacial tension have constant values (taken to be 0° and 0.075 N m^{-1} respectively), ie $\beta_n = \beta$ and $\gamma_n = \gamma$ for all n.

The pore radius distribution f (r) is defined as :

$$f(r) = \frac{d\theta}{dr} \tag{1.2}$$

where θ is the volumetric water content. Use of this equation implies that all pores are fully accessible, and that they independently experience the external applied pressure ψ. Such behaviour would be observed in a structure containing aligned capillary tubes, Figure 1.3, in which all the tubes are open to the surface or surfaces at which pressure is applied. Under these circumstances, $p_n = \psi$ for all n.

Invoking equation (1.2) allows the pore radius distribution function f (r) to be transformed into the capillary pressure distribution function f (ψ), by the following expression :

$$f(\psi) = f(r)\frac{dr}{d\psi} \tag{1.3}$$

Substituting Equation (1.2) into Equation (1.3) yields the pore capillary pressure distribution function:

$$f(\psi) = \frac{d\theta}{d\psi} \tag{1.4}$$

A number of proposals for the pore radius distribution function f (r) have been made. A lognormal function has been proposed by Kosugi [29]:

$$f(r) = \frac{(\theta_s - \theta_r) r_{max}}{(2\pi)^{1/2}\sigma(r_{max} - r)} \exp\left\{\frac{\left[\ln\left(\frac{r}{r_{max} - r}\right) - \mu\right]^2}{2\sigma^2}\right\} \tag{1.5}$$

where r_{max} is the maximum pore radius, and θ_r is defined as the water content at which the capillary pressure ψ is infinitely small and the soil hydraulic conductivity is zero. In practice, however, θ_r is treated as an empirical fitting parameter, with arguable physical significance. θ_S is defined as the water content at saturation, and because it is measured experimentally it is not treated as a fitting parameter. The mean μ and standard deviation σ are the first and second moments of the lognormal pore size distribution function.

The model is based on the assumption that the pore size distribution of a soil is lognormal because many particle size distributions in soils are lognormal. The assumption is not supported by direct experimental evidence but nevertheless the model has been found to fit a number of soil water retention data sets.

An expression relating effective saturation S_e to capillary pressure has been derived for this pore radius distribution function :

$$S_e = \frac{1}{2}\ \mathrm{erfc}\left\{\frac{\ln\left[(\psi_c - \psi)/(\psi_c - \psi_0)\right] - \sigma^2}{2^{1/2}\sigma}\right\} \tag{1.6}$$

where ψ_0 is the pressure at the mode of the distribution f (Ψ), which corresponds to the point of inflection on the water retention curve. ψ_c is the 'bubbling pressure' at which air intrusion begins. The effective saturation is defined as :

$$S_e = \frac{(\theta - \theta_r)}{(\theta_s - \theta_r)} \tag{1.7}$$

Functions other than the lognormal water retention fitting function have also been widely used. van Genuchten [30] has proposed the following fitting function :

$$S_e = \left[\frac{1}{1+(-\alpha\psi)^n}\right]^m \tag{1.8}$$

where α, m, n are fitting parameters and ψ is always negative.

A model proposed by Brooks and Corey [17] relates the effective saturation to a power function of ψ :

$$S_e = \left(\frac{\psi_c}{\psi}\right)^{\lambda} \tag{1.9}$$

where ψ_C , and λ are fitting parameters. The Brooks and Corey expression has been found to be equivalent to a general fractal water retention model [16,31]. However, this fractal model uses a pore size distribution based on the first derivative of the water retention curve [16], and therefore implicitly includes the structure approximations exemplified by Figure 1.3.

Common to all of the functions described in this section is that they have only one point of inflexion and can therefore only apply to uni-modal pore size distributions.

1.2.2 Modelling of Convection and Dispersion Under Unsaturated Conditions

Most soils exists in nature in a partially saturated state. Measurement of unsaturated hydraulic conductivity and dispersivity is time consuming, expensive and difficult. As

mentioned earlier, the models of Mualem and Burdine have been applied by van Genuchten [30] to model unsaturated hydraulic conductivity from a knowledge of the easier to measure saturated hydraulic conductivity and water retention curve. van Genuchten [30] found that the function k_r based on the empirical equation of Mualem was better a predictor of experimental data than k_r functions based on the theory of Burdine, so only the Mualem theory will be considered. In this approach the function k_r is be assumed to take the form ;

$$k_r = \sqrt{S_e}\left[\frac{\int_0^{S_e}\frac{1}{h(z)}\,dz}{\int_0^{1}\frac{1}{h(z)}\,dz}\right]^2 \tag{1.10}$$

where h is the tension, taken to be positive, i.e $-\psi$ and is given as function of the dimensionless water content, Equation (1.7). If the water retention curve can be assumed to take the form of Equation (1.8) and the value of $m = 1$, a near symmetrical 'S' -shaped curve is obtained.

A simple closed from of k_r can be derived when the values of m and n are placed in Equation (1.8). Solving this equation for $h = h(S_e)$ and substituting into Equation (1.10) gives

$$k_r(S_e) = \sqrt{S_e}\left[\frac{f(S_e)}{f(1)}\right] \tag{1.11}$$

where

$$f(S_e) = \int_0^{S_e} \left[\frac{z^{1/m}}{1 - z^{1/m}} \right]^{1/m} dz \qquad (1.12)$$

Substitution of $z = y^m$ into (1.12) effects a change of variable and simplifies the integration, thus

$$f(S_e) = m \int_0^{S_e^{1/m}} y^{m-1+1/n} \, (1-y)^{-1/n} \, dy \qquad (1.13)$$

Equation (1.13) represents the form of the Incomplete Beta-function, in its most general case no closed form can be derived. However for all integer values of k^* such that $k^* = m\text{-}1 + 1/n$ the integration is straightforward. In the particular case, $k^* = 0$, integration of Equation (1.13) yields

$$f(S_e) = 1 - (1 - S_e^{1/m})^m, \qquad (m=1\text{-}1/n) \qquad (1.14)$$

and because $f(1) = 1$ Eqn (1.11) becomes

$$k_r(S_e) = S_e^{1/2} \, [1 - (1 - S_e^{1/m})^{m^2}], \qquad (m=1\text{-}1/n) \text{ and } (0 < m < 1) \qquad (1.15)$$

it is useful to express Equation (1.15) in term of the pressure head h, by substituting equation (1.7) into it, i.e.,

$$k_r = \frac{\left\{ 1 - (\alpha h)^{n-1} \, [1 + (\alpha h)^n]^{-m} \right\}^2}{[1 + (\alpha h)^n]^{m/2}} \qquad (1.16)$$

From the hydraulic conductivity and the soil water retention curve an expression for soil water diffusivity may be defined

$$D(\theta) = k(\theta)\left|\frac{\mathrm{d}h}{\mathrm{d}\theta}\right| \tag{1.17}$$

and lead to the following equation for $D(S_e)$:

$$D(S_e) = \frac{(1-m)k_s}{\alpha m(\theta_s - \theta_r)} S_e^{1/2-1/m}\left[(1-S_e^{1/m})^{-m} + (1-S_e^{1/m})^{m}\right]^2 \tag{1.18}$$

These equations have been derived using a k^* value of 0; other closed forms may also be derived by higher integer values of k^*. However the use of higher k^* values leads to the production of more complex expressions for k_r and therefore does not present an attractive alternative to Equation (1.15).

Equations 1.15 and 1.18 are useful in predicting relative hydraulic conductivity and relative diffusivity (dispersion) from a knowledge of the water retention curve and the saturated conductivity and dispersion co-efficient. Other $S_e(h)$ functions may be substituted for Equation (1.8) such as those of Kosugi, Equation (1.6) or Brooks and Corey, Equation (1.9). Common to all of the substitutable functions is that they are empirical and unimodal. However other $S_e(h)$ functions are not as easily integrated as the form of Equation (1.8) and in the case of Equation (1.6) numerical integration methods must be used.

1.2.3 NETWORK MODELS

One way of tackling the many problems of predicting and modelling water and solute flow is to employ an explicit, precise but simplified model of the soil's void structure. The simplifications are necessary to stay within computing limitations while maintaining a realistically large representative elementary volume (REV). The model should represent other important characteristics, particularly water and solute retention and flow, most usefully at those length scales which are too small for a continuum approach.

Other workers have described a range of simplified geometries within their network models. Early work in this field has been reviewed by Celia et al. [32]. Payatakes and co-worker discuss percolation characteristics within pore systems which include 'hold-ups' for entry into spherical and sinusoidal geometry pores [33,34], and the effects of correlated networks [35]. However, their work has not been extended to the prediction of permeability and hydraulic conductivity, and has not been applied to soils. Many models including those proposed by Rajaram et al. [36] and Lowry & Miller [37] are networks of a ball and stick type. They have many of the features of Pore-Cor, such as variable connectivity and a visualisable structure, and have been used to predict pore level properties such as entrapment [37] and relative hydraulic conductivity [36]. Lowry & Miller [37] argue that for model of a complex porous media to form a representative elementary volume, 8000 or more nodes are required, which both these models possess. Rajaram et al. [36] found that networks at least twelve times longer than the correlation scales (e.g. 67 x 67 x 67 sites for structures correlated over 5 nodes) were sufficiently large to give stable network predictions. Both of these models assume arbitrary pore size distributions.

Although all network models should be capable of modelling a wide range of pore level properties, they are very rarely used to predict saturated hydraulic conductivity. This is attributable to the complexity of applying percolation algorithms to more complex

geometries and the fact that the experimental measurement of saturated hydraulic conductivity is straightforward.

1.2.4 THEORY

THE PORE-COR NETWORK MODEL

The computer modelling package named 'Pore-Cor' has been applied to the void structure of soils. The method, which has been described in detail by Matthews et al. [38,39] has previously been applied to a range of substances including paper coating formulations [40] and reservoir sandstone [38]. The Pore-Cor void geometry consists of a three dimensional array of larger cubes which are connected by cylinders, Figure 1.4. In reservoir sandstones, larger voids are often constrained by smaller apertures. The large voids have traditionally been called pores and the smaller constraining voids throats. To maintain this convention Pore-Cor cubes and cylinders are referred to as pores and throats respectively. The infinitely repeating unit cell of the model comprises a 10 x 10 x 10 network of pores connected by a total of $500c$ throats, where c is the connectivity. These connecting throats form a log-linear distribution, and the 'throat skew' of the model is defined as the percentage of throats of minimum size in the distribution. For simplicity of calculation, the positions of the pores and throats in the model are equally spaced in Cartesian planes in each direction. They therefore do not pack very efficiently, and to achieve the experimental porosity it is necessary to enlarge the pores by a factor known as the 'pore skew', giving pores sizes up to, but never exceeding, the original upper limit determined by the percolation algorithm. Within the context of the discussions of Rajaram et al. [36] and Lowry & Miller [37], the unit cell size is small, its size being limited by the

complexities of the permeability calculation. This calculation, and the method of overcoming the size limitation, are both described below.

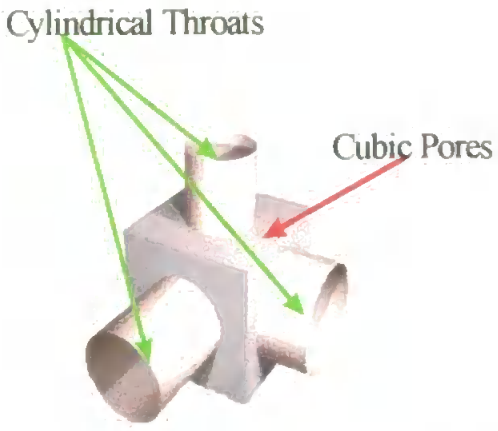

Figure 1.4 : Cubic pore surrounded by cylindrical throats.

The arrangement of pores and throats generates a void space network which has the same percolation characteristics as the experimental sample. In real soils that are unsaturated, water is distributed over the soil matrix in films, which are not necessarily entirely displaced by intruding air. Pore Cor ignores these wetting film effects by assuming that individual pores and throats are completely full of liquid or completely drained, a simplification which Mualem [41] believes limits the accuracy of network models. The approximation is more realistic in the case of the modelling of mercury intrusion experiments, where the non-wetting mercury can be assumed to fully displace the receding residual air in the evacuated sample. However, mercury porosimetry is unsuitable for intact soils, since it destroys the soil structure and is limited to small samples. Furthermore, soil contains pores of diameter greater than 500 μm, larger than can be reliably measured by mercury intrusion [42].

The use of Pore-Cor to model water retention curves removes the necessity of assuming that all voids are accessible and open to the applied pressure, i.e it does not assume that $p_n = \psi$ for all n, as exemplified in Figure 1.3. Instead, only those throats and pores in the

network which are exposed to the applied air pressure are drained by the air. Other voids, deep within the network, may be shielded or shadowed from this effect by intervening smaller voids which are still full of water. This underlines the difference between a soil water retention experiment, and a soil pressure tension experiment. In the latter, a water-filled porous tensiometer is inserted deep within the soil sample, and sets up an equilibrium with all the local menisci, via the continuous water phase. The capillary pressure of all these equilibrated menisci is then measured. Haines [43] described this effect in classic papers early this century, and also pointed out the intractability of exact calculations for poly-disperse, random soil structures.

The Pore-Cor structure has three important characteristics. The first is that it has a real three-dimensional geometry, which can be visualised and is used for the calculation of all properties. The second is that its percolation characteristics are fitted to the experimental data using parameters such as connectivity, which can be verified experimentally as being within a realistic range. Finally, the structure can be used to generate a wide range of other pore-level properties, most importantly the flow capacity of the network for gaseous or liquid flow.

Calculation of Hydraulic Conductivity

The saturated hydraulic conductivity of a soil is one of its most important physical characteristics, but is extremely difficult to model. Pore-Cor calculates the flow capacity of its network by using a Dinic Operational Research network capacity algorithm [44], which calculates the permeability of the whole network from a knowledge of the flow capacity of each pore-throat-pore arc. In a tube, an incompressible fluid under laminar flow conditions assumes a parabolic velocity profile. Integration over the velocity profile yields the Poiselle equation:

$$\left(\frac{dV}{dt}\right)_{tube} = -\frac{\pi\, r_{tube}^4\, \delta P_{tube}}{8\mu_{fv} l_{tube}} \tag{1.18}$$

where $(dV/dt)_{tube}$ is the volumetric flow rate, r_{tube} is the radius of the tube, μ_{fv} is the fluid viscosity and $\delta P_{tube} / l_{tube}$ is the pressure gradient along the tube. This approximation is then applied to the Pore-Cor unit cell, as illustrated in Figure 1.5, in which the outer layer of a soil structure is depicted. Assuming that flow takes place in the negative z direction, i.e from the top to the bottom face of the unit cell Equation 1.19 can be derived.

$$\left(\frac{dV}{dt}\right)_{cell;-z} = -\frac{\pi}{8\mu_{fv}} \Omega\left(r_{tubes;z}^4\right)_{cell} \frac{\delta P_{cell}}{l_{cell}} \tag{1.19}$$

Where Ω is an averaging operator over the whole unit cell operating on the fourth power of the individual radii r_{tube} of all tubes lying parallel to the z axis. Ω is defined such that equation (1.19) is satisfied, and generates a term which is related to the effective Poiseuillian capacity of the cell for flow in the negative z direction. Since, at this stage of the calculation, all the tube lengths l_{tube} are identical and $l_{tube} = l_{cell} / \beta_n$, where β_n is the number of tubes in the z direction in the unit cell. Currently the β_n value is 10 because a 10 x 10 x 10 array is used. These lengths can be included in the averaging function and if tubes in the $\pm$x and $\pm$y directions are also combined it follows that ;

$$k = \frac{\pi}{8\beta_n} \Omega\left(\frac{r_{tube}^4}{l_{tube}}\right) \frac{l_{cell}}{A_{cell}} \tag{1.20}$$

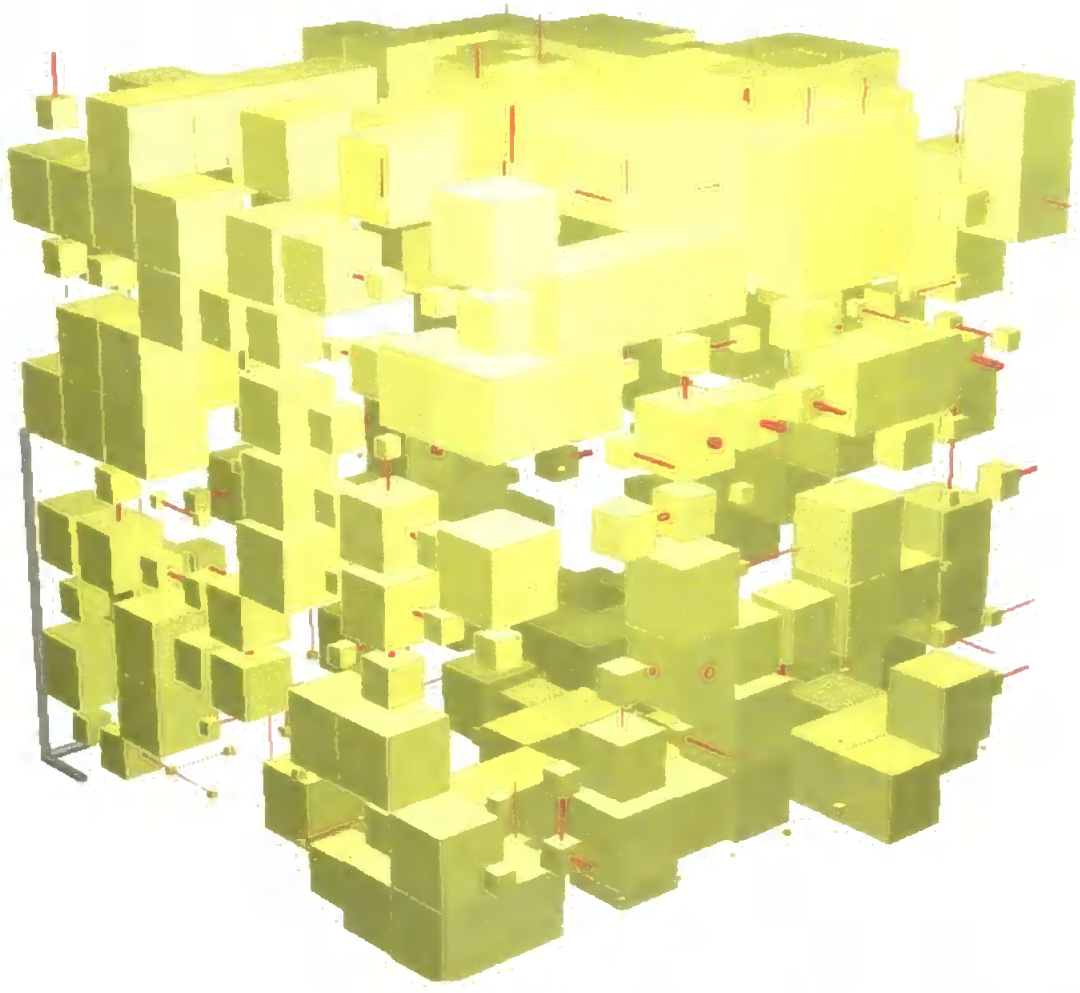

Figure 1.5: Outer layer of soil unit cell. Pore row spacing of 5027 μm represented by small scale bar.

Once this equation is corrected for the square cross area sectional of the pores, and for slip flow [45] the permeability, k may be calculated. The wide range of void sizes in soil generated arc flow capacities over a range of 12 orders of magnitude, and to handle this the Dinic algorithm was converted from its original integer arithmetic to real arithmetic.

The number of possible flow paths, and hence the flow capacity, increases dramatically with increasing connectivity, by 3 orders of magnitude for a change of connectivity from 2.8 to 4 [45]. The flow capacity is also sensitive to the pore and throat size distribution, as characterised by the 'throat skew' parameter.

The fit to a particular water retention characteristic does not produce a unique structure. This is partly due to the relatively small size and simplicity of the unit cell. It also arises from the fact that the amount of information contained within a water retention curve alone is insufficient to produce unique solutions [46]. In principle, water retention curve information can be augmented with other data, such as that from image analysis, to reject some network solutions. As a result of the non-uniqueness of the unit cell structure, the predicted flow capacity, which is based on a single structure, is also not unique. To overcome this shortcoming, it was necessary to take an average of twenty stochastic generations of the unit cell, as described below in Chapter 2.

CALCULATION OF TORTUOSITY

The tortuosity of the network may be calculated by taking 100 probability weighted random walks through the network and the algorithm to calculate this was written by Spearing and Matthews [47]. For this purpose, the tortuosity is simply defined as the ratio of the path length through the sample divided by the length of the sample, although several other definitions exist, based on the square of the definition of this work [48]. The weighting of the random walk corresponds to the path of a single ion moving through the

void space. As yet, no account is taken of multiple, simultaneous ion tracks through the structure, and there is no allowance for the fact that there is a tortuosity in the paths of ions even within a straight, wide tube [48].

EXTRAPOLATION OF EXPERIMENTAL DATA

For Pore-Cor to be able to generate a network which covers the complete range of void sizes within a sample, the sample's water retention curve must arise from the characteristics of the complete void size range. In practice, this is not the case. Even at zero applied pressure, the largest, most conducting voids within a sample can drain by gravity. At the other end of the scale, the smallest pores retain residual water even under the maximum practicable differential pressure of 15 bar. Experimental water drainage curves therefore sample only the middle range of pore sizes, from around 120 μm to 0.2 μm radius.

One approach to this problem is to extrapolate to larger void sizes by use of water retention models. Extrapolation to smaller void sizes is unnecessary, because the smaller voids are assumed to be non conducting. This simplification is necessary because of the geometric simplifications of the model, but does introduce a small level of inaccuracy [49]. The void size ranges actually modelled vary from 0.21 μm - 2500 μm to 2.34 μm - 2500 μm, as explained below in Chapter 2.

1.3 COMPARISON OF PORE-COR THREE DIMENSIONAL STRUCTURES WITH TWO DIMENSIONAL IMAGE ANALYSIS

Quantification of soil pore level characteristics by image analysis is an important component in the understanding of soil physical and chemical processes, it provides complementary information to other measurements such as water retention [46]. The

technique has been used to study a wide range of effects including compaction [50], tillage [51], tracer breakthrough [52] and preferential flow [53].

Image analysis of soil voids is only possible when the voids can be distinguished from the soil matrix. Although direct quantification on unimpregnated samples has been possible with macropores [54] in a few soil types, the standard technique for contrasting pores from background involves filling the voids with a resin containing a UV fluorescent dye [55]. When observed under light of a UV excitation energy, the resin filled pores emit visible light which may be detected by a conventional or charge coupled device camera.

The use of resin impregnators serves two purposes, namely the introduction of the fluorescing dye and mechanical support of the friable soil to allow machining into thin sections or polished blocks. Direct impregnation of soil samples can be achieved with PEG 6000 (Carbowax) [56]. The preferred technique for this impregnant is a gradient introduction of increasingly concentrated solutions of Carbowax dissolved in water, finishing with the immersion of the sample in pure molten Carbowax. Direct impregnation with Carbowax is advantageous in that it does not require acetone drying of the samples prior to impregnation, is non toxic and does not require an initiator to set. However Carbowax impregnated samples are more difficult to machine and must be lubricated during machining with a suitable oil (such as Castrol Honillo) because it has a low melting point (68 Deg C) and is water soluble. Preparation of thin sections from Carbowax impregnated samples is more difficult than preparation from samples impregnated in most other resins [56] and has a practical lower limit of section thickness of around 30 μm, and is unsuitable for soils for which the clay content is less than around 20 % [55].

Other impregnators such as crystic resin [56] have been used to impregnate samples. However, the use of this and many other resins require that the sample be acetone dried prior to impregnation. The method however, is more suitable for the production of thin

sections and is usually preferred to Carbowax impregnation for mineralogical studies [56]. The choice of UV dye is influenced by its solubility in the resin for which it is to be used. Water soluble dyes such as acaradine orange or crystal violet are suitable for use with Carbowax and Uvotex UV - B dye has been used with crystic resin.

The measurement of emitted visible light from fluorescing resin filled voids has been traditionally carried out with a 35mm camera and highly sensitive film. More recently the development of charge coupled cameras has seen their use as a detector increase.

In the 1970s, computerised image analysis was performed with large expensive instruments. The process of quantification and classification of detected images has been greatly improved with the use of image analysis software analysis algorithms and much increased computing power. This automation however does rely upon the software making decisions for the operator with an inevitable set of assumptions built into the decision making process. The process of distinguishing void from soil matrix is called segmentation. In practice, these processes are employed sequentially to ensure that the segmented image resembles the original grey image as closely as possible.

Although soil pores in a three dimensional network may be well connected, observation of a two dimensional section often shows these features to be discrete [57]. The most simple measurements that one can make on two-dimensional features are properties such as area, perimeter, shape index, width and length (or some index thereof e.g., feret width or feret length). Such simple measurements are often not capable of dealing with highly connected two dimensional images [58] and may be further complicated by anisotropic pore networks. Pore size distributions assume discrete features of discernible size and in such cases statistical methods of producing a pore size distribution are often used [59]. These methods infer discrete pore sizes from connected networks. However a three dimensional interpretation of these statistical processes is not straightforward. There is little evidence to

support the three dimensional validity of the use of micromorphological statistical functions to obtain pore size distributions. Further because isotropic soil pore networks are uncommon, the use of fractal scaling laws are of limited use in producing three dimensional extrapolations [46]. There is a great deal of argument as to which method, if any, is suitable for generating pore size distributions and it is accepted that any one method is not universally applicable [58]. Many approaches describing soil structure fail to account for the variability in pore shape, connection, or orientation found in a real soil structure [46].

As mentioned earlier, classical approaches of determining pore size distributions from water retention curves assume that the pore size distribution is simply the first derivative of the water retention curve. This approximation by definition makes the assumption that the soil structure may be described by a bundle of aligned capillary tubes, Figure 1.3. Pore-Cor [60,61] does not intrinsically rely on this structural approximation.

An attempt to compare pore size distributions is not possible because the term pore size infers a three dimensional interpretation of two dimensional data. Other authors have tried to produce three dimensional structures of void space from two dimensional images [27]. These types of model assume that property distributions of the 2D dimensional surface are similar to the three dimensional distributions. This type of approach to the problem can generate three dimensional structures. However, for soils they are often internally inconsistent and the three dimensional networks generated do not have readily calculable properties.

The approach in this work reverses this process; the Pore-Cor three dimensional networks produced in Chapter 2 can be mathematically microtomed into two dimensional surfaces. Properties of the mathematical and experimental two dimensional surfaces can then be compared. Validation of network solutions produced by Pore-Cor is possible by experiment because it has a real structure. This is a major advantage over abstract mathematical models

which can not be validated in this way because they do not have a real geometry [62,63]. Chapter 3 compares two dimensional feature size distributions obtained, (i) experimentally by image analysis, (ii) by use of the classical capillary model and (iii) by microtoming Pore-Cor networks. Comparison with experiment allows the distorting effect of the Pore-Cor geometrical assumptions to be observed.

1.4 ANALYTICAL DETERMINATION OF PHOSPHORUS

Chapters 1 to 3 have described how the Pore-Cor model has been adapted and validated with experimental data for soil. In Chapter 5, a breakthrough experiment is described which requires the interpolative capabilities of Pore-Cor to give a structural interpretation of experimentally observed breakthrough curves. Reliable analytical techniques for the quantification and speciation of phosphorus are essential to the experimental observation of the breakthrough of phosphorus species in solute transport experiments.

1.4.1 PHOSPHORUS SPECIATION

Various physico-chemical forms of phosphorus may be determined as part of water quality monitoring programs, for the study of nutrient budgets and dynamics in oceans, rivers, lakes and groundwater, or for monitoring the efficacy of P-removal and wastewater discharge in sewage treatment processes. However, the importance of phosphorus measurements ultimately relates to its role in photosynthetic and decomposition processes (Figure 1.6), and eutrophication.

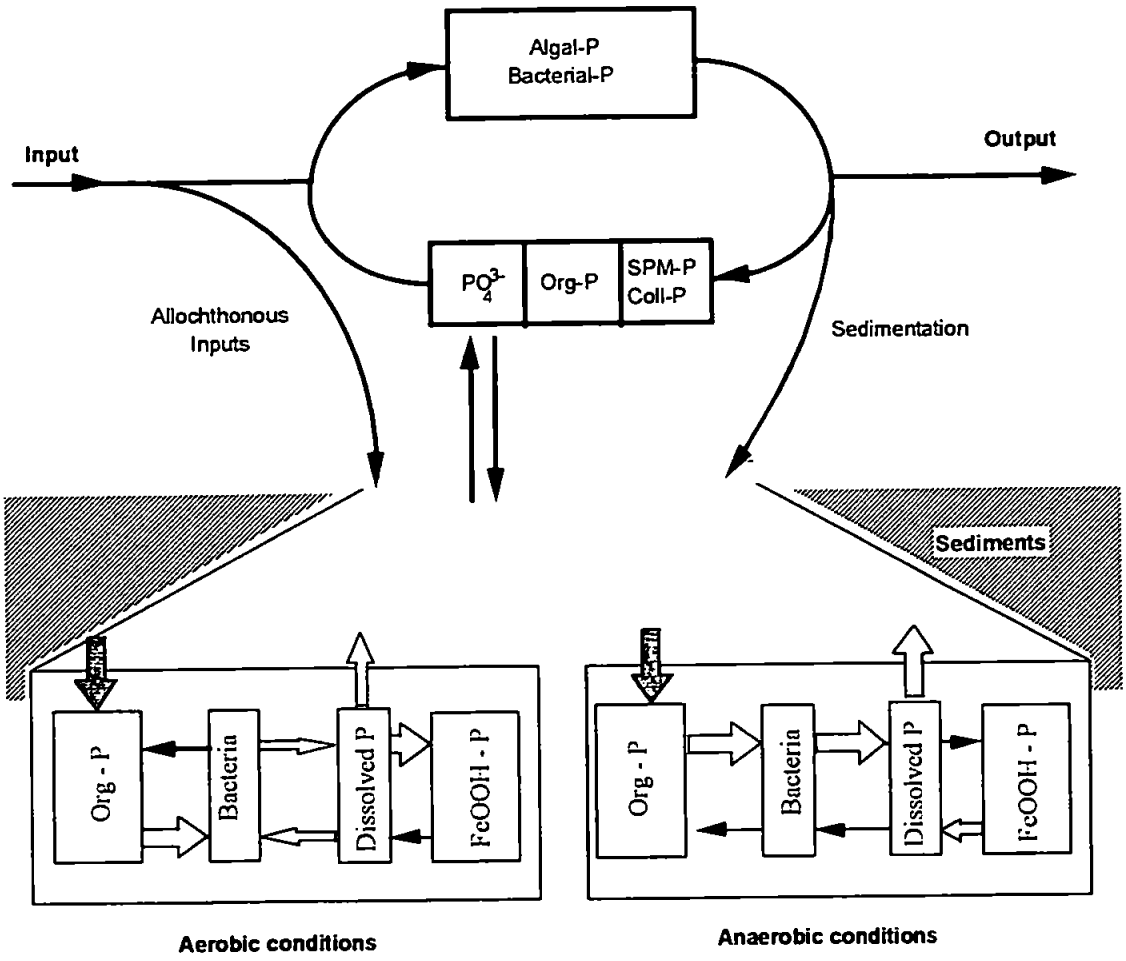

Figure 1.6: Typical aquatic phosphorus cycle showing likely transport paths and transformations within the water column and sediments. Under aerobic conditions, uptake by oxide-coated sediment particles (designated as the FeOOH-P fraction) will be the likely predominant sediment mechanism, whereas release of dissolved phosphorus is likely to occur under anaerobic conditions. SPM = suspended particulate matter, Coll-P = colloidal P, Org-P = organic phosphorus. Adapted from Hart [64].

The most commonly analysed species are total phosphorus (TP) and dissolved reactive phosphorus (DRP), but arguably the criterion for their use has been the relative ease and convenience of their determination, rather than their biological relevance. In order to gain a greater understanding of phosphorus utilisation in and transport into aquatic ecosystems, there is a need for the development of more sensitive and robust phosphorus monitoring techniques and biologically-relevant phosphorus speciation methods.

The total phosphorus content of natural waters comprises both particulate and dissolved forms, the latter being operationally defined as the fraction which will pass through a 0.45

μm pore size filter membrane. However, the so-called dissolved fraction has been clearly shown to include significant amounts of high molecular weight colloidal organic phosphorus species [65] including those associated with humic substances [66]. The filtration process is fraught with uncertainties, including the transmission of particles in excess of the nominal filter pore size [67], clogging, contamination, variation in pore-size and destabilisation of colloids [68].

The total dissolved phosphorus (TDP) fraction can be further subdivided as shown in Figure 1.7. It is composed of dissolved inorganic phosphorus (DIP), comprising orthophosphates and condensed phosphates, and dissolved organic phosphorus (DOP), and may also include a significant proportion of colloidal-sized phosphorus species [65].

Orthophosphates react readily with acidic molybdate, to form 12-phosphomolybdic acid, which on reduction yields strongly-coloured phosphomolybdenum blue species; this reaction is the basis for most spectrophotometric phosphate determinations. However, hydrolysis of labile condensed and organic phosphates may occur under the analytical conditions used, and the orthophosphate concentration will then be overestimated. Orthophosphate measured in this manner is therefore termed dissolved reactive phosphorus (DRP). Indicative concentrations of DRP in a variety of natural waters are shown in Table 1.1.

Dissolved condensed phosphates (DCP) consist of inorganic polyphosphates, metaphosphates and branched ring structures, [68] which do not form 12-phosphomolybdic acid unless they have previously been hydrolysed. The dissolved organic phosphorus (DOP) fraction includes nucleic acids, phospholipids, inositol phosphates, phosphoamides, phosphoproteins, sugar phosphates, aminophosphonic acids, phosphorus-containing pesticides and organic condensed phosphates [10,69]. DOP has traditionally, but incorrectly, been equated with the residual TDP after measurement of DRP and DCP [70].

Table 1.1: Indicative concentrations of phosphorus as dissolved reactive phosphorus in natural waters

	Indicative DRP concentration ranges	
Water type	$\mu g\ P\ l^{-1}$	$\mu mol\ l^{-1}$
MARINE [71]		
Warm surface	< 6	< 0.2
Deep Atlantic	52	1.7
Deep Pacific	78	2.5
FRESH [72]		
Large Rivers	1 - 3000	0.032 - 97
North American Lakes	0.5 - 150	0.016 - 4.8
SOIL [73]		
Runoff	300 - 20000	9.6 - 640
Leachate	2 - 400	0.064 - 12.8
WASTE		
Industrial Effluent	1000 - 25000	32 – 806
Urban Sewage	1000 - 5000	32 - 160

Particulate phosphorus (PP) is defined as that fraction which is retained by a 0.45 μm filter. Figure 8 indicates that PP may comprise material of biological origin (animal, plant, bacterial), weathering products (primary and secondary minerals), inorganic precipitates (authigenic minerals), organic and inorganic coprecipitates, organic aggregates, as well as phosphorus associated with aggregates through metal binding or adsorbed to the surface of clay and mineral particles. The determination of TDP, DOP, DCP and PP in natural waters necessitates a preliminary digestion step to convert the various phosphorus species to the detectable orthophosphate form.

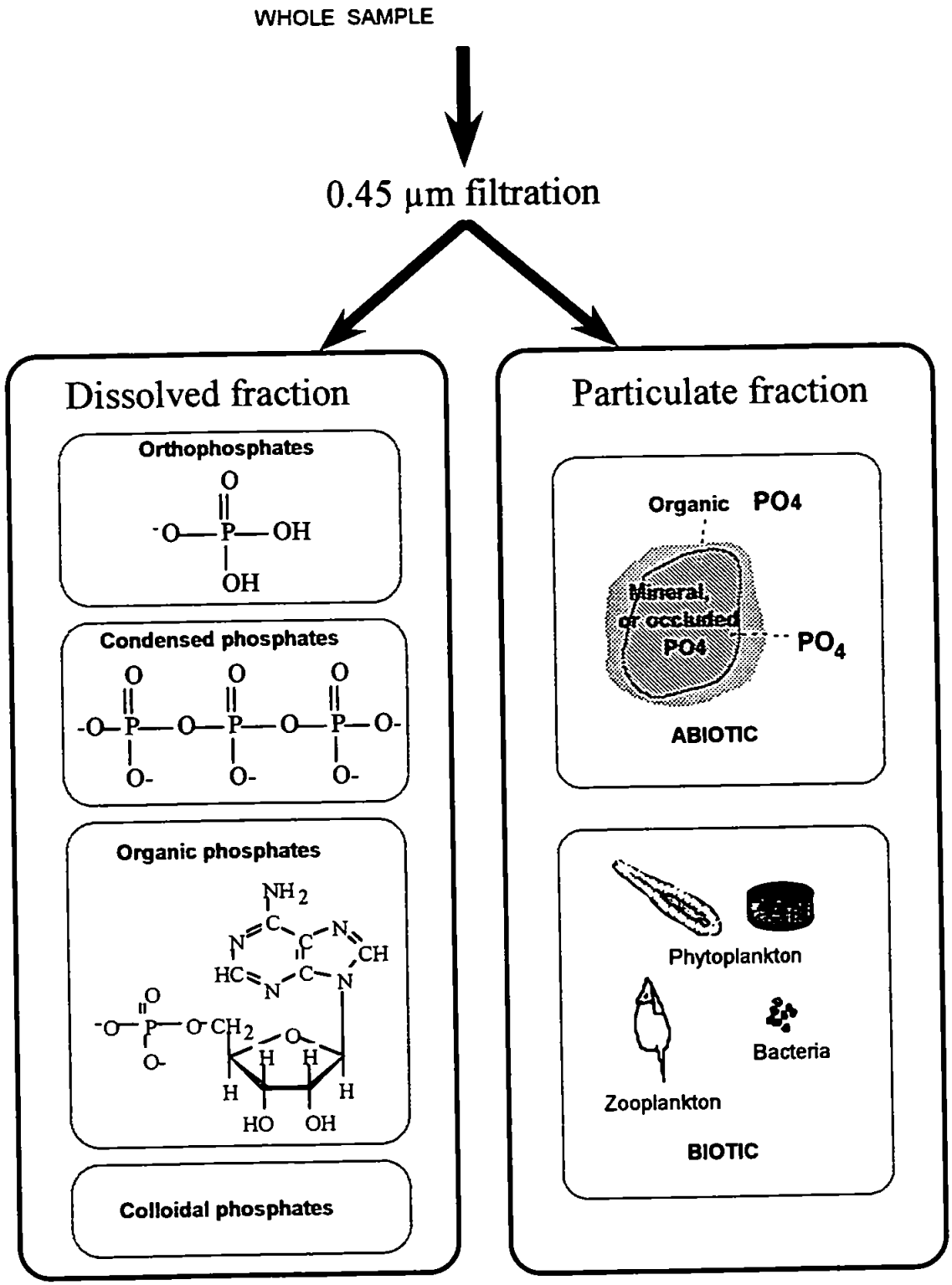

Figure 1.7: Representation of the major phosphorus components in the operationally defined dissolved and particulate fractions of a total sample, showing typical constituents.

It is generally recognised that orthophosphate is the most readily bio-available phosphorus (BAP) species [74] and traditionally this has been equated with the dissolved reactive phosphorus (DRP) fraction of a sample. However, some non molybdate-reactive components of the dissolved organic and condensed phosphate components, and even particulate phosphates, may also be utilised by algae and bacteria after hydrolysis by exocellular enzymes like alkaline phosphatase [75]. These enzymes are usually only exuded under conditions of orthophosphate deficiency, and their production may be inhibited by orthophosphate. Hence TDP and particulate phosphorus may also comprise phosphorus species which are potentially bioavailable, as well as refractory species which are bio-unavailable.

The "bioavailable" phosphorus concentration is conventionally estimated using an algal bioassay, in which water samples and orthophosphate standards are cultured with algae, under phosphorus-limited growth conditions, and the growth rates of the cultures monitored over 7-21 days by measurement of parameters such as cell number, biomass, or chlorophyll concentration [76]. By comparison of growth rates, an estimate can be made of the amount of bioavailable phosphorus that was present originally. Algal bioassays may be performed on filtered samples to provide a measure of the readily or immediately BAP, or on total samples, i.e. including particulate material, in which case they are used, along with chemical extraction techniques, to estimate potential or long-term BAP [77]. Algal bioassays, as well as being slow and labour intensive, are subject to large statistical noise, and are therefore often unsuitable for estimation of BAP in low nutrient waters; for this reason DRP has often been used as a de facto measure of BAP. However, as described below, DRP may overestimate BAP, and hence the development of alternative fast, reliable, and precise chemical indicators for bioavailability is highly desirable.

1.4.2 DETERMINATION OF ORTHOPHOSPHATE

SPECTROPHOTOMETRIC METHODS

The majority of manual and automated methods of phosphate determination are based on the spectrophotometric determination of phosphorus as phosphomolybdenum blue [70], i.e.,

$$PO_4^{3-} + 12MoO_4^{2-} + 27H^+ \longrightarrow \underset{\text{12-phosphomolybdic acid}}{H_3PO_4(MoO_3)_{12}} + 12\,H_2O$$

Followed by:

$$H_3PO_4(MoO_3)_{12} \xrightarrow{\text{Reduction}} \text{Phosphomolybdenum Blue}$$

Many modifications of this method have been reported, usually involving use of reductants such as tin(II) chloride, ascorbic acid, 1-amino-2-napththol-4-sulphonic acid, sodium sulphite, hydrazine sulphate, or combinations thereof [78] or acid strengths in attempts to improve selectivity and stability of the chromophore produced [69]. The most widely-used methods for batch and automated analyses are based on the method of Murphy and Riley [79] which utilise ascorbic acid reduction with a potassium antimonyl tartrate catalyst. The method suffers little interference from silica, which is, however, a common problem in many other phosphomolybdenum blue based procedures. Ascorbic acid is preferred to tin (II) chloride as the reducing agent in batch analysis because the reaction is less salt and temperature sensitive, and a more stable chromophore is produced [80].

Spectrophotometric DRP measurements have been shown to overestimate orthophosphate in a number of studies, because of molybdate and/or acid-induced hydrolysis of labile organic and condensed phosphorus species [2,68,77]. Therefore, use of

DRP as a predictor of readily bioavailable P is questionable. Other workers have found that total reactive phosphorus (TRP), the molybdate reactive phosphorus fraction in unfiltered sample, is as good a measure of BAP as DRP [81], but this may also lead to over estimations because of hydrolysis of labile P-compounds.

A number of authors have examined the "DRP overestimation" and some have proposed techniques to minimise the hydrolysis of labile organic and condensed P compounds. Chamberlain and Shapiro [81], for example, reported a "6-second" technique in which the phosphomolybdate-forming reaction was stopped by adjustment of acid strength prior to formation of phosphomolybdenum blue. Tarapchak [82] confirmed that hydrolysis of DOP occurred very rapidly, in both acidic and acid-free molybdate, and Dick and Tabatai [83] claim to have overcome this problem by complexing surplus molybdate with a citrate-arsenate reagent.

EXTRACTION METHODS

A variety of solvent extraction techniques have been applied to spectrophotometric DRP analyses either before or after the reduction step [78], to improve detection limits and minimise interferences. Solvents such as amyl alcohol, benzene, 1-butanol, 2-butanol, chloroform and butyl acetate have all been used for this purpose [78]. More recently the use of gel phase/sorbent extraction [84-86] has been described, in which phosphomolybdenum blue, or a related ion pair was adsorbed onto Sephadex or C18, and quantitation achieved by absorptiometry or reflectance spectrometry.

The use of classical solvent extraction has fallen out of favour because it is slow, and in some cases involves toxic solvents. Nevertheless, it remains a viable option where enhancement of the detection limit is required, and may become more acceptable if it can be

performed on a micro-scale, by techniques such as flow injection (FI) extraction, which use minimal solvent and are highly reproducible.

ION PAIR METHODS

Some dye substances and organic molecules (e.g. methylene blue, methyl violet, rhodamine B, quinine, crystal violet) form ion pair complexes with phosphomolybdate at low pH [78]. Malachite green has been shown to enhance the sensitivity by as much as 30 times, but is not widely used because of problems with instability of the ion association complex. The ion pair complex formed can be detected by either spectrophotometry or fluorimetry. Application of a sensitive light-scattering method for determining phosphate as a porphyrin-phosphomolybdate ion pair has also be reported [87].

AUTOMATED SPECTROPHOTOMETRIC METHODS

Segmented continuous flow techniques using photometric detection have been applied extensively to the analysis of DRP and TP (post digestion), and some very sensitive procedures have been reported [88]. Flow injection was rapidly adopted for the determination of various phosphorus species in waters, and has been used for the shipboard determination of DRP [89], and the in situ analysis of streams [90] and wastewaters [91] (see below.)

Techniques like FI may enable chemistries that are unsatisfactory in batch mode to be used advantageously in automated mode. In batch mode, for example, the tin (II)chloride reduction of 12-phosphomolybdic acid is prone to salt effects and is very temperature dependent. However in FI mode, these deficiencies can be overcome because the timing of reagent addition and mixing sequences are well-controlled, and frequent recalibration is

possible. Hence, the advantages of the fast kinetics of the tin(II) chloride reduction reaction can be exploited to give improved detection limits.

Typical detection limits for various phosphorus methods, including those based on spectrophometry are shown in Table 1.2.

ELECTROCHEMICAL METHODS

A number of potentiometric methods have been reported for the detection of orthophosphate. These include direct methods [92,93] using phosphate specific electrodes, and indirect methods involving lead, [94] calcium, [95] or cadmium [96] ion selective electrodes (ISE's). However, for dilute waters with a low P concentration, ISE's suffer from a lack of sensitivity, and in the case of the indirect methods, from a lack of selectivity.

Table 1.2: Examples of methods for the analysis of phosphorus species, with indicative detection limits (MRP = molybdate reactive phosphorus).

Technique/Method	Species Detected	Typical Detection Limit for P		Comments	Reference
		$\mu g\ l^{-1}$ P	μM		
Molecular spectroscopic techniques					
Visible photometry Phosphomolybdenum blue - Batch method	MRP	150 10	4.8 0.32	10 mm cell 100 mm cell	[30]
Visible photometry Phosphomolybdenum blue-FI method.	MRP	10	0.32		[97]
Visible photometry Phosphomolybdenum blue-FI ion exchange preconcentration technique.	MRP	0.4	0.013	Lower detection limit possible; detection limit defined by extent of preconcentration used	[98]
Visible photometry Phosphomolybdenum blue-FI reagent injection technique.	MRP	12	0.39	In-situ monitoring system, LED-photodiode detector	[90]

Table 1.2: *Continued*

Technique/Method	Species Detected	Typical Detection Limit for P		Comments	Reference
Molecular spectroscopic techniques continued					
Visible photometry Phosphomolybdenum blue-FI reagent injection technique.	MRP	2.5	0.08	Shipboard monitoring system, LED-photodiode detector	[99]
Visible photometry Phosphomolybdenum blue-Segmented continuous flow system.	MRP	0.4	0.013	50 mm path length detection cell.	[88]
Visible photometry Phosphomolybdate-Malachite green ion pair - FI method	MRP	10	0.32		[100]
Visible Spectrophotometry Phosphomolybdate-Crystal Violet ion pair - FI method	MRP	20	0.64		[101]
Visible Spectrophotometry Phosphomolybdate-Malachite green ion pair - FI solvent extraction method	MRP	0.1	0.003		[102]
Visible Spectrophotometry Phosphomolybdate-Malachite green ion pair - FI solvent extraction method	MRP	0.06	0.002		[103]
Long pathlength capillary spectrophotometry	MRP	0.03	0.001	Off- line color development	[104]
Thermal lens spectroscopy	MRP	0.005	1.6×10^{-4}		[105]
Thermal lens spectroscopy	MRP	0.7	0.023	Solvent extraction pre-treatment	[106]
Fluorescence quenching of phosphomolybdate	MRP	2	0.065	Quenching of Rhodamine 6G by phosphomolybdate. Fluorescence-FI method	[107]
Atomic spectroscopic techniques					
Inductively coupled plasma-atomic emission spectrometry	Total phosphorus	20	6.5	For most sensitive emission line	[108]
Inductively coupled plasma-atomic emission spectrometry-FI	Total phosphorus + MRP	500	16	With 200µL injection in FI mode.	[109]
		70	2.3	Continuous aspiration mode	

Table 1.2: *Continued*

Technique/Method	Species Detected	Typical Detection Limit for P		Comments	Reference
Atomic spectroscopic techniques continued					
Inductively coupled plasma-mass spectrometry	Orthophosphate	8	0.26	Liquid chromatographic separation of model phosphate compounds with ICPMS detection	[110]
Electrochemical techniques					
Potentiometry-FI	Orthophosphate	ca. 310	ca. 10	Indirect detection using Cd(II) electrode	[96]
Potentiometry-FI	Orthophosphate + tripolyphosphate	310	10	Indirect detection using Pb(II) electrode - better selectivity for $SO_4^{=}$	[94]
Enzyme electrode	Orthophosphate	775	25	Biosensor based on glucose 6'phosphate inhibition of hydrolysis by potato acid phosphatase. High selectivity for F^-	[111]
Enzyme electrode-FI	Orthophosphate	3	0.1	Amperometric detection of H_2O_2 produced by interaction of phosphate with co-immobilized nucloside phosphorylase and xanthine oxidase	[112]
Voltammetry-FI	MRP	20	0.65	Amperometric detection of phospho-molybdate species	[113]
Voltammetry-FI	MRP	0.62	0.02	Amperometric detection of phospho-molybdate species. Substantial interference from silicate	[114]
Voltammetry	MRP	ca. 6	ca. 0.2	Differential pulse anodic voltammetry of the phosphomolybdate complex	[115]
Voltammetry	MRP	9	0.29	Differential pulse polarographic detection of catalytic reduction of perchlorate or nitrate by solvent extracted phosphomolybdate	[116]

Table 1.2: *Continued*

Technique/Method	Species Detected	Typical Detection Limit for P		Comments	Reference
Separation Techniques					
High performance liquid chromatography	$H_2PO_4^-$	750	24	HPLC determination of hypoxanthine produced by nucleoside phosphorylase catalysed reaction of phosphate with inosine	[117]
Ion chromatography	$H_2PO_4^-$	14.7	0.47	Unsuppressed IC - Indirect UV detection, 1 mL injections	[118]
Ion chromatography	$H_2PO_4^-$	2	0.06	Suppressed IC, conductivity detection, concentrator column	[119]
Capillary electrophoresis	$H_2PO_4^-$	0.6	0.02	Preconcentration by isotachophoresis, with conductimetric detection	[120]
Capillary electrophoresis	$H_2PO_4^-$	0.3	0.01	Electromigrative preconcentration, UV detection.	[121]

A number of amperometric methods have also been described. Many of these involve the determination of orthophosphate as phosphomolybdate, and as such, they overestimate orthophosphate in the same way that the spectrophotometric DRP method does [113,114]. However, enzyme electrodes have been described in which orthophosphate generates H_2O_2 which is then measured amperometrically. These have high specificity and sensitivity, [122,123] and may prove to be applicable for environmental measurements. For example, a sensitive enzyme electrode consisting of membrane co-immobilized nucleoside phosphorylase and xanthine oxidase has been described by D'Urso and Coulet [112] (see Table 1.2.)

CHROMATOGRAPHIC METHODS

Chromatographic techniques, in which orthophosphate is separated by virtue of its charge or mass/size have been reported extensively, and would satisfy the requirement for specific orthophosphate measurement. Ion-chromatography (IC) may be used for phosphate separations, but is generally slow, relatively insensitive, and usually unsuited to samples with high ionic strength unless some matrix modification is performed. Detection of low levels of phosphate is possible if large sample injections or trace enrichment techniques are used [118,124]. Improved sensitivity of phosphorus detection in IC may also be achieved by post-column molybdate reactions of the type described by Jones et al. [125].

The use of ion-exclusion high performance liquid chromatography (HPLC) for the separation of phosphate from strong acid ions and some condensed phosphates, followed by coulometric and conductometric detection, has also been described [126]. Good separations were obtained but the method was slow (3 h^{-1}) and relatively insensitive.

Capillary electrophoresis (CE) techniques have also been applied to orthophosphate analysis, and while generally offering much faster separations of anions in waters, have suffered from a lack of sensitivity. However recent advances in on-capillary preconcentration using isotachophoresis [120,121] have enabled sub $\mu g\ l^{-1}$ detection limits to be achieved in high ionic strength matrices, and this approach is a most promising one for environmental analysis.

ENZYMATIC METHODS

At least two enzymatic methods for orthophosphate determination have been reported. Petterson [127] utilised the inhibitory effect of orthophosphate on the hydrolysis of alkaline phosphatase substrates. By measuring the fluorescence of the product, as little as 0.1 $\mu g\ l^{-1}$ P could be detected in natural waters. Interference was not caused by trace metals or

oxyacids such as arsenate or silicate, but did occur when phosphomonoesters and organic phosphates were present. Stevens [128] also applied an enzymatic technique to the determination of orthophosphate over the range 5 - 200 $\mu g\ l^{-1}$ P in natural waters. The basis for this determination was the reaction of orthophosphate with glyceraldehyde-3-phosphate to produce 1,3-diglycerophosphate in the presence of glyceraldehyde-3-phosphate dehydrogenase and oxidised nicotinamide-adenine dinucleotide. Reduced nicotinamide-adenine dinucleotide formed by this process was detected spectrophotometrically as formazin and used as a measure of orthophosphate. Both these enzymatic orthophosphate methods gave consistently lower results than phosphomolybdate-based DRP when applied to natural waters.

PRECONCENTRATION METHODS

Significant preconcentration of DRP and other dissolved species prior to spectrophotometric detection has been achieved using ion-exchange, adsorption or coprecipitation, e.g. Freeman et al. [98] achieved a detection limit of 0.4 $\mu g\ l^{-1}$ P using FI with on-line ion-exchange preconcentration of orthophosphate. Because phosphorus is concentrated as ion-exchangeable phosphate, this technique arguably yields "true" orthophosphate values.

Magnesium-induced coprecipitation ("MAGIC") was used [129] to determine DRP and total dissolved phosphorus (TDP) at nanomolar concentrations in seawater, and similar techniques involving hydrous iron(III) oxide in suspended [130] and fibre-bound [131] forms have been described for preconcentration of both inorganic and organo-phosphorus species.

Phosphomolybdenum blue can also be preconcentrated prior to detection, using solvent or gel phase extraction techniques. Susanto et al. [132] have recently reported the

preconcentration of the phosphomolybdate-malachite green ion association complex on cellulose nitrate membrane filters. After dissolution in an organic solvent, a detection limit of 0.06 μg l^{-1} P was achieved using a 10 mL sample in an FI system with spectrophotometric detection.

MISCELLANEOUS METHODS

A wide variety of other analytical techniques has been applied to the analysis of phosphate in waters, e.g. neutron activation analysis, indirect atomic absorption spectrometry, X-ray fluorescence (after phosphate adsorption onto modified silica), and radio-activation analysis [133], but their applicability to routine nutrient analysis is generally limited.

1.4.3 DETERMINATION OF TOTAL PHOSPHORUS

THERMAL DIGESTION

The batch measurement of TP and TDP traditionally involves digestion prior to detection as phosphomolybdenum blue. Commonly-used digestion methods for TDP/TP involve heating or autoclaving of sample with peroxydisulfate alone or with acidic peroxydisulfate. These methods may give incomplete recoveries for some samples, and the use of nitric-sulphuric or nitric-sulphuric-perchloric acid mixtures may be required [70]. Other workers [134,135] have used high temperature fusion with magnesium sulfate or nitrate to convert TDP/TP to orthophosphate. A number of FI methods for TP/TDP have also been reported which involve the use of high temperatures (140-160 °C), increased pressures, and long capillary reactors [136].

Sample throughput of these systems is typically 10 - 15 h^{-1}. Proper evaluation of these, and other digestion methods, should entail the use of both organic and condensed phosphorus spikes, in addition to orthophosphate.

The use of microwave ovens for batch sample digestion has become widespread, and their application in FI for on-line TDP and TP digestion has been described. Hinkamp and Schwedt [137] used perchloric acid/peroxydisulfate digestion with amperometric detection for TDP determination, and obtained recoveries of 91-100% for organic phosphates, and 60-70% for condensed phosphates. A similar FI digestion system, incorporating a filter after the digestion step has been used for the determination of TP [138]. Results obtained using this system were in excellent agreement with those obtained using batch nitric-sulphuric acid digestion.

PHOTOCHEMICAL DIGESTION

Ultraviolet (UV) photo-oxidation can be used to mineralise organic matter and has been applied to the determination of DOP [139,140]. Solorzano and Strickland [141] have suggested that because condensed phosphates are not susceptible to UV photo-oxidation, its use provides a basis for differentiating TDP and DOP. However in soil leachates and runoff waters the concentration of condensed phosphates is generally very low (due to rapid biological breakdown) and the difference in concentration between DOP and TDP is therefore negligible [141].

An FI method for determining DOP in natural waters by photo-oxidation with alkaline peroxydisulphate in a PTFE photoreactor incorporating a low power, medium pressure mercury lamp has been reported by McKelvie et al. [142] but this method while excellent for many natural waters was unsuitable for soil waters containing higher concentrations of dissolved aluminium or iron [143].

ATOMIC SPECTROMETRIC METHODS

Inductively coupled plasma-atomic emission spectrometry (ICP-AES) can be used for the determination of TP in wastewaters and some natural waters [133]. Application of ICP-AES circumvents the need for time-consuming predigestion, and is an effective but insensitive method for TP determination (Table 1.2). Improvements in sensitivity could be achieved using FI preconcentration techniques, or by the use of inductively coupled plasma-mass spectrometry (ICP-MS) [110]. However, the cost and relative complexity of both ICP-AES and ICP-MS largely precludes their application for in situ analysis.

A combined ICP-AES and colorimetric system for quasi-simultaneous determination of DRP and TP in wastewaters has been reported [109]. ICP-AES and ICP-MS may also be used for speciation of dissolved phosphorus if used for post-chromatographic detection [110].

1.4.4 DETERMINATION OF INDIVIDUAL PHOSPHORUS SPECIES

SEPARATION METHODS

Gel filtration has been used to determine the characteristics of dissolved high molecular weight phosphorus (HMWP) in natural waters, and to discriminate between DRP and "true" orthophosphate. For example, Downes and Paerl [144] performed Sephadex G25 - G150 chromatography on lake water DRP. In some water samples, they found significant amounts of molybdate reactive high molecular weight phosphorus (RHMWP) that was bioavailable. They suggested that hydrolysis of this RHMWP may account for the overestimation of orthophosphate by colorimetric DRP methods involving acidic molybdate. White and Payne [145], using the same approach, found that RHMWP comprised as much as 70-80% of total DRP in eutrophic waters, but was undetectable in more pristine waters. Again, RHMWP

was shown to be bioavailable to inorganic P-starved algae. In all of these studies, gel filtration was performed on large columns, and subsequent TDP analysis of the eluted solutes was done on collected fractions. Consequently, one gel filtration separation could take from 30 to 120 minutes, plus several hours for analysis of the fractions by batch methods. Further, solute-gel interactions may cause adsorptive effects which are difficult to eliminate, and it is arguable that some of the elution peaks reported for gel filtration separations of DOP may be artefacts of this effect, rather than identifiable species. The optimization and rapid separation of orthophosphate and HMWP in unconcentrated water samples using gel filtration in conjunction with a photo-oxidation FI system has, recently been described [146].

Ultrafiltration has been used to separate orthophosphate from HMWP species [65], and has been proposed for the determination of BAP [68]. However in both ultrafiltration and gel filtration, membrane or gel interactions with the solute can be problematic, and the separation times very lengthy.

Clarkin et al. [147] recently reported use of an ion exchange HPLC system incorporating a UV-photo-oxidation post-column reactor capable of separating inositol phosphate congeners. While good separation of these species was obtained, the system was slow and samples required extensive preconcentration.

The high resolution of capillary electrophoresis might also be applied to the separation and identification of DOP species in natural waters, but would require the use of preconcentration, or more sensitive detection methods than are currently available.

ENZYMATIC METHODS

Exocellular alkaline phosphatase is important in the utilisation of DOP by algae and bacteria through enzymatic hydrolysis [148,149]. It has been shown that the alkaline

phosphatase hydrolysable phosphorus (APHP) i.e., the orthophosphate liberated following incubation of a water sample with alkaline phosphatase [150,151], is significantly greater (typically 100 – 1500 $\mu g\ l^{-1}$ P) than DRP in hypereutrophic waters. A potential deficiency of this approach is product inhibition of the alkaline phosphatase by orthophosphate already present, or that produced by hydrolysis. This problem is minimised if an immobilised alkaline phosphatase reactor of suitable size and activity is used in conjunction with FI [152]. Results obtained suggest that the APHP pool is very small (less than 10 $\mu g\ l^{-1}$ P) in natural waters, with only appreciable amounts being found in wastewaters [153].

Some organic phosphorus species are not susceptible to hydrolysis by alkaline phosphatase, and consequently may not be as readily bioavailable. Similar enzymatic techniques involving RNase and DNase, [154,155] and phytase [156,157] have been described, and will be important in elucidating the nature of the less bioavailable fractions of aquatic phosphorus.

CHEMICAL EXTRACTION METHODS

While the dissolved fraction contains readily bioavailable phosphorus which can be estimated by DRP, true orthophosphate, or better still by measurement of orthophosphate and enzyme-available phosphorus [153], the particulate phase may contain appreciable amounts of potentially bioavailable phosphorus which must be extracted before analysis. However the relevance of sequential chemical extraction schemes adapted from soil science and applied to the determination of available PP in suspended sediments has been questioned [158], and it is arguable that a simple alkaline extraction with, for example, NaOH may suffice [159,160]. Use of iron oxide-impregnated paper strips as a means of extracting sorbed PP has also been advocated, and has been shown to give results similar to that obtained using NaOH extraction [161]. This approach merits further investigation.

OTHER METHODS

The use of 31P NMR for the identification of phosphorus functional groups in natural waters has been described [162,163]. A disadvantage of this approach however, is the low sensitivity and the attendant requirement for extensive preconcentration. Coprecipitation followed by X-ray fluorescence has also been described for the identification of organophosphate species in marine waters [164].

1.4.5 IN SITU DETERMINATION OF PHOSPHORUS SPECIES

Most of the techniques and methods described have been restricted to laboratory use. However, the application of in situ monitoring techniques for determination of phosphorus species in the field would provide a number of distinct advantages, e.g. it would facilitate the study of the rapid phosphorus transport kinetics that occur in aquatic ecosystems. The development of instruments to measure the concentrations and fluxes of the various forms of phosphorus in aquatic systems with high frequency or even in real-time will allow more reliable estimates of nutrient loads in streams, enable better compliance monitoring, and provide improved control of wastewater treatment processes. Use of in situ analysis techniques would also obviate problems associated with loss of sample integrity during transport or storage pending analysis. FI techniques, with their attendant advantages of rapid sample throughput, good precision, minimal reagent use, ease of calibration and ready adaptability to a wide variety of different applications, are ideally suited to in situ analysis.

FI systems have been successfully used for in-situ monitoring of DRP in natural waters [90], at sea [99] and in sewage treatment plants [91]. As with any in situ monitor, great care must be taken with sample presentation and reagent stability if reliable performance is to be achieved. Two most important issues that must be addressed are the removal of particulate matter (usually by an in-line filter) and minimisation of biofouling [165].

1.4.6 Basic Principles of Flow Injection Analysis

Flow injection (FI) is based on the injection of a liquid sample into a moving, unsegmented carrier stream of a suitable liquid. The injected sample forms a zone which is transported towards a detector that continuously records the absorbance, electrode potential or other parameter as the sample passes through the flow cell [166-168].

FI has found a wide range of applications in research, routine analysis and the teaching of analytical chemistry. Its inherent versatility has allowed it to be adapted to the different detection systems of electrochemistry, molecular spectroscopy and atomic spectroscopy, using a wide variety of manifold configurations. FI systems have also been designed to dilute or preconcentrate the analyte; to perform separations based on solvent extraction [165], ion exchange [90], gas diffusion or dialysis [169]; and to prepare unstable reagents in situ. Optimisation and design of the flow channels to achieve maximum sampling frequency, best reagent and sample economies, and proper exploitation of the chemistries is possible through understanding of the physical and chemical processes taking place during the movement of the fluids through the FI channel.

The simplest FI analyser consists of a pump, which is used to propel the carrier stream through a narrow tube; an injection port, by means of which a well-defined volume of a sample solution is injected into the carrier stream in a reproducible manner; and a microreactor in which the sample zone reacts with the components of the carrier stream, forming a species that is sensed by a flow through detector and recorded. A typical recorder output has the form of a peak (Figure 1.8), the height H, width W, or area A of which is related to the concentration of the analyte. The time span between the sample injection S and the peak height H, is the residence time T during which the chemical reaction takes place. With rapid response times, typically < 1 minute, a sampling frequency of two samples per minute can often be achieved. The injected sample volumes may be between 1 and 600

μl which in turn requires no more than 1.0 ml of reagent per sampling cycle. This makes FI a simple, automated microchemical technique, capable of having a high sampling rate and a low sample and reagent consumption.

FI is based on a combination of three principles: sample injection, controlled dispersion of the injected sample zone, and reproducible timing of its movement from the injection point to the detector. Chemical reactions take place whilst the sample material is dispersing within the reagent. The concentration gradient of the sample zone being formed by the physical dispersion process, where the sample zone broadens as it moves downstream and changes from the original asymmetrical shape to a more symmetrical and eventually Gaussian form [168]. Sample treatment proceeds in exactly the same way for all subsequently injected samples.

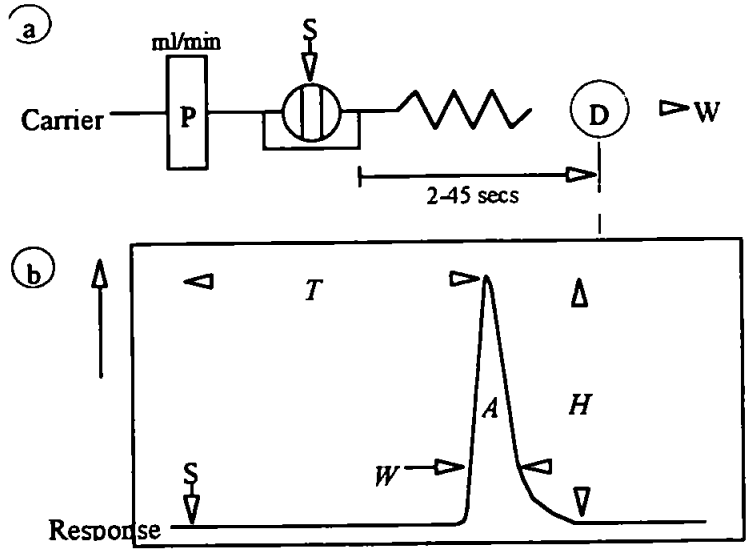

Figure 1.8 : Simple FI manifold; P is the pump, S is the injection valve, D is the flow-through detector and W is waste. b.) Chart recorder Output; the recording starts at *S*, *H* is the peak height, *W* is the peak width, A is the peak area and *T* is the residence time corresponding to the peak height.

DISPERSION COEFFICIENT (D)

A sample contained in the sample loop of the injection valve is homogeneous and has an original concentration C° that, if it could be scanned by a detector, would give a square signal the height of which would be proportional to the sample concentration. When the sample zone is injected, it follows the movement of the carrier stream, forming a dispersed zone, the form of which depends on the geometry of the channel and the flow velocity [170]. Therefore, the response curve has the shape of a peak reflecting a continuum of concentrations, (concentration gradient). This continuum of concentrations can be viewed as being composed of individual elements of fluids, each having a certain concentration, C. The dispersion coefficient, D is defined as the ratio of concentrations of sample material before and after the dispersion process.

$$D = C^{\circ} / C$$

If $D = 2$, the sample solution has been diluted 1:1 with the carrier stream. For convenience, sample dispersion has been defined as limited (D = 1 - 3), medium (D = 3- 10), and large (D > 10). The FI peak is a result of two kinetic processes that occur simultaneously: the physical process of zone dispersion and the chemical process resulting from reactions between sample and reagent species. The underlying physical process is well reproduced for each individual injection cycle; yet it is not a homogeneous mixing, but a dispersion, the result of which is a concentration gradient of sample within the carrier stream. The dispersion coefficient is a theoretical concept, which does not correspond to any actual concentration within the dispersed sample zone. A dispersed sample zone is not composed of discrete elements of fluid, but only imagined by the detector at any time as an apparent discrete section of the concentration gradient. The D value is always related to a certain

time, which in FI is usually the period elapsed from the sample injection, to the moment the dispersed element of sample material passes through the observation field of the detector.

EFFECT OF SAMPLE VOLUME

By injecting increasing volumes of solution, a series of curves will be recorded, all starting from the same point of injection *S*, where the height of the individual peaks will increase until an upper limit 'steady state' has been reached. At this final level the recorded absorbance will correspond to the concentration of undiluted sample $C°$, and $D = 1$. The rising edge of all curves coincides and has the same shape regardless of the injected volumes. Where $n = S_v / S_{1/2}$, S_v is the sample volume, and $S_{1/2}$ is the volume of the sample solution necessary to reach 50 % of the steady state value, corresponding to $D = 2$. By injecting two $S_{1/2}$ volumes, 75 % of $C°$ is reached, corresponding to $D = 1.33$; and so on. Injection of five $S_{1/2}$ volumes results in $D = 1.03$ and injection of seven $S_{1/2}$ volumes results in $D = 1.008$, corresponding to 99.2 % of $C°$. An increase in peak height and in sensitivity of measurement is achieved by increasing the volume of the injected sample solution. Dilution of overly concentrated samples is best achieved by reducing the injected volumes.

EFFECT OF CHANNEL LENGTH AND FLOW RATE

The microreactor between the injection port and the detector may have different lengths, diameters, and geometry. The influence of coil length L and inner diameter of the tubing d on the dispersion has been studied in detail [166]. The use of tubing of a small diameter will result in lower $S_{1/2}$ values, because the same sample volume will occupy a longer length of tube (θ), since $S_v = \pi(0.5d)^2\theta$ and will, owing to the restricted contact with the carrier stream, be less easily mixed and dispersed. If the tube diameter d is halved, the sample will

occupy a fourfold longer portion of the tube (θ), and, hence, the $S_{1/2}$ value will be four times smaller. There are practical considerations that prevent the use of channels with too narrow a bore or too tightly packed reactors because: the flow resistance will increase; the system might easily become blocked by solid particles; and the flow cell used in spectrophotometric detection must have an optical path with an inner diameter of 0.5 - 1 mm, to allow sufficient light to pass through. The optimum internal diameter of tubes (usually PTFE) connecting the injection port and the detector is 0.5 mm although 0.75 mm internal diameter is useful for the construction of systems with large dispersion, and 0.3 mm for systems with limited dispersion.

The mean residence time T will depend, for a reaction system made of tubing of uniform internal diameter, on the tube length L, the tube diameter d, and the pumping rate Q. For systems of medium dispersion where the sample has to be mixed and made to react with the components of the carrier stream, one would tend to increase the tube length L in order to increase T. However, one can expect that dispersion of the sample zone to increase with the distance travelled, and this band broadening will eventually result in loss of sensitivity and lower sampling rate. So, instead of increasing the length L, one can decrease the pumping rate Q and keep L as short as is practically possible.

EFFECT OF CHANNEL GEOMETRY

The effectiveness of various mixing geometries are shown in Figure 1.9. The coiled tube is the most frequently used geometric form of the FI microreactor. There are however different channel geometries; these are straight tube, coiled tube, mixing chamber, single bead string reactor, and 3-D or 'knitted' reactor. The function of these reactors is to increase the intensity of radial mixing. Thus, the reagent becomes more readily mixed with the sample , and the axial dispersion of the sample zone is reduced.

In a straight tube of uniform diameter, the parabolic profile formed by laminar flow remains undisturbed up to a flow velocity not normally reached in a typical FI system, and since the radial diffusion occurring in the time frame of an FI experiment is not sufficient to offset the axial dispersion initially formed during sample injection, an asymmetrical peak is recorded.

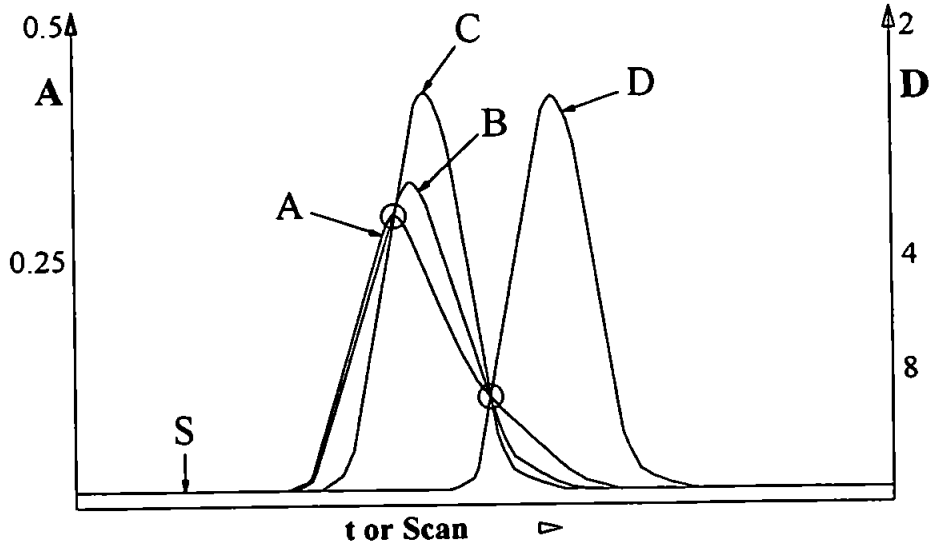

Figure 1.9 : Dispersion of a dye, injected as a sample zone into: A, straight tube; B, coiled tube; C, 'knitted tube'; and D, a SBSR reactor. Peaks were recorded with microreactors of identical length, but different geometry (129).

A coiled tube is the most frequently used reactor geometry, since it can conveniently accommodate any length of tubing in an experimental set-up and also because secondary flow within the coiled tubing promotes mixing in the radial direction. The result is a more symmetrical, higher and narrower peak than if an identical straight tube length had been used. The tighter the coiling of the tube is, the more pronounced this effect. Also, the longer the tube is, the longer the time for mixing and therefore the more symmetrical the obtained peak.

The mixing chamber was first used in the early FI titration systems [166] where a magnetic stirrer was used to promote reproducible homogeneous mixing of sample and

reagents. But the use of this type of geometry has many drawbacks, such as large dispersion giving reduced sensitivity, low sample throughput and large sample and reagent volumes, which is undesirable for systems which need to moderate their consumption. A single bead string reactor (SBSR) [171] is the most effective device to promote radial mixing in a tubular reactor. The SBSR allows symmetrical peaks to be obtained within the time domain and channel length of a typical FI manifold. However, small air bubbles and solid particles tend to be trapped in SBSR which may increase carryover and flow resistance. A three dimensional disoriented (3-D reactor) or 'knitted' reactor can be made by tightly and irregularly knotting a suitable length of tubing. The chaotic movement of the carrier stream through a spatially disoriented path promotes radial dispersion almost as effectively as a SBSR without its drawbacks.

1.5 EFFECT OF COMPACTION ON THE TRANSPORT OF PHOSPHORUS SPECIES THROUGH RE-PACKED SOIL COLUMNS

The use of mechanical farming methods has come of age in the last fifty years. The use of modern agricultural equipment places high stresses on soil and can have direct effects upon soil physical characteristics. In turn, these physical changes affect solute transport, biological activity and crop production.

Compaction of soil occurs when a load is applied to the surface of the soil, usually by agricultural machinery. The extent of compaction is a function of the applied load properties and soil condition (in particular water content) at the time of compaction. Finite Element modelling has been used to the predict the extent of compaction for given input parameters [172]. Models describing the increase in bulk density with applied stress are available, but these are often just fitting functions with one or more arbitrary parameters [173], and these

models are not suited to the prediction of the pore level effects of compaction. Schafer et al. [174] highlight some of the significant knowledge gaps that exist in the description and modelling of soil compaction behaviour.

Compaction also affects hydraulic properties [173] and consequently solute transport properties. However models predicting the effect of compaction on hydraulic conductivity are extremely limited [173]. Despite this the following general trends do apply; compaction decreases porosity (and consequently saturated water content), saturated hydraulic conductivity [175] and increases bulk density. On compaction, the air entry values of water retention models increase due to a decrease in largest pore size in the sample [176-179].

1.5.1 Solute Transport Models

Two distinct types of model are available for the modelling of solute transport in soil. Deterministic models in which a given set of events produce a definable outcome and stochastic models in which a given set of events do not produce a definable outcome.

Transfer Function Models

A transfer function is an application of the principles of linear superposition and mass balance to a finite soil volume bounded by an entrance and exit surface. Essentially they treat soil as a collection of aligned capillaries (Figure 1.3). The solute transport mechanisms within this soil volume are characterised by the application of a narrow pulse of solute tracer of total input mass M added to the entrance surface at time $t = 0$, the mass leaving the finite soil volume at the exit surface may be recorded as a function of time.

Transfer function models do not have a definable outcome and therefore are stochastic. The outflow profile is given as a probabilistic interpretation as follows. If during a period of time t_j to t_{j+1} of length Δt a fraction of the total input mass m_j crosses the outflow surface

and assuming that M is not changed by production or decay of tracer its probability function may by written as ;

$$P(t_{j+1}) - P(t_j) = \frac{m_j}{M} \tag{1.21}$$

where $P(t)$ is the cumulative travel time probability density function describing the probability the a surface applied solute at $t = 0$ will cross the exit surface in a time less than or equal to t [180]. Equation 1.21 is a function of time when water flow is transient and under such conditions is too complex to be of practical use. Under steady state flow m_j simplifies to ;

$$m_j = j_w C^f(t_j)\,\Delta t \tag{1.22}$$

where j_w is the water flux and $C^f(t_j)$ is the concentration between t_j and t_{j+1}. The travel time probability density function $f(t)$ is defined as ;

$$f(t) = \lim_{\Delta t \to 0} \frac{P(t + \Delta t) - P(t)}{\Delta t} \tag{1.23}$$

and may be combined with Equations 1.21 and 1.22 to give probability density function ;

$$f(t) = \frac{C^f(t)}{\int_0^\infty C^f(t)\,dt} \tag{1.24}$$

Essentially, the normalised outflow flux concentration of a steady state flow experiment in which a narrow pulse is applied is equal to f(t).

The probability density function is often assumed to be lognormal, but this assumption is not always valid [181]. Jury [182] has developed a transfer function model which models hetrogeneities in solute transport that are impossible to measure with the convection dispersion equation. Because transfer functions are not directly concerned with physical processes it has been suggested that it will outperform the convection dispersion equation in field situations.

CONVECTION DISPERSION EQUATION MODELS

The convection dispersion equation (CDE) is both deterministic, mechanistic (makes assumption about the nature of the physical processes occurring) and in its most simple form (given in Equation 1.25) one dimensional.

$$\frac{\partial C}{\partial t} = D\frac{\partial^2 C}{\partial x^2} - v\frac{\partial C}{\partial x} \tag{1.25}$$

The equation relates solute concentration C at time t and distance (usually referred to as depth) x along its one dimensional axis. It does this by assuming that solute transport is a mixture of conduction (bulk transport) and dispersion, D. The model assumes that the dispersivity (D/v) remains constant with both time and depth. However, this assumption in field situations becomes progressively less valid as one moves from the time and depth at which the CDE is calibrated because of the heterogeneous nature of the system in question.

The equation due to its deterministic nature is best suited to laboratory situations where D and v can be kept approximately constant (steady state flow). Its application is straightforward if the appropriate boundary conditions can be met.

1.5.3 Phosphorus Transport Models

It is generally accepted that phosphorus adsorption is extremely important to the way in which phosphorus is transported into and through soil. In many cases phosphorus adsorption can be described by a fast reaction, followed by a slow one. Cameron and Klute [183] have described a CDE based model which incorporates kinetic adsorption of tracer. More recently a similar approach for unsaturated soils was proposed by Nielsen et al. [184]. A common difficulty with these models is that their parameters can not be obtained independently. Notodarmojo et al. [185] suggest for phosphorus that adsorption parameters in the CDE may be estimated by the empirical function $Z = k' C^n t^m$, where Z is the time dependant adsorption and k',m and n are parameters fitted from batch experiments. However this method of parameter estimation has been found to be suitable for only large differences (approximately 1000 fold) in adsorption rate [186] and can not be regarded as a quantitative predictor.

1.5.4 Pore-Cor Modelling of Breakthrough Curves

The Pore-Cor model has been used to predict trends in saturated hydraulic conductivity. The tortuosity of the unit cell may also be calculated. Pore-Cor has no parameters for directly predicting adsorption or retardation of a solute but because the generated networks have a readily calculable internal surface area, the adsorption CDE parameters for the breakthrough of phosphorus species may be given structural interpretation.

In Chapter 5 new [187] and existing FI techniques(Tecator Ltd, Method Application ASN 60-03/82) are used to monitor the breakthrough of orthophosphate, phytic acid and bromide through compacted and uncompacted repacked soil columns. The non reactive tracer, bromide is used to obtain convection and dispersion terms for each column and hence calibrate the CDE equation for phosphorus. A modified solution of the general convection dispersion equation is used to model the movement of these three species through the soil columns. The model parameters are then compared to the Pore-Cor predicted change in properties. How chapters 1 to 5 relate to the overall objectives of this thesis is shown in Figure 1.20

1.7 AIMS AND OBJECTIVES OF THIS RESEARCH

Chapter 2: To produce a model of soil void structure which conceptually is capable of predicting a diverse range of pore level properties such as permeability [45], hydrodynamic dispersion coefficient and internal surface area and compare the predictions made with experimental data.

Chapter 3: To compare the size distributions found in a real sample with those modelled by Pore-Cor.

Chapter 4: To develop a technique for the rapid determination if TDP in soil leachate and runoff waters.

Chapter 5: To correlate the change in structureless CDE parameters upon compaction with a change in the Pore-Cor Model parameters.

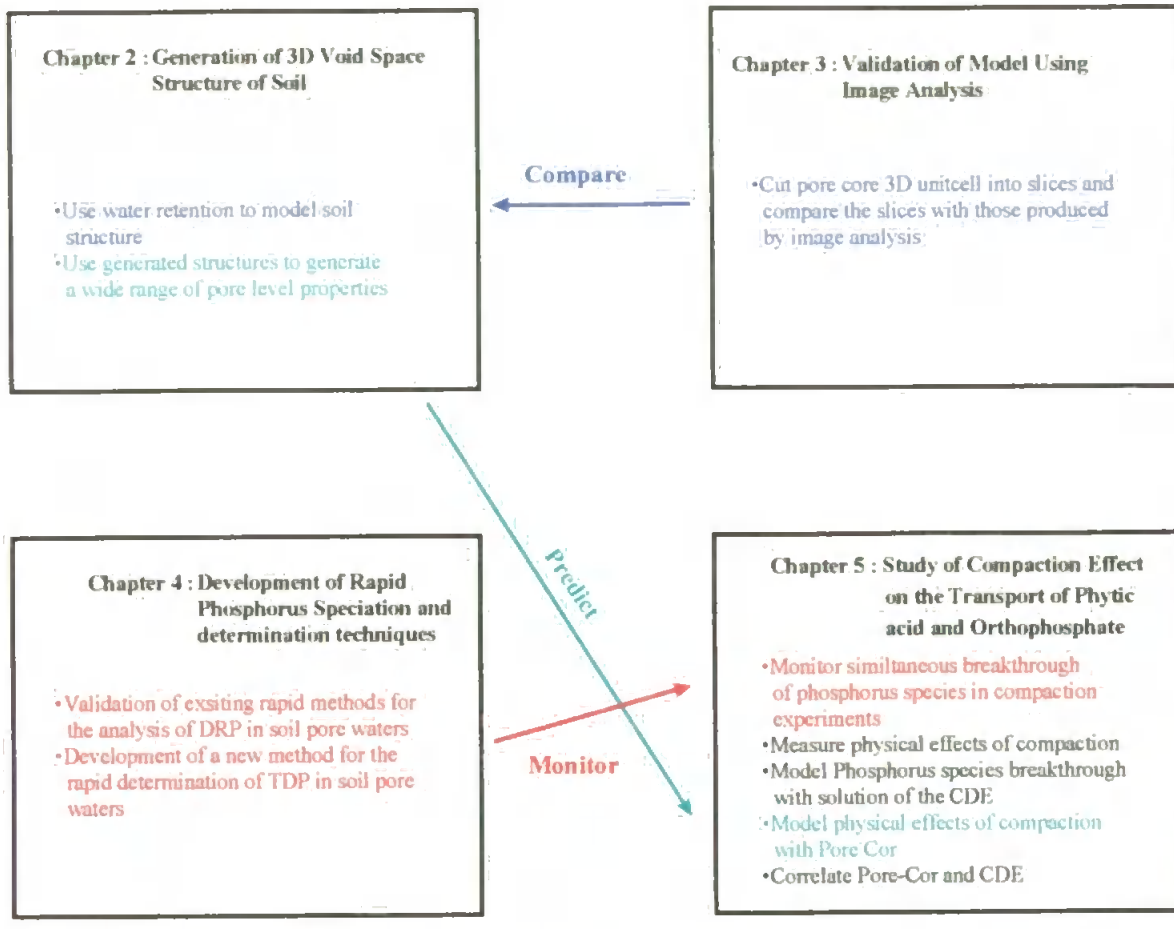

Figure 1.20 Linking of Experimental Chapters. Chapter 2, top LHS: A void space model (Pore-Cor) of soil is produced by simulating experimental water retention curves. Chapter 3, top RHS: The void space distributions are then compared to experiment so that the impact of the Pore-Cor's geometric assumptions can be observed. Chapter 4, bottom LHS: A rapid method for the determination of TDP in soil waters is developed and used later in Chapter 5 to produce breakthrough curves. Chapter 5, bottom RHS: Breakthrough curves are produced for phosphorus species under compacted and uncompacted conditions. The physical effects of compaction are modelled by Pore-Cor and the CDE model is used to quantify both physical and chemical changes. The two models are then correlated.

2.0 CHAPTER 2

THREE-DIMENSIONAL VOID SPACE MODELLING OF SOIL WATER RETENTION AND PREDICTION OF SATURATED HYDRAULIC CONDUCTIVITY

The conduction of water by soil is fundamental to the way in which soils transport nutrients and pollutants into groundwater. The derivation of relationships between water flow and void structure has traditionally relied on the implicit assumption that flow takes place through aligned cylindrical capillary tubes. We have described elsewhere [47] a new software package, called 'Pore-Cor', which uses a three dimensional void-space network geometry to model non-wetting fluid intrusion or wetting fluid drainage. We now describe how the software has been used to generate void space structures of Crediton Series soil samples (Devon, U.K.), such that the simulated water retention curves fit experimental data. The experimental drainage pressures were related to pore-throat entry diameters by the Laplace-Washburn equation. The necessities of using this equation, and of employing a simplified void-space geometry, introduce major approximations into the void space modelling. Nevertheless the model is sufficiently precise and versatile to produce useful predictions of trends in other properties, illustrated in this work by a close correlation between a predicted and experimental change in permeability with depth.

2.1 EXPERIMENTAL

The water retention curves used for modelling purposes were obtained from other laboratories, in which standard experimental techniques had been used. Water displacement was induced by applying differential pressure to a wet soil sample, using a sand table at low differential pressures and transferring to a sintered pressure plate at higher differential pressures [188]. The measurements of volumetric water content versus differential pressure produced the water retention curves. It was assumed that the soil structures were not significantly affected by shrinkage as the water drained out, a good approximation for soils without a high clay content.

Three different data sets were obtained. Two were derived from a soil named De Bathe, and one from a soil from the same classification series, named Crediton. The De Bathe soil is a sandy loam, which has been classified as a stony member of the Crediton series, located at Bathe Cross, near IGER North Wyke, Devon, UK [189]. Two laboratories were involved in obtaining the data - the Geography Department of the University of Plymouth, and the Soil Survey and Land Research Centre (SSLRC) at Shardlow. The data sets will be referred to as Set 1 (De Bathe Plymouth), Set 2 (De Bathe Shardlow) [190], and Set 3 (Crediton Seismic.) (Seismic is an SSLRC acronym for Spatial Environmental Information System for Modelling the Impact of Chemicals.) Set 2 was measured at the same depth intervals as Set 1, as described below.

A sample of the De Bathe soil was intruded with resin containing an ultra-violet fluorescent dye, and then examined by image analysis. This showed that the voids within the soil were randomly arranged.

2.2 RESULTS AND DISCUSSION

The Set 1 and Set 2 drainage curves are shown in Figures 2.1 and 2.2 respectively. The volumetric water content is the fraction of water in the sample relative to the overall bulk volume of the sample, expressed as a percentage. The missing data in Set 2 were described as being due to a calibration failure. Set 3 is shown in Figure 2.3.

2.2.1 FITTING EXPERIMENTAL DATA TO WATER RETENTION MODELS

As mentioned in Chapter 1, a primary requirement for modelling the water retention curves is that they can be extrapolated to low and high applied pressures (high and low void diameters) so that they give a representation of the entire void size distribution. The extrapolation to zero applied pressure must asymptote towards the water content of the completely saturated sample, i.e. the volumetric water content must approach the total porosity of the sample. Figure 2.4 shows the low pressure end of the Set 1 water retention curves. The volumetric water contents at zero tension correspond to the total porosities of each sample. There are clear discontinuities between 0 and 250 Pascals in all the drainage curves of set 1 and set 2. It was not possible for sets 1 and 2, to fit a curve with only one point of inflection through both the experimental data and the total porosity asymptotes, and therefore both these data sets were unsuitable for modelling purposes. The apparent discontinuity between the water retention curves and the total porosities may arise from a bimodal void size distribution, or from gravity drainage at low pressures.

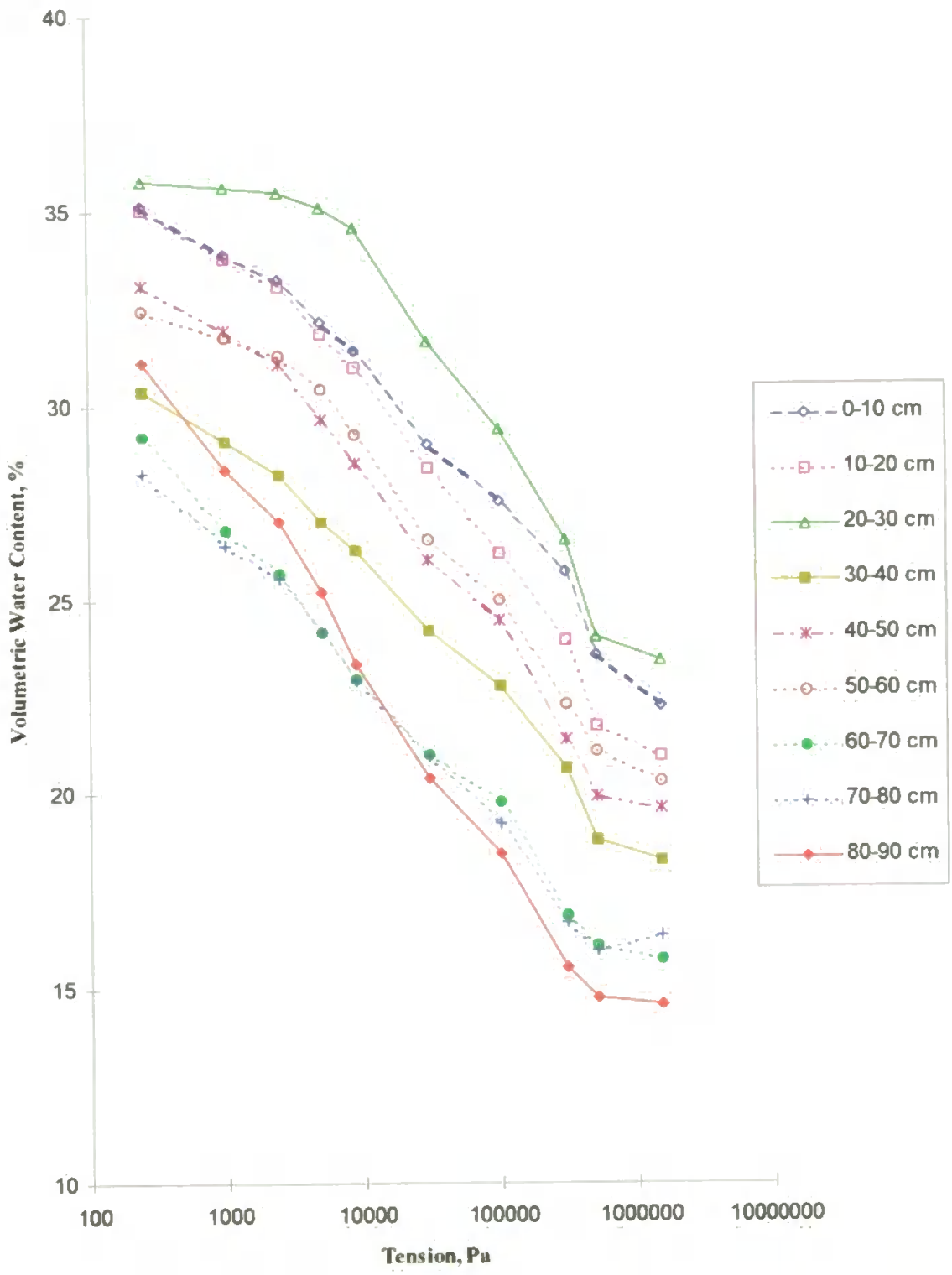

Figure 2.1 : De Bathe Plymouth drainage curves (set 1). Sample depths (0-90cm) are shown in the RHS legend.

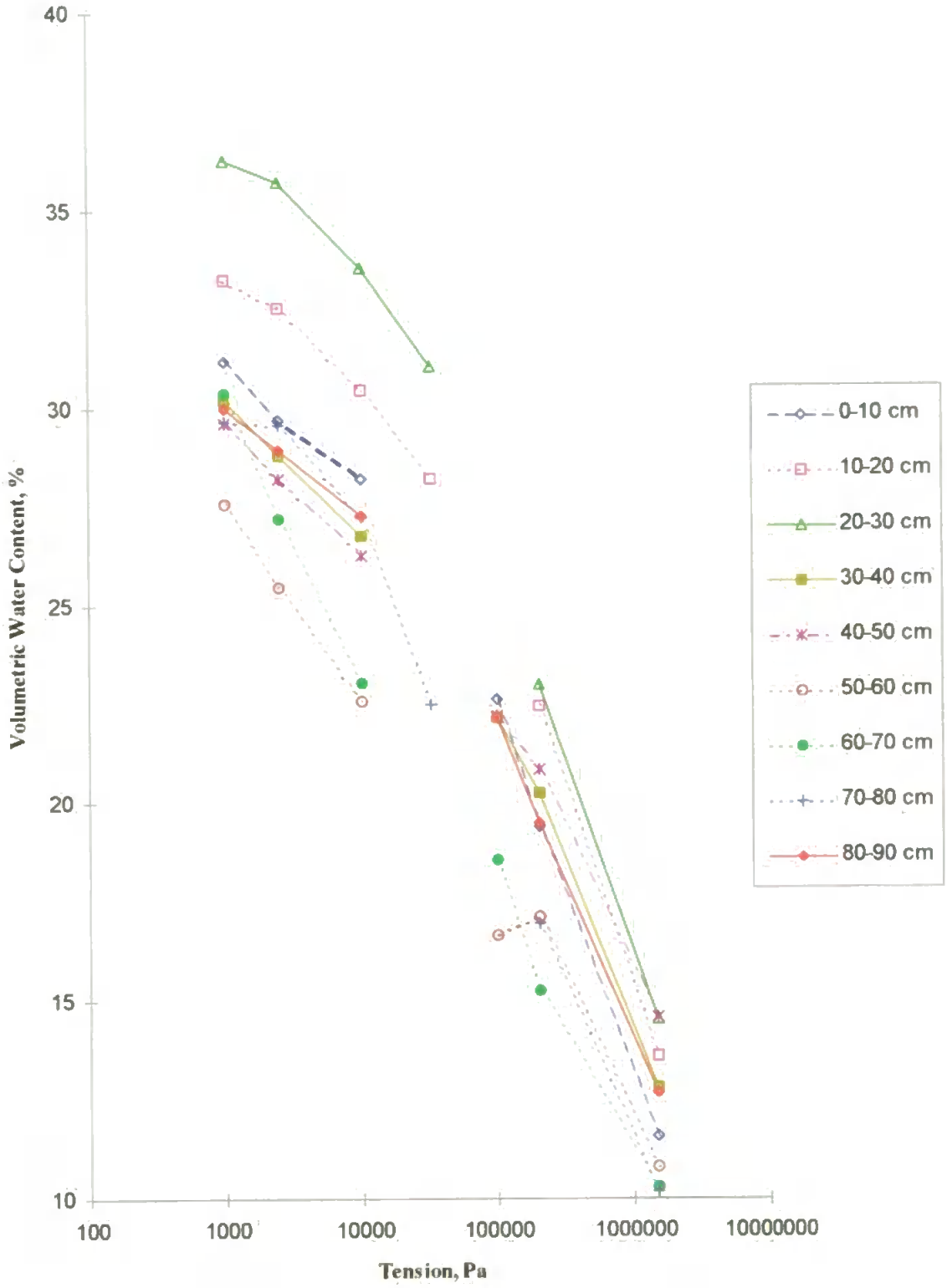

Figure 2.2 : De Bathe Shardlow water retention curves (set 2). Sample depths (0-90cm) are shown in the RHS legend.

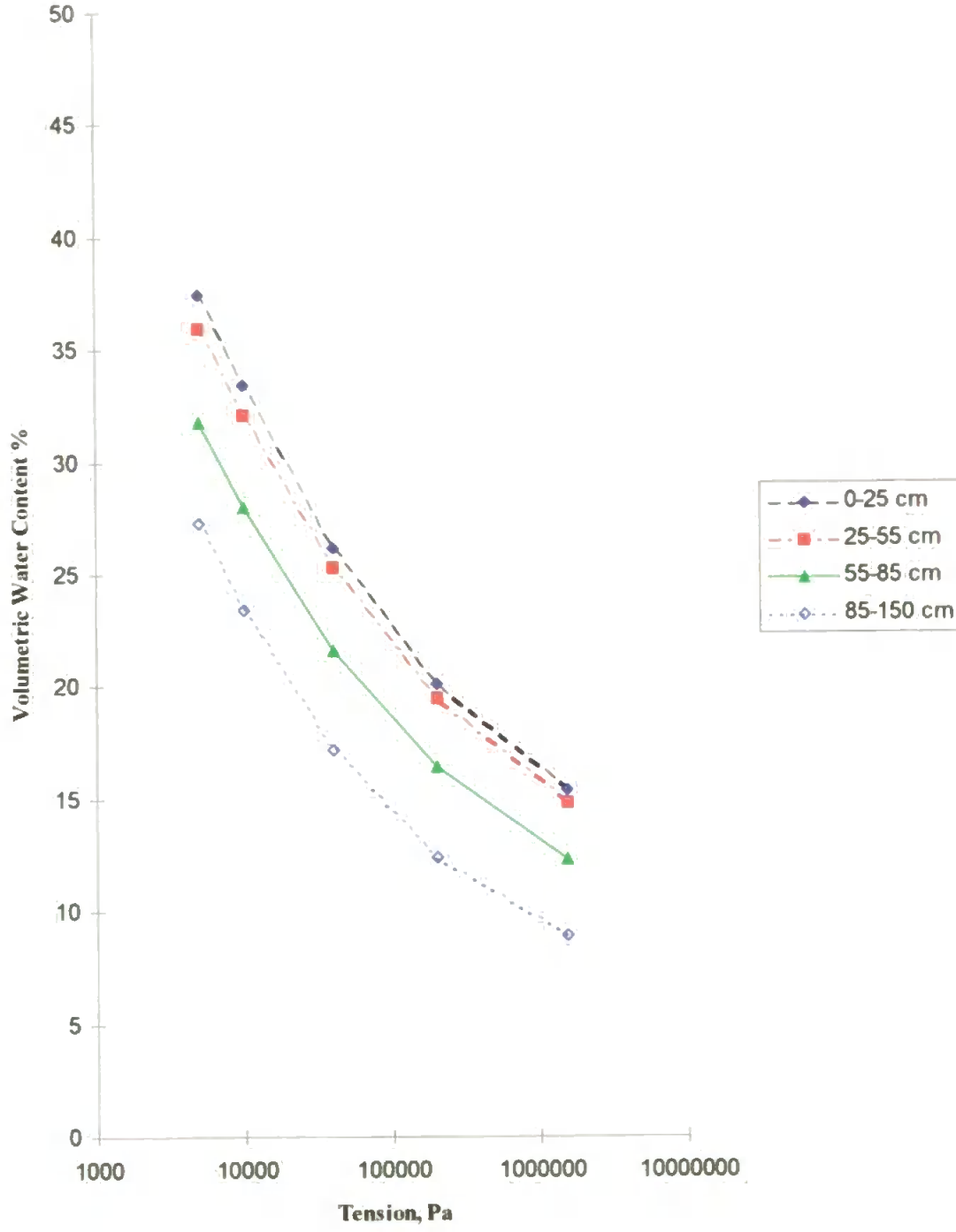

Figure 2.3 : Crediton Seismic water retention data (set 3). Sample depths (0-90cm) are shown in the RHS legend.

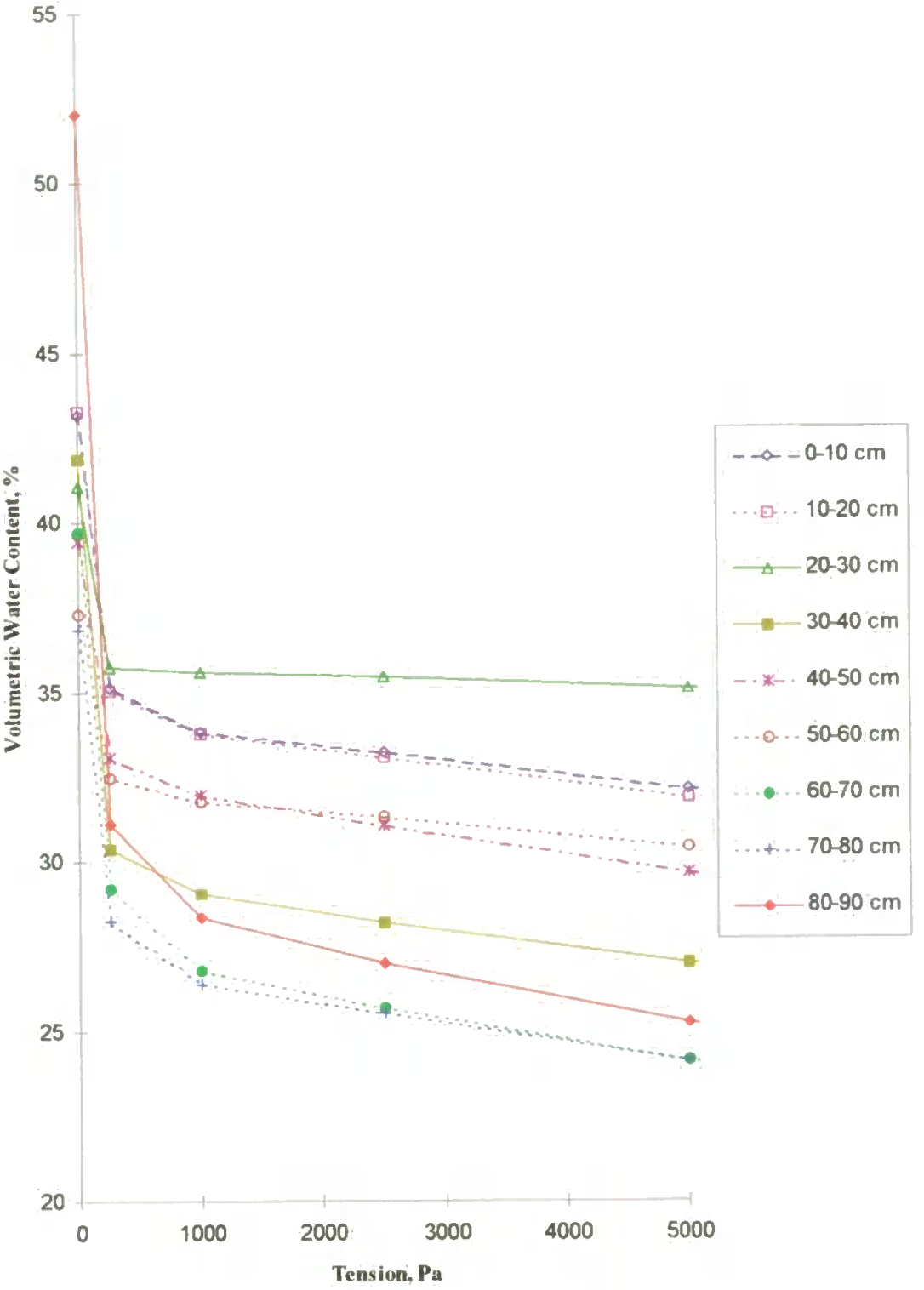

Figure 2.4 : Low pressure end of the set 1 curves. Sample depths (0-90cm) are shown in the RHS legend.

With regard to set 3, Figure 2.5 shows a least squares regression fit of the lognormal model of Kosugi (LN) and the power law models of Brooks and Corey (BC) and Van Genuchten (VG) to the 85 - 150 cm depth curve. It can be seen from three fits of the Kosugi model that there can be large differences in the extrapolations even when the same mathematical form of f(r) is assumed. The fitting parameters of the Kosugi and Brooks and Corey models are listed in Table 2.1. The corresponding Van Genuchten parameters can be found in Table 2.2. The only fitting parameter which is constant is θ_s, which we assume to be the total porosity of the sample and therefore provides the upper asymptote of all the fitted curves in Figure 2.5. The value of the bubbling pressure ψ_c of 1 Pascal, derived from solution 1 of the Kosugi equation, is unrealistic and therefore this solution can be ignored.

Parameter	LN1	LN2	LN3		BC
Ψ_c / Pa	-1	-250	-385.11		
Ψ_o / Pa	-2.20	-252	-386	h_b / Pa	-671
s	2.91	2.787	2.937	l	0.273
θ_r	0.0797	0.0853	0.0804		0.0804
θ_s	0.445	0.445	0.445		0.445
Variance	2.1E-05	3.26E-05	1.61E-05		1.84E-6

Table 2.1: Kosugi (LN1-3) and Brooks and Corey (BC) parameters used to fit the 85 - 150 cm curve of data set 3.

It can be seen from Figure 2.5 that the Van Genuchten fit gives rise to a sigmoid shape of curve which lies between the other fits. These characteristics, together with the fact that

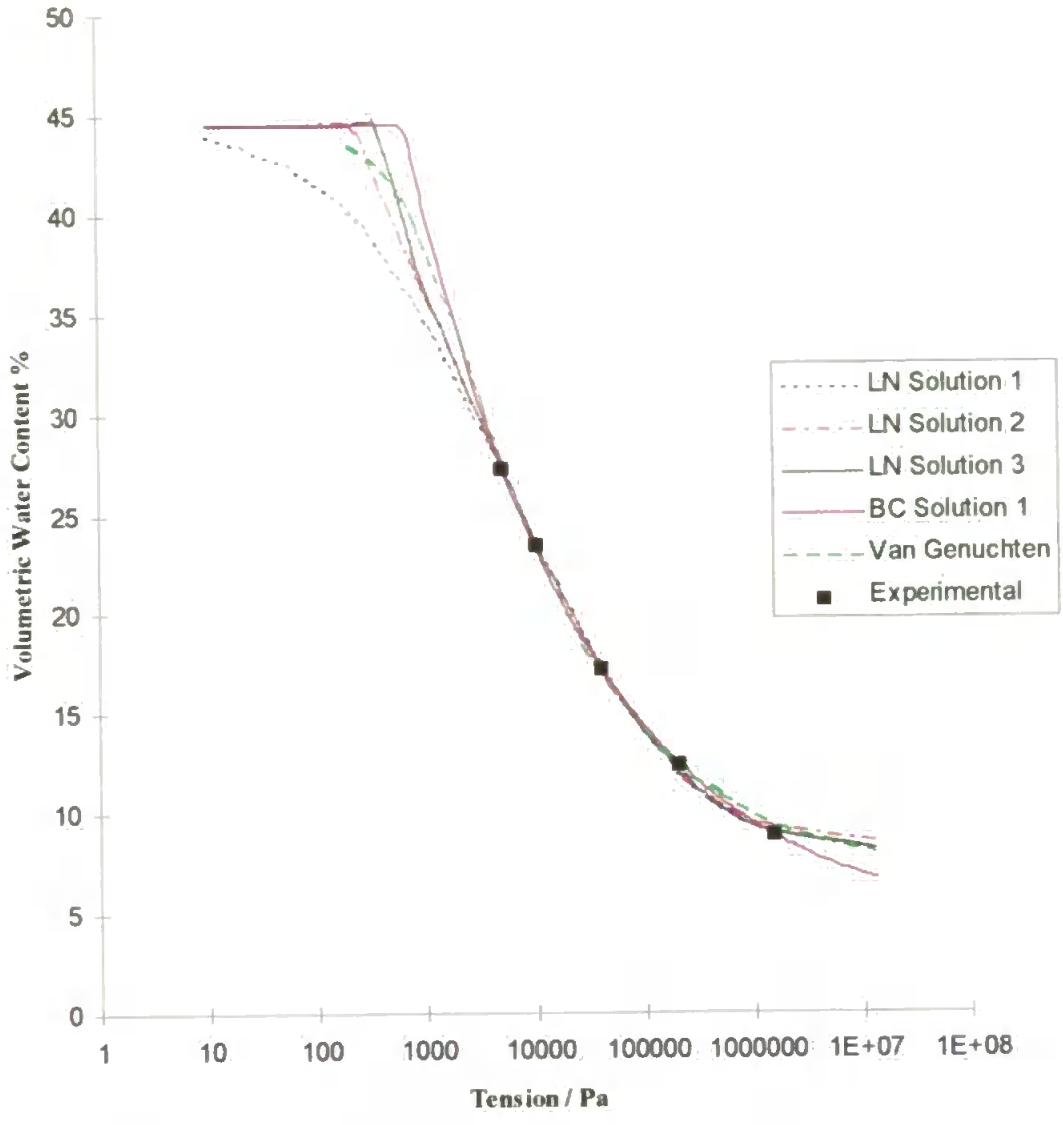

Figure 2.5 : Possible water retention model fits of the experimental Crediton Siesmic 85 - 150 cm curve.

curve shape is not necessarily based on the approximation exemplified by Figure 1.3, led us to use it as our standard extrapolation for the experimental curves at all depths. The fitted curves are shown in Figure 2.6 and the Van Genuchten fitting parameters in Table 2.2.

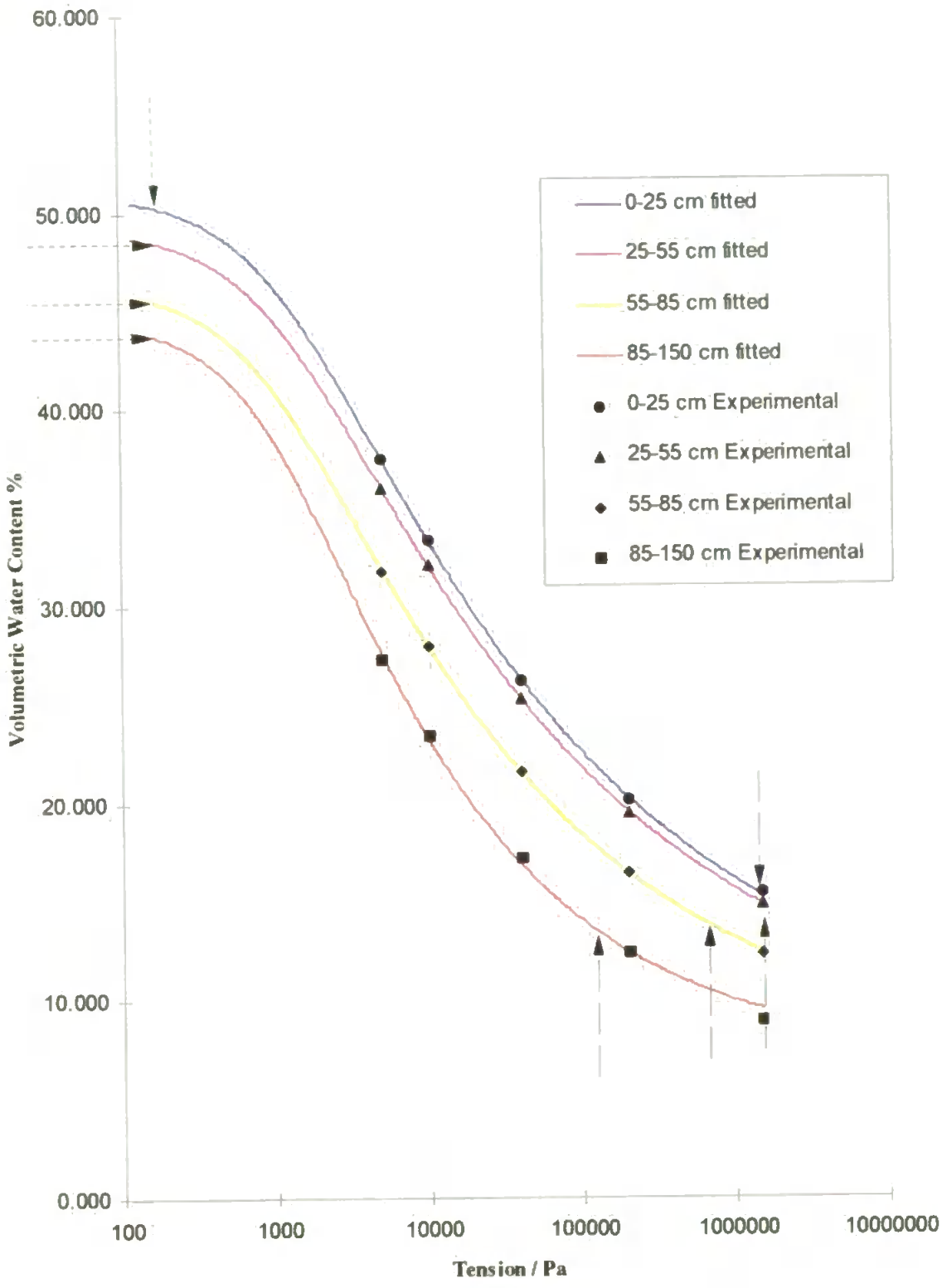

Figure 2.6 : Set 3 Data fitted to Van Genuchten model. Truncation points shown by dashed arrows.

Depth	0 - 25	25 - 50	50 -85	85 - 150
Parameter	cm	cm	cm	cm
Ψ_c / Pa	-516.00	-532.12	-364.65	-385.11
Ψ_o / Pa	-523.30	-538.86	-369.44	-386.11
σ	2.719	2.723	2.722	2.937
θ_r	0.140	0.138	0.119	0.080
θ_s	0.510	0.492	0.463	0.445

Table 2.2: Van Genuchten parameters obtained by fitting set 3 data

2.2.2 TRUNCATION OF THE EXTRAPOLATED EXPERIMENTAL CURVES

We have now reached the stage of generating a set of water retention curves which represent an infinite size range. However, it is, in practice, impossible to produce a computer model with such a range, and the curves are therefore truncated to a range which nevertheless retains substantially larger voids than were represented by the original experimental data. The simplest way of truncating the curves is to limit the upper and lower void sizes. However, this process leads to an inclusion of different information about the pore size distribution being included in each curve, which obscures the depth trend. A better approach is to model the same fraction of the porosity of each sample. The choice of 68.8% of the total porosity produced modelled porosities and truncated water retention curves over ranges covering the large majority of significant void sizes, Table 2.3. The lower truncation pore diameters are in the range 0.207 μm to 2.344 μm, close to the wilting point diameter 0.2 μm for plants of [4]. We also impose an upper limit of 2500 μm which is around five times larger than the typical air entry diameter given by the Kosugi model fits of set 3 data. The truncation is carried out by re-scaling the truncated drainage curves so that they cover the range 0 to 100 % air intrusion of the modelled porosity (Figures 2.7a and 2.7b).

Depth Range	0-25 cm	25-55 cm	55-85 cm	85-150 cm
Experimental porosity, %	51	49.2	46.3	44.5
Truncated porosity, %	35.1	33.8	31.8	30.6
Upper pore size limit, µm	2500	2500	2500	2500
Lower pore size limit, µm	0.214	0.207	0.508	2.344

Table 2.3: Effect of truncating to 68.8 % of the total porosity.

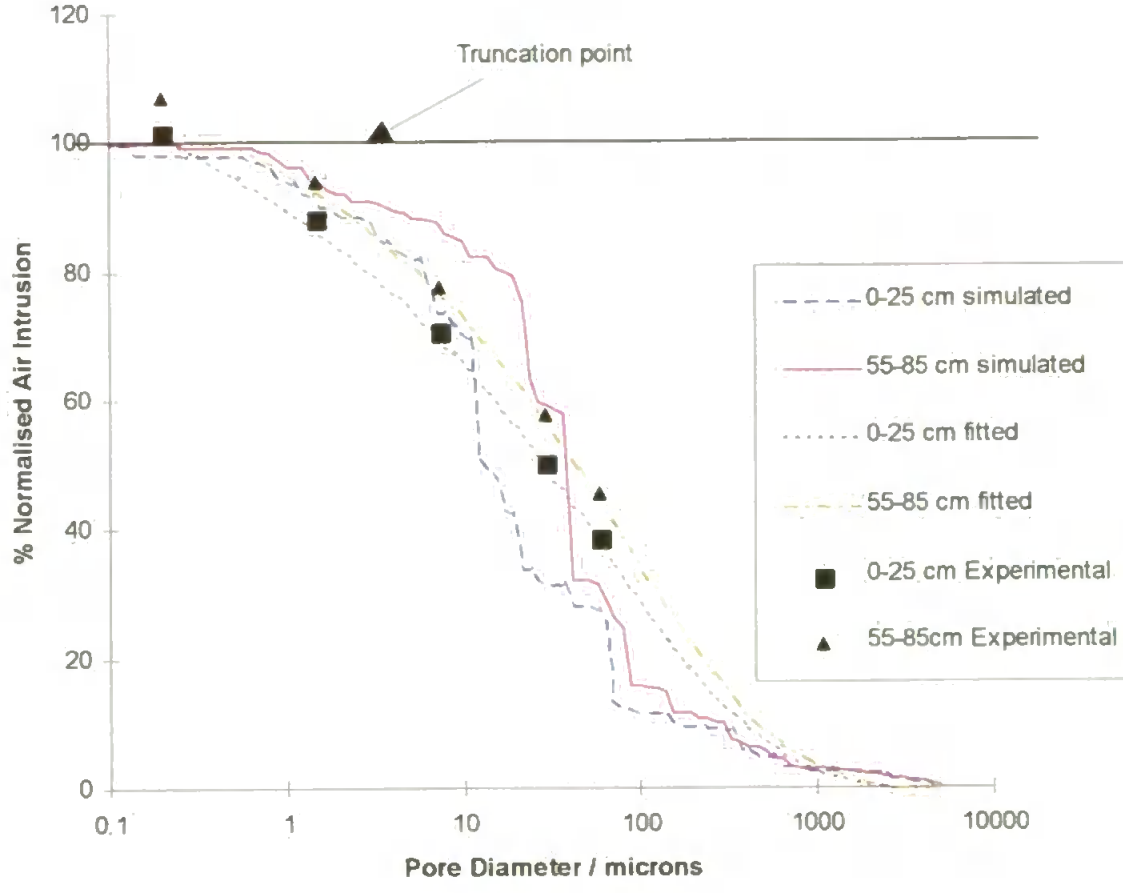

Figure 2.7a : Truncation of set 3 curves and Pore-Cor simulated intrusion curves

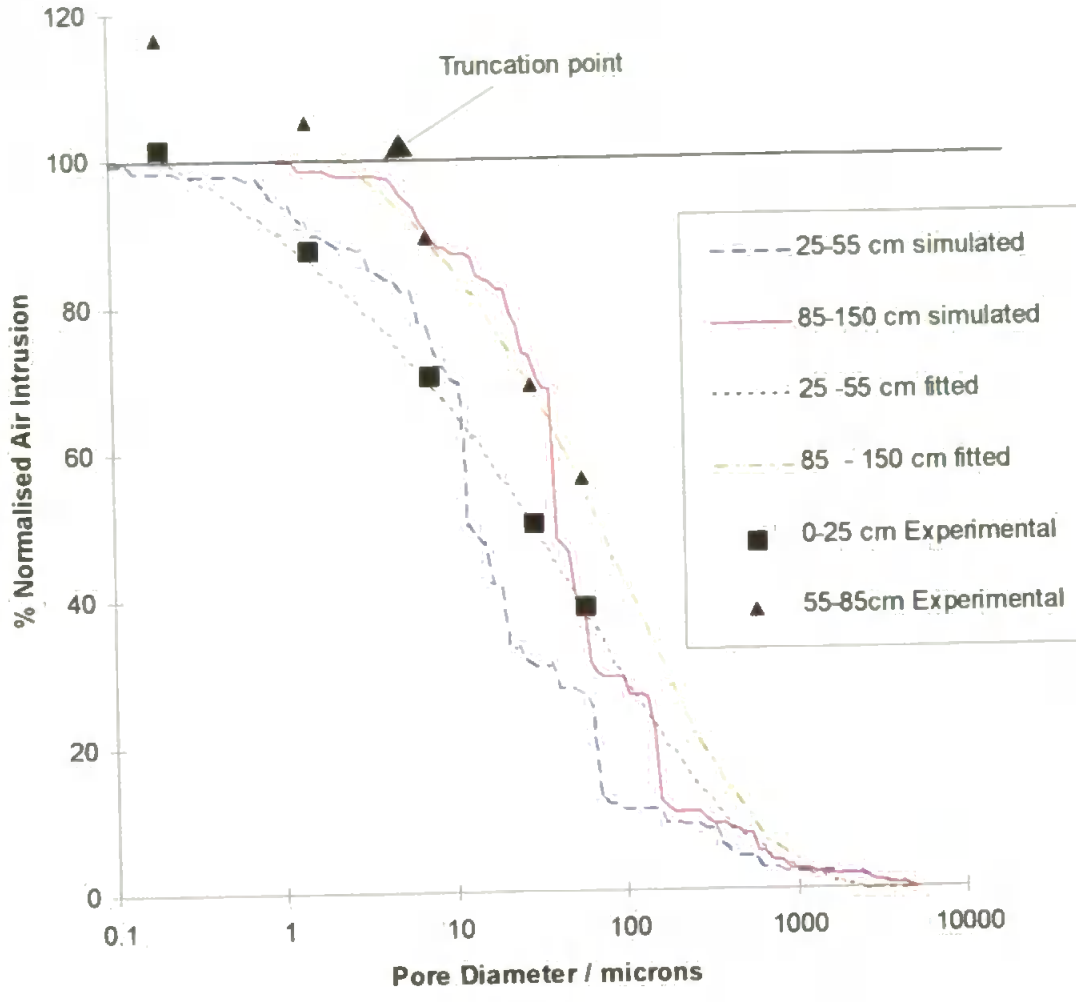

Figure 2.7b : Truncation of set 3 curves and Pore-Cor simulated intrusion curves

2.2.3 Fitting the Pore-Cor Model

The three dimensional soil void structures are obtained by finding networks that have the same normalised water retention curves as those shown in Figures 2.7a and 2.7b. In practice it is not possible with a Pore-Cor unit cell of only 1000 pores to obtain an exact match between experimental and simulated curves. We fit the curves by choosing a log / least-squares-deviation fit, giving equal weighting to the all of the curve in terms of a logarithmic

abscissa. This method of fitting is exemplified by Figure 2.7a and 2.7b, which shows the simulated and experimental curves for set 3. A random distribution of voids was chosen, in accord with the random structure of the soil found by image analysis. In the absence of any other information, the correlation between pore and neighbouring throat sizes was assumed to be sandstone-like, i.e. each pore was the same size as the diameter of the largest throat entering it [45]. In other models the size correlation between throats emanating from the same site has been found to be important [36].

As mentioned previously, the relationship between water retention curve and the Pore-Cor unit cell structure is not unique. Pore Cor fits the water retention curve by altering the connectivity and the throat skew of the network. The corresponding fitting surface is a measure of the variance between simulation and experiment as the connectivity and throat skew changes. Four such fitting surfaces for the 0-25 cm set 3 curve are shown in Figure 2.8, each resulting from a different stochastic generation of the unit cell structure. The surface fits of four these different stochastic generations are clearly very different, as are the corresponding modelled parameters are given in Table 2.4. However, the variation in the fitting parameters is not random, higher co-ordination numbers are compensated by higher throat skews (larger numbers of small throats), as shown for 20 stochastic generations in Fig 2.9. It can also be seen that the correlations vary for the different experimental samples.

There is a strongly linearly correlated trend (R^2=0.921) in pore skew with depth, as indicated in Table 2.5 which shows the mean values over 20 stochastic generations. As mentioned previously, pore skew compensates for the lack of efficient packing of the voids within the unit cell, which arises from their equal spacing in Cartesian planes. The strongly linear correlation may be rationalised in terms of decreasing porosity and pore size range

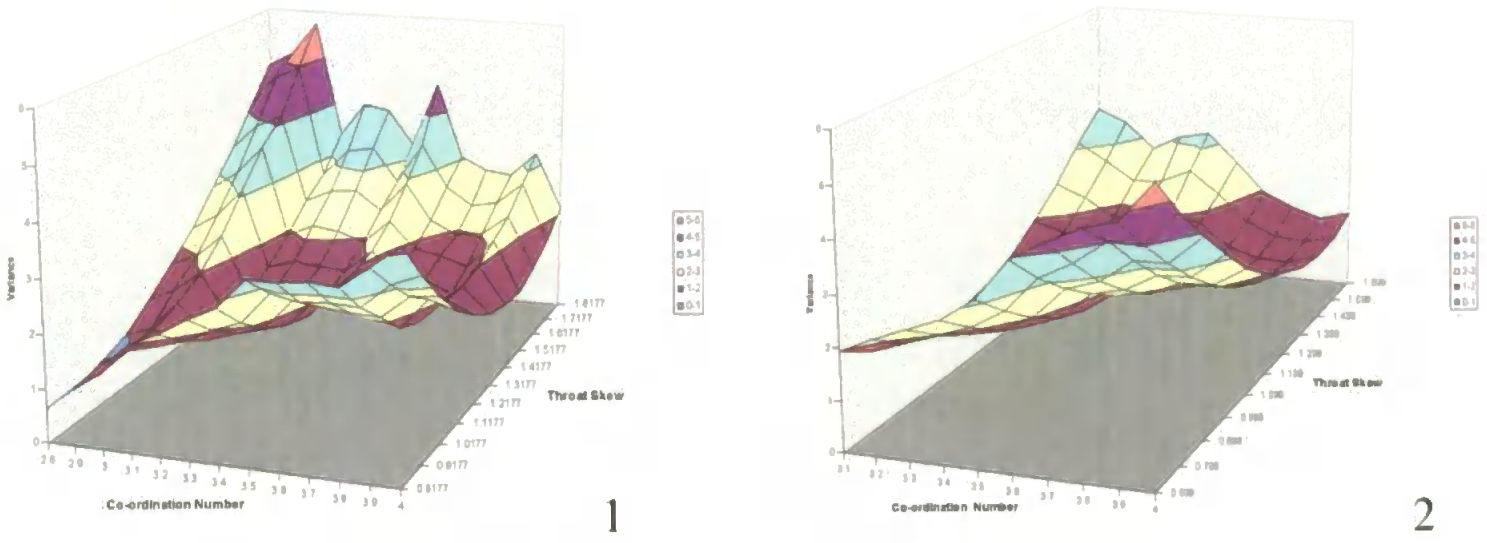

Figure 2.8. Pore-Cor output for four stochastic generations, with minima as shown in Table 2.4

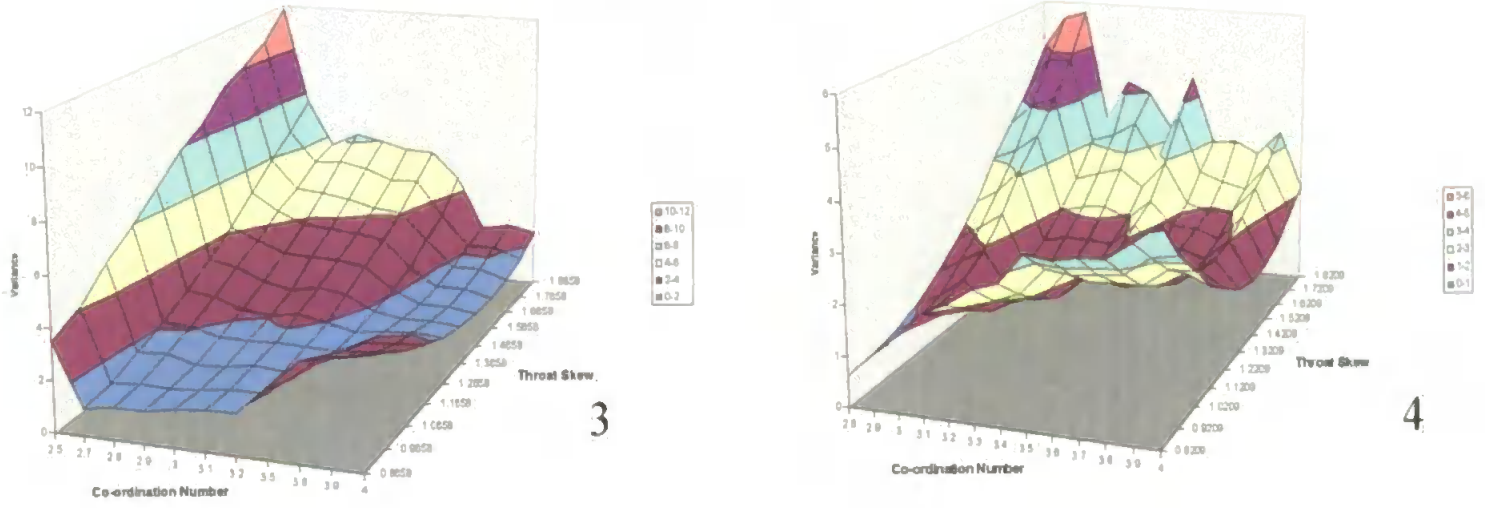

with depth shown in Table 2.5, which necessitates progressively less compensation for inefficient packing.

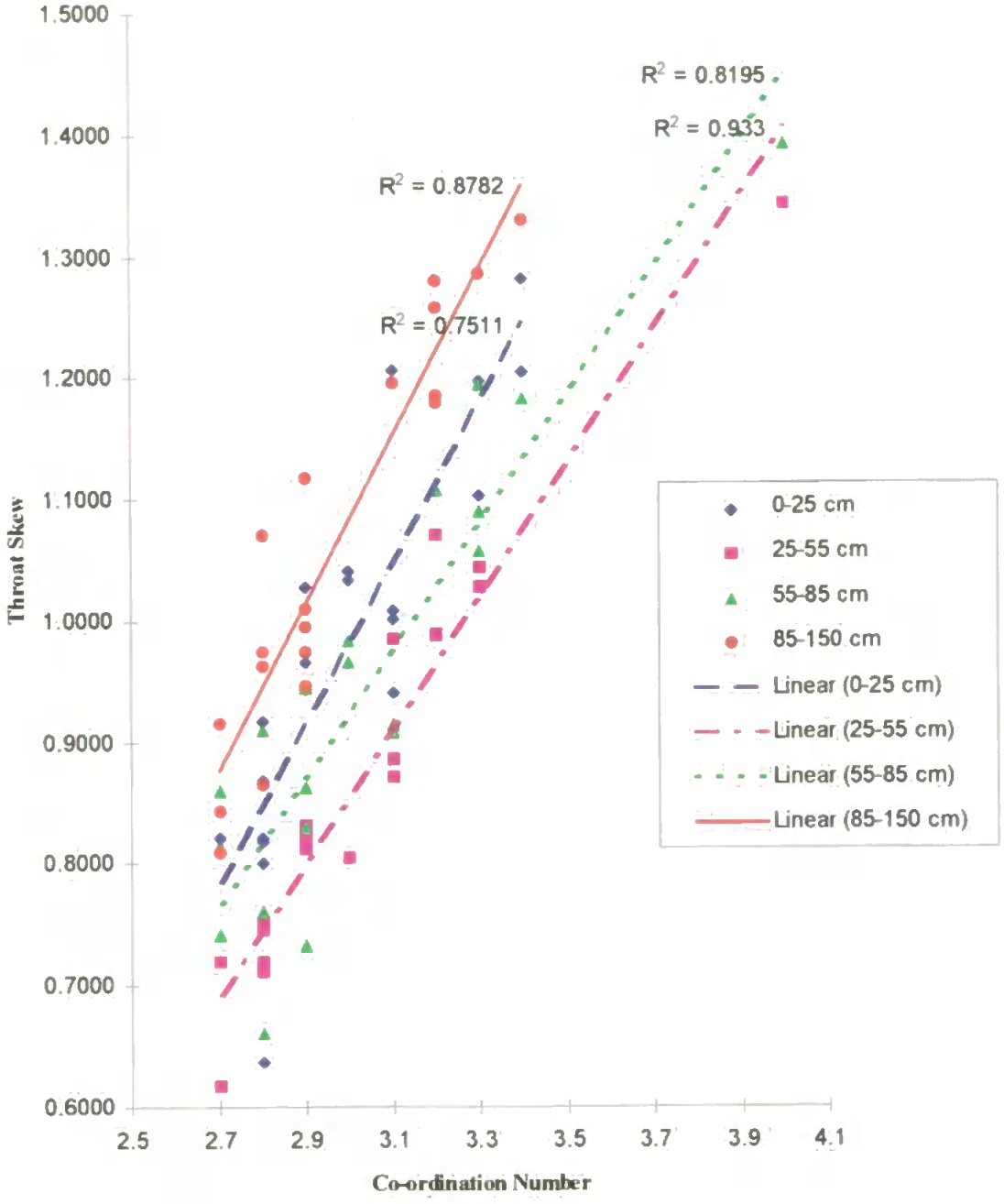

Figure 2.9: Correlation of Co-ordination number and throat skew

Pore-Cor Parameters	C/N	Throat skew	pore skew	porosity %
Generation				
1	2.8	0.805	3.1	35.3
2	3.1	1.03	3.5	35.3
3	2.7	0.771	3.1	35.3
4	2.8	0.700	3.1	35.3
mean	2.85	0.827	3.2	35.3
std	0.173	0.144	0.2	

Table 2.4: Pore-Cor output from four different stochastic generations

Mean Depth cm	68.8 % of the Total Porosity	Upper Pore Size Boundary µm	Lower Pore Size Boundary µm	Pore Skew
12.5	35.06	2500	0.21	3.39
40	33.82	2500	0.21	3.13
70	31.83	2500	0.51	2.43
117.5	30.59	2500	2.34	2.19

Table 2.5: Relation between pore skew and depth.

Two way ANOVA analyses of the four sets of predicted hydraulic conductivities, figure 2.10 showed that there were statistically significant differences between them, ($F = 28.6$, $F_{crit}=2.8$ and $p < 0.05$). Further paired t- tests revealed each of the individual data sets to be significantly different to each other, P(two-tail) < 0.05 for all sets.

Figure 2.11 illustrates the experimentally observed and predicted permeabilities for each depth. The correlation between the predicted and experimental values is excellent, with $R^2 = 0.99$. The absolute values of the predicted permeability are three to four orders of magnitude below the experimental value, due to the complexity of the sample and the oversimplicity of the network model. Simpler samples modelled with Pore-Cor match experimental and simulated permeabilities more closely [38,45,191].

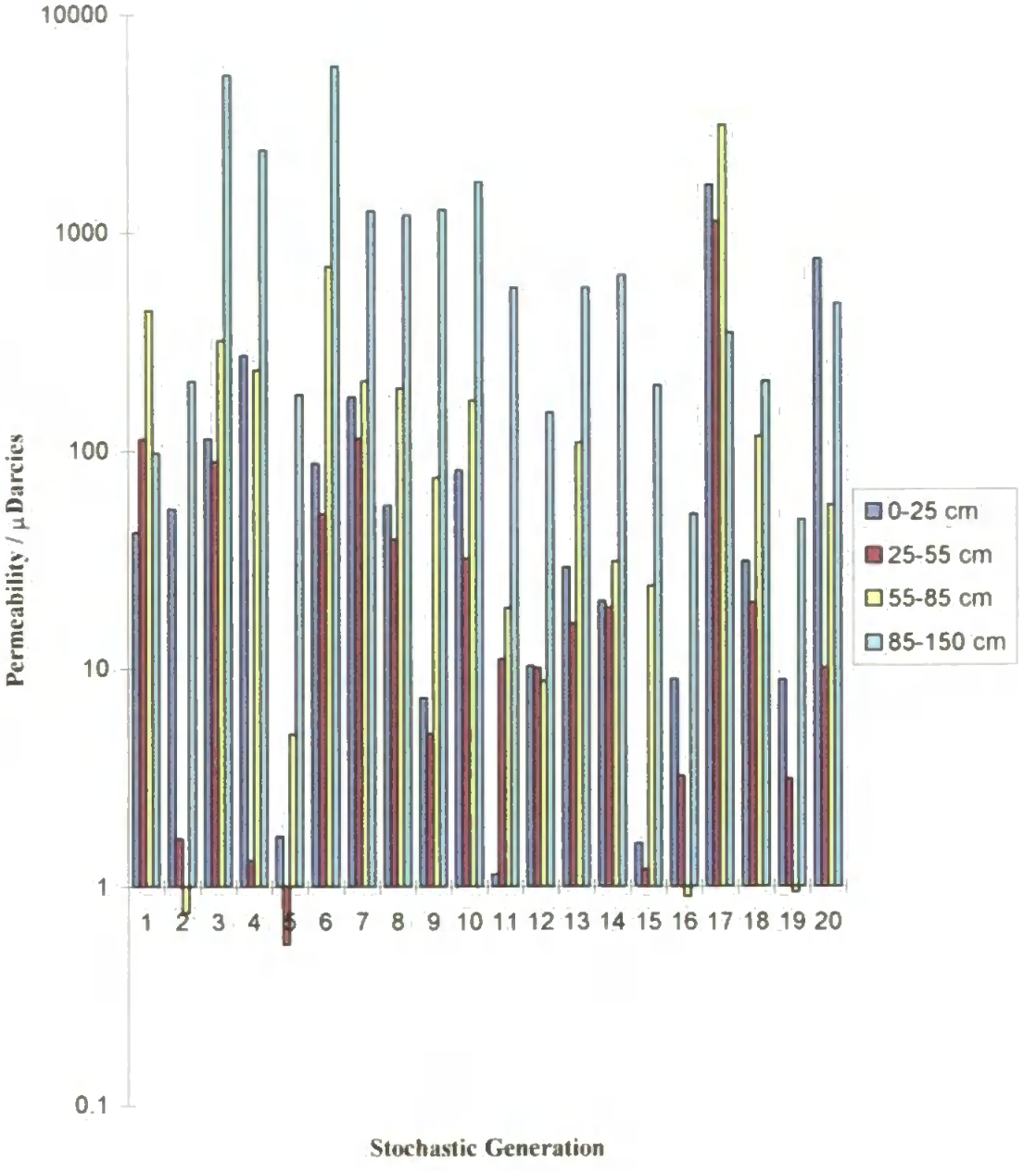

Figure 2.10: Pore-Cor permeability output over twenty stochastic generations. Each generation produces a different unit cell with a different permeability.

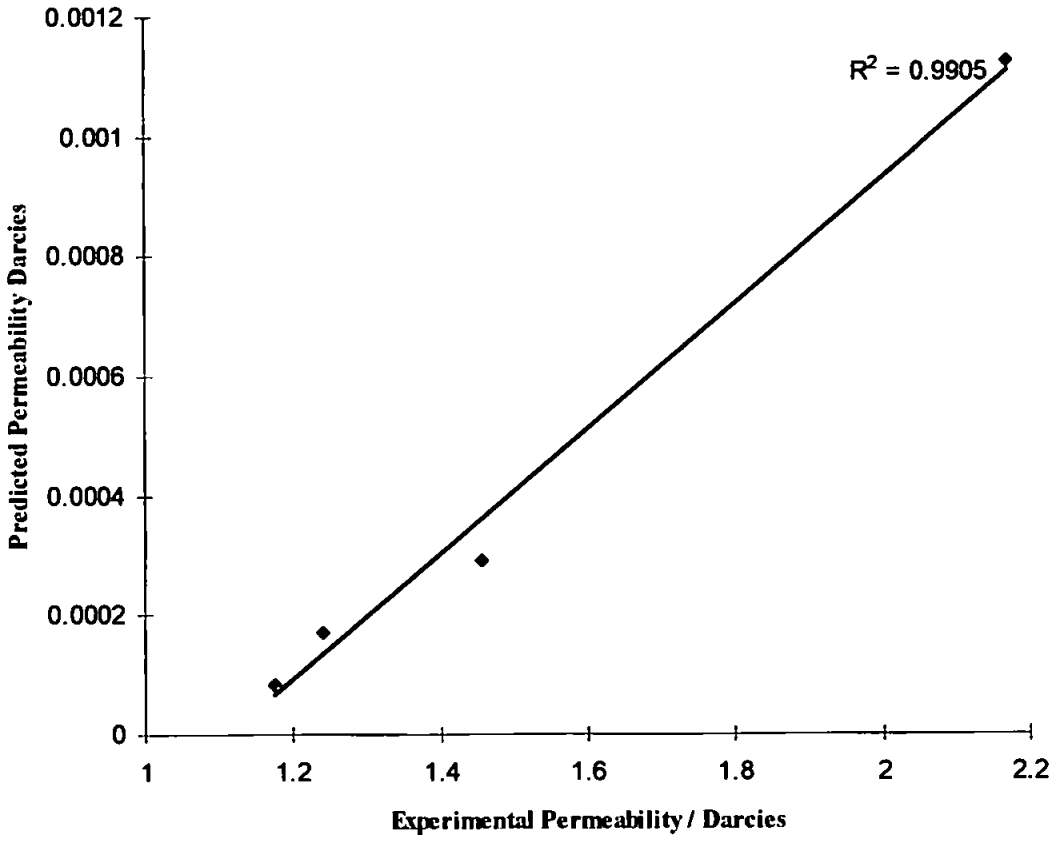

Figure 2.11: Correlation of predicted and experimental permeabilities

2.3 CONCLUSIONS

Pore-Cor has been used to produce networks that resemble the percolation characteristics of experimental soil samples. Although the fit to experiment is not exact, the model does track trends. The values of saturated hydraulic conductivity predicted by Pore-Cor are three orders of magnitude too small and is attributable to a network which is too small, and a non unique relationship between water retention and network solution. However, the relationship is sufficient to cause the modelling parameters to compensate for each other,

Figure 2.9. Averaging over a number of stochastic generations does produce trends which match experiment very closely.

Enlargement of the unit cell would allow the simulation to match experiment more closely and give more realistic permeabilities. It would also reduce the need to use averages of stochastic generations but would require greater software complexity and the power of a super-computer. Other properties of the network, such as its hydrodynamic dispersion coefficient and internal surface area, can be predicted from the generated networks and then compared to experimental values. The prediction of these properties using Pore-Cor would breakaway from the classical capillary (exemplified in Figure 1.3) and structureless black box models which dominate the soil literature and should facilitate an improved understanding of the fundamental processes of solute transport through soil.

3.0 CHAPTER 3

COMPARISON OF THE PORE-COR THREE DIMENSIONAL VOID STRUCTURE OF SOIL WITH TWO DIMENSIONAL IMAGE ANALYSIS

The Pore-Cor model was used to generate 3D structures in Chapter 2. These simulated structures were then compared to a first derivative interpretation of the soil water retention curve and also to experimental images.

Two sets of samples were studied, one impregnated with PEG 6000 and the other with Crystic resin. The samples impregnated with PEG 6000 had abnormally low porosities and it was later discovered that the site from which these samples had been taken had undergone compaction by grazing steers. Only the Crystic resin set was comparable to the Pore-Cor generated structures.

The Pore-Cor void structure contained a higher proportion of large voids than did the experimental samples due to packing problems when a large range of void sizes are to be simulated in a restricted geometry. Differences in the normalised frequency distribution of the experimental samples varied by seven orders of magnitude which Pore-Cor can not model because it is limited to a total of 500*c* throats. Nevertheless, the comparative study permits the effects of the model's limitations to be observed and opens the way for refinement of the model.

3.1 EXPERIMENTAL

3.1.1 CHOICE OF SAMPLING PROTOCOL

The objective of the sampling protocol was to provide an experimental data set which could be compared to two dimensional surfaces generated by Pore-Cor. In Chapter 2, the site specific data sets (1 and 2) were found to be unsuitable for modelling purposes. Set 3 data is not specific to any one site but is a general encapsulation (from the SESIMIC data set) of the Credition series with a depth profile. Samples were taken randomly from the part of the DeBathe site Near North Wyke, at depths of 0 - 55 cm depth, which was under grassland management and occasionally grazed.

3.1.2 SAMPLE COLLECTION

In February 1996, two sets of four field moist samples of De Bathe soil were collected in circular aluminium rings 6.5 cm in diameter and 5 cm deep. Samples which were subsequently impregnated with Crystic resin were collected at depths of 0 to 55 cm below the soil surface. The other samples, which were to be later impregnated with PEG 6000 were collected in the depth range 0 - 25 cm. The tins were pressed gently into the appropriate part of the soil profile. A sharp knife was used to cut around the edge of the tin as it was pressed in to reduce disturbance to and compression of the sample. When the tin was full, any excess soil was trimmed away and the sample secured with a nylon mesh (an unpatterned net curtain). One set was then impregnated with Crystic resin and the other with PEG 6000.

3.1.3 SAMPLE IMPREGNATION

IMPREGNATION WITH PEG 6000

One set of samples were immersed in PEG 6000 solutions containing 0.25 mg l^{-1} Acradine Orange, such that the liquid meniscus was around 0.5 cm from the top of the sample. Immersion began in a 10% v/v PEG 6000 solution for 30 minutes, transferred to a 25 % v/v PEG 6000 solution and left overnight. The samples were then transferred into a 50 % v/v PEG 6000 solution and the temperature raised by placing the immersion vessel on a hotplate to a temperature of 65 ^{0}C. Impregnation was then completed by immersing the sample in molten PEG 6000 for six days, replacing with fresh wax every two days. Samples were then removed from the molten wax and slowly rotated for two minutes until the ends of the core samples began to set. The samples were then wrapped in an insulating jacket of bubbled plastic wrap to avoid the build up of temperature gradients while cooling, and then left for two days to set.

IMPREGNATION WITH CRYSTIC RESIN

The other set of samples was placed in a sealed container containing acetone. At the end of the first week the acetone was replaced with fresh acetone. This was repeated for three subsequent weeks. The samples were then removed, allowed to stand for ten minutes and then placed into impregnating chambers.

2 litre batches of impregnating mixture were used. Firstly the 0.6 g of Uvitex OB dye was dissolved in 200 ml of acetone by mechanically stirring for five minutes. This was the added to 1800 ml of Crystic resin (SR17449) and 15 ml of catalyst (Q17447). This impregnation mixture was then poured into the impregnating chamber until half way up the sample. The

sample was then left for about one hour to allow the resin to penetrate by capillary action and then completely covered by the resin mixture. When air bubbles were no longer observed, the sample chamber and sample were placed under vacuum for 12 hours. After this period the sample was placed into a fume cupboard and over a six week period, losses due to evaporation were replaced by a mixture of 2000 ml of Crystic resin and 15 ml of accelerator.

3.1.4 Mechanical Treatment of Impregnated Samples

PEG 6000 impregnated samples was then cut into 10 mm thick sections using a diamond tipped circular saw which was cooled by Castrol Honillo oil. The 10 mm sections were then polished using a LP-30 lapping machine (Logitech) lubricated with the same oil. To prepare them for image analysis the samples were cleaned up with 1,1,1 trichloroethane. Crystic resin samples were treated in the same way but were lubricated with water and did not need to be cleaned up with 1,1,1 trichloroethane.

3.2 EXPERIMENTAL IMAGE ANALYSIS

3.2.1 Examination of Soil Background Fluorescence

A single set of samples was impregnated in PEG 6000 as previously outlined, but without the addition of a UV dye. The samples were then examined under at high and low magnifications. No background fluorescence was detected.

3.2.2 DETECTION OF FEATURES > 250 μm

SAMPLE IRRADIATION

Excitation of the samples was achieved with a 50 Hz Viber Lourmat UV Lamp which had a major emission line at 365 nm.

USE OF 35 MM AND CCD CAMERA AS A DETECTOR OF FEATURES >250 μm

A 35 mm SLR camera set on a tripod directly above the irradiated sample was used in conjunction with 1000 ISO black and white film. Images taken at exposure times of 1, 2, 3, 5, 10 and 30 seconds and 1, 2, 3 and 5 minutes were used to determine the optimal exposure time. The developed prints were then analysed using a Hitachi camera. Images were also detected by a low light level camera (Fujitsu General) fitted with a 55 mm Comptar lens mounted on a tripod. The size of the large frames was 36 x 36 mm as checked with a calibrated projectline ruler (CH 9435 Heerbrugg, Switzerland), giving a resolution of of 85 μm $pixel^{-1}$.

3.2.3 DETECTION OF FEATURES <250 μm

SAMPLE IRRADIATION

Sample irradiation was achieved using a blue excitation source (Olympus BH attachment, with EPPIFLUORESENCE.) The exciting energy was channelled through the optics of the system onto the sample.

COLLECTION OF INDIVIDUAL AND COMPOUND IMAGES

The Fujitsu General camera was attached to a monocular vertical lens using a C adapter. Individual areas of 0.9 x 0.9 mm which were calibrated using a micrometer slide (Graticules Ltd, Tonbridge, Kent, England). The camera was connected to a Quantimet 570 image analyser and each image represented by a grid of 487 x 487 pixels. The Quantimet image analyser has a maximum resolution of 512 x 512 pixels; the remaining pixels were used as a buffer to match up the 487 x 487 individual frames as shown in Figure 3.1. After measurement of the individual frame the sample was viewed under a visible light source (Scholly Flexilux fibre optic with ring illuminator). A 512 x 512 image was then collected and then the image greyshifted to the left or upwards by 487 pixels. It was then possible to switch to display mode and match up the image by manually moving the sample right or down. The images were collected in a stepwise fashion as shown in Figure 3.2 to form a set of 16 images. The composite image was generated by zooming each individual image by -4 and then placing it into a grey plane in the correct relative position. The Quick Basic programme used to achieve this is given in Appendix 1. Composite images were used to measure features of size 25 to 250 μm equivalent circle diameter and the smaller individual component frames were used to measure feature of size 25 to 2.5 μm equivalent circle diameter. The resolution of the small and compound frame images was 1.85 and 7.77 μm $pixel^{-1}$ respectively.

3.2.4 MEASUREMENT OF FEATURES

The gain of the camera was adjusted to a gain of x 18 with an offset of zero by the computer programme listed in appendix 1 and the greydetect level was adjusted to a value of 43 such that the visible features were being detected above the background darkness. The Quantimet image analyser was then used to measure the area, equivalent circle diameter,

and X and Y centres of gravity of the detected features, and the data stored to disk. A segmentation algorithm was used to examine the two dimensional discreteness of the detected images.

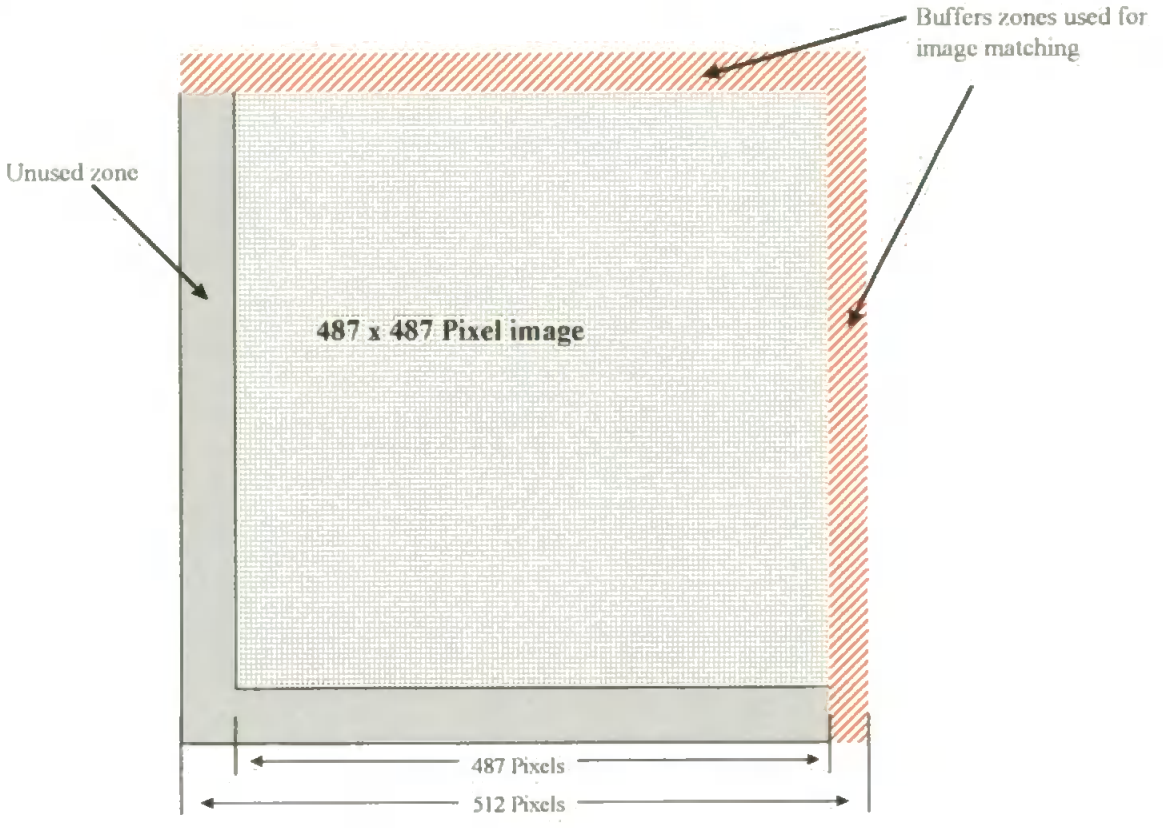

Figure 3.1 : Collection of Individual Small Images. Buffer zones used to match up sample are shown in red.

3.2.5 CREDITON SEISMIC EXPERIMENTAL DATA AND THREE DIMENSIONAL STRUCTURE GENERATION

The Soil Survey and Land Research Centre (SSLRC) at Shardlow provided a set of water retention curves referred to in Chapter 2 as set 3 curves. By fitting the water retention curves three dimensional Pore-Cor structures were obtained. The details of the model 3D structure generation are given in Chapter 2.

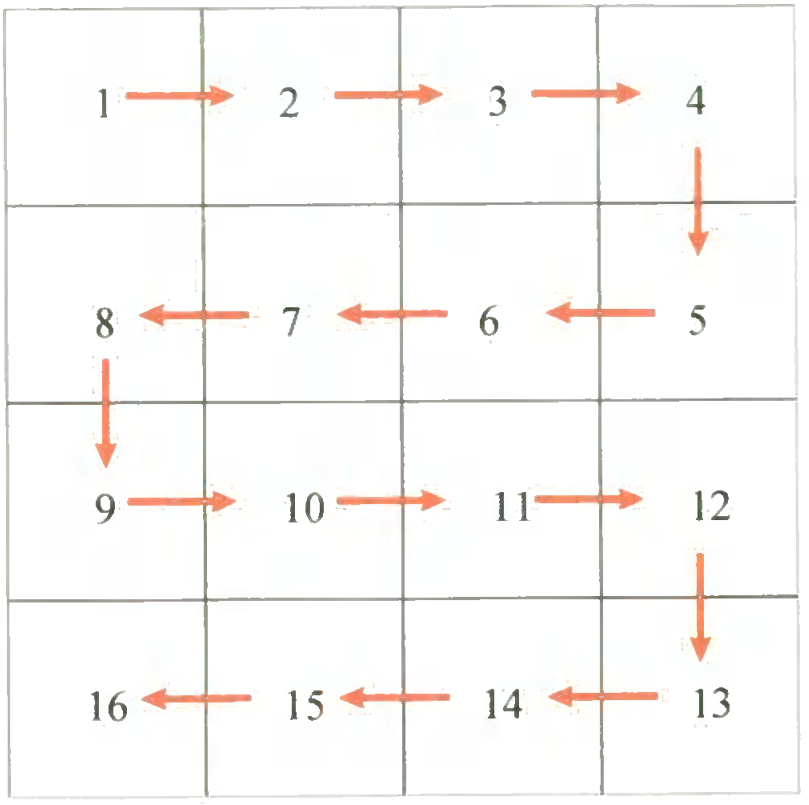

Figure 3.2 : Generation of a Compound Image

3.2.6 Producing Two Dimensional Images of the Three Dimensional Pore-Cor Network by Ray Tracing

In order to generate a two dimensional image from Pore-Cor we placed the Euclidean array of cubes and cylinders into a ray tracing programme using a Visual Basic conversion programme. We then defined an infinite plane bisecting the cube in the xy plane at a chosen angles about the origin. To observe the intersection of the plane and the array of Euclidean objects we set our imaginary camera at a distance of 1 meter away along a normal vector to the centre of each quarter of the intersecting plane focused at the centre of each quadrant, Figure 3.3. The intersection of our Euclidean array and our defined plane is a two dimensional surface representing a slice of the inside the network. This is the mathematical analogue to cutting the impregnated cores with a saw and visualising the exposed 2D surface.

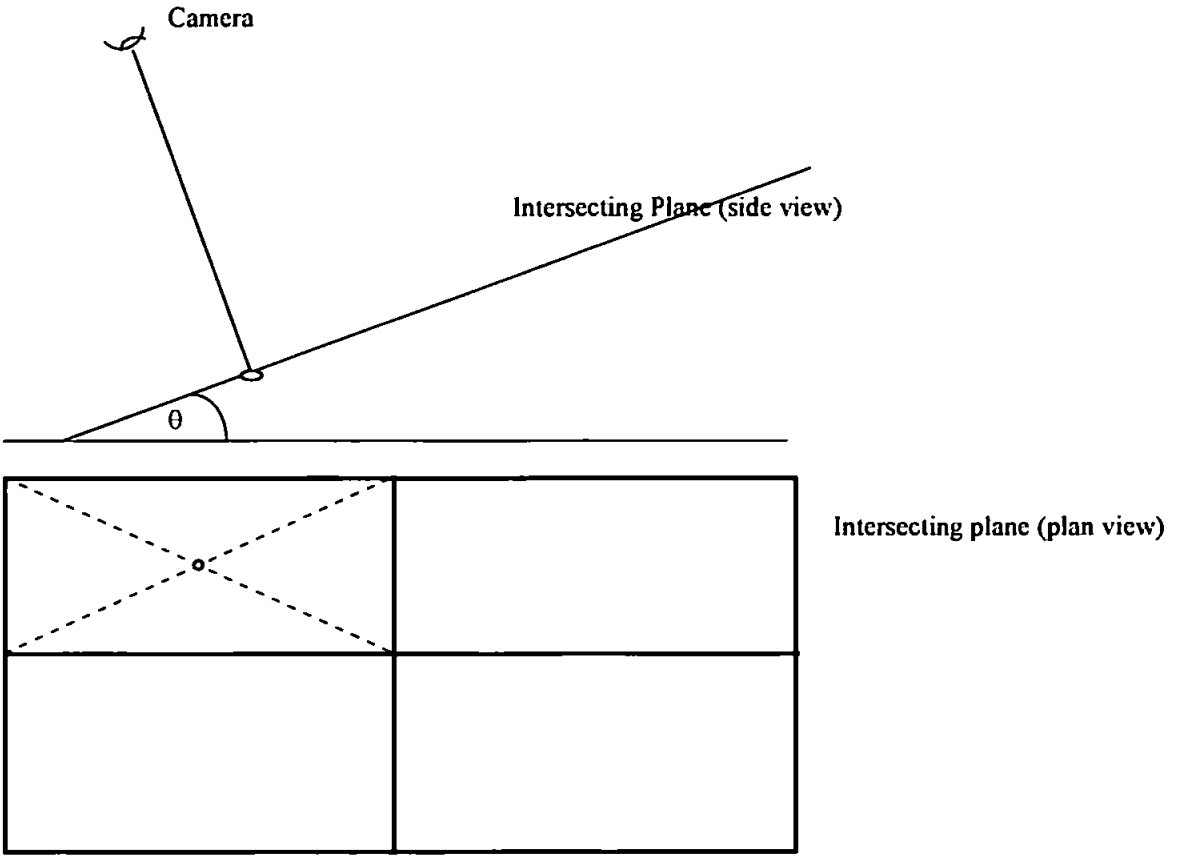

Figure 3.3 : Microtoming by use of a ray tracer.

3.2.7 PRODUCTION OF TWO DIMENSIONAL VOID SIZE DISTRIBUTIONS BY MICROTOMING ALONG THE X, Y AND Z PLANES

An analogous but simplified microtoming of the network was carried out using a FORTRAN 77 algorithm to mathematically cut the Pore-Cor network the x, y and z planes at one hundred intervals and measuring the area of intersection of the pores and throats. Pores and throats were measured as two separate voids even if connected together.

3.2.8 SCALING OF TWO DIMENSIONAL SURFACES

In order to produce complete feature size distributions across the scale 2500 to 2 μm it is necessary to combine the feature size distributions at each resolution because each resolution is appropriate for measuring only one range of sizes. By multiplying the number

of features in the smaller observations to represent an area equivalent to those of the larger observations complete distributions were estimated.

3.2.9 Measurement of Stone Content

A set of four soil samples, each 20 x 20 cm area by 25 cm deep, was collected from the same part of the De Bathe site. Samples were sieved through a 2 mm sieve to determine stone content. Stones were assumed to be non porous and to have an average density of 2.65 g cm^{-1}.

3.2.10 Measurement of Particle Size Distributions

Three sets of % sand (2000-600 μm), silt (600- 63 μm) and clay (<63 μm) were determined in the depth range 10 to 90 cm at intervals of 10 cm. This data was supplied by the Institute of Grassland and Environmental Research (IGER) at North Wyke in Devon. The determinations were carried out in accordance with the methods set out in BS 1337: Part 1: 1990 (British standard methods for soils for civil engineering purposes.)

Generation of Pore-Cor Particle Size Distributions

Particle size distributions were generated by using a FORTRAN algorithm. The maximum size of sphere that will fit between eight cubes (which represent voids in the Pore-Cor unit cell) is found iteratively by the algorithm. The final result of this process is shown in Figure 3.4. The algorithm works through the entire unit cell to find 1000 spheres in total. This set of 1000 spheres is taken to be the particle size distribution. A detailed description of how this algorithm operates in practice is given by Mathews et al. [192].

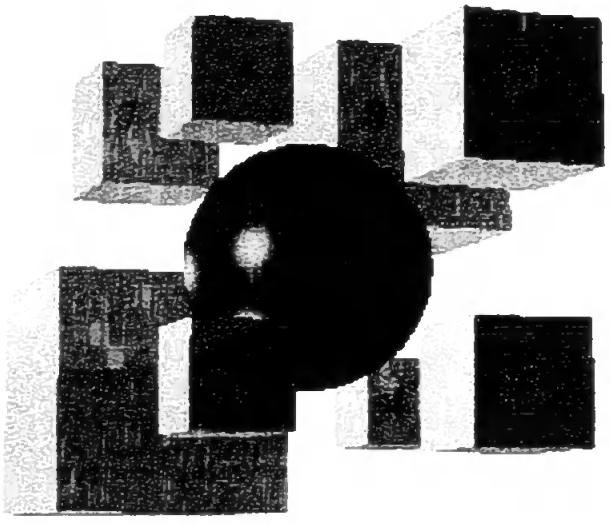

Figure 3.4 : Generation of a particle size distribution by finding the maximum sized sphere which will fit inside between the eight surrounding cubic voids.

3.3 RESULTS AND DISCUSSION

3.3.1 COMPARISON OF 35 MM CAMERA AND CCD CAMERA IMAGES

An image of a impregnated soil block was taken using the 35 mm camera and the CCD camera. The optimal exposure time was found to be 30 seconds for the 35 mm camera and the CCD camera is capable of producing near real time images. The developed 35 mm film was then digitised using the Fujitsu General camera and the Quantimet image analyser. The resulting images from the use of the 35 mm camera and the CCD camera are shown in Figures 3.5a and 3.5b respectively. The image shown in Figure 3.5a is significantly more blurred than that of Figure 3.5b. Also the features in Figure 3.5a appear to have been shifted outwards due to spherical aberration. This is not the case when the CCD camera is used as only a small part of the lens is utilised. It must therefore be concluded that the CCD camera

is capable of producing much higher quality images than the 35 mm camera and was therefore used throughout this work.

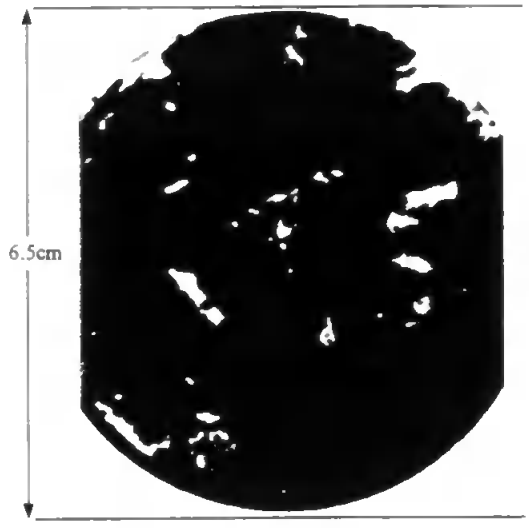

Figure 3.5a : 35 mm Camera Image

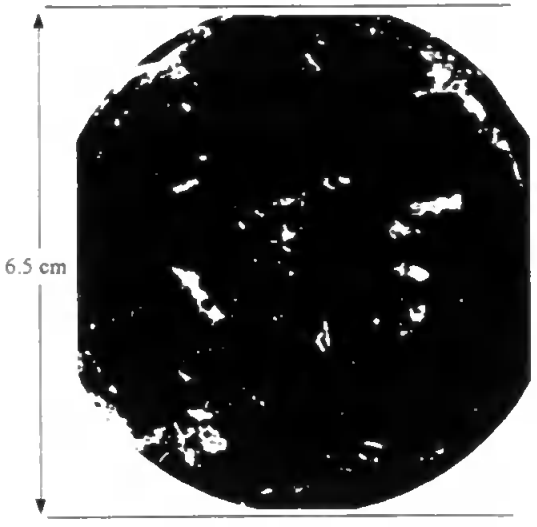

Figure 3.5b : CCD Camera Image

3.3.2 Evaluation of Compound Image Technique

Individual images can be gathered by to form a composite image by matching up the edges of each individual image. Edge matching is achieved by using the buffer zones as shown in Figure 3.1. The live image is then matched with the stored edge to form the image. In the case of the PEG 6000 impregnated samples however, large regions of the compound images are almost completely without fluorescing voids (e.g Figure 3.6, section 3.3.2) Given that the compound images are themselves comprised of a 4 x 4 grid of individual images, entire individual images can often be featureless and therefore impossible to match up with the next image. For this reason, images were taken under visible light, for the purpose of matching up grids of images which have large featureless areas. The problem is not so acute in the analysis of the Crystic resin impregnated sample set because of their higher porosity and the fluorescence images generally have many more features as

contrasted by comparing Figures 3.6 and 3.10. This method of producing compound images is generically useful for the analysis of low porosity surfaces such as those found in compacted soil or high stone content.

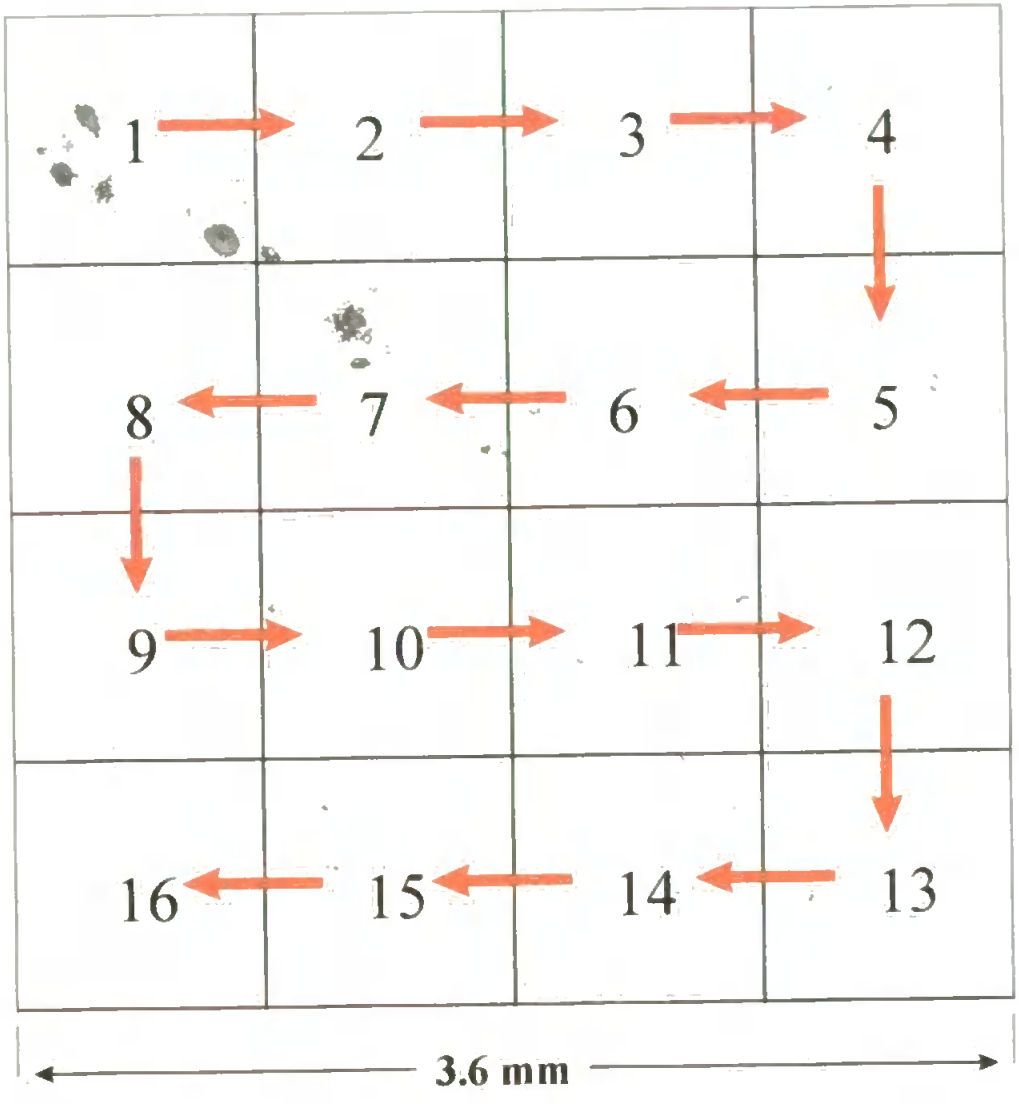

Figure 3.6 : Compound 4x4 grid inverted image of a PEG 6000 impregnated sample taken a depth of 5cm. The inverted image has 132 voids and are shown in black. The porosity of this images is 1.58 %.

3.3.3 Comparison of Experimentally Determined Porosity and Porosities Predicted by Water Retention Models

The experimentally determined porosities at low and high magnification are given in Table 3.1. Comparative estimates of the porosity were made using the water retention models of

Kosugi [29], Brooks and Corey [17] and van Genuchten [30] and are also given in Table 3.1.

For the purposes of the comparison it was assumed that the low magnification used to obtain large frame images made all voids < 85 μm invisible, 85 μm pixel^{-1} being the resolution of the image analyser at this magnification. The porosity of the fraction of pores > 85 μm equivalent circle diameter was estimated by subtracting the empirically derived volumetric water content at the equivalent Laplace / Washburn pressure by use of Equation 1.1. The calculated porosity for the high smaller high magnification images was calculated in the same manner under the assumption that all void < 1.85 μm were invisible, which was again the resolution of the image analyser at this magnification.

Description	Fine Earth Porosity (Low Magnification)	Fine Earth Porosity (High Magnification)
PEG 6000 Samples, (0-25 cm depth)	mean =1.62, (n=90)	mean = 4.11, (n=320)
Crystic Resin Samples (0-25 cm depth)	mean = 19.85, (n=90)	mean = 24.27, (n=320)
Crystic Resin Samples (25-55 cm depth)	mean = 20.27, (n=90)	mean = 24.65, (n=320)
Kosugi Predicted (0-55 cm averaged)	12.1	25.4
Brooks & Corey, Predicted (0-55 cm averaged)	11.8	25.7
van Genuchten, Predicted (0-55 cm averaged)	11.6	25.8

Table 3.1: Experimentally determined and water retention predicted porosities at low and high magnifications.

The experimental porosities given in Table 3.1 are fine earth porosities, and to obtain these values it was necessary to scale upwards the observed porosities to account for stone content. The mean stone content was found to be 12.6% (v/v), a reasonably high value.

High stone content is one of the primary features of Crediton series soils in the South West of England and stone contents accounting for up to 50 % of the soil volume are not unknown [193].

The predicted porosity from each water retention model generated nearly identical porosities for both 0-25 and 25-55 cm depths and are therefore presented as averages shown in Table 3.1. The similarity is not surprising because of the similarity of the two water retention curves used to calibrate the water retention models at these depths, Figure 2.3. These curves cover the 0 - 55 cm depth range which encompass the A (0-20 cm) and B (20-55 cm) horizons of the soil. For this soil series (Crediton) the A and B horizons are only weakly distinguishable [193].

POROSITIES OF PEG 6000 IMPREGNATED SAMPLES AT LOW MAGNIFICATION

The differences between experimental and water retention derived porosities are very large (almost an order of magnitude) and the experimental porosity very low. The experimental and modelled porosities will in practice never agree precisely for two reasons. Firstly as discussed in Chapter 2 the water retention models produce fits which are not unique, and therefore it is not possible to determine a unique porosity. Secondly, the aligned capillaries model is not exact for soil [43]. However it is unlikely that the water retention models are so grossly inaccurate and this led us to look for a systematic explanation of the porosity discrepancy.

POROSITIES OF PEG 6000 IMPREGNATED SAMPLES AT HIGH MAGNIFICATION

In the PEG 6000 sample set, four samples were taken in the depth range 0-25 cm. Each 25 cm was cut into 1 cm sections. A set of 16 images as shown in Figure 3.2 was obtained for each core in the depth range 0-5 cm, 5 - 10 cm 10 - 15 cm and so forth up to 25 cm. In

total 320 small frames, representing a total area of 10^5 μm^2 were analysed and the mean porosity of these samples was 3.59% and fine the earth porosity was 4.11% as shown in Table 3.1. The use of a larger number of frames is necessary to obtain a representative set when smaller individual frames are used. The porosity given by these small images is higher than those observed at low magnifications. This is partly because fluorescence microscopy works in the opposite way to reflectance microscopy. At higher magnifications the lens is closer to the sample and more light is collected by the instrument because the sample is an emitter of light. In addition the smaller frame size allows for a much higher resolution (1.85 x 1.85 μm per pixel), this enables the visualisation of smaller, fainter features and all features appear in more detail.

Water retention models of Kosugi, Van Genuchten and Brooks & Corey all generated porosities of around 26% assuming a 2 micron cut off (see Table 3.1.) The porosity of image analysed PEG 6000 samples was still much lower than the predicted ones and the smaller voids account for an unusually large proportion of the porosity, around 60%. This is consistent with a collapse of the macropore structure which would be observed if the area had been trampled by steers. The PEG 6000 samples were therefore not representative of the typical Crediton profile and therefore could not be used for comparison with the Pore-Cor modelled data.

A later investigation revealed that the sampling site at which the PEG 6000 samples were collected had been accidentally grazed by steers. The most probable explanation is that the topsoil had been compacted by steers and the macropore structure had largely collapsed causing the low observed porosities.

3.3.4 Porosity Images of Crystic Resin Impregnated Samples

The porosity analysis carried out on the PEG 6000 samples was repeated for the Crystic resin samples. For the Crystic resin samples the experimental porosity at low magnification was around 20% (see Table 3.1), much closer to the porosity of around 12% predicted by the water retention models at this scale. The porosities of experimental samples at both low and high magnification were very similar at the two depth intervals studied. The experimental porosities at high magnification were around 24.5% again in reasonable agreement with the prediction of the water retention models.

3.3.5 Feature Size Distributions

Because of the porosity discrepancies in porosity found in the PEG 6000 impregnated samples only the measurements made on the Crystic resin samples are used for comparison with the Pore-Cor model.

Large Features

Large frame images obtained using the CCD camera feature measurements made on frame areas of around 36 mm x 36 mm. Only features, or parts of features within the observation fame were measured. A more traditional approach to this would be to use a guard frame to determine feature acceptance or rejection. However, because the observation frame area is very large with respect to the area of the measured features, edge effects at this sale of observation are small and the used of a guard frame irrelevant.

The resulting experimental distributions can be seen in Figure 3.7. They have been adjusted to a logarithmic percentage scale. At this scale of observation, features with

equivalent circle diameters less than twice the resolution of the images analyser are not

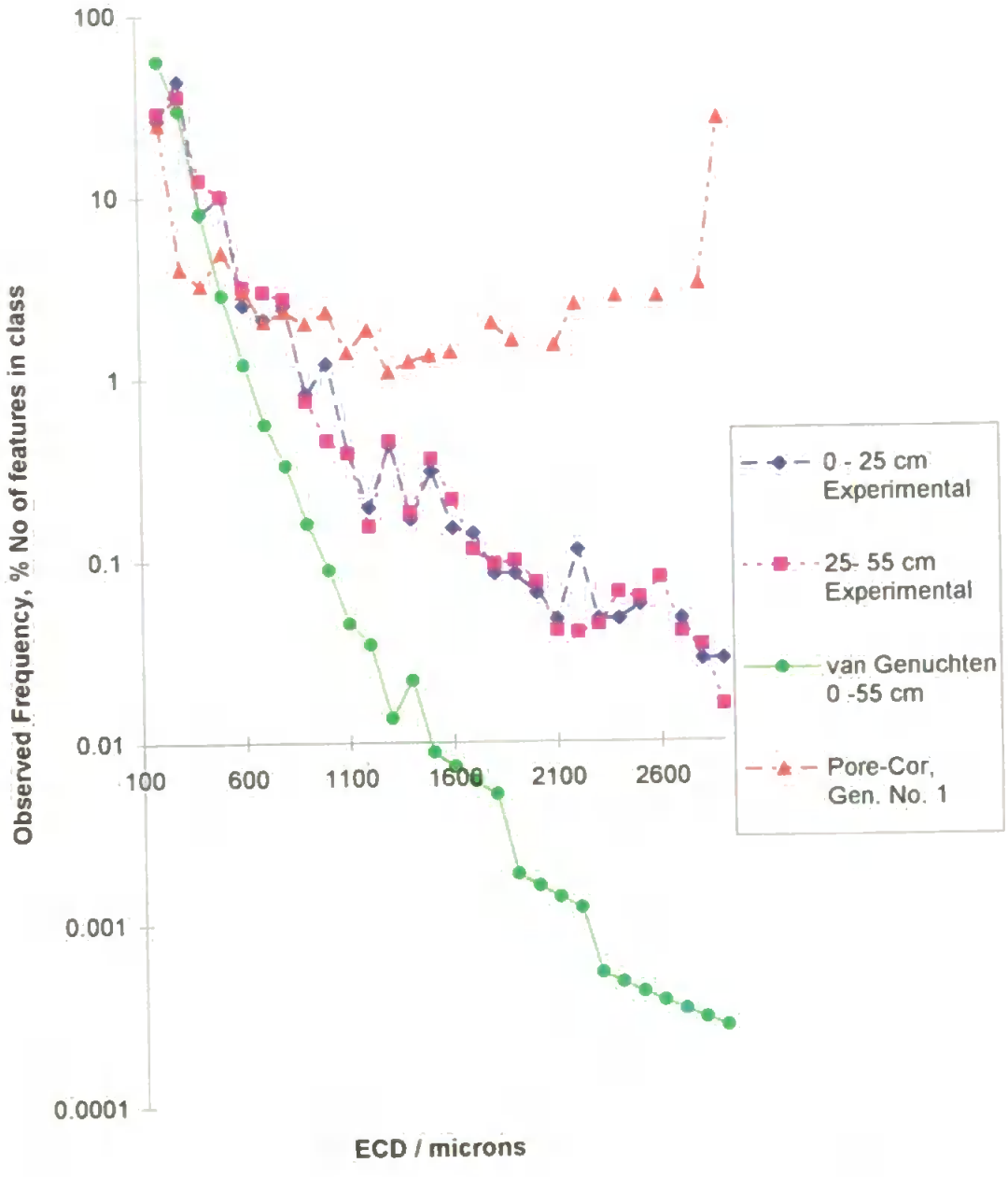

Figure 3.7 : Pore size distributions in the range 100-2900 μm equivalent circle diameter.

measured. The experimental data therefore end at 170 microns diameter. Comparing the 0-25 and 25-55 cm experimental distributions using a chi squared test gave χ^2 equal to 0.06, with a critical value of χ^2 of 41.33 (with 27 d.f , and a 95 % confidence interval.) The null hypothesis that they were the same could therefore not be rejected. Both experimental

distributions have a percentage frequency drop-off below 200 microns, because this size is close to the resolution limit of 85 μm of the analyser.

The frequency distribution based upon the first derivative of the corresponding van Genuchten fitted curve to an average of the 0-25 and 25-55 cm depth curves shown in Figure 2.3 is also shown in Figure 3.7. Taking the first derivative approximation implies that all of the voids are open to external pressure as discussed in Chapters 1 and 2.

Between each pore diameter interval the change in water content is $d\theta$. The volume change $d\theta$ can be transformed into the relative number of three dimensional features by assuming that in each range features has a volume proportional to r^3 in the interval $d\theta$. However further approximations are necessary for the three dimensional distribution to be made two dimensional. In Figure 3.7, the distributions are give relatively, because they are expressed as percentages.

In Figure 3.8 an arbitrary three dimensional structure is shown along with a corresponding two dimensional slice. If this were the only slice taken, then in the three dimensional structure, 8 or 22.9% of the spheres are large and 27 or 77.1% of the spheres are small. In the two dimensional structure 30.7 % of the spheres are large and 69.3% of the spheres are small. However an infinite number of two dimensional slices would give the same big to small number ratio as the three dimensional structure. Because many experimental two dimensional slices have been taken, the assumption that the percentage ratios are comparable in Figure 3.7 is a valid one.

The void size distributions given by van Genuchten appear to be very different to the experimentally measured ones in Figure 3.7. However the variation occurs mainly at relative frequencies below 1% and therefore the absolute difference between them is negligible. A Chi square analysis revealed that there was no significant difference between the 0-25 cm

experimental and van Genuchten distributions. The corresponding values were $\chi^2 = 0.50$ with a critical value of 41.33 for 27 d.f and a 95% confidence interval. If the void size distributions are compared in the 300-2900 micron ECD (equivalent circle diameter, the diameter of a circle with the same area as a measured feature) the range to eliminate the drop off in frequency observed due to the resolution limit of the analyser and without a log scale they appear very similar, Figure 3.9.

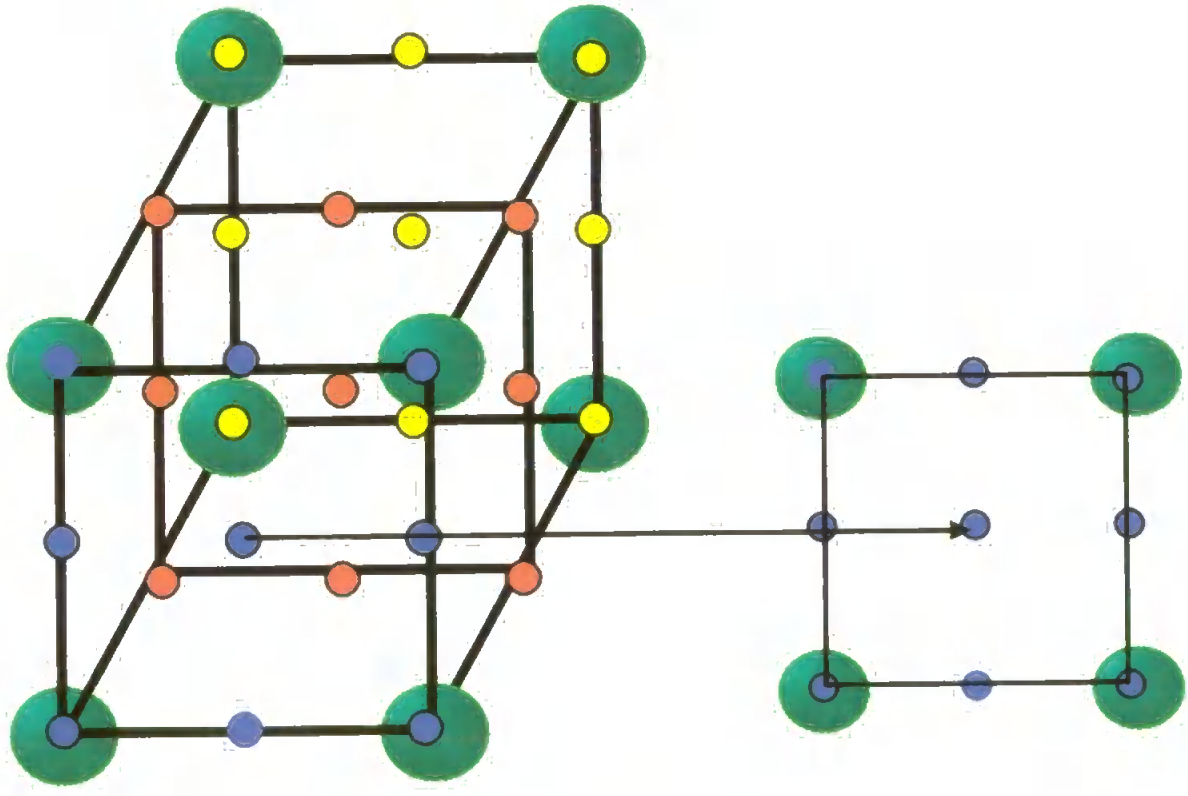

Figure 3.8 : Isotropic homogeneous structure showing how the ratio of void sizes is altered if too few slices are taken.

The Pore-Cor void size distribution, shown by the dotted red line with red triangular points is very different to the 0 - 25 experimental distribution. The large differences seen Figure 3.6 are significant and $\chi^2 = 247.94$ considerably greater than the critical χ^2 value of 41.33. The other noticeable feature of the Pore-Cor distribution is the large peak which occurs at

2900 microns. This peak is caused by the use of the pore skew parameter which multiplies the size of all pores up to the pore row spacing. In table 2.5, the pore skews used in the generation of Pore-Cor structures are given. The use of the pore skew parameter is necessary to compensate for the inefficient packing geometry as discussed in Chapter 2.

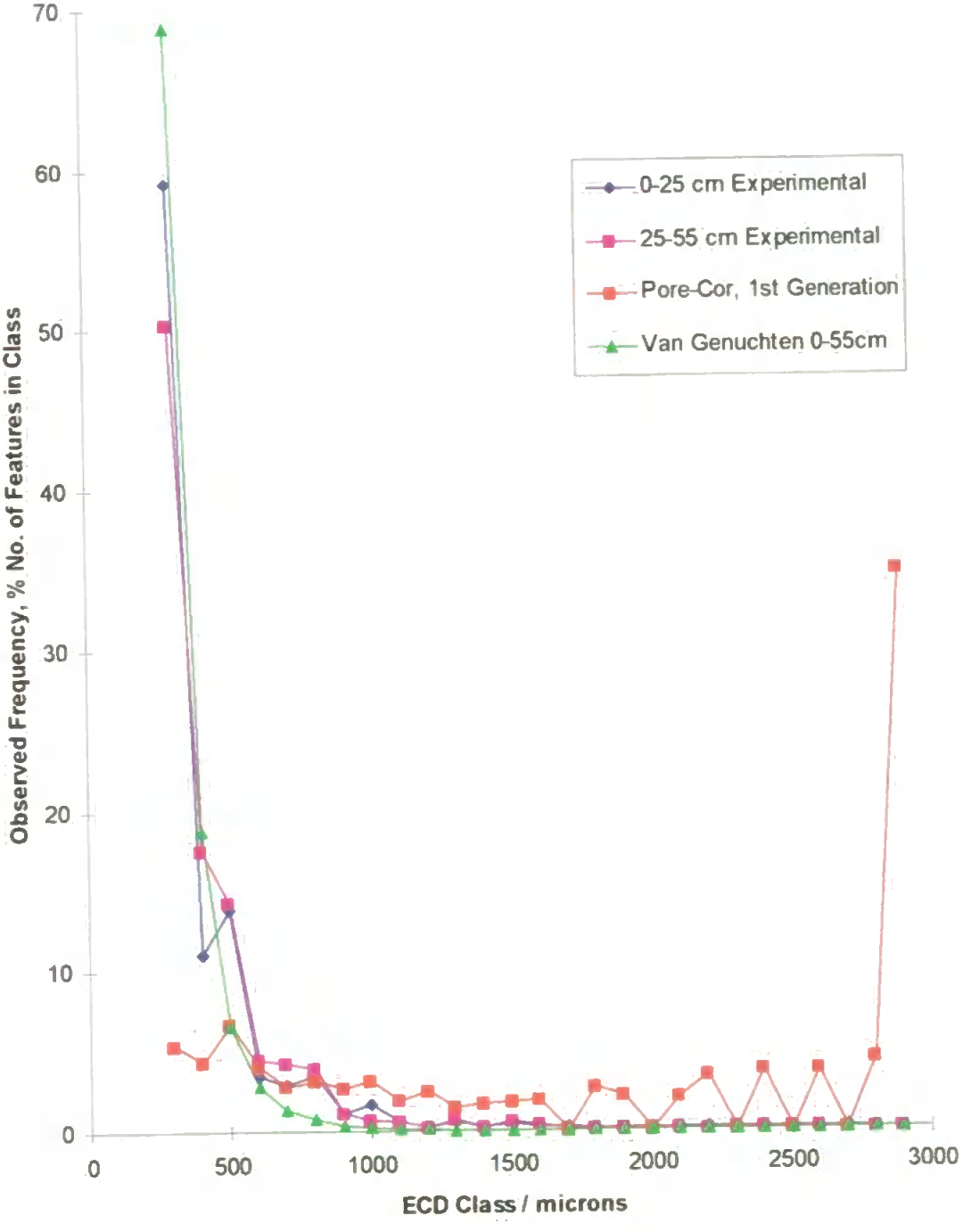

Figure 3.9 Void size distributions in the range 300 to 2900 microns equivalent circle diameter.

3.3.6 CONSISTENCY OF OBSERVATIONS

EXPERIMENTAL VOID SIZE DISTRIBUTIONS

The experimental distributions previously mentioned have been measured with the assumption that the two dimensional images produce discrete features. This assumption is valid for the PEG 6000 samples, where the porosity is low, Figure 3.5b. The identification of discrete features by inspection alone in the case of the Crystic resin fluorescence images is less valid because the images are complex and have a higher porosity Figure 3.10.

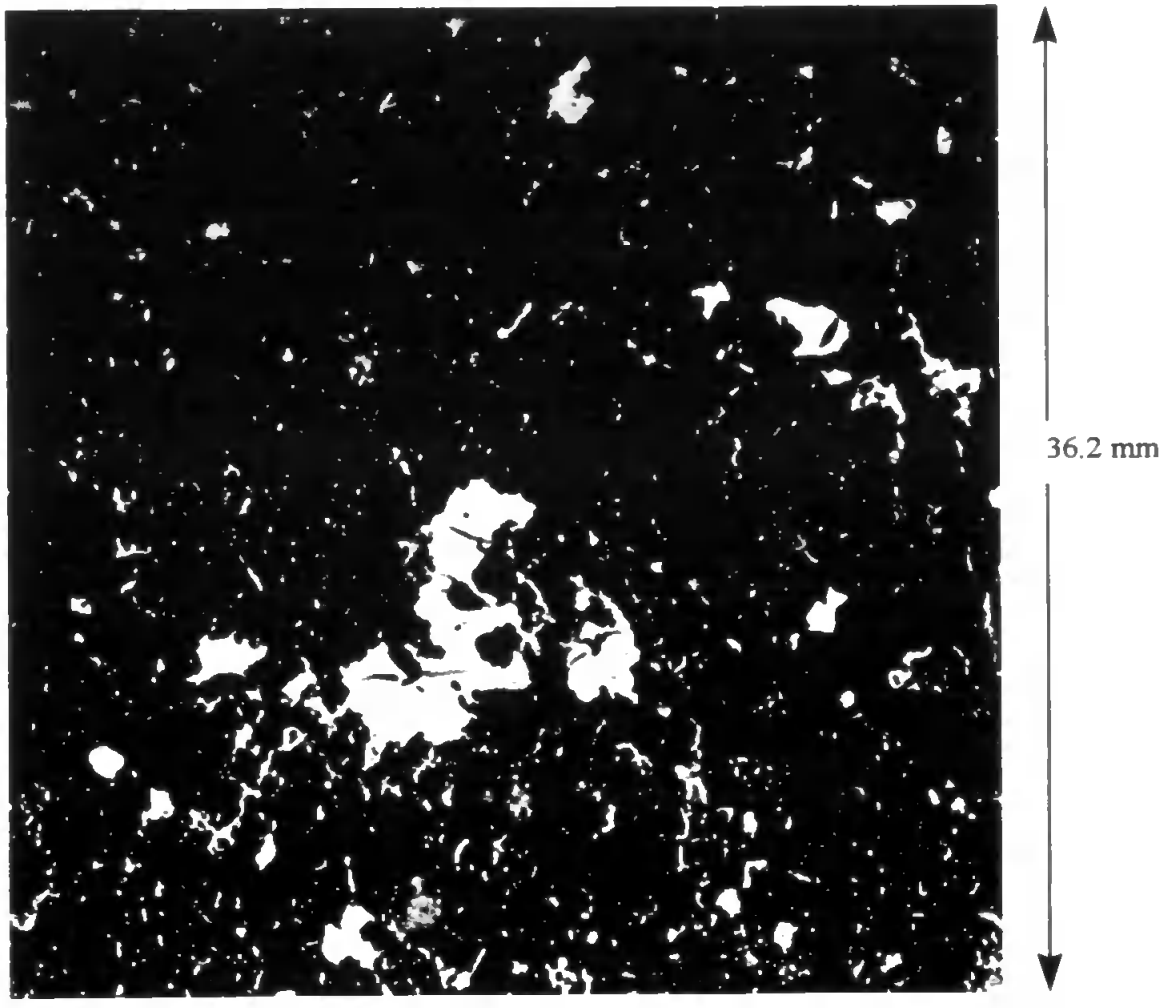

Figure 3.10. Fluorescence image of a Crystic resin impregnated soil sample. Taken at a depth of 4 cm. This image has a porosity of 14.05 % and a total of 1473 features. Voids are shown by the white areas.

The image analysers segmentation routine was used to determine the discreteness of the voids in the Crytic resin impregnated surface images. The segmentation process erodes the outer pixel of each detected feature. When the eroded image was then re-constructed, pixels were added to the perimeter of each feature to rebuild it. Features are prevented from joining back up together by ensuring that a one pixel boundary remains when then image is rebuilt.

For comparison, four images at depths of 5,10,15 and 20 cm were used and analysed together. The original unsegmented images were analysed and then the same images eroded one pixel, then rebuilt. The resulting distributions can be seen in Figure 3.11. The resulting distributions are very similar which would be expected for images which have discrete features. The three dimensional interpretation of the segmentation is not straightforward and makes little difference to these samples and was therefore not used further.

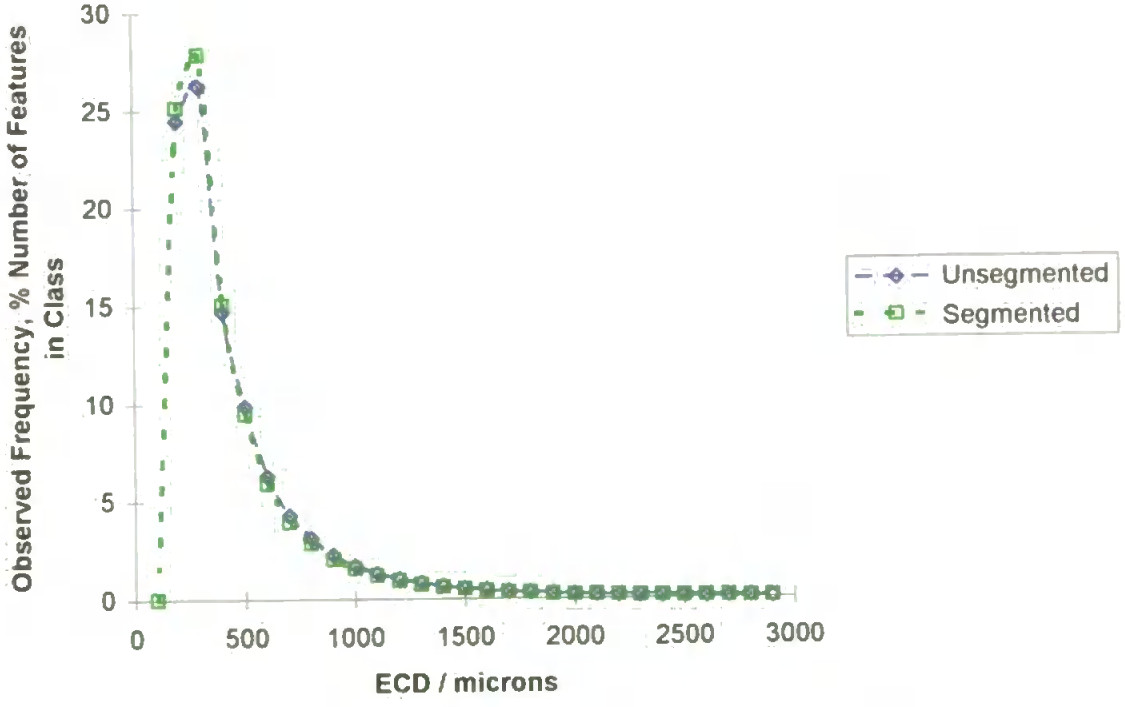

Figure 3.11 : Effect of segmentation on the shape of the experimental void size distributions. Both distributions are derived by combining the observations for four surfaces as described above.

PORE-COR VOID SIZE DISTRIBUTIONS

In Chapter 2, the non-uniqueness of the Pore-Cor fitted network was discussed. By changing the random seeding number, alternative networks that also fit the water retention curve can be found. Therefore, the void size distribution will also change. To illustrate this point, the pore size distributions generated over five stochastic generations of networks based on the 0-25 cm set 3 curve are shown in Figure 3.12.

The pore size distributions generated from random generations are very similar. They all have a large peak at the upper pore diameter end of the distribution. The similarity of the distributions is an artefact of the distortion of the network through the use of the pore skew parameter needed to fit the experimental porosity. Packing problems therefore dominate the Pore-Cor soil structures. Figure 3.13 depicts the structure used to fit the 0-25 cm curve and is clearly distorted by pores of limiting size and very small diameter and length throats.

The Pore-Cor distributions produced so far have been based upon the FORTRAN linear microtoming algorithm which only cuts the unit cell in the x, y or z planes. The intersection between a plane at 15 Deg and a Pore-Cor unit cell is shown in Figure 3.14.

The image shown is comprised of 471 x512 pixels and therefore has a resolution of 66μm pixel^{-1}. The size of the grid must be less than 512 x 512 pixels to fit in the image analyser. This resolution was too low to be of use in the production of pore size distributions. To increase the resolution of the ray tracing technique, the camera was placed such that each grid was split into four (as shown in Figure 3.3), giving a resolution of 33 μm pixel^{-1}. The ray tracing of these images is an extremely slow process because a large number of computing calculations are necessary to produce a single image. The production a single image on an Pentium Pro 200 MHz workstation takes over eight hours. To analyse a single unit cell at cutting intervals of 5 degrees required 72 such images. To economise on computing time, only one unit cell corresponding to the first stochastic generation was

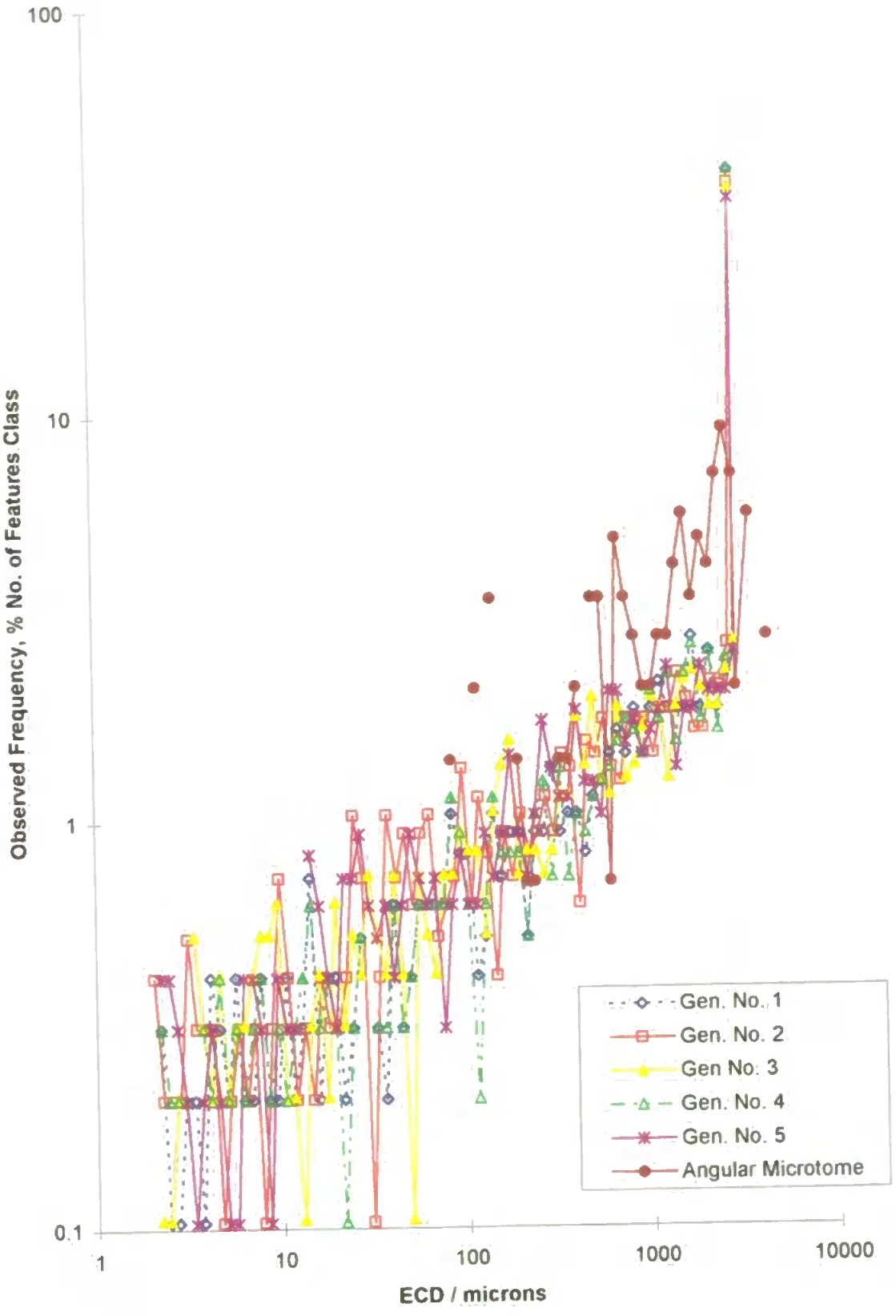

Figure 3.12 : Pore size distributions generated by fits of different stochastic generations to the 0-25 cm set 3 curve.

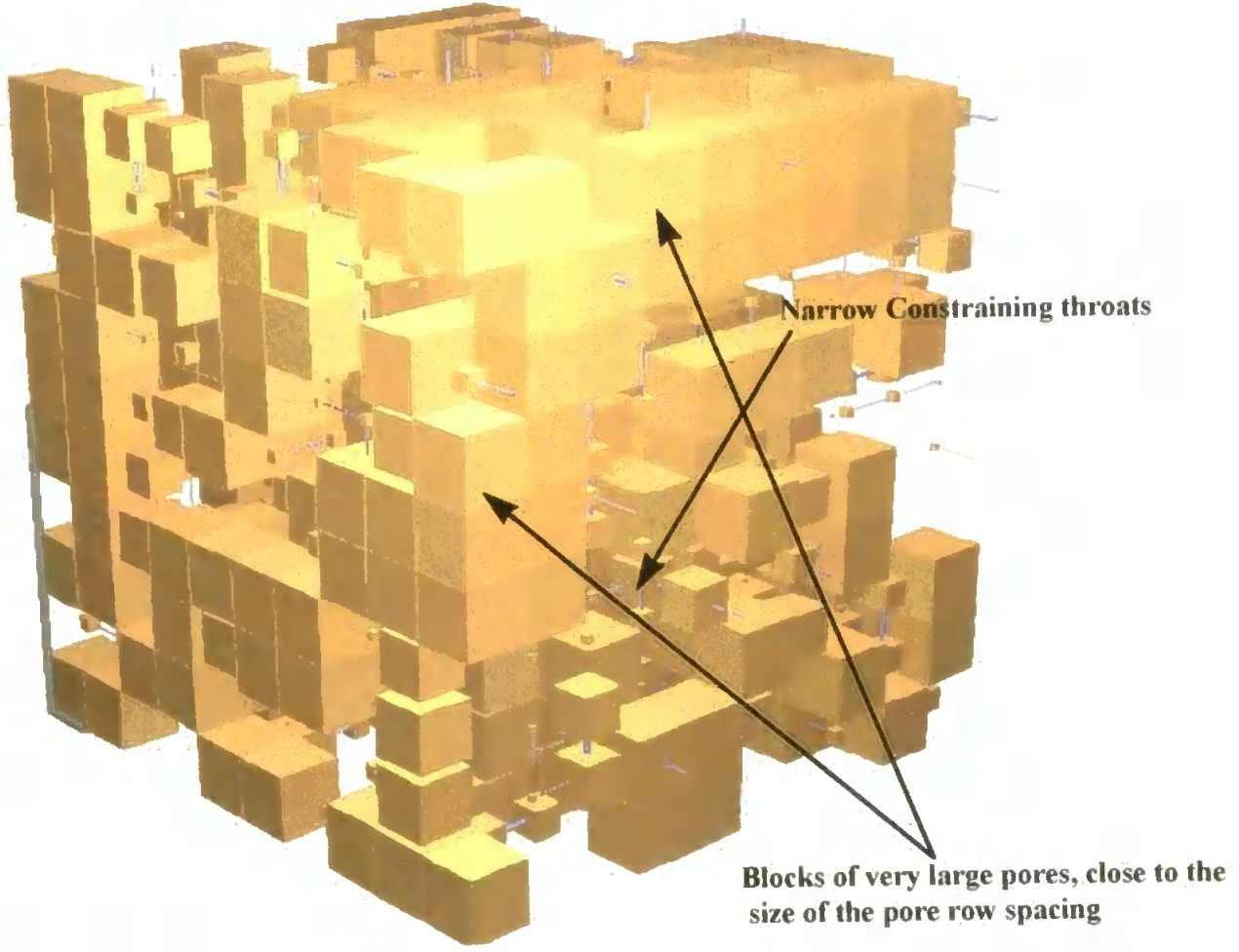

Figure 3.13 : Pore-Cor generated structure for the set 3, 0- 25 cm modelled curve, with one stochastic generation.

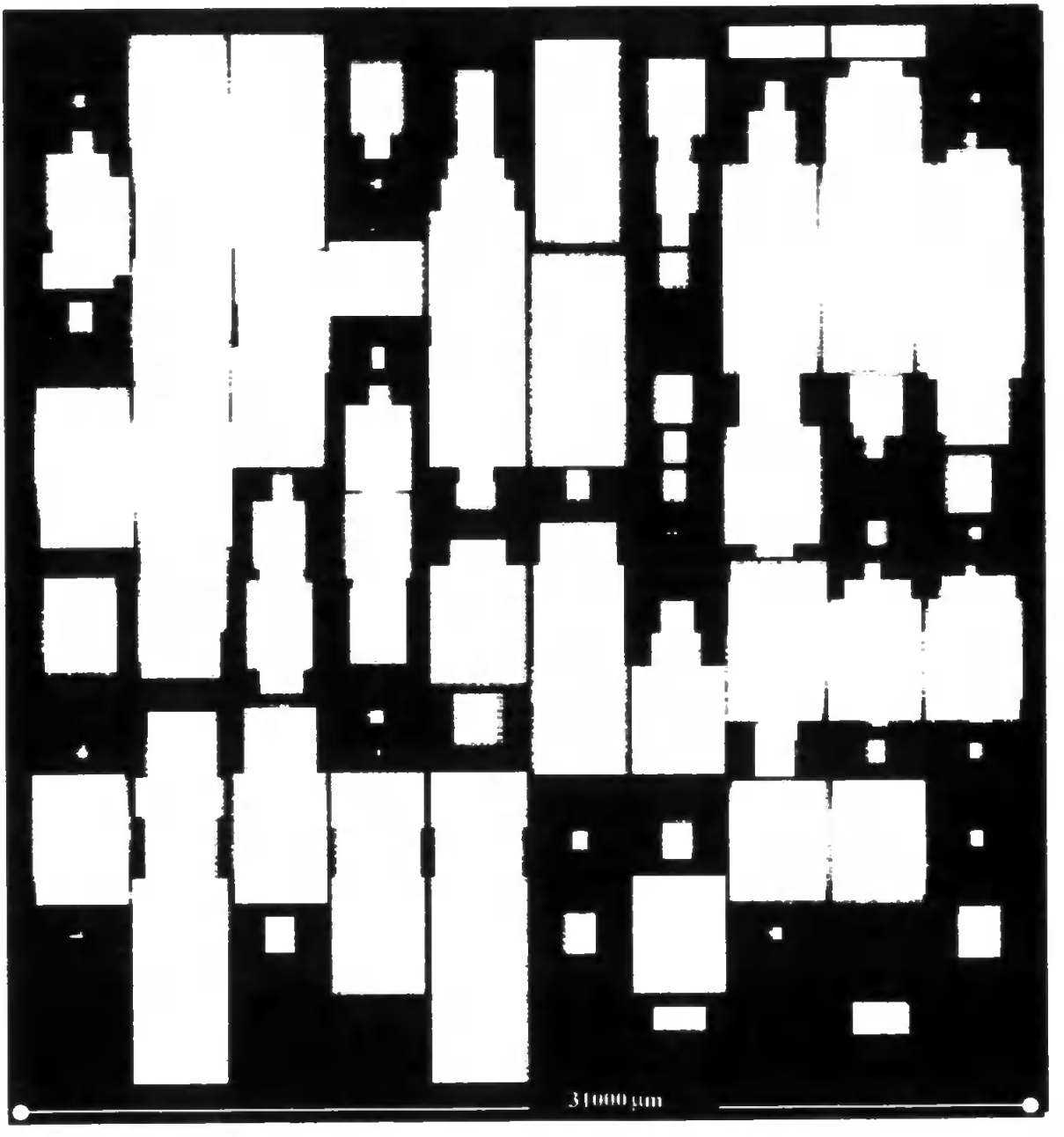

Figure 3.14 : Low resolution image of the intersection of a plane with the Pore-Cor unit cell.

microtomed. Given that the unit cells produced by different stochastic generations themselves are very similar this approximation is reasonable.

The distribution obtained by angular microtoming is slightly different to the linearly microtomed distributions. Firstly the maximum ECD is greater due to the plane intersecting

with large pores at angles. Secondly the peak of large pores is split up because of the partial exposure of the largest pores. Thirdly pores < 60 μm ECD were not resolved, shifting the remainder of the distribution upwards. This effect is however insignificant because of the relatively small numbers of small features. The angular microtoming therefore does not present a significantly different interpretation of the Pore-Cor structure.

3.3.7 Combining High and Low Magnification Measurements

The combination of the experimental void size distributions at different magnifications is not straightforward. However, because our images appear to be discrete and isotropic, it was possible to make an estimation of pore size distribution in the range 4 - 2900 μm ECD. The porosity each size fraction was calculated by using the summed area of all of the features in the size range and dividing by the total area of all of the measured frames. Porosities of 19.61 %, 2.97%, and 0.39% were found in the ECD classes 4-25, 25-250, 250-2900 microns respectively. The sum of these porosities is 22.97 %, about 1.5% lower than the equivalent high magnification porosities of 24.65% and 24.27% quoted in Table 3.1. The reason for this is the way in which the measurements were made. In section 3.3.3 the porosity is simply calculated from the fraction of void to matrix and no features were rejected. Given that the selection criteria used for the acceptance or rejection of features is such that features wholly within the frame are accepted and those wholly or partially outside are rejected the porosities were lower.

The frame size was kept much larger (an order of magnitude higher than the largest feature's ECD) to reduce edge effects and for this reason, the porosities measured by this method were only slightly lower because edge effects were small.

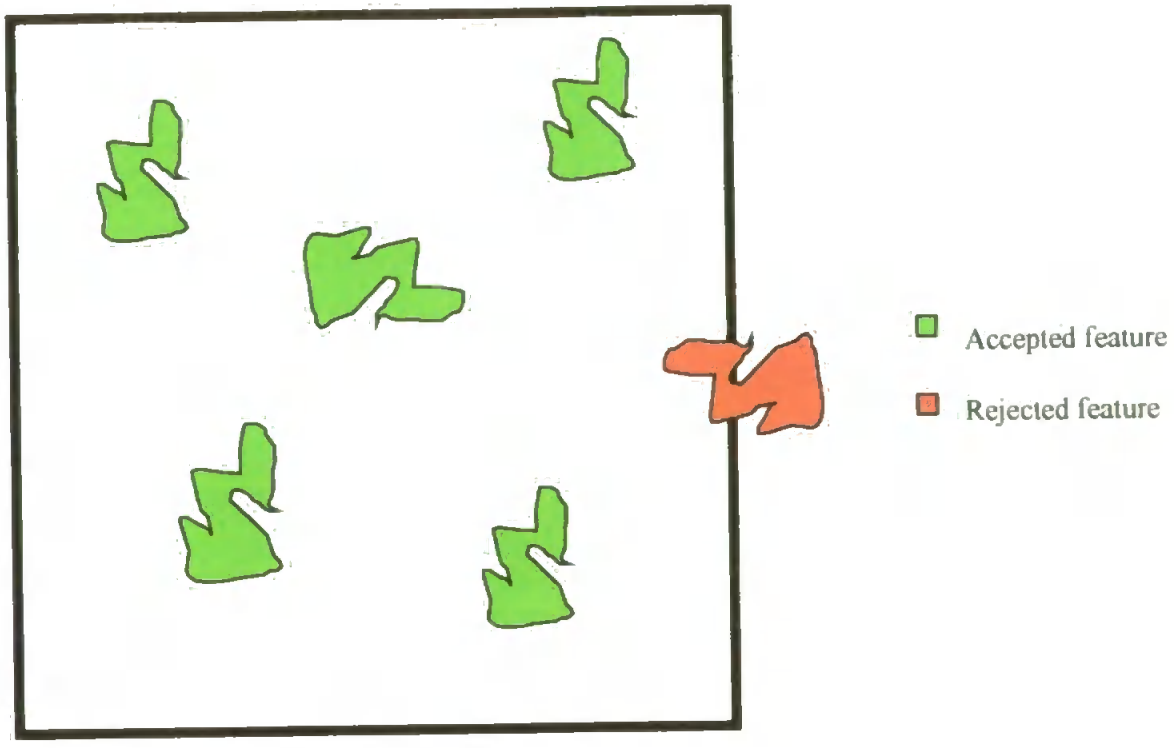

Figure 3.15 : Feature acceptance

The combined experimental distribution is given in Figure 3.16, and the ECD intervals at successively higher magnifications are smaller. The absolute frequencies have therefore been adjusted to compensate for the size of the interval by dividing by the size of the interval. Because there is no significant difference in the experimental distributions in the depth interval 0-55, they have been combined. The distribution does follows a pattern of decreasing frequency with size of feature. The drop in frequency at the 4 and 6 micron intervals is due to these sizes approaching the resolution limit of the analyser (1.85 mm pixel^{-1}).

The small discontinuities in the combined distribution are caused because it is assumed that the observations of the smaller features may be scaled up to the frame areas of the larger ones. However with 320 small frames measured, this approximation is more reasonable if the sample is isotropic.

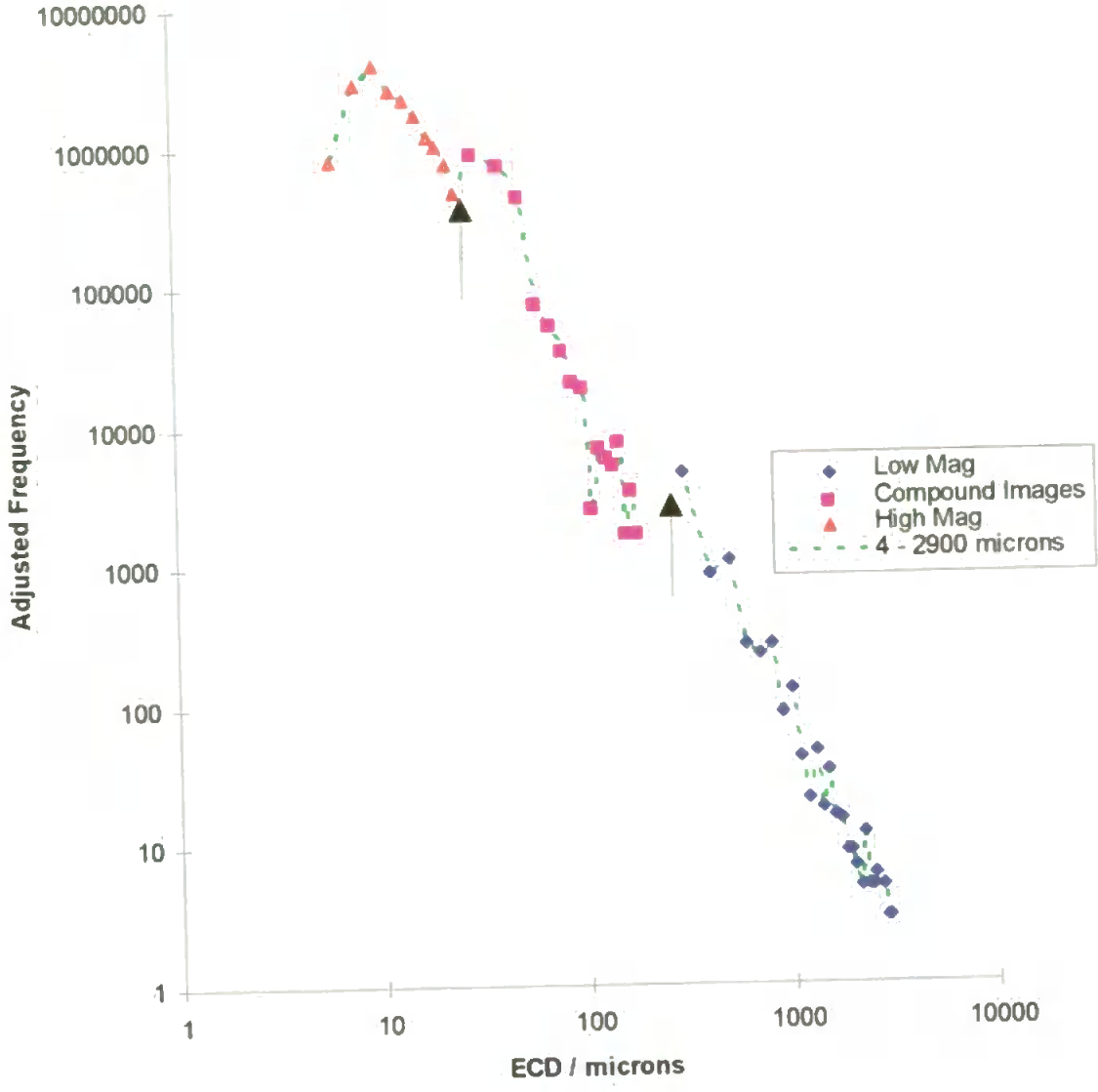

Figure 3.16: Experimental distribution in the range 4 to 2900 μm ECD obtained by combining individual distributions. The adjusted frequencies shown are scaled to represent the same area.

Comparison of the normalised combined experimental distribution in Figure 3.17 reveals some of the other Pore-Cor geometric assumptions. The Pore-Cor geometry limits the number of pores to 1000 and the number of throats to 500*c*. In a typical structure the co-ordination number is three, giving a total of 2000 features. As mentioned previously the throats are spilt into 100 sizes distributed along a log linear axis. The lowest number of features in a class is 1 (typically 0.05% of the total features). This is the smallest frequency

which may be represented by the Pore-Cor unit cell. The Pore-Cor unit cell is therefore incapable of representing the full range of pore sizes found in real soil samples because it has too few nodes. Comparison in a more limited ECD range may, such as shown in Figure 3.7, be a more valid approach. However, the restriction of pore size range as discussed in Chapter 2 reduces the accuracy of the model.

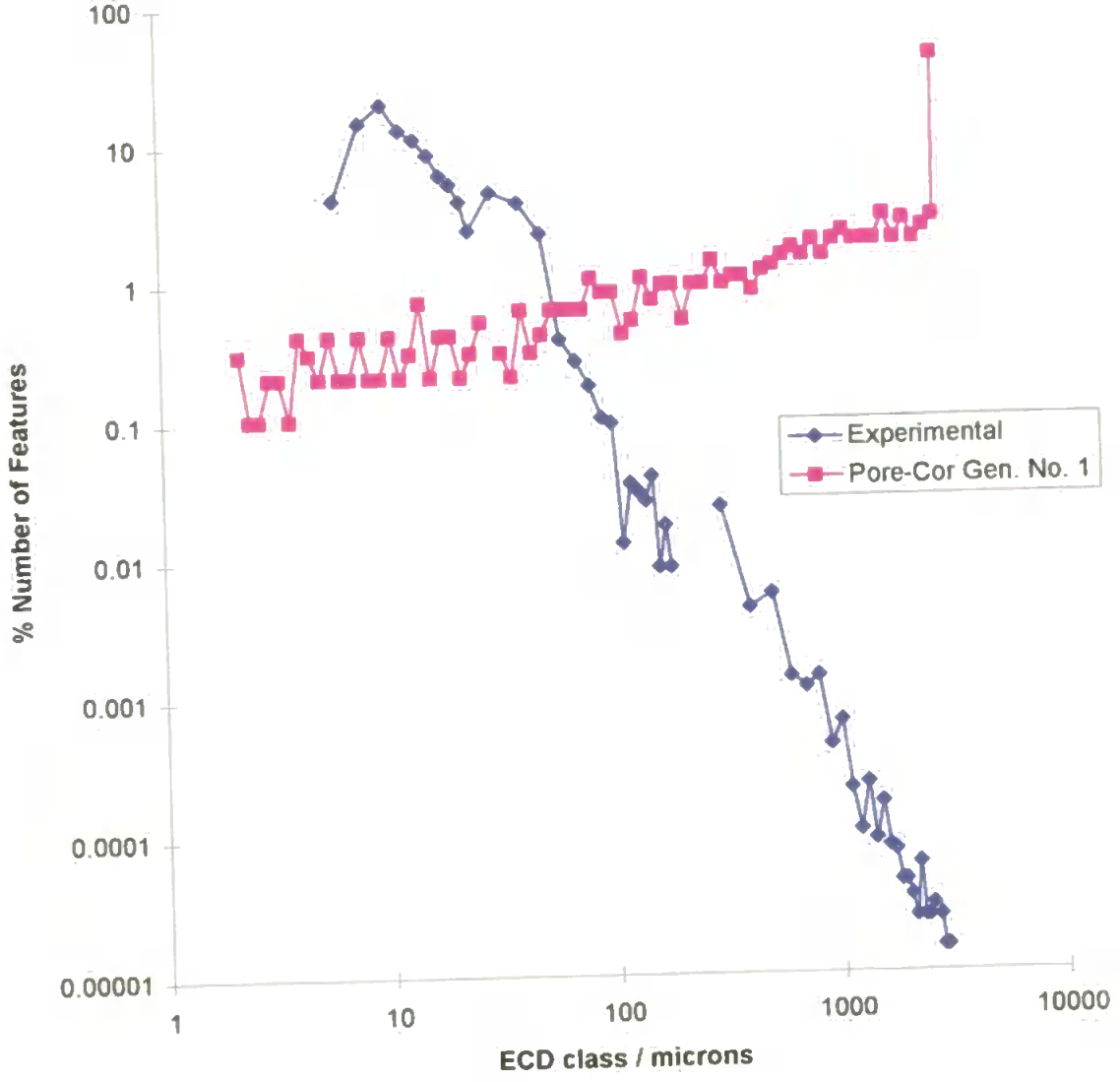

Figure 3.17 : Comparison of Pore-Cor (by linear microtoming) and normalised Experimental pore size distributions over the 4 to 2900 micron ECD size class range

3.3.8 Comparison of Particle Size Distributions

Particle size distributions obtained experimentally at depths between 10 and 90 cm, are shown in Figure 3.18. All of the crosses corresponding to each depth, are in the sandy loam area.

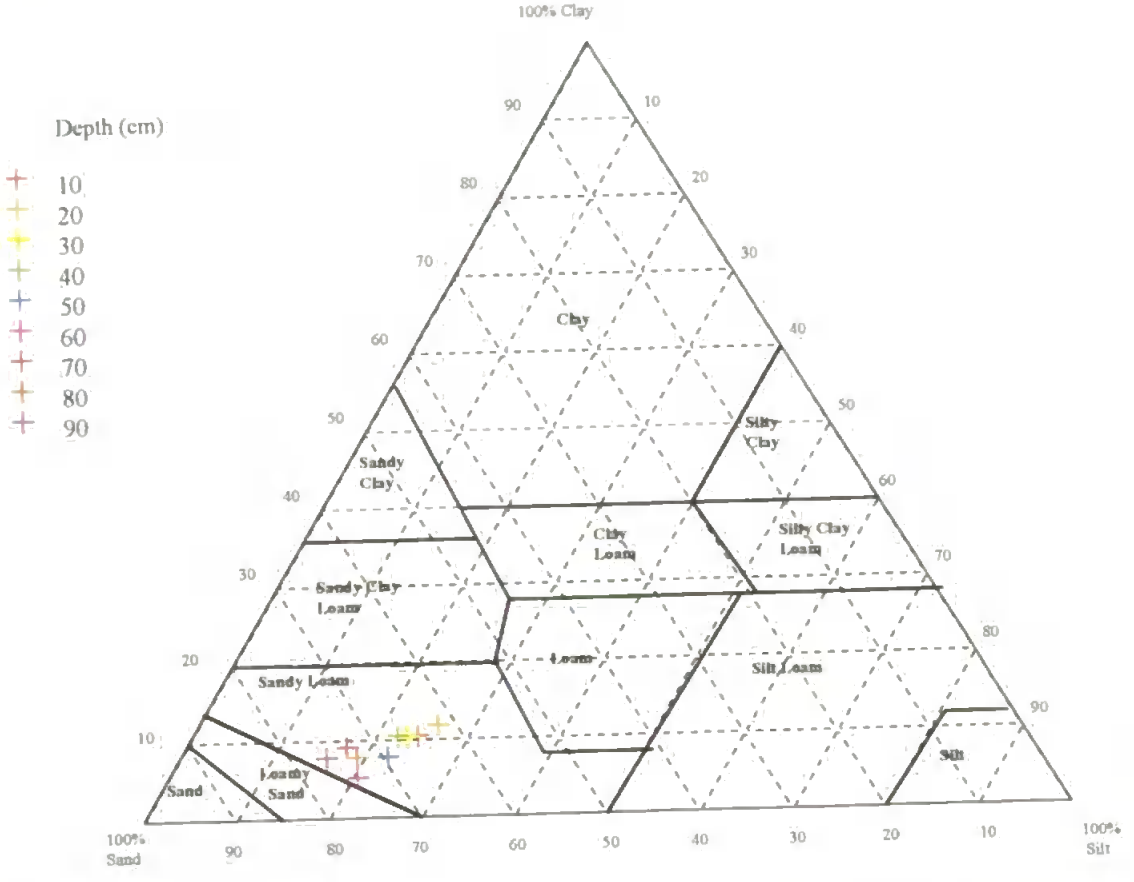

Figure 3.18 : Textural class diagram showing the experimental particle size classifications with depth. The system of classification used here is the UK one.

Figure 3.19 which is a scaling up of the lower left hand portion reveals a particle size depth trend. There is a trend of increasing particle size with depth. This is often the case in soils which are more like their forming bedrock at increasing depth and more weathered in the upper layers.

The trend is also repeated in the Pore-Cor simulated data, although the absolute sizes are too coarse (Figure 3.20). Pore-Cor predicts that there are no clay particles in the

distribution and that the percentage of silt particles decreases with depth. This can be rationalised in terms of Figure 3.4. At increasing depths the pore skew decreases (Table 2.5) and therefore the probability that a particle of minimum size will be generated by eight pores of maximum size decreases with decreasing Pore-Skew.

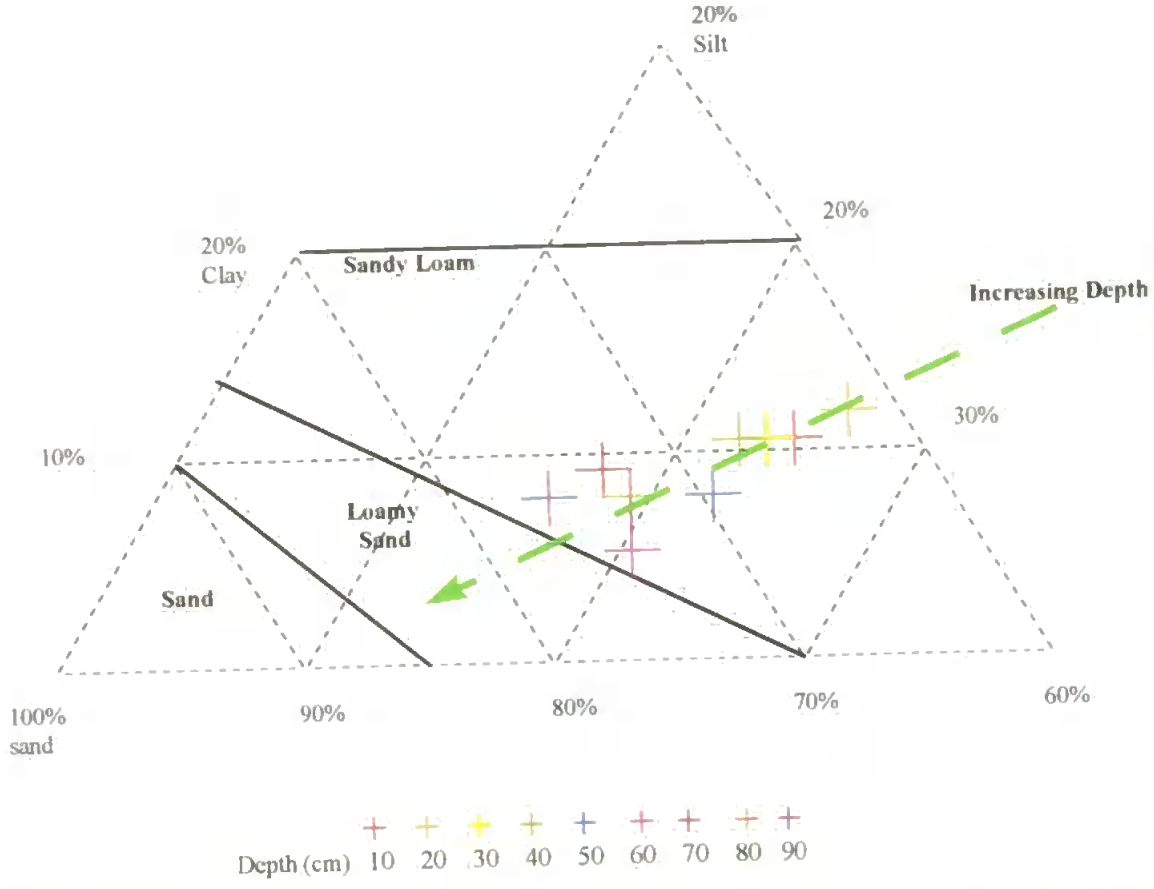

Figure 3.19 : Lower left hand portion of textural class diagram showing increasing sand like characteristics with depth

The data in Figures 3.18-20 are not directly comparable, because the experimental data are measured in terms of percentage mass and the Pore-Cor predicted ones are in percentage number of features. Clearly Figure 3.20 shows that most of the Pore-Cor predicted particles are stones and if we assume that the volume and mass of each individual

stone is proportional to the cube of its radius, then almost all > 99% of the mass would be accounted for by stones which is unrealistic. Therefore the Pore-Cor generated particle size distributions are grossly inaccurate but do map trends.

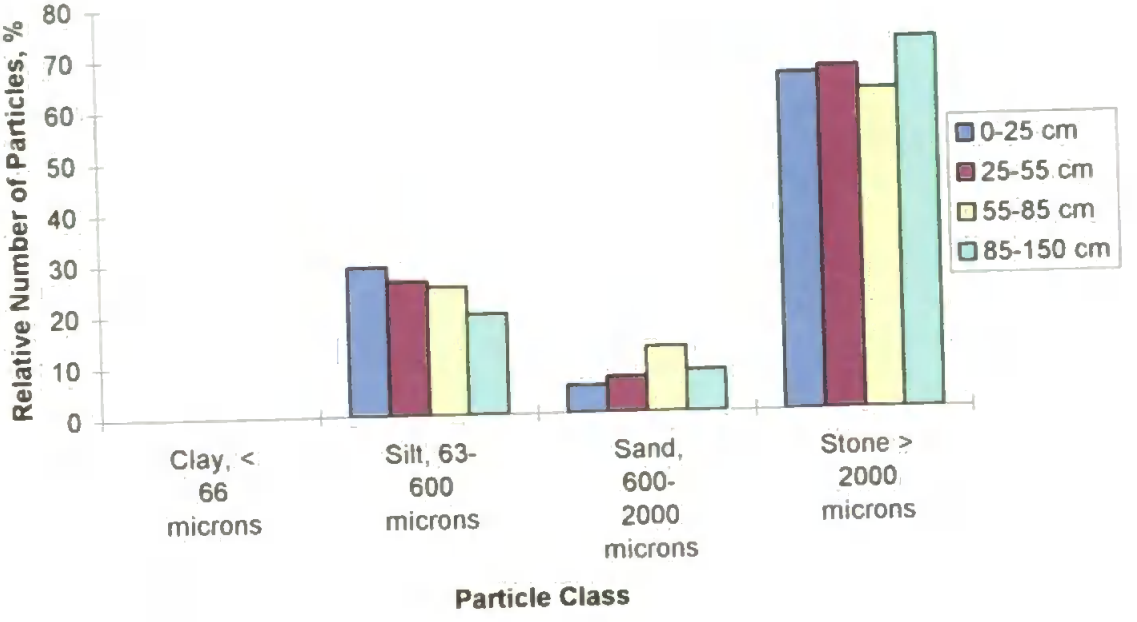

Figure 3.20 : Pore -Cor textural information output

3.4 CONCLUSIONS

The Pore-Cor structure is not representative of the experimental range of pore sizes or shapes found in soil. Limitation of the model to only 1000 pores and 500*c* throats prevents the model from representing the range of void size frequencies found in real samples. Enlargement of the Pore-Cor unit cell would overcome this problem. The bounding restriction that pores may only lie within Cartesian planes leads to inefficient packing and the pore skew parameter which is used to compensate by bulking up the porosity leads to a significant distortion of the network with too many large pores being produced. This distortion is so great that different stochastic generations of the network appear to produce

very similar pore size distributions, Figure 3.12. The A and B horizons of the soil at this site are very similar and no significant difference in the distributions was observed. This has been found to be a general characteristic of this series of soils this series in the Devon region [193]. A weak particle size with depth trend was observed experimentally and predicted. This however may be attributed to the trend of decreasing pore skew with depth and is therefore probably internally inconsistent.

CHAPTER 4

FLOW INJECTION TECHNIQUES FOR THE QUANTIFICATION AND SPECIATION OF PHOSPHORUS IN SOIL LEACHATES AND RUNOFF WATERS

The concentrations of TP, RP, TDP and DRP in soil leachate and runoff waters can vary dramatically in a short space of time (minutes) when subjected to a storm or breakthrough event. Current methods for the determination of TDP are not ideally suited to the monitoring of breakthrough events in soil waters [187]. This work presents two FI methods, one of which is suitable for the rapid determination of TDP and DRP in natural waters.

The TDP method described is an advance on an earlier FI method [142] for the determination of TDP in natural waters. Its modified chemistry incorporates two strategies for the removal of interferences, viz; pre-treatment of the sample by cation exchange to remove interfering Fe(III) and the use of acidic photo-oxidation conditions to prevent metal-phosphate complex formation. The proposed method was validated against batch analyses performed by independent laboratories at the Water Studies Centre (Caulfield Campus, Melbourne) and the Dairy Research Institute (Ellinbank, Victoria).

The molybdenum blue spectrophotometric method for the determination of RP is almost universally used in routine analysis [194] and FI methods based upon it are also widely used. The RP method described method in this work is a modification of a commercially available (Tecator Ltd, Method Application ASN 60-03/82.) method.

4.1 EXPERIMENTAL

4.1.1 REAGENTS

FI DETERMINATION OF REACTIVE PHOSPHORUS

Two streams of Milli-Q water are used in this manifold (OC1 and OC2 as shown in Figure 4.1). The acid molybdate reagent (OR1) was prepared by dissolving ammonium heptamolybdate, 8.1×10^{-3} M (BDH, AnalaR) in 0.56 M H_2SO_4 (BDH, AnalaR). The tin(II) chloride reagent (OR2) was prepared by dissolving tin(II) chloride, 8.9×10^{-4} M (May and Baker) and hydrazine sulphate (0.015 M) in 0.66 M H_2SO_4 (BDH, AnalaR).

FI DETERMINATION OF DOP

The acid peroxydisulphate reagent (R1, as shown in Fig 4.4) was prepared by dissolving potassium peroxydisulphate, 50 g l^{-1} (BDH, AnalaR) in 0.12 M H_2SO_4 (BDH, AnalaR). The acid molybdate reagent (R2) was prepared by dissolving ammonium heptamolybdate, 8.1×10^{-3} M (BDH, AnalaR) in 0.41 M H_2SO_4 (BDH, AnalaR). The tin(II) chloride reagent (R3) was prepared by dissolving tin(II) chloride, 8.9×10^{-4} M (May and Baker) and hydrazine sulphate (0.015 M) in 0.41 M H_2SO_4 (BDH, AnalaR).

DAIRY RESEARCH INSTITUTE (DRI) BATCH METHOD

Reagent DR1 was 2.5 M sulphuric acid, (AnalaR). Reagent DR2 (potassium antimonyl tartrate solution) was prepared by dissolving 1.3715 g of $K(SbO)C_4H_4O_6.1/2\ H_2O$, (AnalaR) in 500 ml of distilled water. Reagent DR3 (ammonium molybdate solution) was prepared by dissolving 6 g of $(NH_4)_6Mo_7O_{24}.4H_2O$, (AnalaR) in 150 ml of distilled water.

Reagent DR4 was ascorbic acid solution (0.01M), (AnalaR). The combined reagent consisted of 125 ml DR1, 12.5 ml DR2, 37.5 ml DR3 and 75 ml DR4.

MODEL PHOSPHORUS COMPOUNDS

Model compounds used in the recovery experiments were chosen to represent a range of compound stabilities and functional groups [195], viz., potassium dihydrogen orthophosphate (BDH, Pronalys) ; sodium tripolyphosphate (Ajax), phytic acid dodecasodium salt hydrate (purity 78 %; Aldrich), p-nitrophenyl phosphate (purity 99 %; Sigma), D-glucose-6'-phosphate (purity 98 %; source), cocarboxylase (purity 98 %; Sigma), o-phosphoryl ethanol (purity 99 %; Sigma) and adenosine-5'-triphosphate disodium salt (purity 98 %; Sigma.)

INTERFERENCES

Separate solutions of interfering ions (Al(III), As(V), Ca(II), Fe(II), Fe(III), Si(IV)), were prepared by dilution of the appropriate 1000 mg l^{-1} Spectrosol (BDH) stock solution.

4.1.2 INSTRUMENTATION

REACTIVE PHOSPHORUS MANIFOLD

The manifold used is shown in Figure 4.1. PTFE tubing (0.75 mm i.d.) was used throughout. Coils OC1, OC2 and OC3 were mixing coils of lengths 10, 30 and 100 cm respectively. A flow injection analyser (Tecator 5020) and a single beam spectrophotometer (Philips PU8620 Series UV/VIS/NIR) were used as a pumping unit and detector respectively. The flow cell used for the detection of phosphomolybdenum blue at 690 nm had an optical path length of 10 mm and an analytical volume of 18 µl.

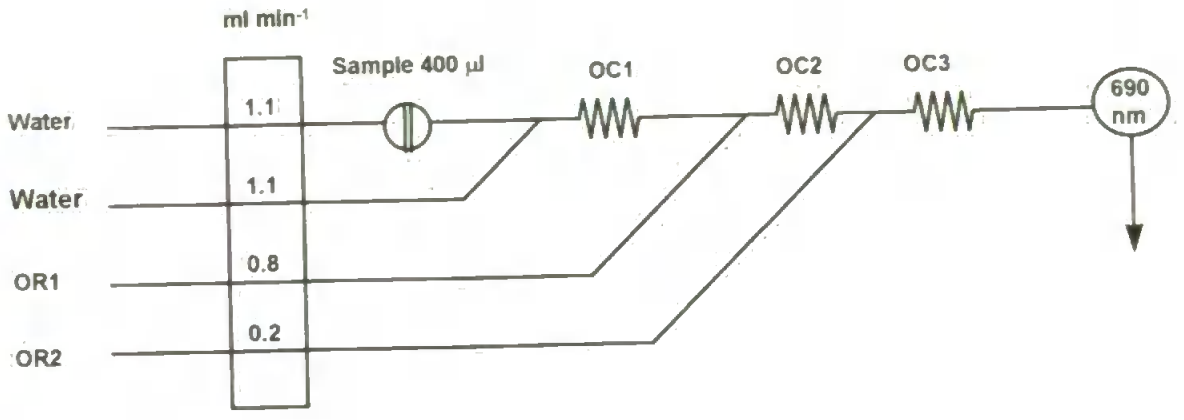

Figure 4.1 : Flow injection manifold for the determination of DRP and TRP

SPECTROPHOTOMETER CONTROL AND DATA COLLECTION

A Windows 95 / NT Visual Basic application was specifically written to control and store and process data from the PU8620 spectrophotometer. In the absence of any specialised communication hardware a serial communication (RS232C) protocol was used to link computer and instrument as shown in Figure 4.2.

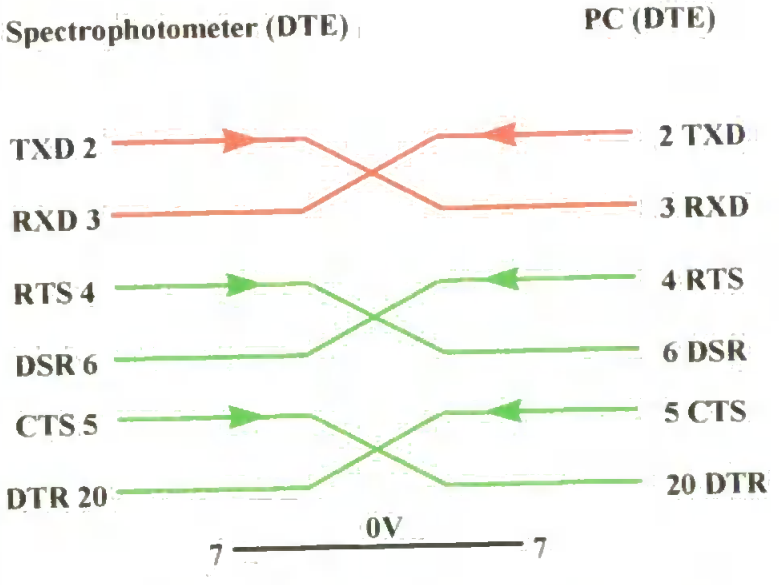

Figure 4.2 : Serial communications protocol used. Lines shown in red are used for data transfer and the green lines for handshaking. TXD (Pin 2) - Transmitted data from the spectrophotometer. RXD (pin 3) - Received data from the PC. RTS (Pin 4) - Request to send. DSR (Pin6) - Data set ready. CTS (Pin 5) Clear to send. DTR (Pin 20) Data terminal Ready. No. 7 is a reference pin.

The RS232C standard defines all signal lines from the perspective of the DTE (Data Terminal Equipment) and this configuration is designed for direct interconnection between the PU8620 and a PC with a null modem. Pins TXD and RXD channels (pins 2 and 3) are used to transmit and receive data respectively. The PU8620 uses a number of hardware handshakes and each signal is described from the perspective of the spectrophotometer. The DTR channel (pin 20 - output) is held on by the spectrophotometer during initialisation and remains active until switched off. It indicates the spectrophotometer is present and ready to receive data. The RTS channel (pin 4 - output) is held on by the spectrophotometer during initialisation and remains held active until the instrument is switched off. It indicates that the instrument is ready to transmit data. The CTS channel (pin 5 - input) is held on by the PC to signify that it is ready to receive data. If this signal is held off then the spectrophotometer would cease to transmit data. The DSR channel (pin6 - output) is held on by the PC to signify that it is ready to transmit data. When this signal is switched the link between instrument and PC is severed and the spectrophotometer reverts to manual control.

The baud rate used throughout was 4800 bits s^{-1} and each data byte (1 byte = 8 bits) consisted of seven data transmission bits and one stop bit, no parity bits were used. The MSComm [196] event procedure was used to monitor the serial port. The PU8620 transmits data every 0.5 seconds and the MSComm reacts to this event by storing the instruments output into the system memory. The main window of the programme can be seen in Figure 4.3. The top left hand frame is used to Activate or deactivate the remote link to the instrument and record or retrieve data. The three frames to the right are use to run the instrument and emulate the functionality of the PU8620 interface. The graph on the bottom left is an OLE (object linking and embedding) compliant Excel object which is used

to display the data as it comes from the instrument in real time. To achieve this the PU8620 programme is run as a client application of Excel. Excel is the server application because it exposes its objects, one example of which is its graph, to the client PU8620 application. The whole of Excel need not be open to use the an object (a similar example is editing an Excel chart in a word processor) and only the required part need be loaded and the entire process is invisible to the user. The Excel analysis toolpack may also be used by clicking the command button on the lower right. The use of Excel macros is also incorporated and could be used to insert a smoothing line or run a curve fitting procedure.

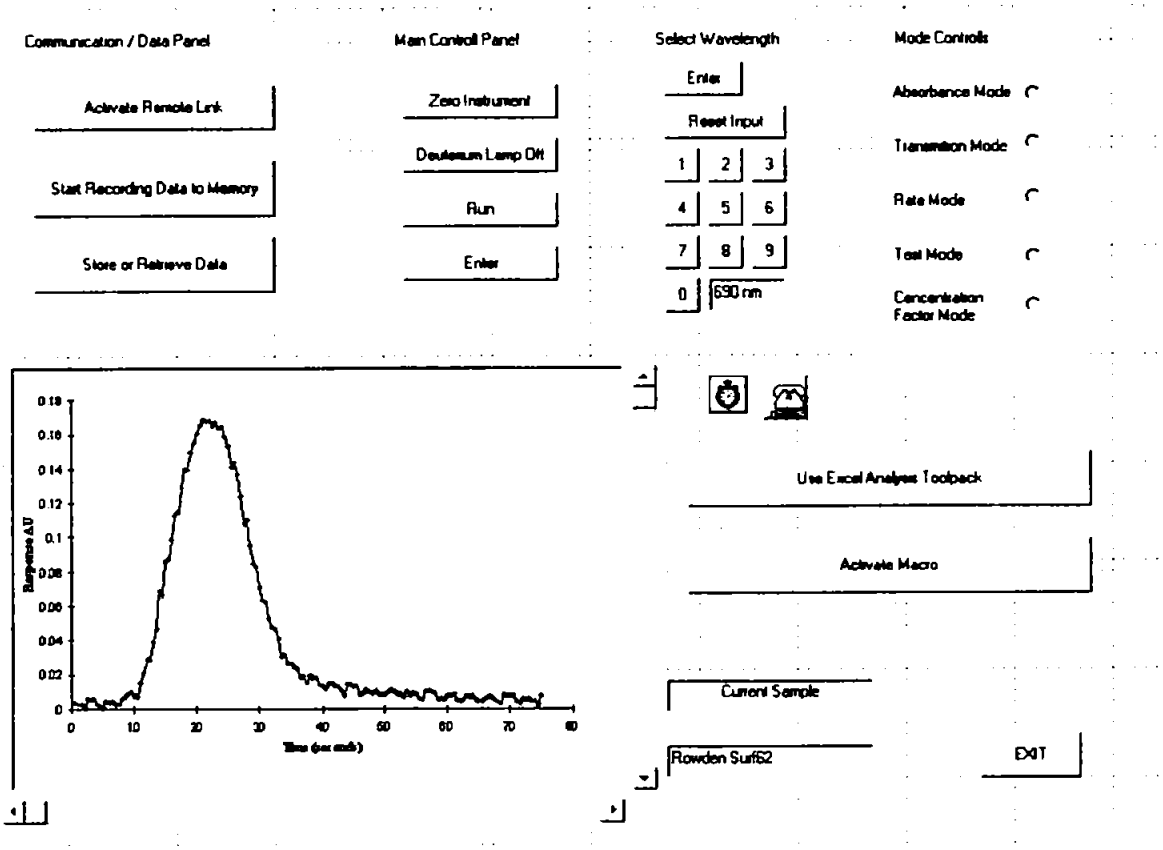

Figure 4.3 : PU8620 user interface. The communication panel is used to connect to the remote instrument. The other top three panels are used to control instrument settings. The display is an OLE imbedded chart and Excel macros can be used for data analysis

DOP MANIFOLD

The manifold used is shown in Figure 4.4. PTFE tubing (0.5 mm i.d.) was used throughout and C1 and C2 were mixing coils with lengths of 30 and 60 cm respectively. Ismatec Mini-S 840 and 820 pumps were used for carrier and reagent delivery respectively. Sample (600 µl) was injected using a motor driven Rheodyne 5020 injection valve. The UV source was a germicidal U tube (G36 T15 NU, UV Air Pty Ltd, South Australia) that had a major emission line at 254 nm and a power consumption of 40 W, and was housed in a light-tight, fan ventilated box. Oxygen and ozone bubbles formed during photoxidation were removed using two 10 cm lengths of lightly knotted Accurel (S6/2 Enka, AG) microporous tubing (D1 and D2). The absorbance was measured with a spectrophotometer (LKB Novaspec) fitted with a 10 mm path length glass flow-through cuvette (75 µl; Starna Pty Ltd) and the output recorded on an analogue chart recorder (ICI Instruments, DP600).

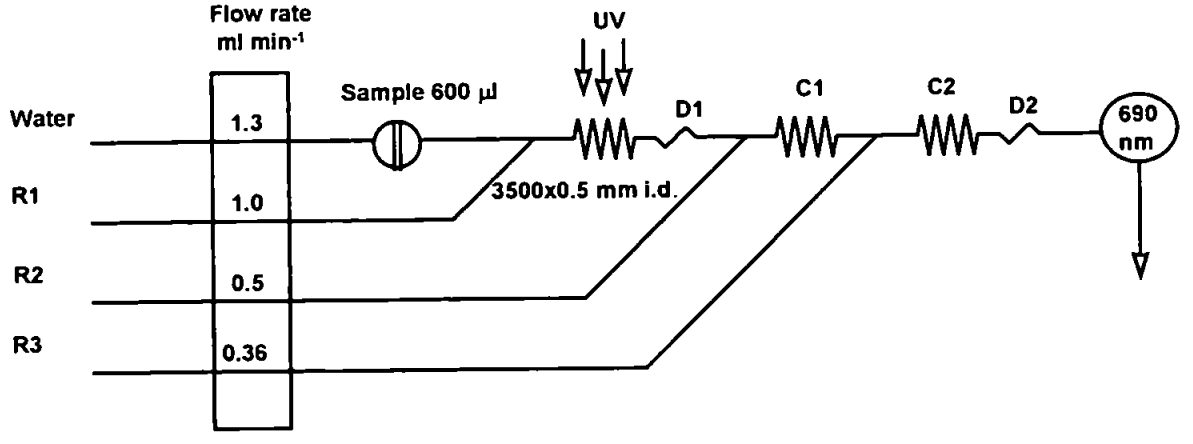

Figure 4.4: Flow injection manifold for the determination of DOP utilising a PTFE coil

ION EXCHANGE COLUMN FOR SAMPLE PRE-TREATMENT

The columns were packed with Dowex W50 X8 (BDH) cation exchange resin. The resin was initially cleaned in 10 % (v/v) concentrated H_2SO_4 and then flushed with Milli-Q grade water. The columns were regenerated by flushing on-line with 10 ml of 10 % (v/v) concentrated H_2SO_4 followed by Milli-Q water after each use.

DRI BATCH METHOD

Samples were autoclaved (Siltex) at 121 °C and 200 kPa in borosilicate glass digestion vials (40 ml) with autoclavable PTFE faced, black phenolic solid top screw cap closures. Absorbances were measured using a spectrophotometer (CARY 1E) was operated at 880 nm with a 10 mm cuvette.

4.1.3 DRI PROCEDURES

5.0 to 20.0 ml aliquots of each water sample containing between 0 and 4 mg l^{-1} phosphorus were pipetted into 40 ml digestion vials. 0.0, 2.5, 5.0, 7.5 and 10.0 ml aliquots of a 2 mg P l^{-1} working standard were pipetted into separate digestion vials. Each vial's contents were diluted to 20.0 ml with distilled water and 5.0 ml of 20 % sulphuric acid added. Then 0.2 g of ammonium persulphate was added to each vial, the vials capped and the contents mixed by inversion. The sealed vials were transferred to a suitable tray and placed in the autoclave for 60 min. The autoclave was then left for 15 min to allow the vials to cool and return to atmospheric pressure before opening. The volume of 4 M NaOH required to neutralise each digest was determined by adding 1 to 2 drops of phenolphthalein indicator to the vial followed by successive 1.0 ml aliquots of 4 M NaOH, mixing well between additions until the solution just turned pink. 5 ml of the combined colour reagent

(DR1) was added to each vial, mixed well and allowed to stand for a minimum of 30 min before measuring the absorbance of the contents of each vial at 880 nm.

4.1.4 SAMPLE COLLECTION SITES

ROWDEN SITE

A set of 14 samples were taken from a grassland site (Rowden) which is managed by the Institute of Grassland and Environmental Research (IGER North Wyke) [197]; its location lies 7 km to the north of Dartmoor at grid location SX 65099 and lies on a slope of 5 to 10 %. The site provides a unique resource for the study of chemical transfer from grassland soil systems to groundwaters and has been described in detail by Scholefield et al., [198]. The existing sward is dominated by *Lolium perenne* L. and other grass species. The soil is a clayey non-calcerous pelostagnolgley of the Hallsworth Series (USDA typic haplaquepts, FAO dystric gleysols), overlaying clay shales of the Crackington Formation. The site is divided into fourteen plot lysimeters (numbered 1-7 and given the suffix A or B) of approximately 1 ha. The suffix A or B indicates a replicate treatment, i.e B3 is a replicate of A3 Each plot is isolated from the other by gravel filled ditches 30 cm in depth. The phosphorus load of each plot was as follows; Plots 1 to 4 received an annual input of P of 25 kg TSP - P ha^{-1} (Triple Super Phosphate) and plots 2,3,5 and 6 received 16 kg TSP - P ha^{-1} plus cattle slurry P equivalent to 16 kg P ha^{-1}. Plot 7 received no P input. All plots were grazed with four steers ha^{-1} in the months April to October.

BLACKBURN LAKE MELBOURNE

Blackburn lake is urban and has a substantial input from storm water drains. It is used as a buffer between the drains and the Yarra river. It is located in Melbourne Victoria at E33800 5811.44 S on the Australian Map Grid (AMG). On the day of sample collection, a large petroleum fuel spillage the previous day had contaminated large areas of the lake.

DARNUM SITE WEST GIPPSLAND

The Darnum site is located in West Gippsland, Victoria, Australia (146deg 03' S, 38deg 10' E). It is a single pasture and is dominated by Boolarra Loam series and is subject to yearly inputs of 60 kg P. This site has been described in detail by Nash and Murdoch [73].

4.2 RESULTS AND DISCUSSION

4.2.1 PERFORMANCE OF THE REACTIVE PHOSPHORUS FI MANIFOLD

The manifold shown in Figure 4.1 is an adaptation of a previously reported method for the determination of DRP (Tecator Ltd, Method Application ASN 60-03/82.) incorporating 0.75 mm i.d tubing to produce a manifold less susceptible to clogging when unfiltered samples are injected.

FIGURES OF MERIT

The linear range and the limit of detection of the method were 0 to 1000 $\mu g\ l^{-1}$ PO_4-P and 2.9 $\mu g\ l^{-1}$, calculated using 3s (n=5) of the blank signal, respectively. A typical calibration graph is given in Figure 4.5. The required sample injection volume of 400 µl was higher than the 200 µl volume used in the original Tecator method in order to offset the increased

dispersion of the larger i.d tubing. The residence time T (the time elapsed between sample injection and recorded peak maximum) was 37 s and more than 80 samples per hour could be analysed. Tolerance to Si(IV) interference was excellent and no enhanced signal was observed at Si(IV) concentrations below 10 mg l^{-1} on a blank signal.

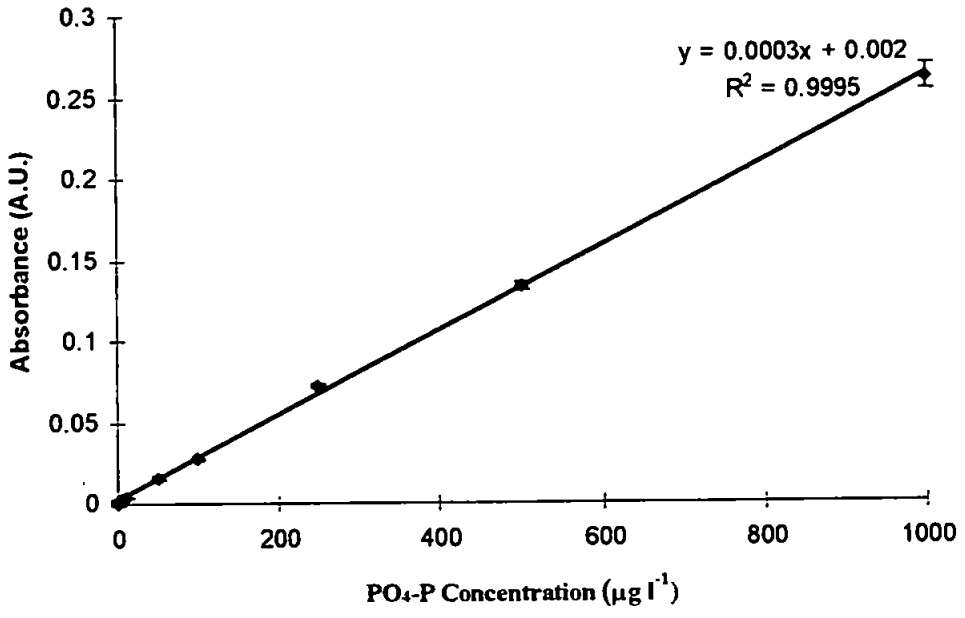

Figure 4.5 : Typical calibration graph for PO_4-P the manifold described in Figure 4.1. Error bars are shown with a 99% confidence interval (3s) and n=5.

VALIDATION WITH ROWDEN SAMPLES

The 16 collected Samples were analysed for TRP and DRP (post 0.45 µm filtration) using the manifold shown in Figure 4.1 and a reference batch method [194]. Figure 4.5 shows their TRP and DRP PO_4-P concentrations and, despite the closeness of sample concentrations to the detection limit, the concentration of TRP was greater than DRP in all samples. A paired T test confirmed that the two data sets were significantly different at P = 0.01, a 99% confidence interval ($t = 4.27 > t_{crit} = 2.97$).

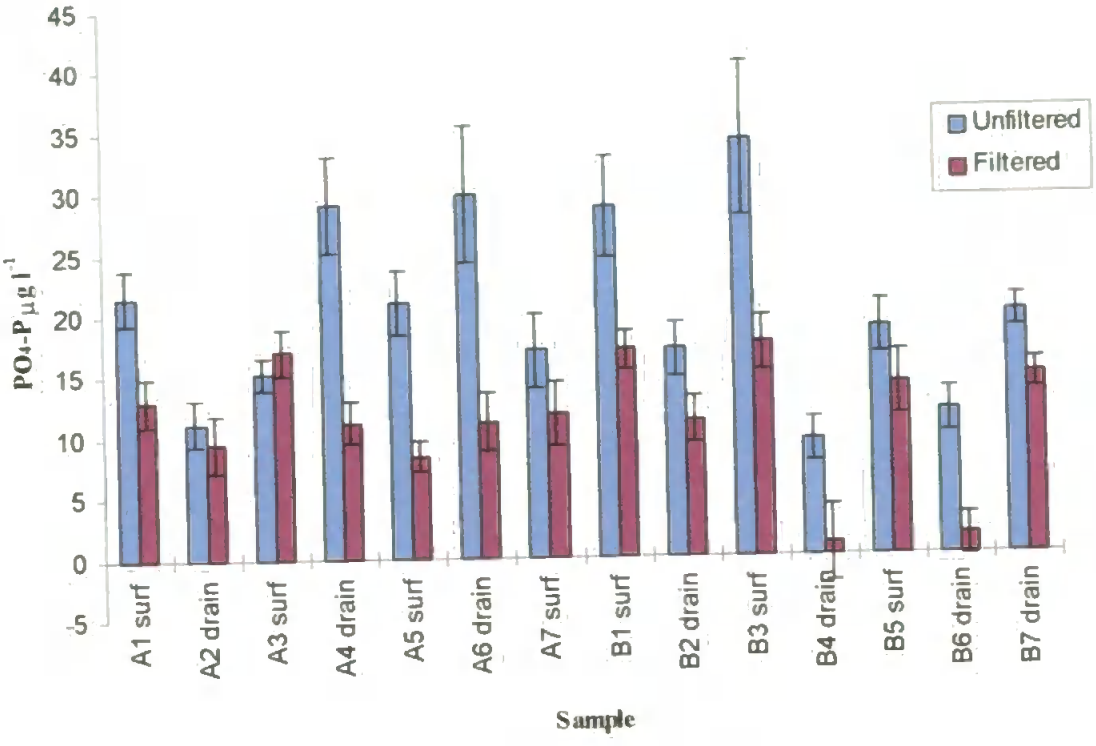

Figure 4.6 : Determined TRP and DRP in samples from the Rowden site. Error bars are shown at 3s (n=3.) Runoff and groundwater samples are denoted by surf are surface and interflow samples to a depth of 30 cm and samples denoted drain are drainage waters from the depths 30-85 cm.

The agreement between the batch and FI methods was excellent for both the filtered and unfiltered sample sets. A paired T test showed that there was no significant difference between the two methods ($t = 1.56 < t_{crit} = 2.46$ at the 99 % confidence interval). The correlation between batch an FI methods was excellent (R^2=0.9644) given that some sample PO_4-P concentrations were close to the detection limit. The intercept of the regression was close to zero (1.156 µg l^{-1}) indicating that there was no systematic bias between the methods. The correlation between the methods is shown graphically in Figure 4.7.

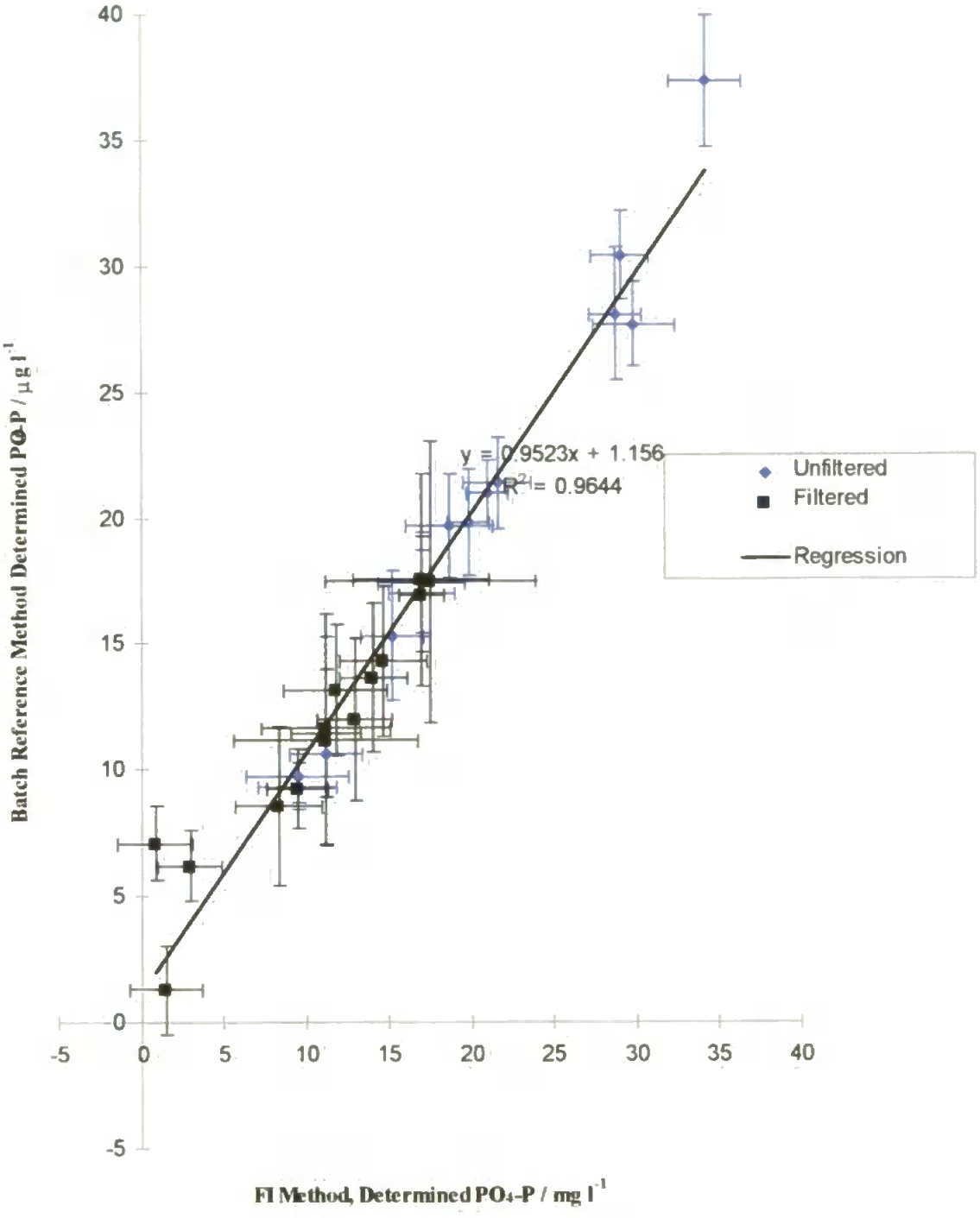

Figure 4.7 : Correlation between FI and Batch methods for the determination of TRP and DRP in filtered and unfiltered samples. Error bars for the reference batch method are assumed to have an RSD of 15% at these low concentrations. Error bars for the FI method are shown as 3s (n=5.)

4.2.2 Optimisation of DOP Manifold

Initially the flow rates reported by McKelvie et al. [199] were used (1.3 ml min^{-1}) for the water carrier and peroxydisulphate (R1) streams. Samples were injected into the carrier stream and subsequently merged with the peroxydisulphate stream in order to provide a constant refractive index and hence a stable baseline for the merged streams. The advantage of this approach outweighed the negative effect of on-line sample dilution on the detection limit. In order to minimise sample dilution however the peroxydisulphate concentration was increased to 50 g l^{-1} (the limit of solubility) from 40 g l^{-1} which allowed a decrease in the flow rate of R1 to 1.0 ml min^{-1}, with no loss in oxidation efficiency. To avoid problems with back pressure, the i.d. of the PTFE reactor coil was increased from 0.3 to 0.5 mm with minimal effect on dispersion. The reactor coil was also wrapped around the U shaped lamp in a figure of eight configuration to maximise photochemical efficiency.

4.2.3 Photo-oxidation and Detection Chemistry

The principle problem when using alkaline peroxydisulphate photoreactor chemistry is a susceptibility to interference [200] from metal ions, e.g. Al(III), Ca(II), and Fe(III) which form complexes and precipitates with orthophosphate at high pH. Whilst these interfering species are not usually present in sufficient concentrations to cause problems with the analysis of natural waters, they commonly occur at relatively high concentrations in soil leachates and runoff waters. In order to prevent phosphate-metal complex formation, a low pH photo-oxidation chemistry was used for this work. The formation of bubbles can be more problematic at low pH due to the evolution of CO_2 but this has been overcome in the manifold presented here by improved on-line debubbling using microporous tubing. The tubing is impervious to liquid but permeable to gasses. Best results were achieved using a

wide - narrow configuration which introduced a pressure gradient assisting the expulsion of unwanted bubbles as shown in Figure 4.8.

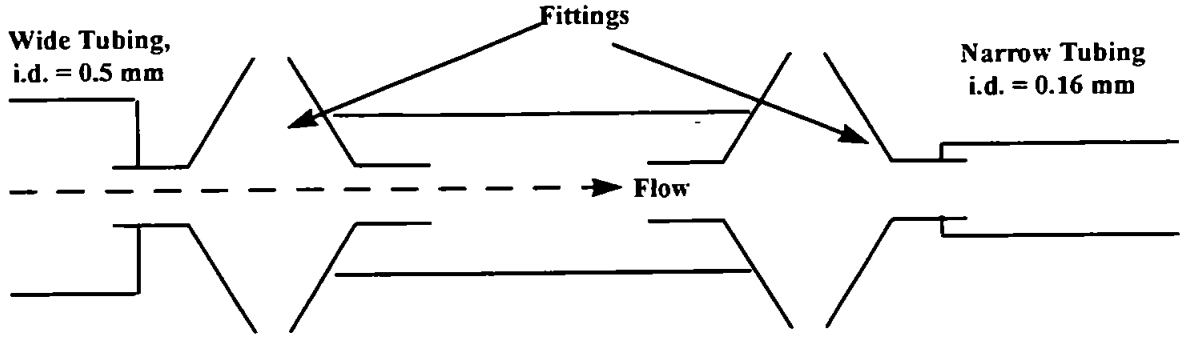

Figure 4.8 : Microporous debubbler setup. The microporous accurel tubing is located between the fittings

The stream entering the photoreactor is acidic, due to the 0.12 M H_2SO_4 initially used. In the photoreactor, more acid is produced an the acidity further increase by the photolysis of peroxydisulphate, the reaction in dilute acid also produces peroxide which itself quickly decomposes.

$$S_2O_8^{2-} + 2H_2O \xrightarrow{h\nu} 2HSO_4^- + H_2O_2$$

The rate of this reaction obeys a first order rate law with respect to peroxydisulphate concentration and is independent of pH [201]. The reaction is known to be catalysed by Ag(I) ions [202] and obeys the following first order rate law.

$$d[S_2O_8]/dt = k'[S_2O_8^{2-}][Ag^+]$$

A smaller catalytic effect has also been noted with Cu(II) ions [202]. In many natural water samples catalytic traces of these ions are present.

The kinetics of the molybdate detection chemistry, unlike the kinetics of the oxidation chemistry, are highly susceptible to variations in the concentration of sulphuric acid [203,204] and it has been reported that at concentrations above 0.7 M H_2SO_4 the formation of the heteropoly acid becomes inverse fourth order with respect to acid concentration [205]. The acidity in the peroxydisulphate stream has been compensated by reducing the acidity of the molybdate and reductant streams with respect to those quoted in FI methods which determine DRP in a water carrier stream [206].

4.2.4 Figures of Merit

The linear range and detection limit of the system were determined using orthophosphate standards in the range 0 to 1.5 mg l^{-1} PO_4-P. The relative standard deviations (n=5) for standards above 0.5 mg l^{-1} were generally < 1%. The reduction in noise compared with the previously reported manifold [142] is attributed to bubble formation causing less serious fragmentation of the flowing stream in the larger diameter photoreactor. The sensitivity of the system was 0.2699 AU per mg l^{-1} PO_4-P and the detection limit was 7 μg l^{-1}, calculated using 3s (n=5) of the blank signal.

4.2.5 Recoveries of Model Phosphorus Compounds

Six model compounds were chosen to form a representative range of stabilities of phosphorus compounds found in soil leachates and runoff waters [195] e.g. labile (D-glucose-6'-phosphate (a naturally occurring sugar) and o-phosphoryl ethanol) and refractory (phytic acid). Phytic acid is a particularly useful model compound for soil because it is found in a wide range of plant materials such as oil seeds, legumes and cereal grains and is one of the most refactory organic phosphorus compounds [70].

Model Compound	PO_4-P mg l^{-1}	RSD %
Phytic acid	0.97	0.7
p-Nitrophenyl phosphate	1.01	0.6
D-glucose-6'-phosphate	1.01	1.6
o-Phosphoryl ethanol	1.02	0.4
Cocarboxylase	0.19	2.1
Tripolyphosphate	0.04	16.2
Orthophosphate	1.00	0.3

Table 4.1: Recoveries of 1.0 mg l^{-1} standards of model P compounds using on line acid peroxydisulphate digestion.

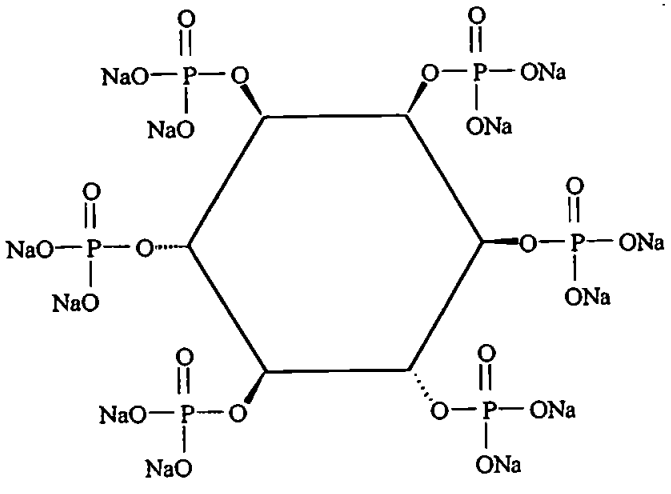

Phytic acid (dodecasodium salt)

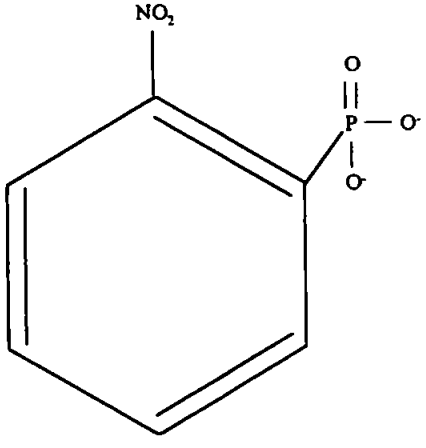

p- Nitrophenyl phosphate

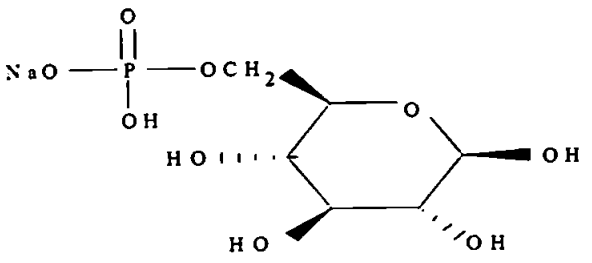

D-glucose-6'-phosphate

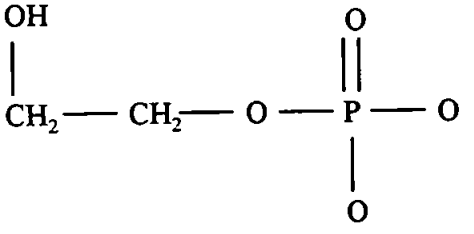

o-Phosphoryl ethanol

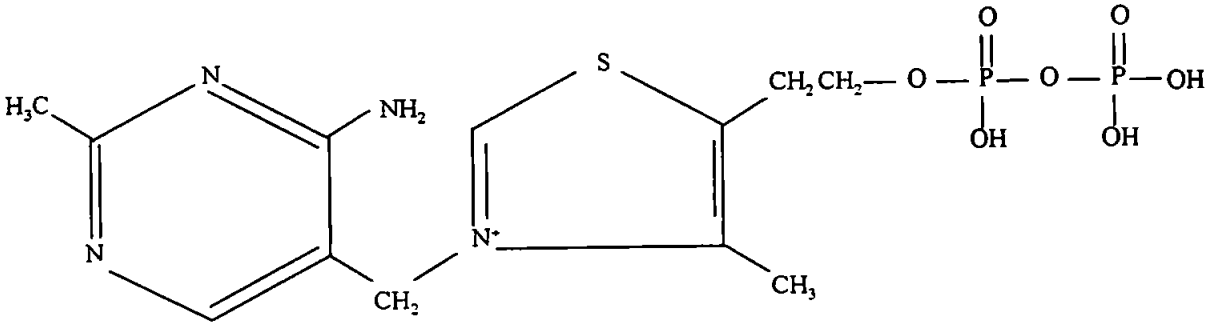

Cocarboxylase

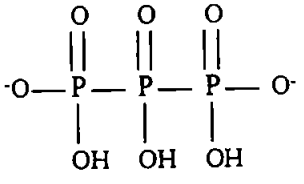

Tripolyphosphate

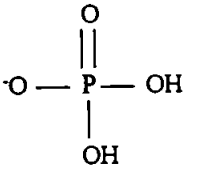

Orthophosphate

Figure 4.9 : Structures of phosphorus compounds used in recovery trials.

The recoveries for 1.0 mg l^{-1} P in the organic phosphorus model compounds and a 1.0 mg l^{-1} PO_4-P standard using the manifold shown in Figure 4.4 are given in Table 4.1. The condensed phosphates, co-carboxylase and tripolyphosphate gave low recoveries (< 20%)

despite the acidic conditions used in the photoreactor. This is attributed to the fact that these compounds are not susceptible to destruction by UV irradiation [141] and did not undergo hydrolysis because the experimental conditions were not sufficiently harsh. Quantitative recoveries for these compounds have only been reported with long exposure times (up to 2 h) and high temperatures (> 110 °C) in acidic conditions [139] and in an FI system which combined UV photo-oxidation and thermal digestion [207]. Recoveries for all of the other compounds were quantitative, including phytic acid (97 %). Recovery was quantitative for D-glucose-6'-phosphate over the range 0 to 1.5 mg l^{-1} PO_4-P as shown in Figure 4.10.

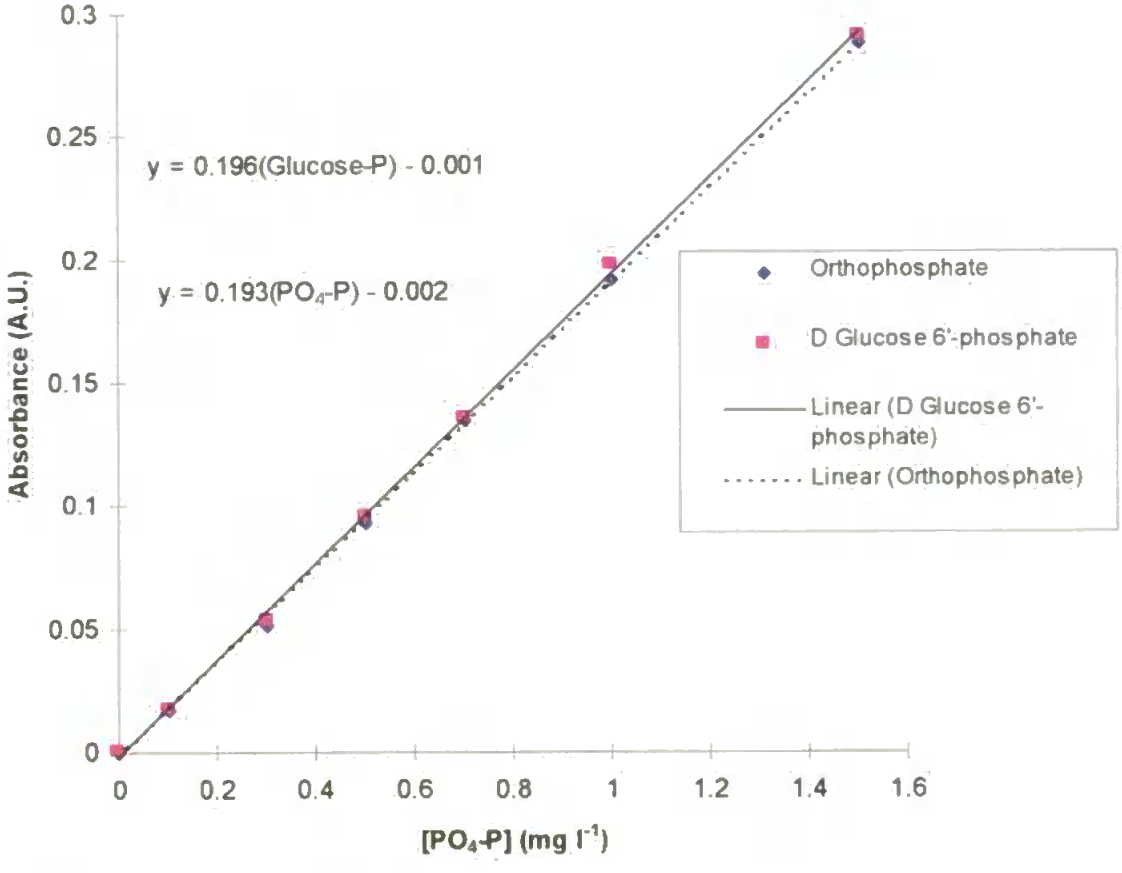

Figure 4.10 :Linearity of recovery for D-glucose-6'-phosphate

4.2.6 INTERFERENCES

The determination of organic phosphorus via photo-oxidation and the formation of phosphomolybdenum blue has some potentially serious interferences when applied to the analysis of soil leachates and runoff waters. These can be classified into three types; those that also form molybdate complexes resulting in enhanced absorbance (additive interference), those that form compounds with orthophosphate or organic phosphates and inhibit either the formation of phosphomolybdenum blue or organic compound breakdown (subtractive interference) and those that act as radical scavengers in the photoreactor and hence lower recovery of organic phosphorus (subtractive by radical scavenging).

ADDITIVE INTERFERENCES

Si(IV) forms a complex with molybdate that has a broad band absorbance (λ_{max} 790 nm [208]), which overlaps the 690 nm detection wavelength used in this method, causing an increase in detected peak height and overestimation of the phosphorus concentration. This is potentially the most serious interference in the analysis of soil leachates and runoff waters because the Si/P concentration ratio may be as high as 5000 [209]. In batch studies acid stability plateaus for the rate of formation of phosphomolybdenum blue have been found with nitric [204] and sulphuric [205] acids. The acid stability plateau ends at sulphuric acid concentrations above 0.3 M and at concentrations above this the reaction becomes increasingly inverse fourth order. The rate of formation of the silicon chromophore can be minimised by increasing the acidity to just below the pH at which the rate of formation of phosphomolybdenum blue becomes inverse fourth order with respect to acid concentration i.e. the rate of formation of the silicon molybdate complex is much slower at this acidity and therefore does not interfere within the timescale of an FI determination. Si(IV) standards were therefore analysed using the TDP manifold in order to determine the overestimation of

orthophosphate. The results (Table 4.2) show no significant interference below 8 mg l^{-1} Si(IV), which represents the high end of the concentration range typically found in soil leachates and runoff waters. Even at 60 mg l^{-1} Si(IV) the overestimation is small, being equivalent to 17 μg l^{-1} PO_4-P.

Si(IV) mg l^{-1}	Response A.U.	Equivalent [PO_4-P] μg l^{-1}	RSD %
2	0.000	0.2	-
5	0.003	3.2	39.5
8	0.004	5.7	28.6
10	0.006	8.5	10.1
60	0.011	17.6	10.9

Table 4.2: Response for Si(IV) standards with zero PO_4-P concentration. Silicon as sodium metasilicate (Na_2SiO_3)

It is well known that arsenate forms an absorbing complex with molybdate [210] which interferes strongly in the determination of phosphate. The molybdenum blue chemistry is so sensitive to arsenate that it is the basis of a spectrophotometric method for its determination [211]. Arsenate standards were analysed using the TDP manifold and Table 4.3 shows the equivalent PO_4-P response for arsenate standards at various concentrations. For most environmental analyses, the concentration of total arsenic is not sufficiently high to be problematic but care must be taken when heavily polluted waters are analysed [212].

As(V)	Response	Equivalent [PO_4-P]	RSD
mg l^{-1}	A.U.	mg l^{-1}	%
0.1	0.006	-0.015	10.2
0.5	0.034	0.063	4.5
1	0.067	0.153	6.8
2	0.167	0.472	0.6

Table 4.3: As(V) interference in the on-line DOP method with zero PO_4-P concentration

SUBTRACTIVE INTERFERENCES

Several ions which commonly occur in soil leachates and runoff waters, i.e. Al(III), Ca(II), Cu(II), Fe(II) and Fe(III), can combine with orthophosphate and some organic species to form complexes and precipitates. Al(III), which is abundant in soil clay minerals [24], is known to cause underestimation of phosphorus concentration by a mechanism that involves the formation of aluminium phosphates at high pH [143]. In the method reported here, there was no reduction in the response for a 0.5 mg l^{-1} PO_4-P standard when spiked with up to 10 mg l^{-1} Al(III) (Table 4.4) because of the low pH used. This tolerance exceeds the concentration of Al(III) found in most soil leachates and runoff waters. Similarly Ca(II), often present in soils as calcium carbonate, can cause an underestimation of PO_4-P by forming insoluble phosphates. However no reduction in the response for a 0.5 mg l^{-1} PO_4-P standard when spiked with up to 10 mg l^{-1} Ca(II) was observed using the manifold reported here. Fe(II) did not suppress a 1 mg l^{-1} PO_4-P signal at spike concentrations up to 10 mg l^{-1} . Table 4.5 shows that 0.5 mg l^{-1} Cu(II) and 0.1 mg l^{-1} Fe(III) do however cause suppression of the response for a 1 mg l^{-1} PO_4-P standard.

Al(III)	Response	PO_4-P determined	RSD
mg l^{-1}	A.U	µg l^{-1}	%
0.5	0.174	500	0.8
1.0	0.172	510	1.6
2.0	0.172	510	1.4
10.0	0.171	510	1.6

Table 4.4 : Al(III) interference in the determination of 0.5 mg l^{-1} PO_4-P

Added Cu(II)	Response	[PO_4-P] determined	RSD
mg l^{-1}	A.U.	µg l^{-1}	%
0.5	0.345	930	0.6
1.0	0341	910	2.1
2.0	0.315	850	0.5
10.0	0.320	870	0.5
Added Fe(III)			
mg l^{-1}			
0.1	0.3900	960	0.6
0.5	0.354	860	1.1
1	0.319	790	0.8
2	0.257	690	1.3
10	0.183	480	1.4

Table 4.5 : Cu(II) and Fe(III) interference in the determination of 1 mg l^{-1} PO_4-P

The Cu(II) concentration in soil leachates and runoff waters is usually much less than 0.5 mg l^{-1} [213] and therefore does not represent a serious problem. The binding of Fe(III) to

phosphates is well documented [e.g. [214] and, in contrast to Cu(II), is a potentially serious interference in this method.

SUBTRACTIVE INTERFERENCES (BY RADICAL SCAVENGING MECHANISM)

Carbonate and bicarbonate ions act as radical scavenging agents [202] which may deplete the number of radicals available to attack organic compounds, thereby resulting in lower organic compound recovery. The levels of these ions in natural waters are generally not sufficient to affect recovery but problems may be encountered in the analysis of soil and sediment extracts where carbonate or bicarbonate is used as the extractant in combination with alkaline photo-oxidation conditions. The low pH photo-oxidation conditions used in the method reported here eliminates this potential interference by converting carbonate and bicarbonate to carbon dioxide.

4.2.7 ELIMINATION OF IRON(III) INTERFERENCE USING A CATION EXCHANGE COLUMN

A strong cation exchange column in the H^+ form was introduced as a sample pre-treatment line with the aim of eliminating interference from Fe(III). Two types of packed column geometry were evaluated, a small 1 mm i.d. tube of 45 mm length and a larger 5 mm i.d. tube of 30 mm length. Sample was pumped through both columns at a flow rate of 0.4 ml min^{-1}. For the smaller i.d. column, Fe(III) interference was not observed below 1 mg l^{-1}, as shown in Table 4.6. The use of a larger i.d. column produced a slightly worse interference threshold for Fe(III), probably due to the formation of preferential flow paths and a shorter residence time in the larger i.d. column. The smaller column was therefore used for the analysis of lake water and soil leachate samples.

Fe(III) mg l^{-1}	[PO_4-P] determined µg l^{-1}		RSD %	
	Small i.d. Column	Large i.d. Column	Small i.d. Column	Large i.d. Column
10.0	830	800	1.1	1.0
3.0	870	1000	0.9	0.6
1.0	1000	1000	0.7	0.9
0.5	1000	1000	1.6	0.6
0.1	1000	1000	0.2	0.3

Table 4.6 : Removal of Fe(III) interference on spiked 1 mg l^{-1} PO_4-P standards using ion exchange columns

4.2.8 Comparison of On-Line and Batch Methods

Fourteen natural water (lake water) samples were collected from Blackburn Lake, Melbourne, Australia. Filtered samples (0.45 µm) were digested with nitric-sulphuric acid and analysed by a batch method [215] and the proposed FI method for TDP incorporating the 1 mm i.d. ion exchange column. The levels found were all below 40 µg l^{-1} TDP but nonetheless the determined concentrations in thirteen of the samples agreed within experimental error (3s) and are shown in Figure 4.11. The higher concentrations observed in the batch analysis are likely to arise due to the presence of condensed phosphates in the samples which the batch method does convert and the on-line method does not. The difference however is very small cam 5 µg l^{-1}, but is statistically significant $t = 4.72 > t_{crit} = 3.01$ at the 99 % confidence interval. However if the assumption is made that 5 ug l^{-1} of condensed P is present in the samples and that this may be subtracted from the batch analysed concentrations, there is no significant difference between them, $t = 1.00 < t_{crit} =$

3.01 at the 99% confidence interval. The samples were also analysed by a standard FI method for DRP [206] and the results were consistently lower than those obtained for TDP by both methods.

Three soil leachate samples from Darnum, West Gibbsland, Australia were also analysed by the batch method and the proposed FI method and there was good agreement ($t = 0.017 < t_{crit} = 6.96$ for all samples, which covered the range 22 - 50 $\mu g\ l^{-1}$ P, as shown in Table 4.7.

TDP - Batch $\mu g\ l^{-1}$	RSD %	TDP- on line $\mu g\ l^{-1}$	RSD %
22.4	5.0	21.2	0.0
29.4	5.0	33.0	7.5
49.6	5.0	47.1	14.8

Table 4.7 : Comparison of DRI batch method with on line FI method

4.3 CONCLUSIONS

The RP manifold described has a wide linear range 0 - 1000 $\mu g\ l^{-1}$, an rsd generally less then 1%, a detection limit of 2.9 $\mu g\ l^{-1}$ and tolerance to silicon interference up to 10 $mg\ l^{-1}$ Si(IV) and a high sample throughput, 80 samples h^{-1}. There was good agreement with the reference method with $R^2 = 0.9644$. Therefore the manifold is suitable for the rapid analysis of RP in soil leachate and runoff waters.

The DOP manifold described is suitable for the determination of TDP in natural waters having PO_4-P concentrations between 7 - 1500 $\mu g\ l^{-1}$. A combination of low pH (<1.5)

reactor chemistry and an ion exchange column is sufficient to eliminate interferences at concentrations significantly in excess of those likely to be encountered in soil leachates and runoff waters. Sample volume required is low (600 µl), sample throughput is excellent (40 h^{-1}), making it ideal for near real time analysis, and the use of a low powered UV lamp and PTFE photoreactor makes the method suitable for field deployment.

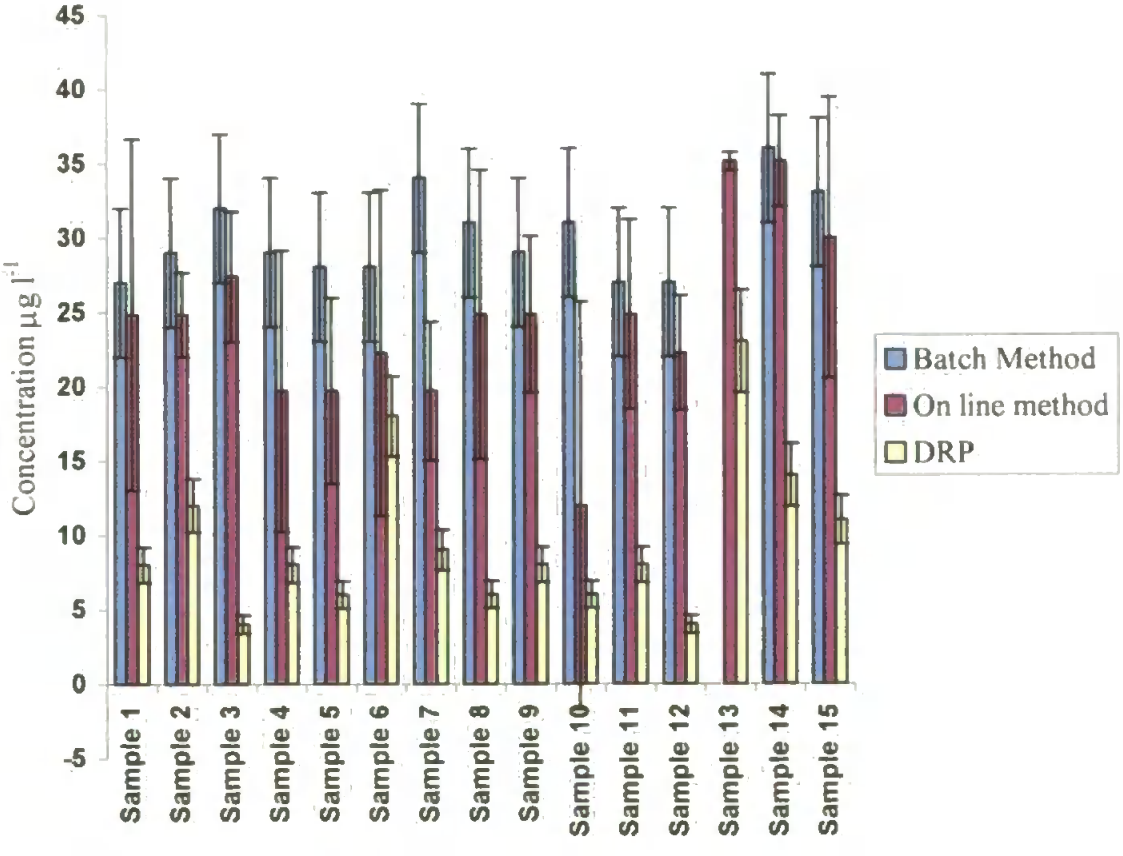

Figure 4.11: Blackburn lake samples

CHAPTER 5

EFFECT OF COMPACTION ON THE TRANSPORT OF PHOSPHORUS SPECIES THROUGH RE-PACKED SOIL COLUMNS

Two cores, one uncompacted and the other compacted were used to study the effect of compaction on the breakthrough behaviour of bromide, phytic acid and orthophosphate. Bromide is used as an inert tracer and is used to calibrate the convection dispersion equation for phytic acid and orthophosphate. The extent of compaction was carefully controlled to bring about a drop in saturated hydraulic conductivity of only one order of magnitude so that the permeability of the compacted core was sufficiently high to carry out breakthrough experiments. The Pore-Cor network model was then calibrated using mercury porosimetry curves of the uncompacted and compacted samples. The Pore-Cor network output was then correlated with CDE parameters which have been previously calibrated on each breakthrough experiment data to give a structural interpretation of the data.

5.1 EXPERIMENTAL

5.1.1 PHYSICAL MEASUREMENTS

STONE REMOVAL AND SAMPLE COMPRESSION

Approximately 30 kg of topsoil (0-20 cm depth) was taken from the De Bathe site described in Chapter 2. This soil was used throughout for the both the physical measurements of compaction and repacked cores for breakthrough experiments. Stones were removed from all samples by gently grinding sample with a large pestle and mortar and the sieving through a 2 mm mesh sieve. Uncompacted samples were prepared by pouring the sieved granules into the desired dimensions. Sample compression was achieved by applying a load of 146 kN m^{-2} using a stepless compression machine (Wykenham Farrence Ltd, Weston Rd, Slough, Berkshire. SL1 4HW) and a 16.82 N $division^{-1}$ calibrated force measurement ring (ELE Ltd, Hemel Hemsted, Hertfordshire, HP2 7HB, serial number 2574) to samples of varying gravimetric water content. Compression took place by placing the soil column inside a 6.5 cm diameter PVC jacket between a plate rising at a rate of 0.5 mm s^{-1} and a circular stainless steel block (tight fitting inside the PVC jacket as shown in Figure 5.1.) When the required pressure was reached the sample was released 3 seconds later by lowering the plate.

MEASUREMENT OF SATURATED HYDRAULIC CONDICTIVITY

Compacted and uncompacted samples were placed into a permeameter cell (11.7 cm high by 5.07 cm radius, (ELE Ltd) and measured by the method of falling head permeametry.

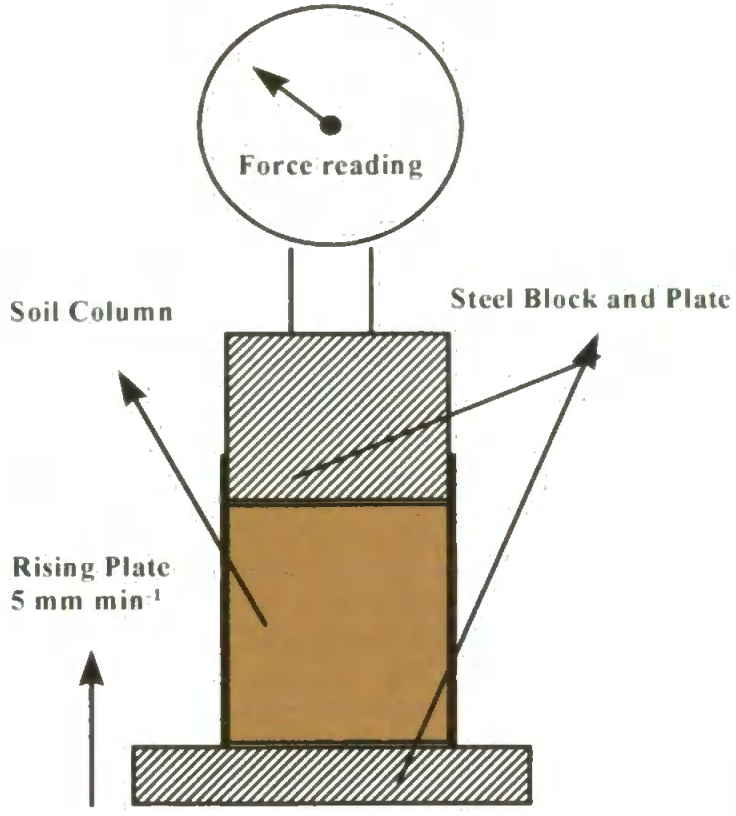

Figure 5.1 : Stepless compression machine setup used to compact small repacked soil columns.

MEASUREMENT OF VOLUMETRIC WATER CONTENT

Measured volumes of wet sample were placed into an oven thermostated at 102 ^{0}C, allowed to dry out overnight and then re-weighed.

MERCURY POROSIMETRY MEASUREMENTS

Uncompacted samples (approximately 0.8 g of dried granules) were placed directly into penetrometers (having a volume of 5.19 cm^{3}) prior to analysis. Compacted samples were prepared cutting pellets of moist soil from compacted cores and oven drying them at 102 ^{0}C for four hours. Dried pellets (approximately 1 g) were then placed into penetrometers. Mercury intrusion was then performed using a Micromeritics Autopore III porosimeter. The resulting mercury intrusion curves were then corrected for sample compression and

penotrometer expansion using a spreadsheet programme (Pore-Comp) which is described in detail by Gane et al., [40]. The program uses information from a blank run with the Tait equation to correct for the compressibility of the mercury and the expansion of the holding penotrometer itself.

5.1.2 Breakthrough Curve Experiments

Core Setup

Repacked cores were set up as shown in Figure 5.2. The cores consist of 6.5 cm diameter PVC tubes which are packed with soil 11 cm deep and an upper layer of sand (Redhill 65, Hepworth Minerals and Chemicals Ltd.) 1 cm deep was used to disperse the carrier. Carrier (0.001 M KNO_3, BDH AnalaR) was applied at constant rate of 1.81 $x10^{-3}$ pore volumes per minute by a variable flow rate Minpuls peristaltic pump (Gilson, Villiers-le-bel, France) and then percolated through the sand and soil. Percolated carrier then passes though a coarse Whatman 52 filter (W & R Balston Ltd). When steady state flow was achieved (input flow rate = output flow rate) leachates was collected at ten minute intervals in 20 ml capacity PTFE bottles and diluted 5 fold. Further dilutions were performed as necessary to bring the sample analyte concentration within the linear range of each method.

Uncompacted cores were packed by pouring in dry sieved soil into the PVC tubes to a depth of 11.2 cm. A 1cm layer of sand was then placed on top of the soil. It was necessary to use an 11.2 cm soil layer because of settling during initial percolation to a volume of 11 ± 0.2 cm. Compacted samples were prepared by first mixing the dry sieved soil with 18.6 % (w/w) tap water. Wetted sample was then placed into the PVC tubes to a depth of 14.3 cm. Upon compression with a force of 146 kN m^{-2} the length of the soil layer reduced to 11 ±

0.2 cm. Measurement of the depth of the soil layer was best carried out by first marking the inside of the PVC core with coloured masking tape at relevant depths.

TRACER INJECTION

A 1 ml volume of Milli - Q water containing 1000 mg l^{-1} Br^-, PO_4-P, and Phytic Acid - P (i.e. a total applied flux of 1 mg) was injected to the top of the cores using a syringe. The 1 ml slug applied to compacted samples contained 10 g l^{-1} PO_4-P.

5.1.3 ANALYTICAL DETERMINATION OF Br^-, PO_4-P AND PHYTIC ACID - P

PHOSPHORUS DETERMINATION

Sample leachate collected from the bottom of the core after dilution was analysed for PO_4-P and phytic acid - P by the FI techniques described in Chapter 4.

BROMIDE DETERMINATION

A method adapted from Freeman et al. [216] was used to determine bromide in leachate samples during breakthrough experiments. Milli - Q water was used to prepare all reagents and also in the water stream as shown in Figure 5.3. The acid stream comprised 2.8 mM HCl (BDH, AnalaR).The Phenol red and chloramine T streams were: phenol red (20 mg l^{-1}, BDH AnalaR) in 0.05 M acetate buffer (BDH, AnalaR) and chloramine T (200 mg l^{-1}, BDH AnalaR). The manifold used is shown in Figure 5.3 and 0.5 mm i.d. tubing was used throughout. The injection valve was a Rheodyne 5020, and the injection volume was the dead volume (73 µl) of the valve. Sample was injected using a syringe fitted with a silicon rubber seal.

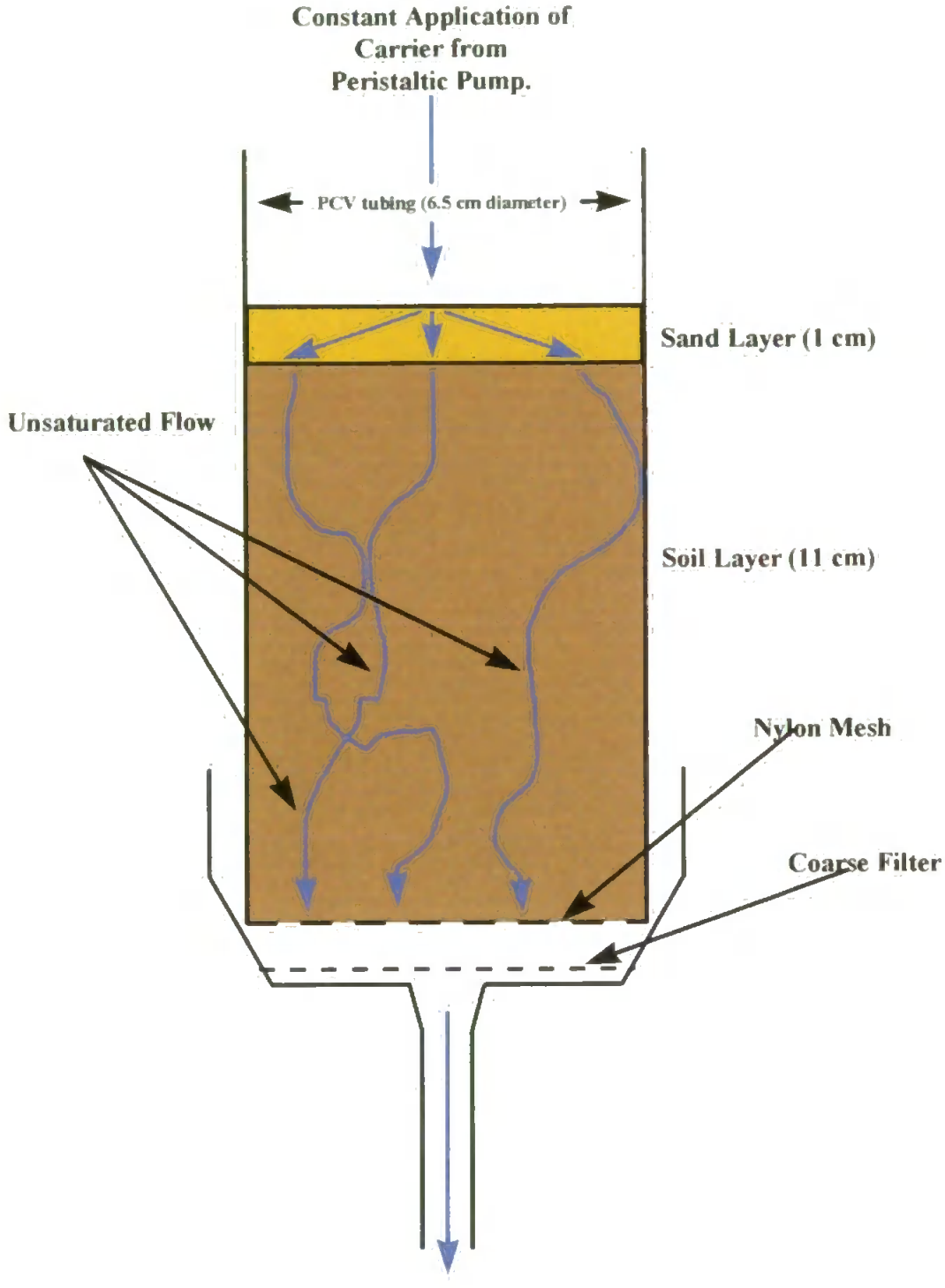

Figure 5.2 : Solute transport experiment setup for unsaturated flow.

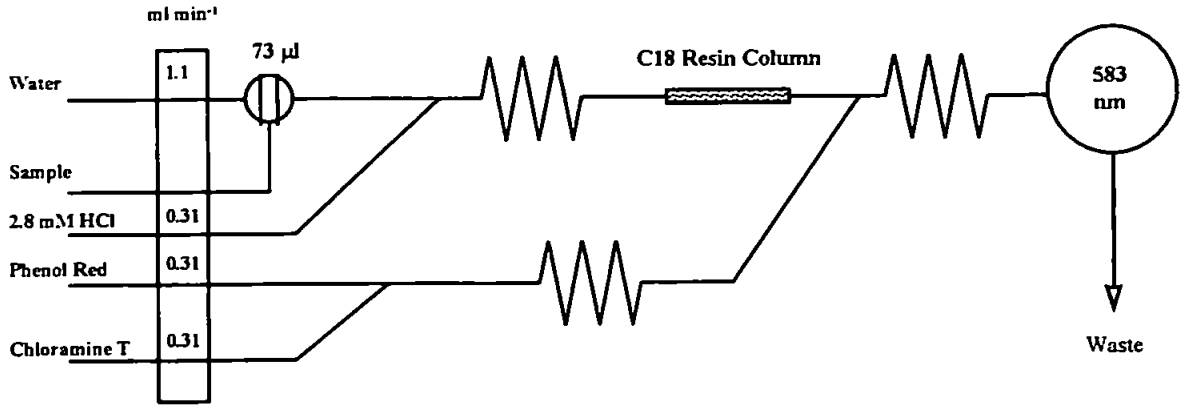

Figure 5.3 : FI manifold for the determination of Br^- in soil leachate samples

5.2 THEORY

5.2.1 SELECTION OF BOUNDARY CONDITIONS AND MODIFICATION OF THE CONVECTION DISPERSION EQUATION TO ACCOUNT FOR TRACER REACTIVITY

Given that the breakthrough experiments operate under steady state flow, the CDE simplifies greatly to the following form of Equation 5.1.

$$D \frac{\partial^2 C}{\partial x^2} - v \frac{\partial C}{\partial x} - R \frac{\partial C}{\partial t} = \mu C - \gamma \qquad (5.1)$$

where D is the dispersion coefficient ($cm^2\ s^{-1}$) of the system, C is the tracer solution concentration ($g\ cm^{-3}$), t is the time (s), v is the pore water velocity ($cm\ s^{-1}$), R is the retardation factor, x is the distance (cm) and $\mu\,(s^{-1})$ and $\gamma\,(s^{-1})$ are the tracer decay and production rate coefficients respectively.

Phosphorus species are extremely reactive in the soil environment and readily adsorb (often irreversibly) onto minerals containing calcium, iron and aluminium [217]. Assuming that the process of tracer (phosphorus) adsorption is irreversible within the short timescale

of our experiments (< 1 day) we can also assume that no phosphorus species are produced during the experiment and can set γ (the production rate coefficient) to zero. We further assume that the irreversible adsorption of phosphorus species onto the solid soil matrix may be described by a linear isotherm of the form ;

$$s = k\,C \tag{5.2}$$

where s is the adsorbed concentration and C is the solution concentration.

In line with the experimental set up the following boundary conditions are applied to solve the equation. The first boundary condition is met at the start of the experiment just prior to application of tracer, where the concentration of tracer at any point x is C_i. In practice we can set C_i to zero by subtracting the background tracer concentration.

$$C(x, 0) = C_i \tag{5.3}$$

The next boundary condition is such that when the tracer is applied between $t = 0$ and $t = t_0$ the concentration of tracer at the top of the core ($x = 0$) is the applied concentration C_0. This condition is met by Equation 5.4a.

$$\left(-D\frac{\partial C}{\partial x} + vC\right)\Big|_{x=0} = vC_0 \qquad 0 < t < t_0 \tag{5.4a}$$

After application has stopped, we apply the condition that the concentration of tracer at the top of the core drops instantly to zero as soon as the application of tracer stops (at time $t > t_0$) and is satisfied by equation 5.4b.

$$\left(-D\frac{\partial C}{\partial x}+vC\right)\Big|_{x=0}=0 \qquad t>t_0 \qquad (5.4b)$$

The final boundary condition makes the assumption that the core is semi-infinite. This approximation can be problematic if the experimental core is too short and is expressed by Equation 5.5.

$$\frac{\partial C}{\partial x}(\infty,t)=0 \qquad (5.5)$$

Subtracting the background concentration and setting C_i to zero allows the equation to be simplified to the form of Equation 5.6, which is a particular solution of the CDE (convection dispersion equation)

$C(x,t) = C_0B(x,t) - C_0B(x,t-t_0)$, where

$$B(x,t)=\frac{v}{v+u}\exp\left[\frac{(v-u)x}{2D}\right]erfc\left[\frac{Rx-ut}{2(DRt)^{\frac{1}{2}}}\right]+\frac{v}{v-u}\exp\left[\frac{(v+u)x}{2D}\right]erfc\left[\frac{Rx-ut}{2(DRt)^{\frac{1}{2}}}\right]$$

$$+\frac{v^2}{2\mu D}\exp\left[\frac{vx}{D}-\frac{\mu t}{R}\right]erfc\left[\frac{Rx+ut}{2(DRt)^{\frac{1}{2}}}\right] \qquad (5.6)$$

5.3 RESULTS AND DISCUSSION

DEMONSTRATION OF THE CONVECTION DISPERSION EQUATION

Graphically the equation may be displayed as a function of concentration varying with time, at a distance x. Figure 5.4 shows a series of time concentration profiles for arbitrary model parameter values (Table 5.1) at depths ranging from 1 to 11 cm.

Symbol	Value	Explanation	Dimensions	Units
μ	0.00001	decay term for a reactive solute	T^{-1}	s^{-1}
R	36	retardation factor	dimensionless	
x	11	distance	L	cm
v	5.00E-02	pore water velocity	$L\,T^{-1}$	$cm\,s^{-1}$
D	0.1	dispersion coefficient	$L^2\,T^{-1}$	cm^2s^{-1}
t_0	1	time at end of applied pulse	T	s
C_i	0	concentration at any point & t=0	ML^{-3}	$mg\,cm^{-3}$
C_0	1	pulse concentration	$M\,L^{-4}$	$mg\,cm^{-3}$

Table 5.1 : Arbitrary CDE parameters used to generate curves shown in Figure 5.4

Figure 5.4 shows how a tracer breaks through at various depths throughout an 11 cm core. In the case of the breakthrough experiments described later the length of the core is set to 11.2 cm. It also shows graphically how this relates concentration to a function of space, x and time t.

5.3.1 PHYSICAL MEASUREMENTS

BULK DENSITY, SATURATED HYDRAULIC CONDUCTIVITY AND EFFECT OF COMPACTION

A set of five cores were repacked from sieved soil granules into PVC tubing (6.5 cm diameter) and 11.2 cm depth to achieve the same geometry as used for the solute transport experiments. The mean bulk density of the samples was 1.065 g cm^{-3} with an RSD of only

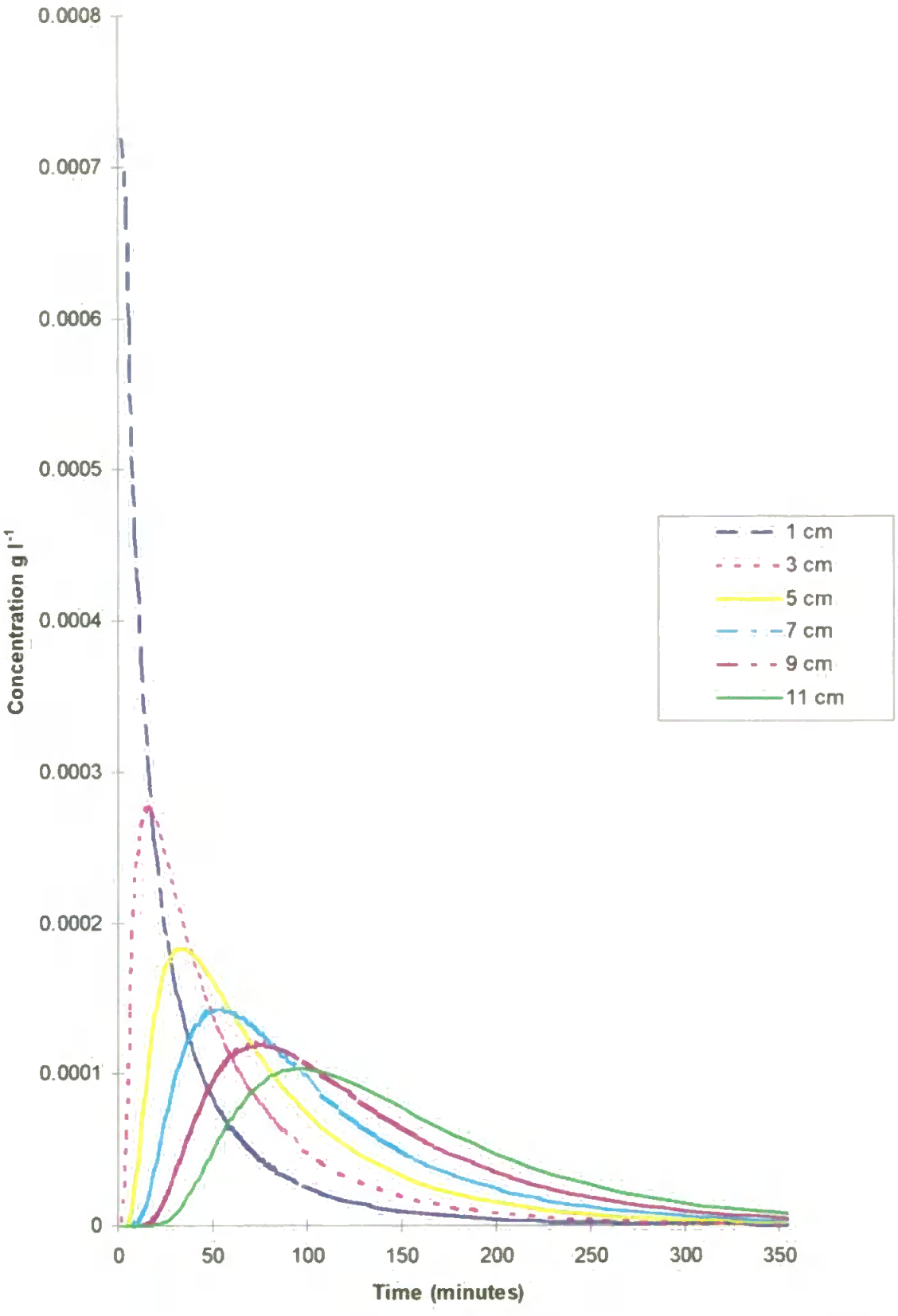

Figure 5.4 : Series of concentration / time graphs for depths in the range 1 - 11 cm produced by application of the model parameters given in Table 5.1.

0.36 %. The saturated hydraulic conductivities of a set of five uncompacted cores were also measured. The mean value was 73.23 milliDarcies with an RSD of 7.23 %. The reproducibility of the permeability measurements, though higher than that of the bulk density, is excellent given that this property of a material is subject to variation of many orders of magnitude.

The extent of compaction must be controlled if a solute transport experiment is to be performed on compacted samples. If the compaction of the sample too severe, the hydraulic conductivity will be so low that the sample will be impervious and if too slight, too similar to the uncompacted sample. The extent of compaction is determined by the size and nature of the load applied to it and the soil's water content at the time of compaction [174,218]. For these samples, we found that the size of the applied load had only a small effect on the extent of compaction at a given gravimetric water content. However, the extent of compaction with varying water content, at a given applied load was much more dramatic. The effect of varying water content on the bulk density samples compacted using a pressure of 146 kN m^{-2} was investigated and is shown in Figure 5.5. The corresponding permeabilities are given in Figure 5.6. The bulk density of samples increase with increasing water content in the gravimetric water content range 0 - 20 % and then decrease again. Bulk densities increase again because at gravimetric water contents greater than 20 % the mixture of soil and water behaves increasingly like an incompressible liquid (water.) The permeabilities follow a similar inverse trend, i.e increasing bulk density gives a lower permeability. The permeability measurements however are much more variable, as shown by the logarithmic scale of Figure 5.6. When compaction proceeds with an initial gravimetric water content of 18.6 % the saturated hydraulic conductivity dropped to 2.92 milliDarcies, a 26-fold drop in saturated hydraulic conductivity relative to the mean of the uncompacted samples (73.23 milliDarcies). These conditions were therefore chosen to form part of the

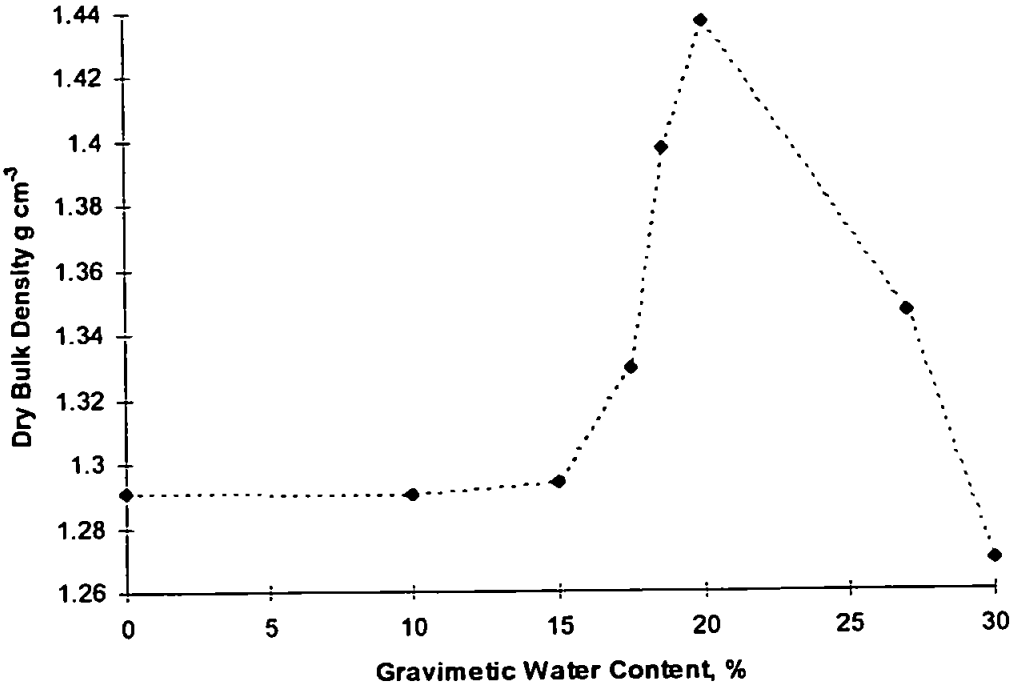

Figure 5.5 : Effect of water content on the bulk density of samples compacted with a pressure of 146 kN m^{-2}.

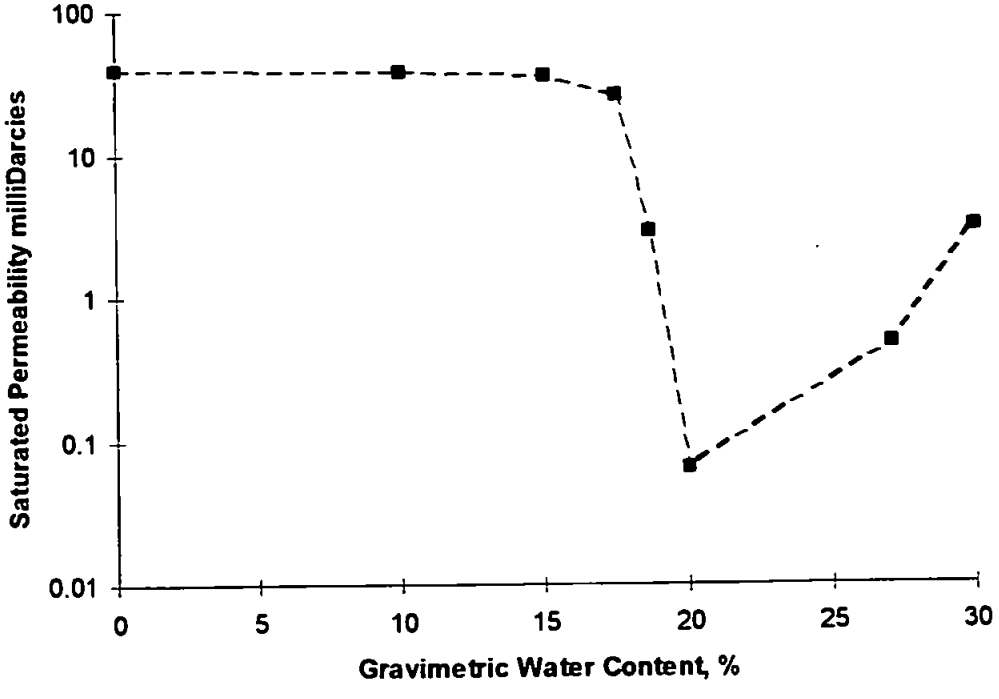

Figure 5.6 : Effect of water content on the saturated permeabilities of samples compacted with a pressure of 146 kN m^{-2}.

compaction protocol because the drop in permeability is in a suitable range for solute transport experiments as discussed earlier.

The reproducibility of the compaction protocol was tested with a set of five compacted cores. The mean bulk density was 1.38 g cm^{-3} with an RSD of 1.45 % and the corresponding mean saturated hydraulic conductivity was 4.21 milliDarcies with an RSD of 27.25%. Given that permeability is a very difficult parameter to control, the reproducibility is excellent.

MERCURY POROSIMETRY

Mercury intrusion / extrusion curves for the uncompacted and a uncompacted samples and their corresponding corrected curves are shown in Figures 5.7 and 5.8. In Figure 5.7 the uncorrected and corrected curves are nearly identical at lower applied pressures. Divergence is encountered at high pressure because expansion of the penetrometer and compression of the intruding mercury and sample are more pronounced at higher pressures. The curves shown in Figure 5.8 are also nearly identical at the low pressure end and the corrected curves show that the increase in volume intruded is mainly due to penetrometer expansion and mercury compression.

Normalisation of the fully corrected curves, such that intrusion proceeds from 0 to 100%, in Figures 5.7 and 5.8 shows that a collapse of the macropore structure occurs with compaction. This is further underlined by the decrease in porosity from 48.11 % to 34.34 % on compaction.

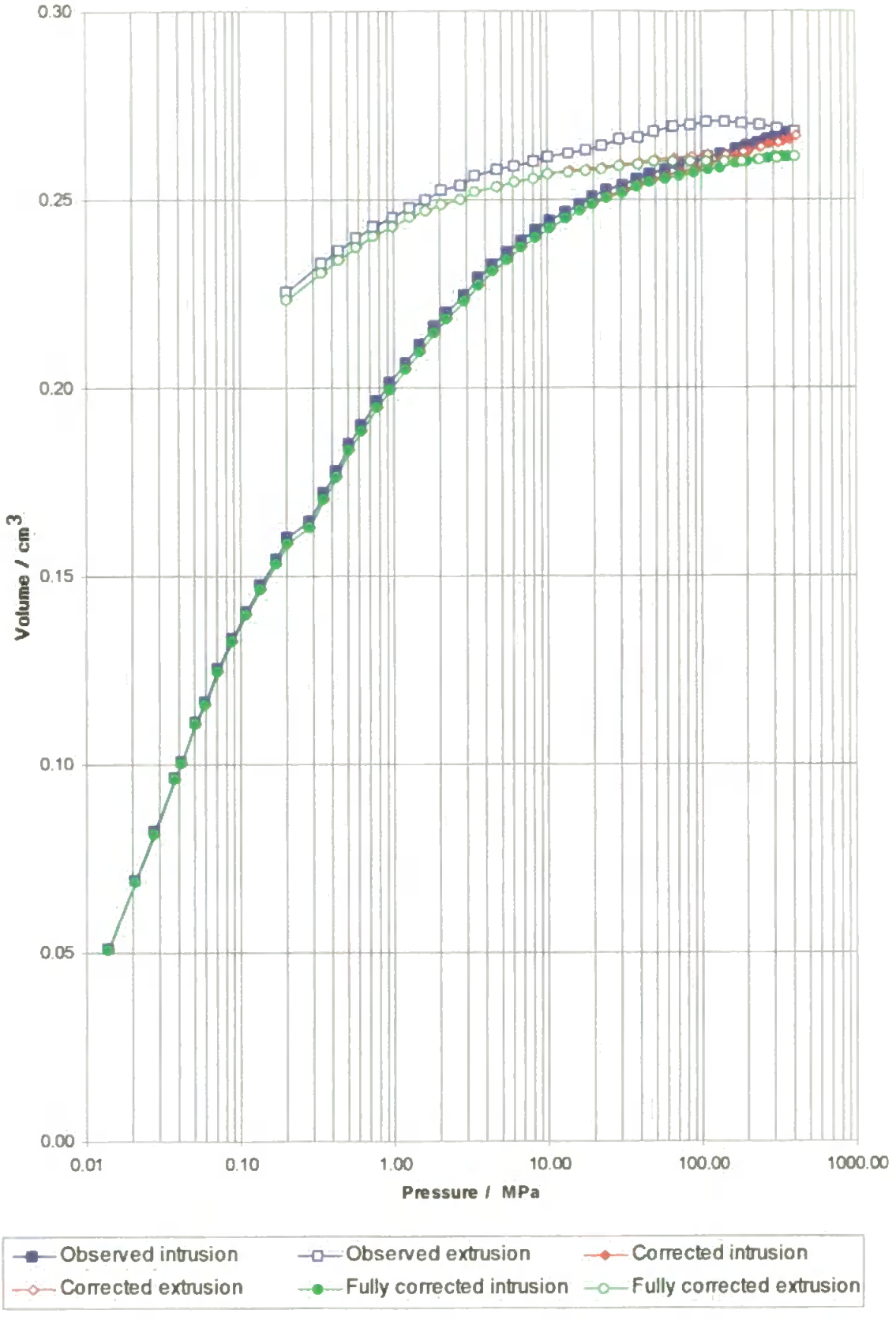

Figure 5.7 : Mercury Porosimetry curves of uncompacted soil samples and the effect of the corrective method (Pore-Comp.) Uncompacted soil samples have a fully corrected porosity of 48.11%.

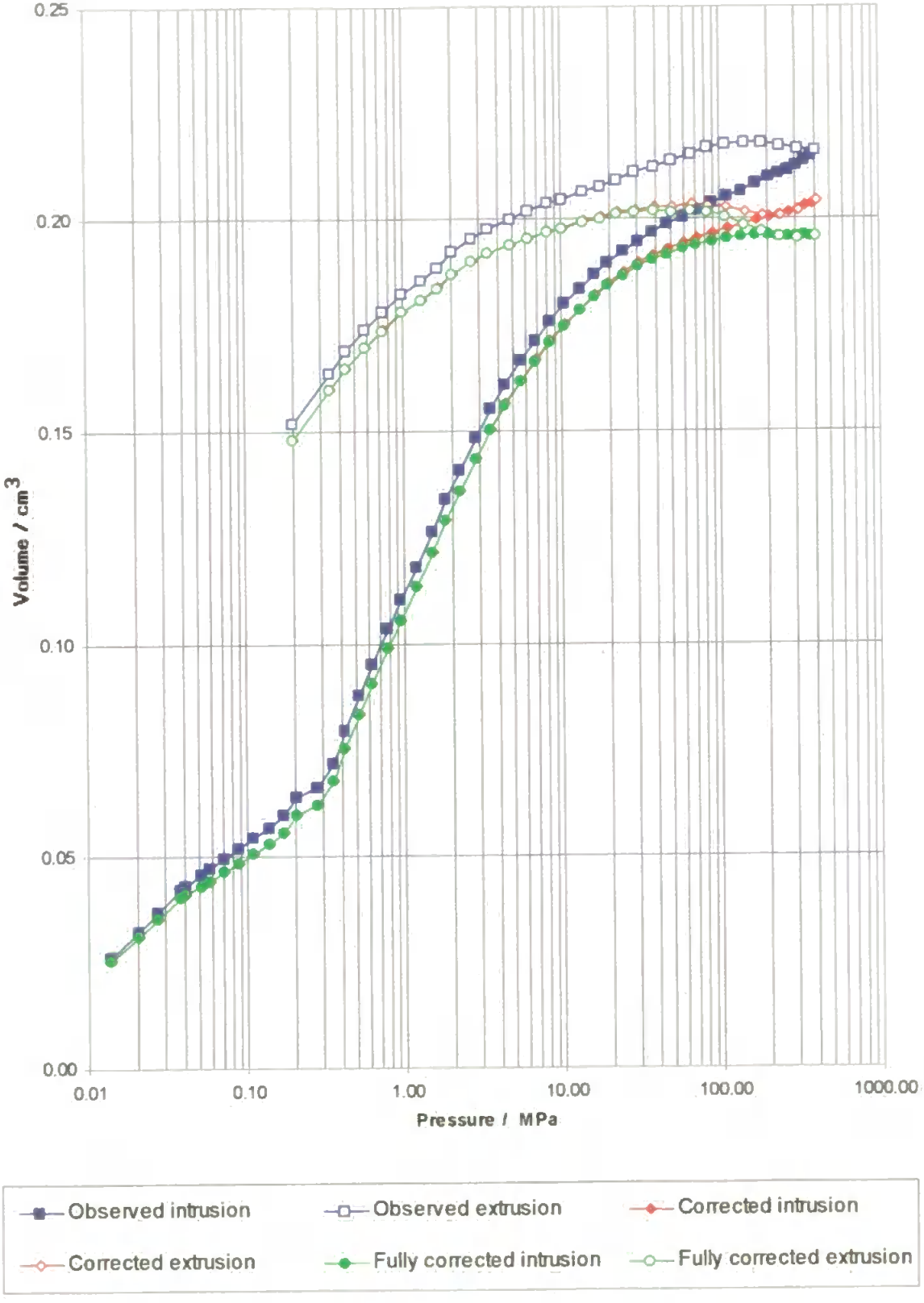

Figure 5.8 : Mercury Porosimetry curves of compacted soil samples and the effect of the corrective method (Pore-Comp.) Compacted soil samples have a fully corrected porosity of 34.34%.

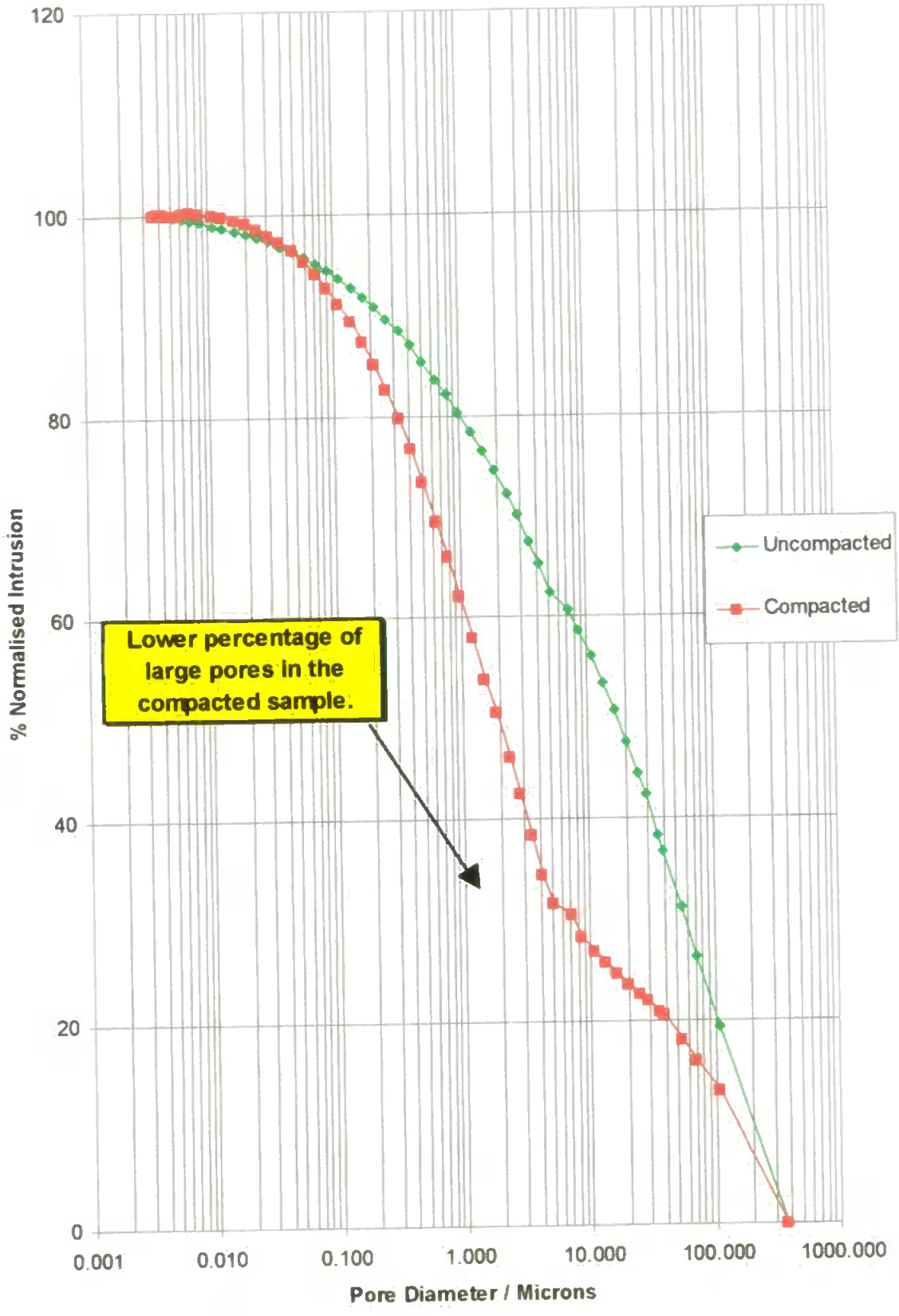

Figure 5.9 : Normalised fully corrected intrusion curves for compacted and uncompacted samples.

The size of sample in mercury porosimetry is limited by the size of the mercury penotrometer used which usually permits the use of about 1 g of sample. In a water retention experiment, more than a hundred grams of material are used. Water retention experiments are therefore more suited to giving information at a larger scale than mercury porosimetry because they operate on much larger samples. The study of intact samples with heterogoneities is possible when larger sample sizes are used. Mercury porosimetry can be used with repacked samples which have a more homogenous structure than would be found in an intact soil sample, because a lower size of sample required to represent it. The unsuitability of mercury porosimetry to study pores >500 μm [42] is not problematic in repacked samples because heterogeneities such as very large pores are removed.

Mercury porosimetry has a number of important advantages over water retention techniques for the study of repacked samples. Firstly, it is much faster and a complete mercury intrusion curve can be produced in one day. Water retention experiments can take months to complete depending upon the nature of the soil sample being studied. Secondly, comparison of Figures 2.3 and 5.7 or 5.8 shows that the mercury porosimetry curves are much more detailed. In Figure 2.3 volumetric water contents are given only at five different equilibration pressures whereas the mercury intrusion curves give the volume of mercury intruded at 80 equilibration pressures.

5.3.2 Solute Transport

Analysis of Bromide Breakthrough Curves

The experimental and CDE fitted breakthrough curves for bromide are shown in Figure 5.10. Carrier was applied more quickly to the uncompacted core as shown in Table 5.2 to keep the ratio between these flow velocities the same as the ratio of the porosities giving

identical pore water velocities for each experiment. The lower breakthrough Br^- concentrations seen in Figure 5.10 and the pulse concentration drop in Table 5.3 reflects the increased diluting effect of the higher flow rate used in the uncompacted experiment.

The primary feature of the breakthrough curves is that the maximum concentration occurs well before the elution of one pore volume. The speed with which the maximum concentration breaks through is closely related to the velocity of tracer movement. If the maxima had occurred after the elution of one pore volume, then it would indicate the use of the entire pore network. The breakthrough experiments described are carried out under unsaturated conditions (i.e. the porosity exceeds the volumetric water content as shown in Table 5.2) and only the water filled part of the network can conduct water and even some parts of the network which do contain water may not be involved in transport. Secondly the area under the breakthrough curve of the compacted sample is lower because the flow rates are different as shown in Table 5.2.

Sample	Porosity %	Carrier Flow Rate ml min^{-1}	Volumetric Water Content
Uncompacted soil	48.11	0.30	12.62
Compacted soil	34.34	0.21	28.72

Table 5.2 : Physical conditions used in the production of breakthrough curves

A method of estimating the transport porosity, θ_a has been suggested by Jury et al., [219]. This approach estimates θ_a as the ratio of the drainage flux density, F_d to the pore water velocity. The pore water velocity, v is to a first approximation the first moment of an

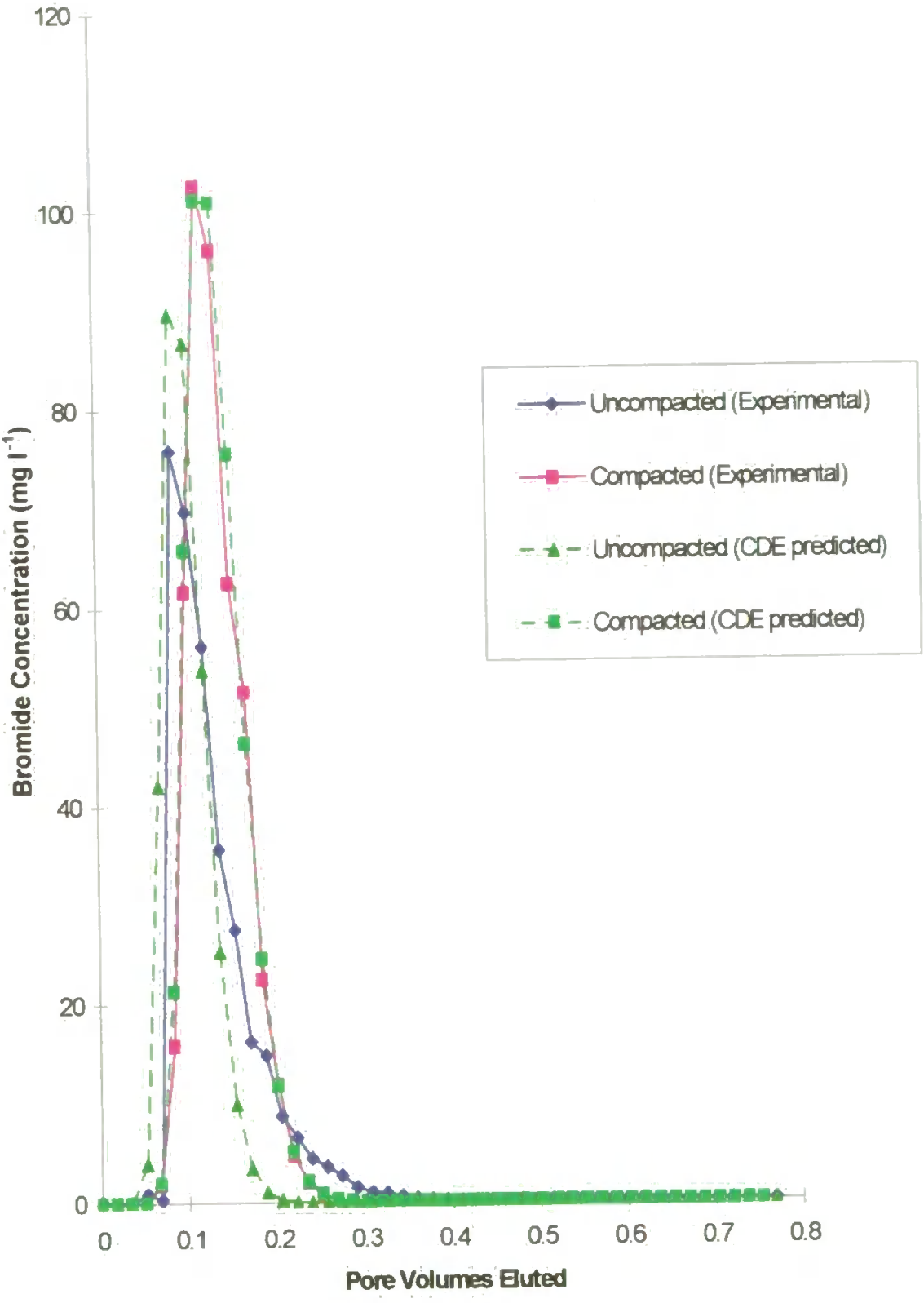

Figure 5.10 : Bromide breakthrough curves for compacted and uncompacted soil columns. Recovery of applied bromide flux was > 95% both cases indicating that it is not retained in this soil.

unreactive tracer's breakthrough distribution. In this case we estimate v empirically by fitting the CDE (Equation 5.6) to the bromide breakthrough curves. CDE parameters used to fit both the compacted and uncompacted samples are given in Table 5.2 along with their calculated transport porosities.

Experimental setup determines the values of the parameters, x, and C_i. C_0 is the pulse concentration and is a scalar multiplier in Equation 5.6 and is applied between $t = 0$ and $t = t_0$ as defined in the boundary condition (Equation 5.4a.) At the beginning of the experiment, 1 mg in a volume of 1 ml of tracer is injected with a syringe in less than one second. The time taken to inject the sample (t_0) is insignificant with respect the total duration of the experiment (some 30000 seconds). For the purposes of fitting the CDE to experimental data we assume that the pulse is applied in an arbitrarily small amount of volume and time, allowing the concentration C_o to be used as a fitting parameter.

Bromide is assumed to be an unreactive tracer and accordingly should not be retarded or adsorbed (i.e. $\mu = 0$ and $R = 0$.) However the form of the CDE given in Equation 5.6 is not

CDE parameter	Description	Value uncompacted core	Value compacted core
D	Dispersion coefficient, $cm^2\ s^{-1}$	1.66×10^{-4}	0.91×10^{-5}
R	Retardation factor, dimensionless	0.166	0.166
v	Pore water velocity, $cm\ s^{-1}$	5.3×10^{-4}	3.95×10^{-4}
μ	decay factor, s^{-1}	10^{-9}	10^{-9}
C_i	Background concentration, $mg\ cm^{-3}$	0	0
C_o	Initial concentration, $mg\ cm^{-3}$	190	255
t_o	time, s	1	1
x	depth, cm	11.2	11.2
θ_{st} $(=F_d/v)$	Transport porosity, dimensionless,%	28.43	27.21
(D/v)	dispersivity, cm	0.31	0.23

Table 5.3 : CDE parameters used to fit the experimental curves given in Figure 5.10. Recovery of the applied bromide flux was > 95 % in both cases.

well behaved when $\mu = 0$ or $R = 0$, and therefore not usually used to fit unreactive tracers. However if the same equation is to be used to model phosphorus species as well then the derived form of the CDE given in Equation 5.6 must be used. Given that R and μ can not be set to zero they were fitted to the experimental curves. A fitted value of R for the uncompacted sample was found to be 0.166 and if we assume that in both cases the soil - bromide interaction is negligible the same value of R may be used for the compacted sample. Similarly, μ was set to be very small (10^{-9} s^{-1}) and had no effect on predicted curve shape at μ values < 10^{-7} s^{-1} and had no affect on the curve fitting. The fitted values of R and μ were significantly higher for phytic acid and orthophosphate as shown in Table 5.3. Faster breakthrough in the uncompacted core is indicated by the higher fitted pore water velocity v. The dispersion co-efficient also decreases upon compaction and is probably attributable to a decrease in the number of larger pores, which themselves have a greater dispersion co-efficient. The transport porosity, θ_{st} is fairly similar but in the case of the uncompacted sample it exceeds the volumetric water content. A situation which is a physical impossibility, but has been observed by other workers, [220-222] and has been attributed to preferential flow.

The interpretation of the experimental bromide breakthrough curves and consequently the CDE modelled parameters is dependent upon the nature of the causal processes. If the assumption is made that bromide is entirely non reacting, then the changes in parameters may be attributed to only physical phenomena. However if the bromide ions transport properties were affected by its charge this assumption would be invalid.

Figure 5.11 shows a simplified schematic of the charges operating during transport. In temperate regions, the clay minerals typically carry a negative charge which is counterbalanced by metal cations [223]. The DeBathe soil used in these experiments is a

member of the Crediton series and its clay minerals follow this typical behaviour [224]. If by electrostatic attraction, the bromide ion is drawn into a slower moving part of the parabolic profile of flow velocities then breakthrough will be delayed. However, the carrier itself contains a background electrolyte (0.001 M KNO_3) which largely swamps out this type of clay mineral - tracer effect. The assumption that bromide transport is dependent only on changes in physical characteristics is therefore reasonable, and we use the bromide curve to calibrate CDE physical parameters (v, D, C_0) when fitting the breakthrough curves of orthophosphate and phytic acid.

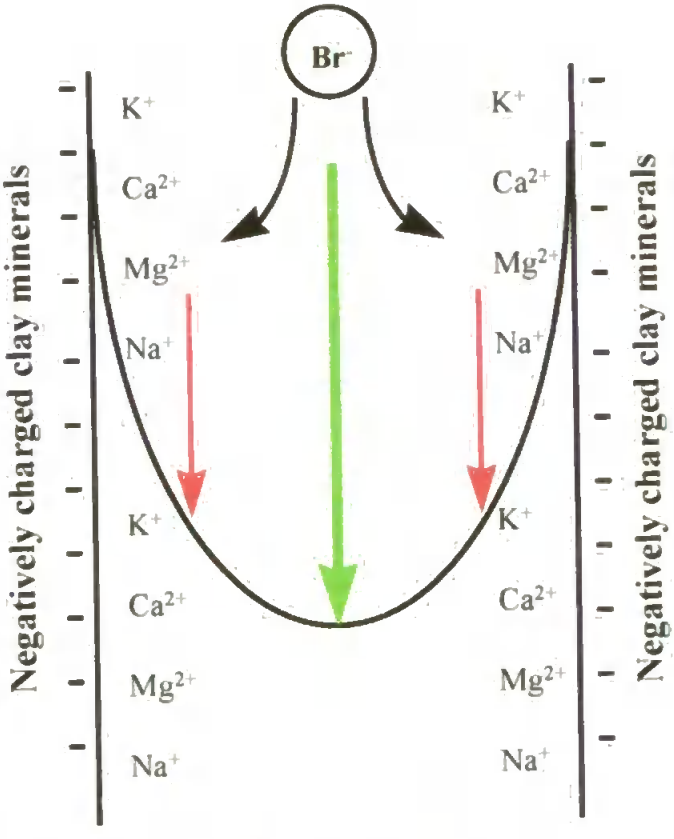

Figure 5.11 : Potential slow down of the Br^- ion during transport through a soil pore. Red arrows indicate regions of slow flow and the green arrow in the centre indicates a flow rate twice the average. The parabolic profile of flow velocities is based on the assumption of a laminar flow regime.

ANALYSIS OF PHYTIC ACID BREAKTHROUGH CURVES

Experimental phytic acid breakthrough curves with their corresponding CDE fitted curves are given in Figure 5.12. The CDE physical parameters used to fit these curves are given in table 5.3 and the remaining parameters in table 5.4. The effect of compaction is to increase the phytic acid - soil interaction resulting in greater retardation of the mobile phase and increased adsorption. This is reflected by an increase in R and μ on compaction. In both experiments R and μ increase, relative to their equivalent bromide values indicating that the phytic acid tracer is more reactive than the bromide.

ANALYSIS OF ORTHOPHOSPHATE BREAKTHROUGH CURVES

A similar pattern is observed in the breakthrough curves of orthophosphate, the fitted parameters shown in table 5.4 show that R and μ values are larger than the corresponding values of bromide and phytic acid. The increase in orthophosphate adsorption on compaction is so large that no breakthrough was observed when a flux of 1 mg was applied. The applied flux had to be increased to 10 mg in order to observe breakthrough. Correspondingly, the pulse concentration parameter, C_0 was set an order of magnitude higher.

The order of reactivity of the tracers in this system is bromide < phytic acid < orthophosphate. Bromide which is used as a physical parameter calibration tracer is the least reactive. The next least reactive is phytic acid and its lower reactivity is probably due to its connection to the hydrocarbon ring, Figure 5.13. The corresponding breakthrough and CDE fitted curves are shown in Figure 5.14.

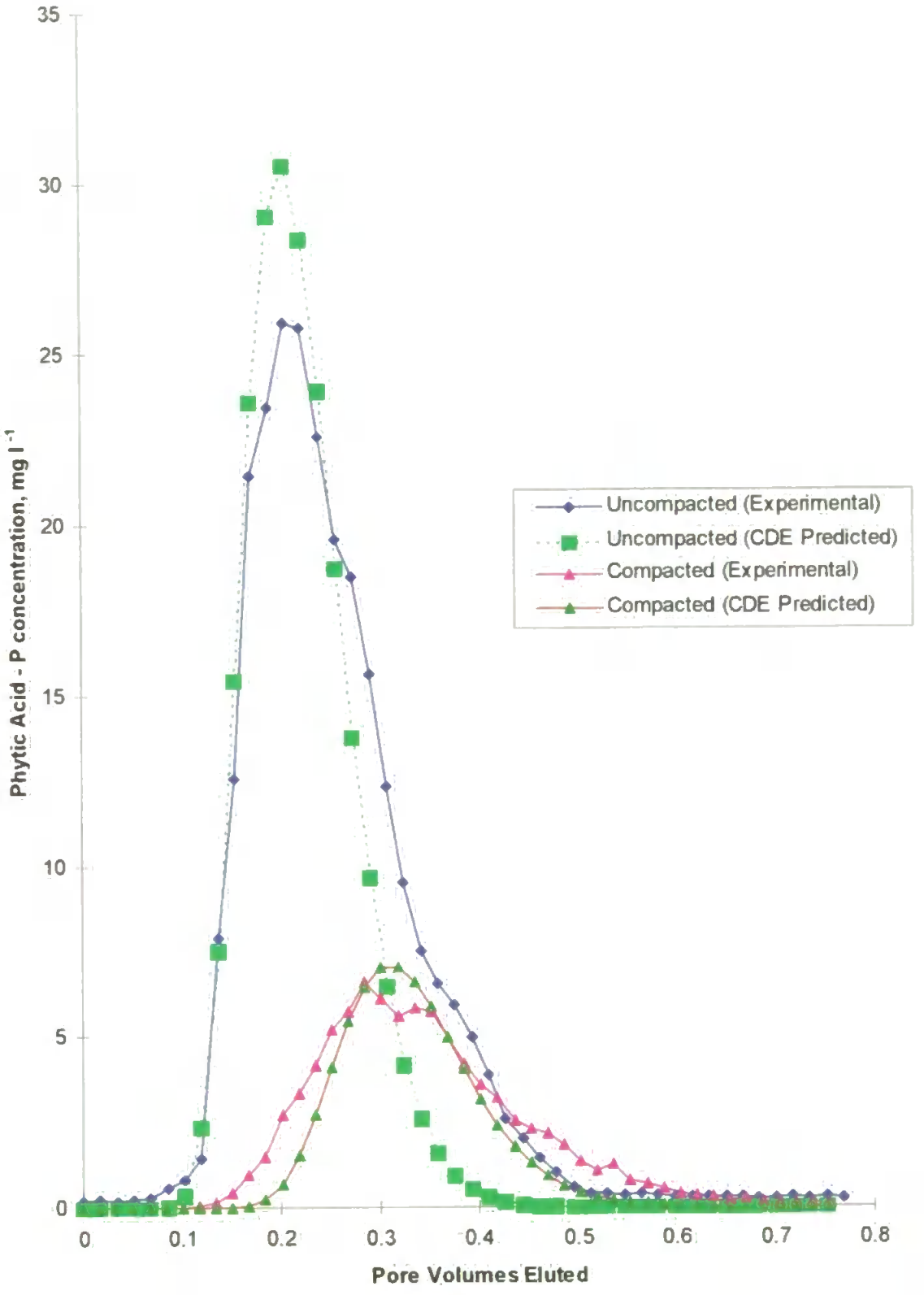

Figure 5.12 : Experimental and CDE fitted breakthrough curves of phytic acid.

CDE parameter	Value (uncompacted core)	Value (compacted core)
***R* (Bromide)**	0.166	0.166
μ (Bromide) s^{-1}	10^{-9}	10^{-9}
***R* (Phytic Acid)**	0.37	0.42
μ (Phytic Acid) s^{-1}	1.7×10^{-5}	6.5×10^{-5}
***R* (Orthophosphate)**	0.68	0.88
μ (Orthophosphate) s^{-1}	1.4×10^{-4}	2.2×10^{-4}

Table 5.4 : Parameters used to fit the phytic acid and orthophosphate breakthrough curves to the CDE for uncompacted and compacted cores. Recovery of the applied phytic acid - P flux was 72.2% and 18.1% in the uncompacted and compacted experiments respectively. Recovery of the orthophosphate flux was 5.4 % and 0.4% in the uncompacted and compacted experiments respectively. All other parameters are given in Table 5.1 except for the C_0 value orthophosphate which was 2550 mg cm^{-3}.

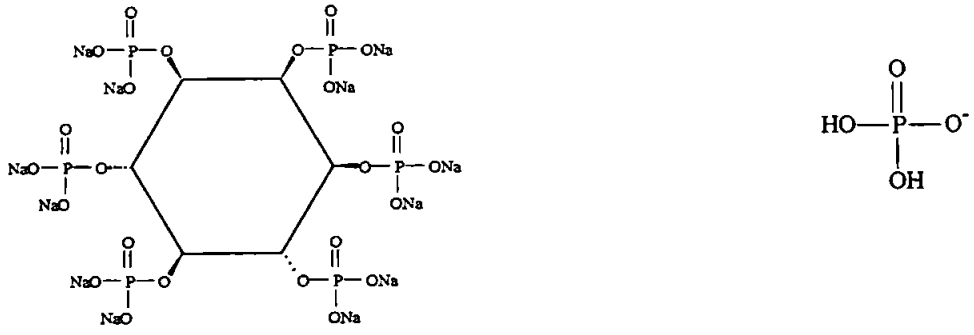

Figure 5.13 : Phytic acid dodecasodium salt (shown left) and orthophosphate (shown right). Form of orthophosphate shown is typically found in soils and is the dominant form at pH 2-7[213].

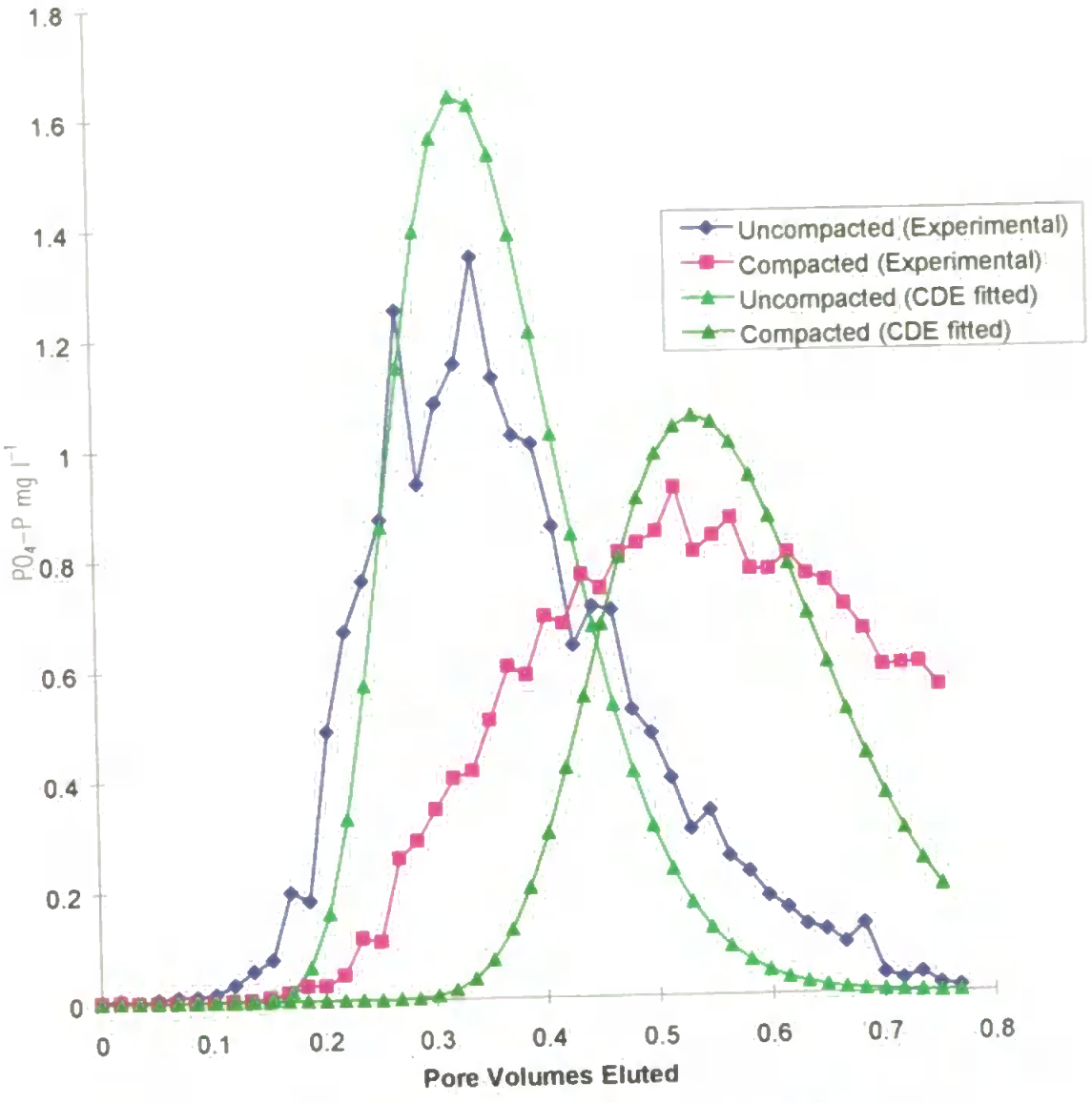

Figure 5.14 : Experimental and CDE fitted breakthrough curves of orthophosphate.

SOIL AND LEACHATE ACIDITY

The form of orthophosphate and phytic acid is affected by pH. In order to determine which form was dominant in solution and if those forms changed during the breakthrough experiments, the pH of the soil and the leachate was determined. The sieved soil pH was 5.45±0.18 measured by making a thick paste with 0.01 M $CaCl_2$ solution and 6.44±0.65 with milli Q water, based on five measurements and a 99% confidence interval. The pH of the leachate was monitored at the steady state flow conditions used in the solute transport

experiments. Leachate from the uncompacted and compacted cores had a similar pH which remained in the range 5.6-5.9 for a ten hour period. The duration of the solute transport experiments was 7 hours 30 minutes. The dominant form of orthophosphate was therefore $H_2PO_4^-$ as shown in Figure 5.13 and does not change during the experiment. Similarly phytic acid does also not change its form during the experiment.

5.3.3 Modelling Compaction with the Pore-Cor Network Model

Fitting Mercury Porosimetry Curves

The normalised mercury intrusion curves for compacted and uncompacted samples were modelled using the Pore-Cor package, described in Chapters 2 and 3 and the corresponding simulated intrusion curves are shown in Figure 5.15. Clearly, neither experimental curves are very well fitted, but the simulated curves do track the trend of a reduction in the number of large pores evident in the experimental curves. The Pore-Cor for each of the stochastic generations has modelled the compaction by increasing the percentage of throat of minimum size (the pore skew). The other fitted model parameters are identical or very similar and are shown in Table 5.5. The corresponding simulated structures, for the first stochastic generation are shown in Figure 5.16a and 5.16b respectively.

Parameter	Units	Value (Uncompacted Sample)	Value (Compacted Sample)
Porosity	%	48.11	34.34
Co-ordination Number		2.8	2.8
Throat Skew	%	0.523	1.056
Pore Skew		3.5	3.4

Table 5.5 : Pore-Cor model parameters for the first stochastic generation

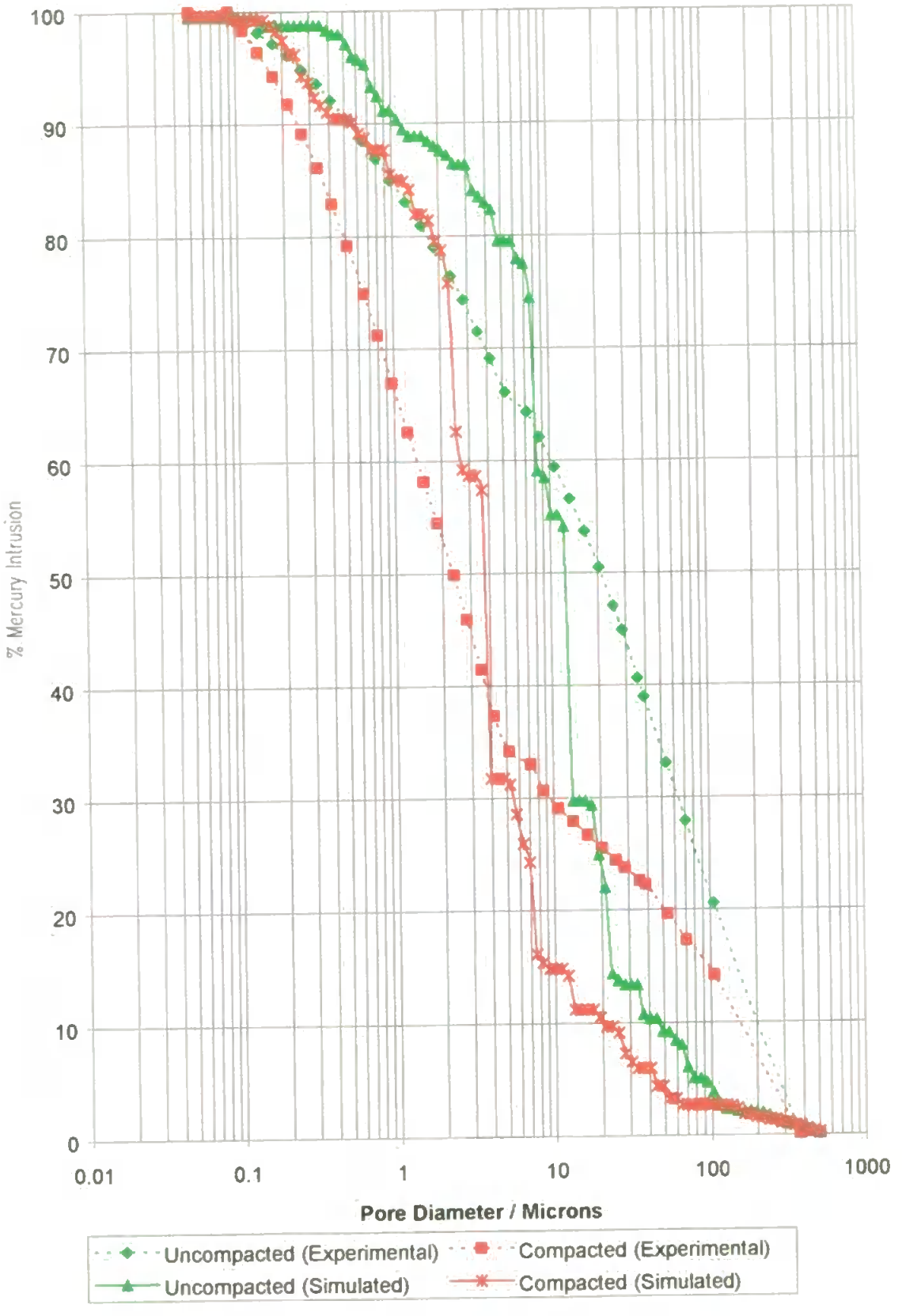

Figure 5.15 : Experimental and Pore-Cor simulated mercury intrusion curves.

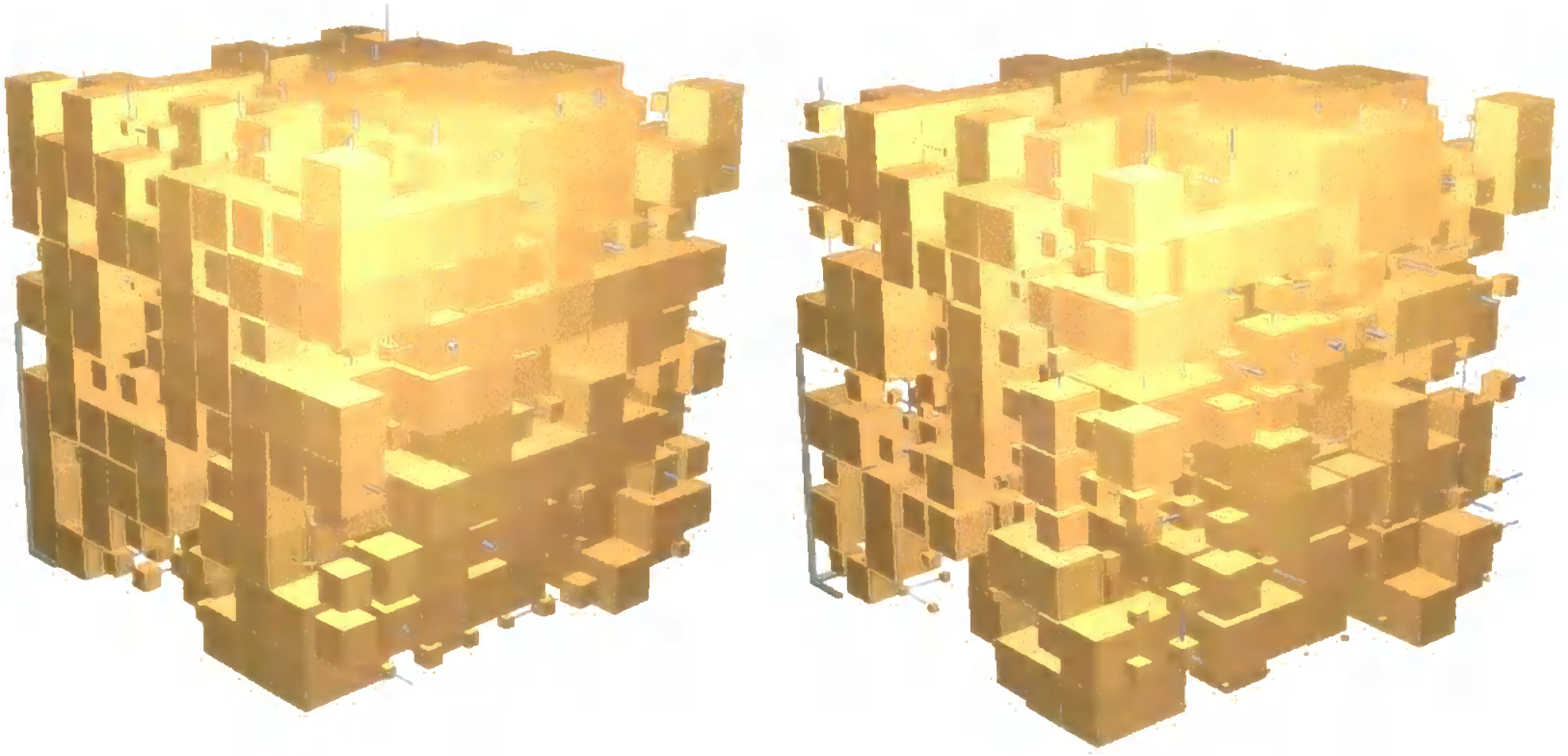

Figure 5.16a, shown left: Simulated uncompacted soil structure with a porosity of 48.11 %. Small scale bar is the pore row spacing (516 μm) and the unitcell is a cube with a length of 5.16 mm. Pore skew = 3.4.

Figure 5.16b, shown right: Simulated uncompacted soil structure with a porosity of 34.34%.Small scale bar is the pore row spacing (516 μm) and the unitcell is a cube with a length of 5.16 mm. Pore skew = 3.4

Changes in model the simulated co-ordination number, throat skew and pore skew are shown in Figures 5.17 to 5.19 respectively. A paired t test showed the fitted co-ordination numbers and pore skews for the uncompacted and compacted structures are not significantly different at the 99% confidence interval, ($t = 0.73 < t_{crit} = 3.25$) and ($t = 1.58 < t_{crit} = 3.25$) respectively and the throat skews are significantly different ($t = 5.89 < t_{crit} = 3.25$).

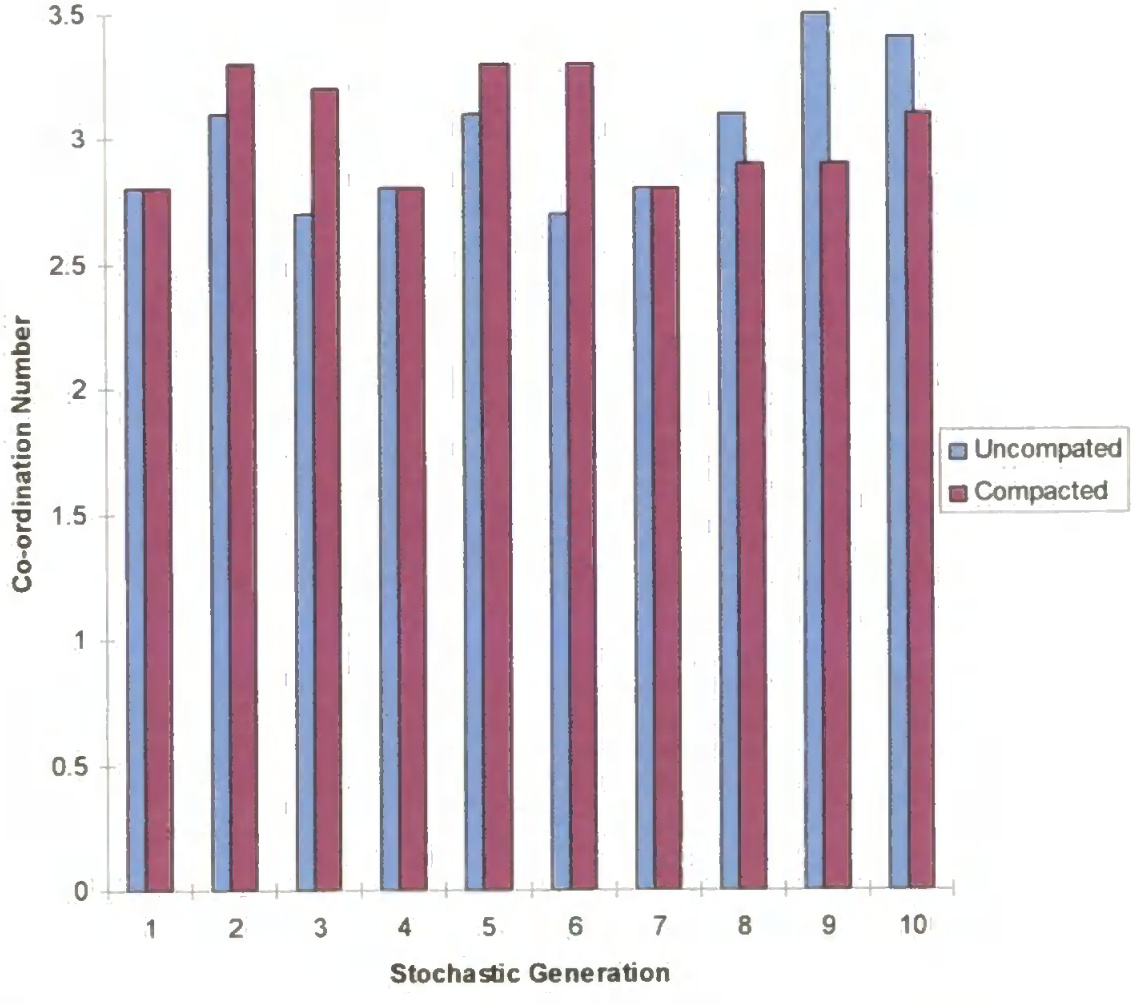

Figure 5.17 : Fitted co-ordination numbers for compacted and uncompacted samples across ten stochastic generations.

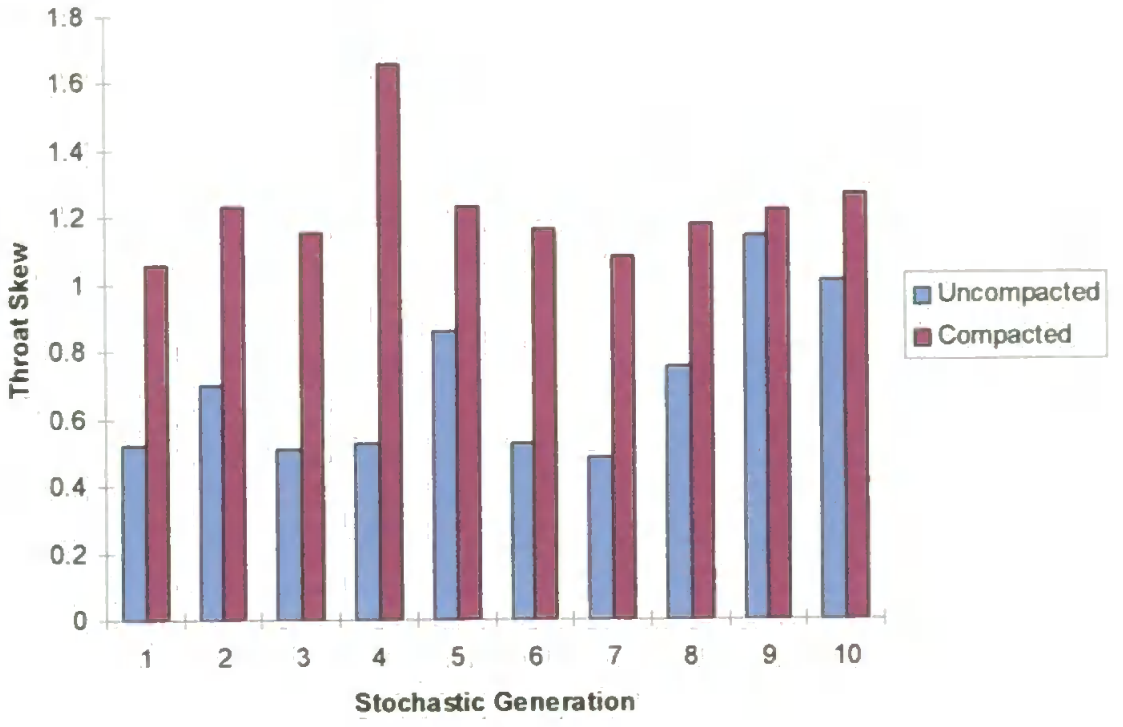

Figure 5.18 : Fitted throat skews for compacted and uncompacted samples across ten stochastic generations.

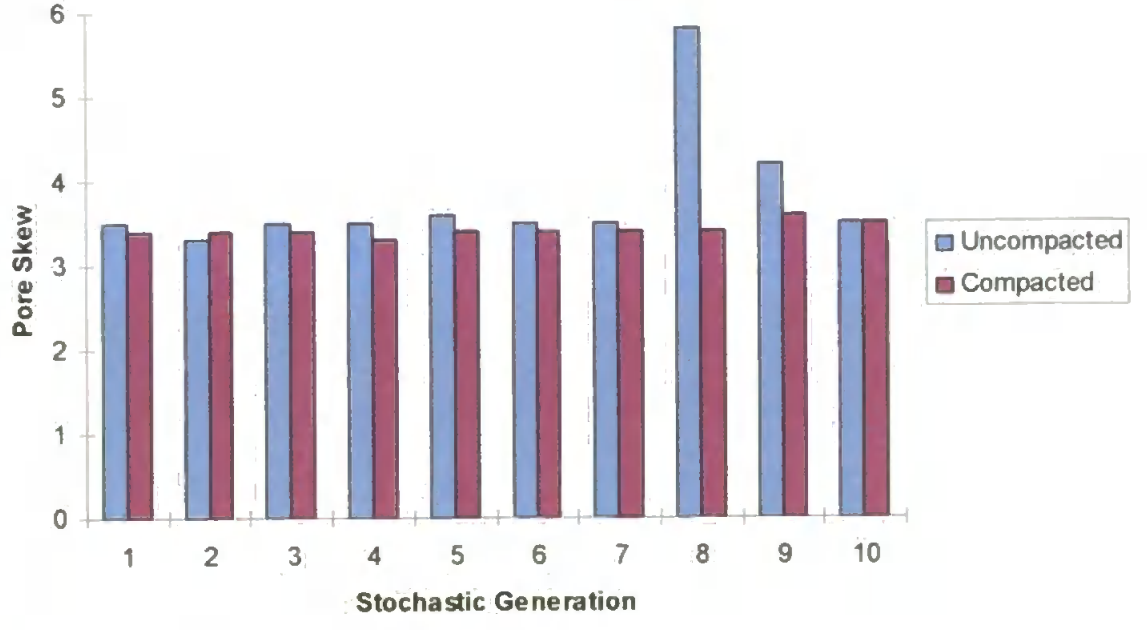

Figure 5.19 : Fitted pore skews for compacted and uncompacted samples across ten stochastic generations. The large spike in pore skew for uncompacted generation 8 is caused by inefficient packing.

The effect compaction on the pore and throat size distributions can be seen in Figure 5.20 for the first stochastic generation. The uncompacted structure has a higher proportion of large throats than the compacted structure. The other nine stochastic generations show similar patterns, Figure 5.18.

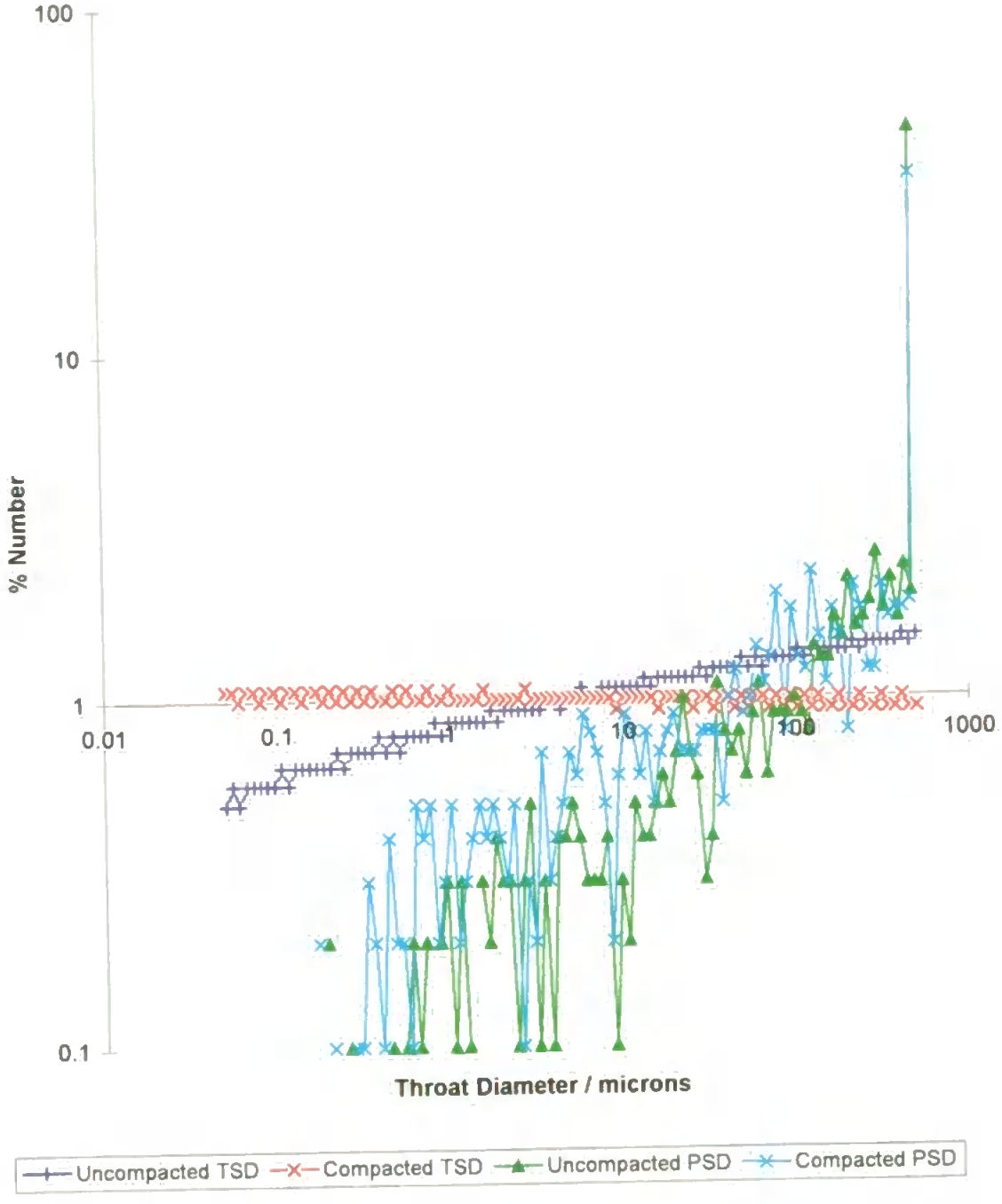

Figure 5.20 : Throat size distributions for the uncompacted and compacted samples. First stochastic generation.

MODELLING HYDRAULIC CONDUCTIVITY

From each randomly generated structure a saturated hydraulic conductivity was calculated and the results are shown in Figure 5.21. The results predict that the conductivity drops by an average factor of 210. The experimental permeability dropped on average by a factor of 26. The overestimation of the permeability drop has two causes. Firstly the rapid axial compression may cause non uniform compaction of the sample. If the core were non-uniform, the single sample taken from its centre may not represent the entire core. Secondly the Pore-Cor simulated curves do not fit the experimental curves very well and this will cause the network predictions to be inaccurate.

MODELLING TORTUOSITY AND DISPERSIVITY

The final property which can be calculated from the Pore-Cor unitcell is the tortuosity. As discussed previously in Chapter 2 the network solutions are not unique and therefore any calculated property from them is also not unique, including the tortuosity. For the ten random generations of the unitcell, the calculated tortuosities are shown in Figure 5.21. The median tortuosities of the uncompacted and compacted samples were 4.44 and 3.77 respectively. However the modelled sets of ten tortuosities were not significantly different ($t = 0.98 < t_{crit} = 3.25$ at a 99 % confidence interval) and is consistent with an unchanged connectivity.

Experimentally, the dispersivity of the sample decreases on compaction (Table 5.2.) It might therefore be inferred that the tortuosity of the sample should also decrease with compaction. However, the simulated values of tortuosity do not change. The most obvious explanation of this discrepancy is that, as explained in section 1.2.4, the simulated tortuosities do not take into account the tortuosity which can occur due to curved paths

within wide straight tubes. The pores and throats of the unitcells which simulate compaction are narrower than those in the unitcells which simulate the uncompacted sample, as illustrated in Figures 5.20 and 5.21.

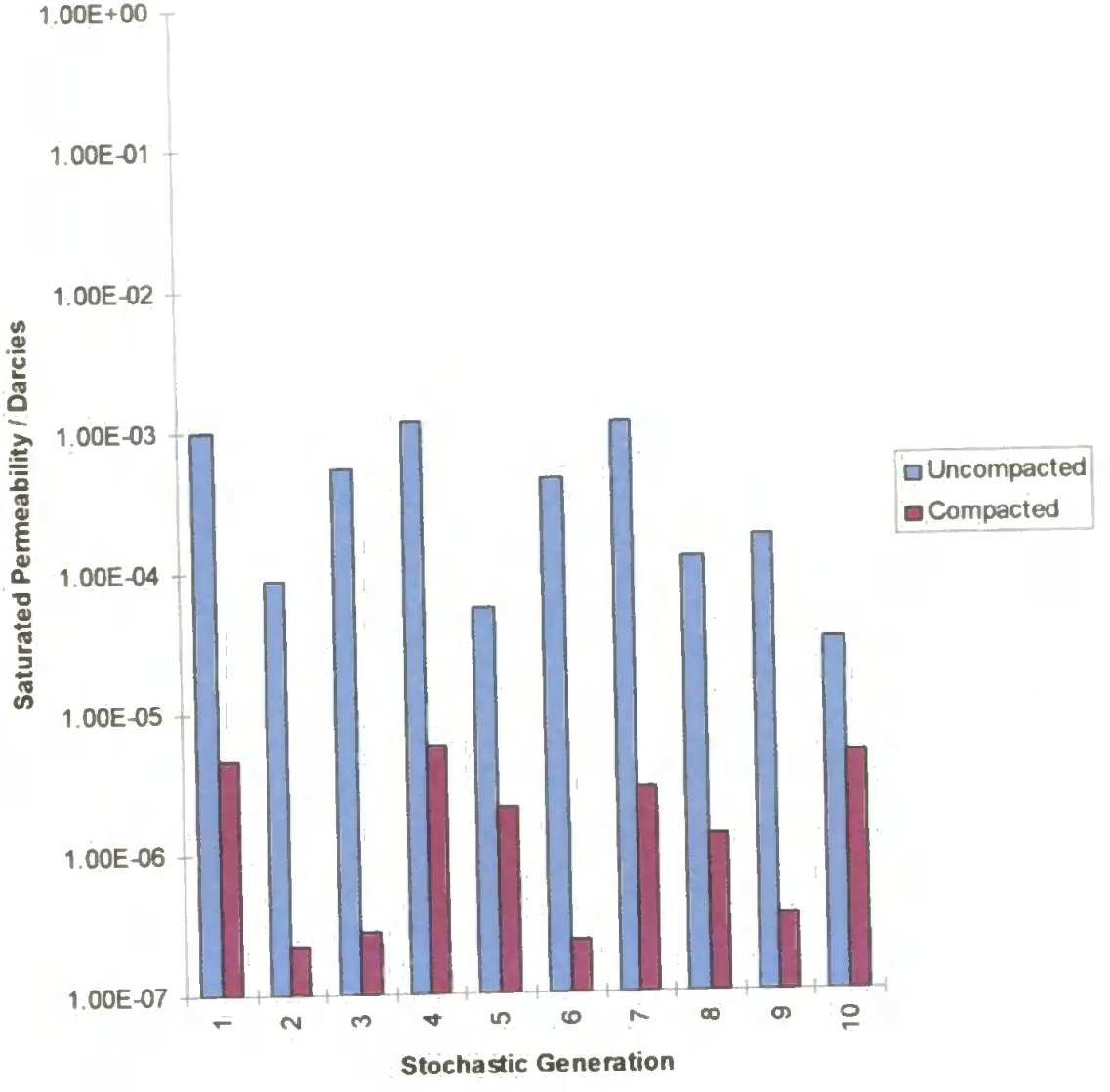

Figure 5.21 : Pore-Cor generated permeabilities for ten different stochastic generations of the Pore-Cor network.

Thus it may be that the connectivity, and hence paths, within the uncompacted and compacted sample do not change, whereas the extent of tortuosity within individual paths

decreases. This would explain why the simulated tortuosity does not decrease on compaction whereas the inferred experimental tortuosity does.

A further complication to this scenario is that the experiments show that preferential flow is occurring (section 5.2.4). Within the Pore-Cor unit cell, flow occurs within every element. Preferential flow does occur, because the flow capacity of each element is approximately proportional to radius^4/length (section 1.2.4) but is not explicitly modelled.

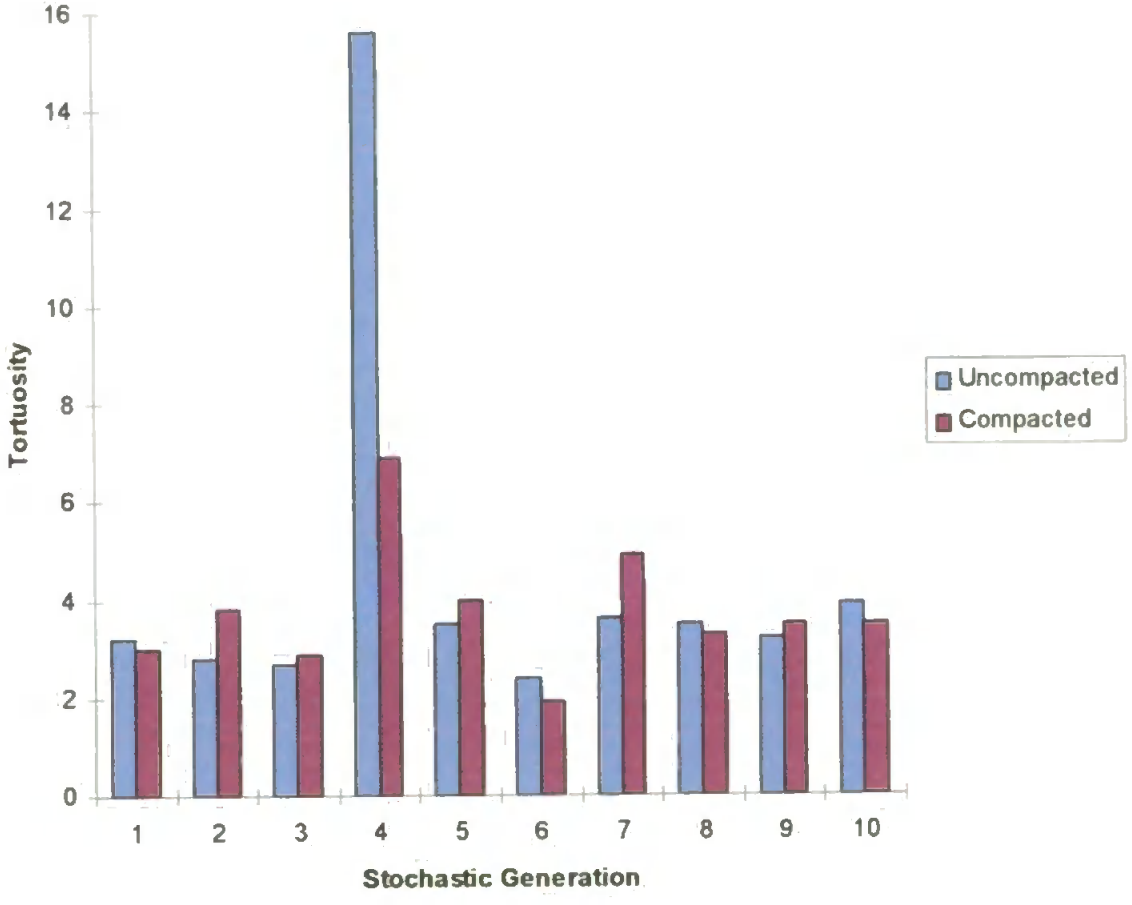

Figure 5.22 : Tortuosities of uncompacted and compacted simulated structures across ten stochastic generations

In principle, the change in adsorption of phosphorus species due to compaction could be incorporated into the network model by using an internal surface area interaction term. The calculated mean internal surface areas of the compacted and uncompacted Pore-Cor unit cells were 8587 m^2 m^{-3} and 5799 m^2 m^{-3} respectively, giving a surface area ratio of 1 to 0.68. The simulated porosity ratio was very similar, 1 to 0.71, indicating a linear decrease in surface area with porosity on compaction. This is clearly unrealistic because the macropores collapse first [176-179], but have only a small impact on reducing the surface area. The cause of this discrepancy is attributable to having too many large pores. As discussed in Chapters 2 and 3 the geometric restrictions inhibit maximal packing efficiency and necessitate the use of the pore skew parameter. Pore-Cor with its current geometrical restrictions is therefore incapable accurately modelling the effect of compaction on the internal surface area of a sample as complex as soil. Removal of some of the geometrical simplifications will form a fundamental part of improving Pore-Cor for soils.

5.4 CONCLUSIONS

Pore-Cor predicted a decrease in saturated hydraulic conductivity on compaction but overestimated its extent. This is attributable to the oversimplified experimental methodology and the poor fit of the simulation to the raw experimental data.

Pore-Cor was insensitive to inferred changes in tortuosity and dispersivity because it ignores the tortuous nature of each individual network element. The modification of the tortuosity algorithm to include these factors would improve accuracy of the tortuosity prediction of the model.

The geometrical constraints of the model distort the simulated structure. Simulated structures have too many large voids. The internal surface area prediction is therefore to small and changes in surface area trends on compaction inaccurate. In order to overcome the systematic of the model it is essential that some of the geometrical simplicities be removed. The simple geometry discussed in section 1.2.4 is less suited to soil than simpler materials such as sandstone.

CHAPTER 6

NERC DIAGNOSTIC PILOT PROJECT TO INVESTIGATE THE FEASABILITY OF EXTENDING PORE-COR TO A RANGE OF TEXTURAL CLASSES

6.1 SSLRC SUPPLIED DATA

The modelling work presented this far has only been applied to the analysis of Crediton series soils. However for the model to be considered more generally useful, it must be extended to a wide variety of textural classes. With this in mind, sets of water retention data were obtained under license from the Soil Survey and Land Research Centre's comprehensive soil database under contract number 81/4103 with the aim of these data forming the basis of a pilot project. Data comprised thirteen experimental water retention curves, porosities and stone contents for ten subsoil (C or BC horizon) textures ranging from sand to clay. Experimental measurements had been carried out by the methods described in Avery and Bascombe [188].

6.2 TRANSFORMATION OF DATA SETS AND ASSESSMENT OF DATA QUALITY

CONVERSION OF FINE EARTH VALUES TO WHOLE SAMPLE VALUES

To model the whole sample it was necessary to take account for volume of stones in each sample and scale the given fine earth values accordingly. The porosities of samples containing stones were lowered. Most samples had a low stone content (typically <4 % (v/v)) and the scaling effects were therefore not significant.

ASSESSMENT OF THE AVAILABILITY AND QUALITY OF EXPERIMENTAL DATA

Ideally each data set within a textural class should comprise a representative set of soil series. However the supply database is not sufficiently large to meet these requirements, and data had to be used as available.

Measurement of volumetric water content is problematic at low applied suction, mainly because of pre-drainage by gravity. However, in order to model the data by the method described later, it is essential that the water retention curve extrapolates at low pressures towards a complete saturation value which equals the total porosity value for the soil. A significant proportion (>40%) of water retention curves do not meet this requirement.

Large variations in volumetric water content measurements at low tension (negative pressure) are shown strikingly by the sand water retention curves, Figure 6.1. Variation within the textural class as a whole is large and can also be large within a series. Shirrel Heath shows this intra-class variability for sands.

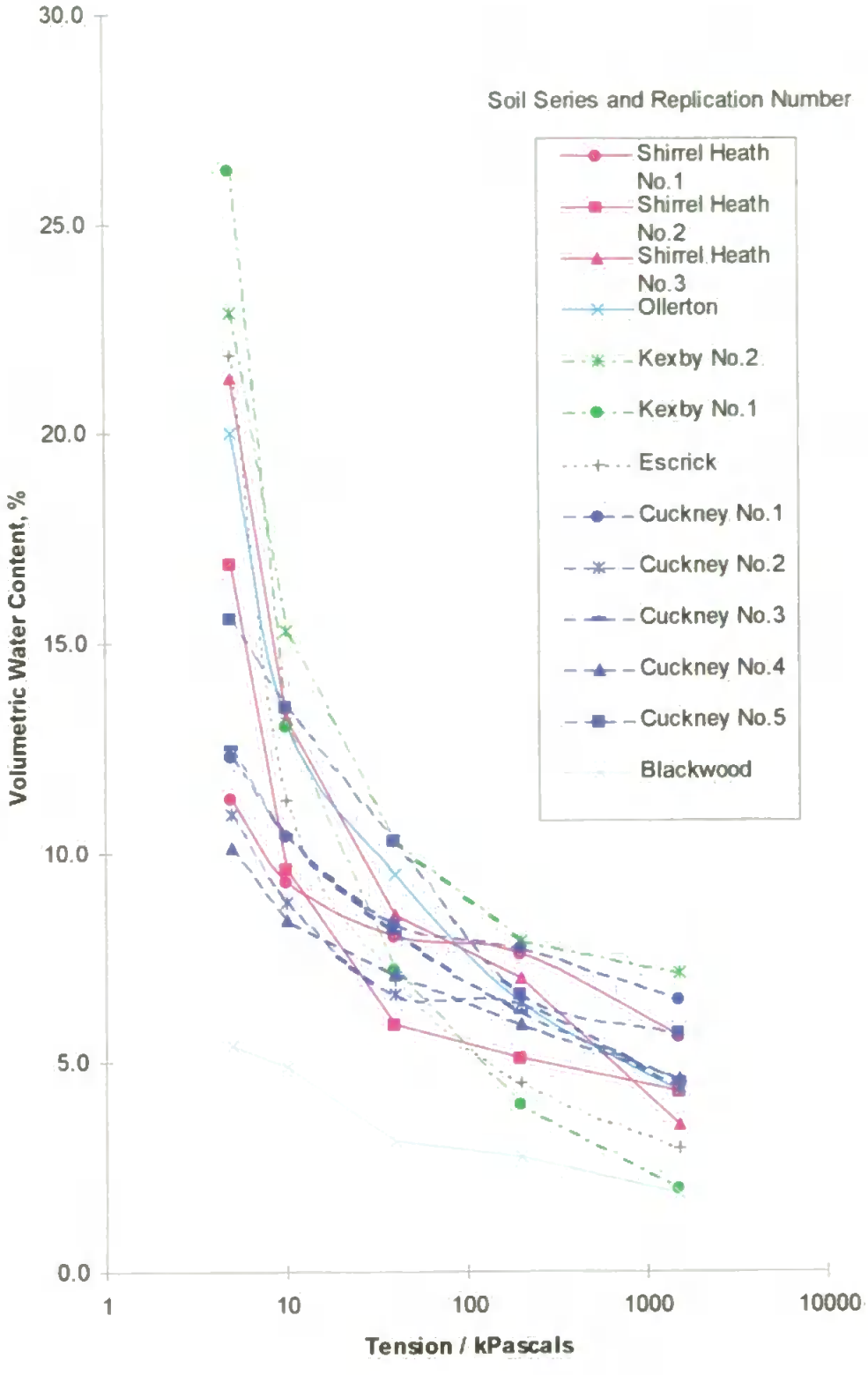

Figure 6.1: Water retention curves for the sand SSLRC data set.

A water retention model proposed by Kosugi [29] is suitable for testing the shape of water retention curves because it describes the shape of curves in terms of an air entry pressure ψ_c, a point of inflexion ψ_o and the second moment of the lognormal pore size distribution σ. The other model parameters are θ_s and θ_r, the saturated water and the residual water contents respectively. The model was used to test the shape of all of the supplied curves by a partial least squares fitting method.

Extrapolating water retention curves of the coarse textured soils to saturation is problematic because the experimental water content at 5 kPa is much less than the saturated water content. Consequently, lognormal Kosugi fitted parameter solutions to these curves are not always unique, Figure 6.2, and the model had to be modified to search for other solutions.

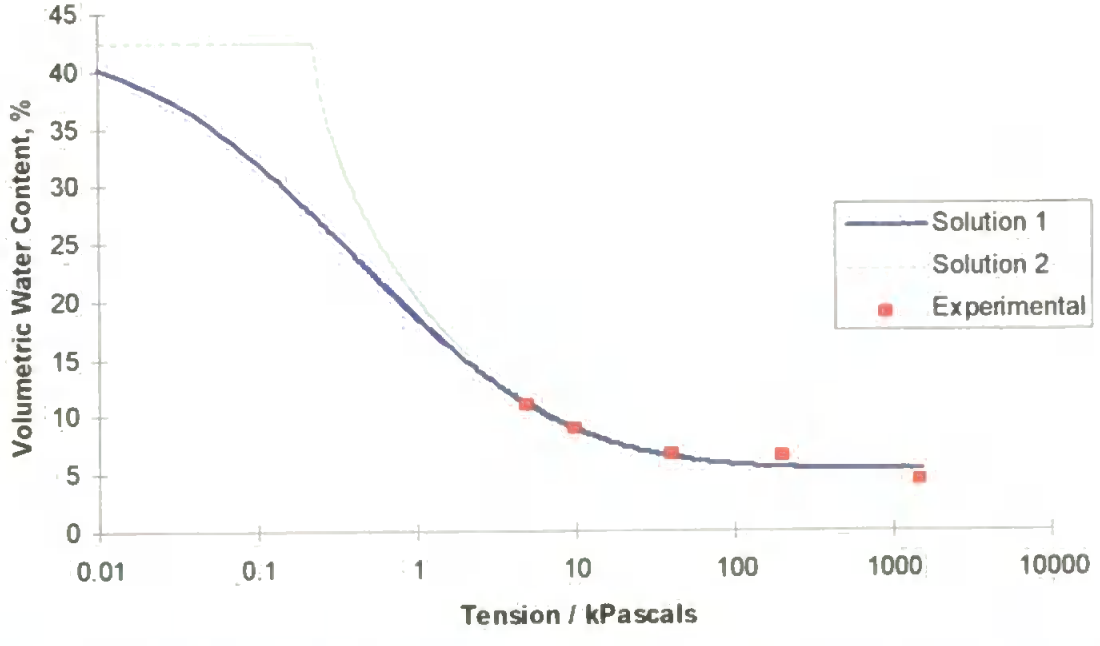

Figure 6.2: Different possible lognormal Kosugi extrapolations of Cuckney sand soil data. Solution 1, ψ_c = -1 Pascal, ψ_o= -2Pascals, σ = 2.451 and θr = 5.3 %. Solution 2. , ψ_c = -220 Pascals, ψ_o= -222 Pascals, σ = 2.32 and θ_r = 5.4 %. Value of θ_s was 42.4 % for both solutions.

Fitting finely textured soils is more straightforward because the experimental data cover more of water retention curve and require less extrapolation. Examples of accepted (Evesham No.5) and rejected (Evesham No.2) clay curves are given in Figure 6.3. The total porosity of both of these samples is 49.9%. The Evesham 2 curve clearly does not head toward the porosity asymptote at low applied pressures whereas Evesham 5 does. The incorrectness of the Evesham 2 curve is confirmed by erroneous near zero values (-1 Pascal, which was used as an upper boundary because the function is ill behaved at values of zero) of Ψ_c and Ψ_o, in contrast to corresponding values for Evesham 5 of -0.20 and -10.26 kPascals respectively.

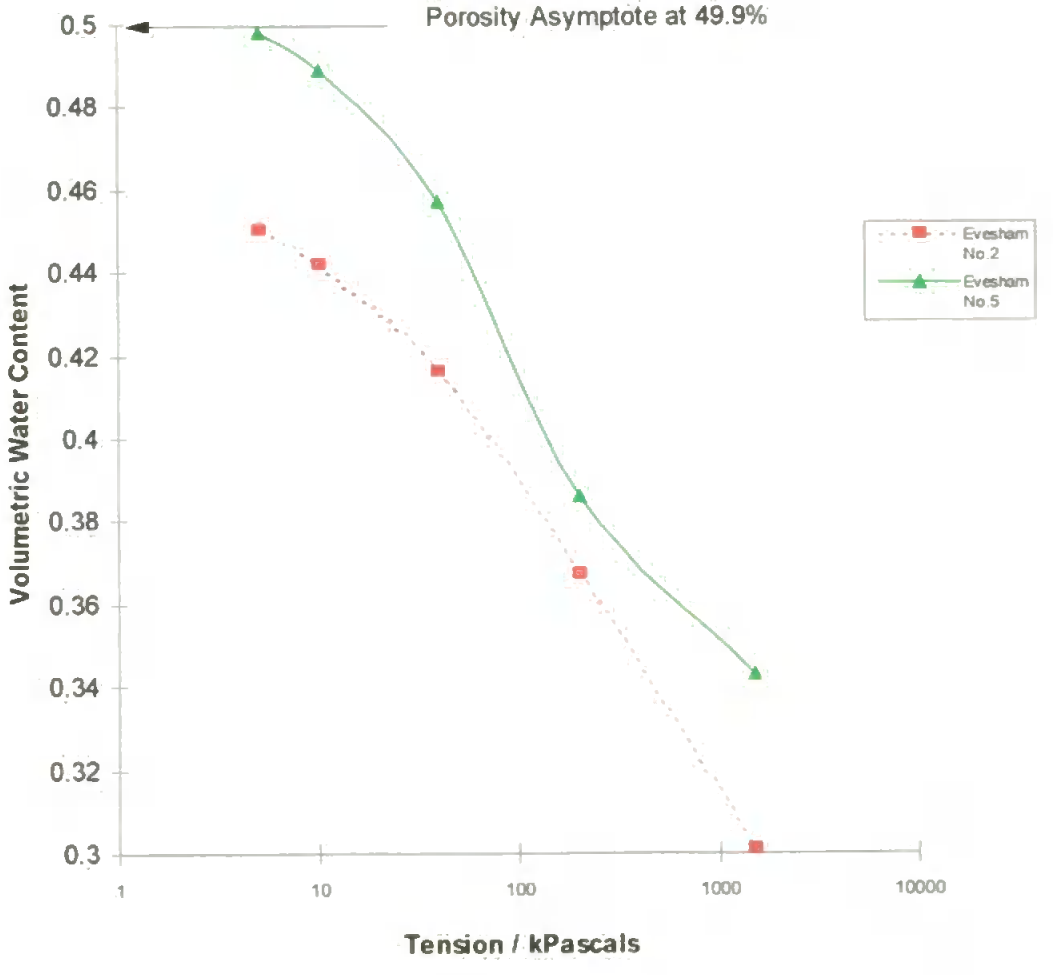

Figure 6.3: Examples of acceptable and unacceptable Evesham data

6.1.2 Producing Averaged Water Retention Curves Across Textural Classes

Water retention curves have normally been used to represent a particular textural class by averaging all the curves within that class [225]. However, for modelling purposes, better water retention curves result from averaging only those curves which can be extrapolated to the correct shape. Such averaged curves are shown in figure 6.4 along with their accompanying fitted Kosugi lognormal curves. The average clay loam curve is anomalous, possibly because only three of the thirteen curves in this textural class were of acceptable shape.

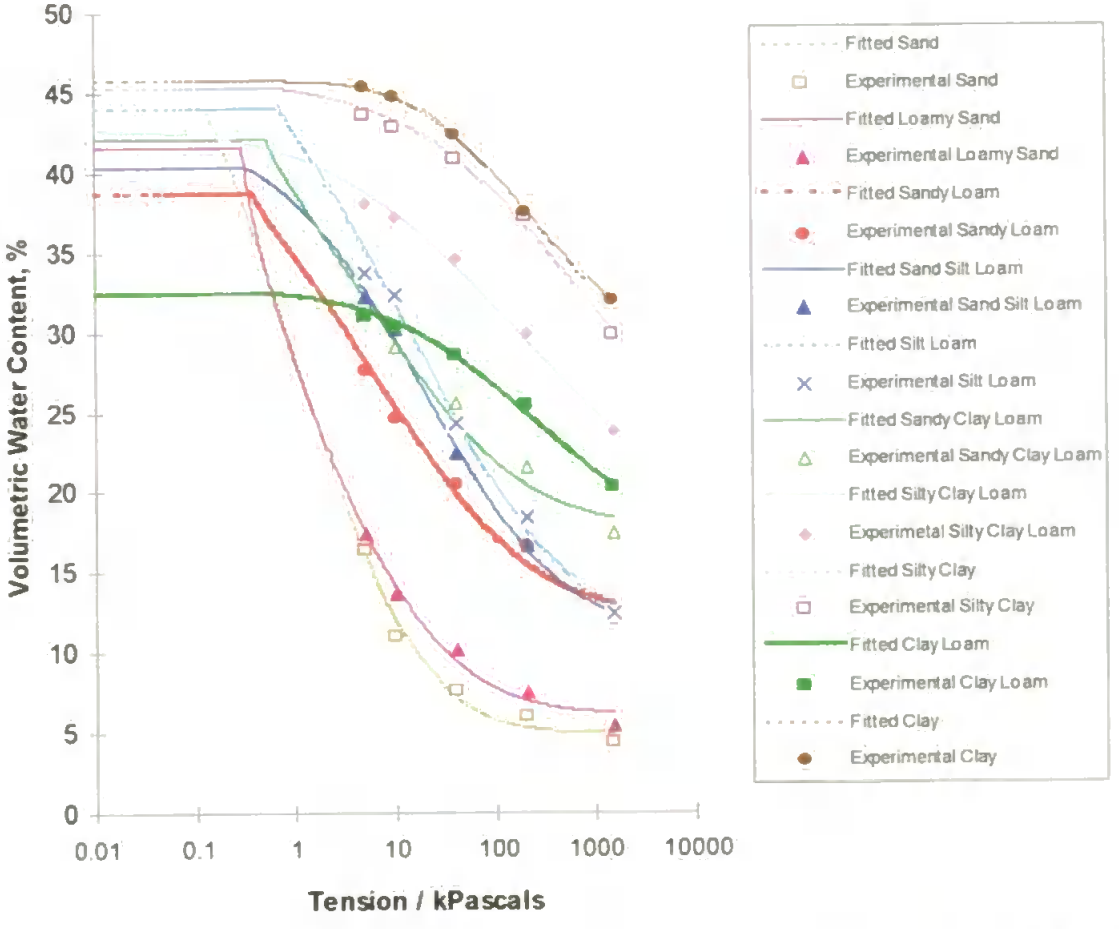

Figure 6.4: Average of accepted water retention data and corresponding lognormal Kosugi extrapolations

6.2.2 GENERATION OF THREE DIMENSIONAL SOIL VOID STRUCTURE

The Pore-Cor model described in Chapter 2 was used to fit the accepted extrapolated water retention curves for sand, sandy clay loam and clay. As mentioned earlier in Chapter 2, each network is generated such that the percolation characteristics of the network fit the experimentally derived drainage curve as closely as possible [226]. The percolation algorithm on which the model generation is based assumes that the experimental data arise from the drainage of a complete network. In practice it is not possible to model the complete range of pore sizes found in soil as they span more than seven orders of magnitude. Current geometric restrictions on the model and mathematical restrictions within the permeability algorithm make it necessary to constrain the range of pore sizes modelled. We have therefore assumed that all pores < 1 μm diameter are non conducting. It is also necessary to assume that pores larger than 2500 μm are isolated in the experimental samples and do not contribute significantly to the modelled effects. Water retention curves, and corresponding air intrusion curves and porosities, are normalised onto a scale of 0 - 100%, representing the modelled void space between these two cut-off points. This approach to truncation has to differ from that of Chapter 2 because in finer soils such as clay, the residual water content (typically 22.5% for clay) exceeds 68.8% of the total porosity modelled in Section 2.2.2 of the sample making this approach impossible.

The simulated void network is fitted to the experimental water retention curve by finding the optimum values of the network connectivity, and pore and throat size distributions (the latter being parameterised in terms of 'pore skew' and 'throat skew' respectively). The experimental and simulated curves for sand and clay are given in Figure 6.5.

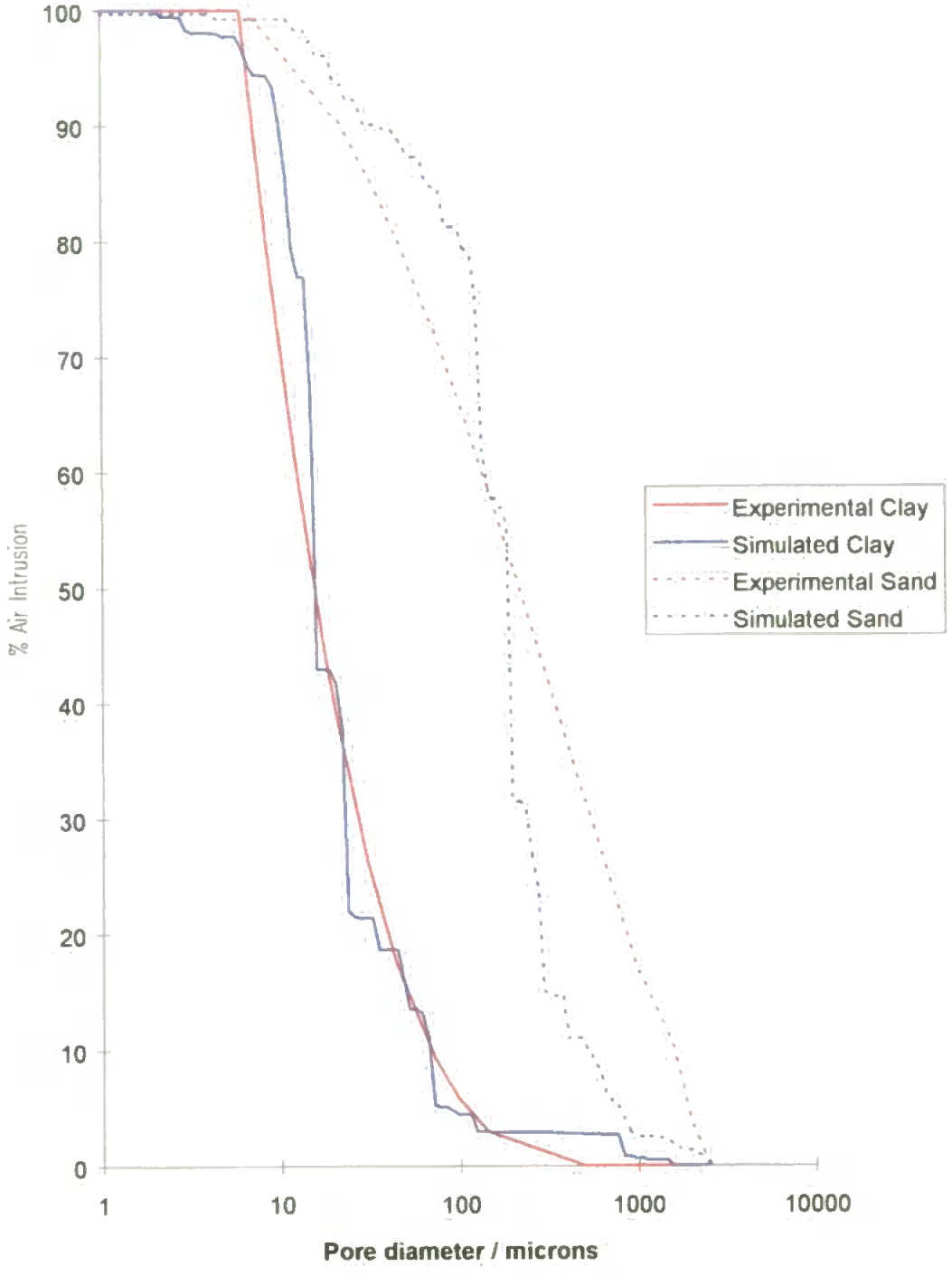

Figure 6.5: Experimental and simulated sand and clay water retention curves

The outer layers of the unit cells of the sand and clay model are shown in Figures 6.6 and 6.8, and the model of the intermediate case, sandy clay loam, in Figure 6.7. The advantage of basing the model on a real visualised geometry, rather than a purely mathematical network, is that the model can be verified or refined by image analysis or electron microscopy of experimental samples as exemplified in Chapter 3.

Figure 6.6: Simulated Clay Structure. Normalised porosity 4.03%. Unit cell length is 3.240 cm. Small scale bar is the pore row spacing of 3240 μm.

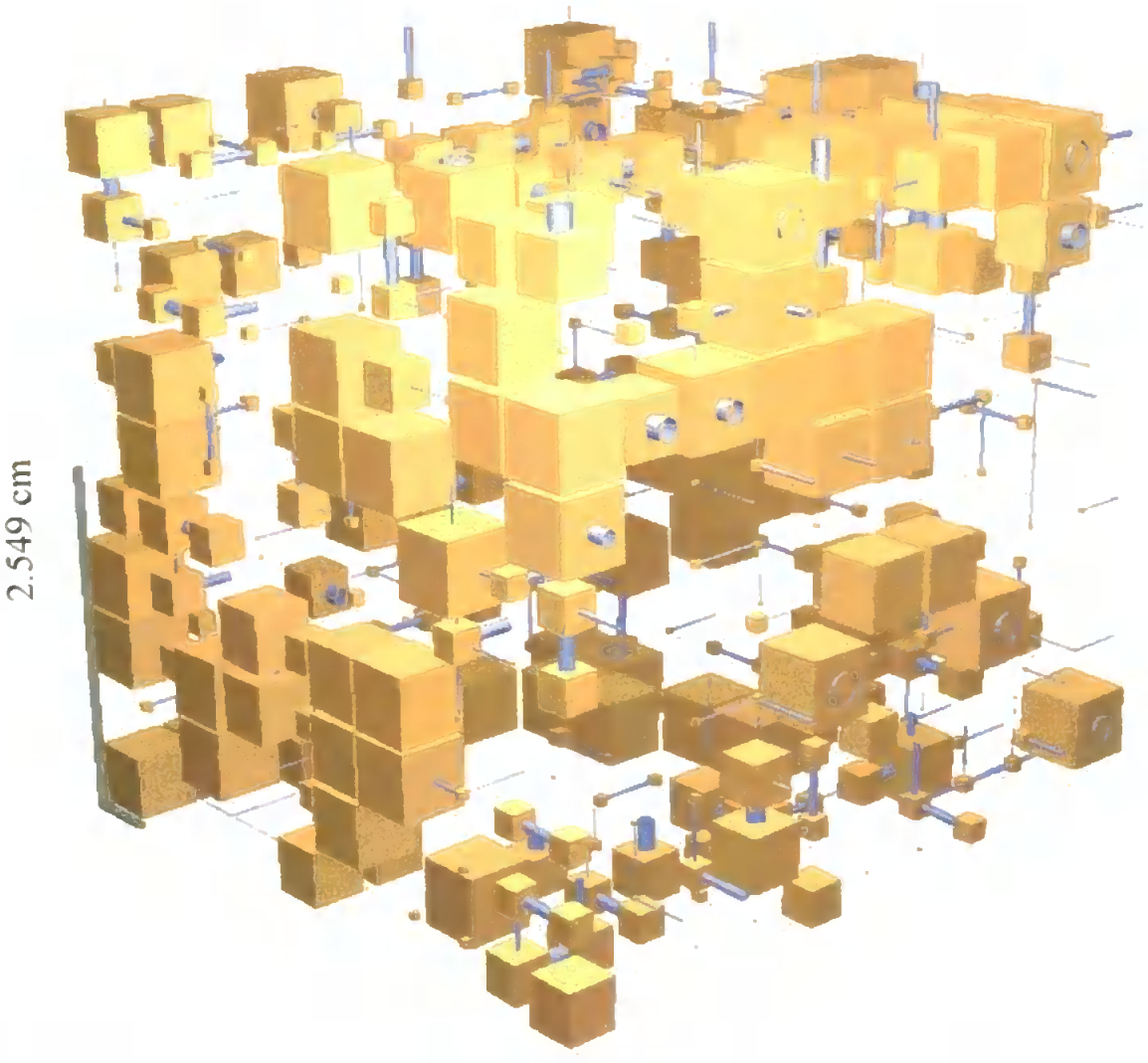

Figure 6.7: Simulated Sandy Clay Loam. Normalised porosity 18.3 %. Unit cell length is 2.549 cm. Small scale bar is the pore row spacing of 2549 μm

Looking back to Figure 6.5, it can be seen that the simulated curves for sand fit the experimental data less well than clay. The root cause of the discrepancy is that the geometric limitations on the model's unit cell, evident in Figures 6.6 to 6.8. Each unit cell contains only 1000 pores and up to 3000 throats, and the efficiency of packing of these pores and throats (and hence simulated porosity) is limited by the current restriction that all pores and throats are sited in equally-spaced Cartesian planes.

Figure 6.8: Simulated Sand. Normalised porosity 37.4%. Unit cell length is 2.538 cm. Small scale bar is the pore row spacing of 2538 μm

6.1.4 CALCULATION OF SIMULATED PROPERTIES BASED ON THE VOID STRUCTURES

From the network of pores and throats, it is possible to calculate the permeability using a Dinic operation research algorithm [44]. (The re-programming of this substantial algorithm to accept a very wide range of flow capacities formed a significant part of this pilot project.) Table 6.1 lists the Pore Cor model parameters and their corresponding predicted and the range of typical permeabilities for each textural class. The results were averaged over 5

stochastic generations of each model structure. A higher throat skew (percentage of throats of minimum size) is necessary to fit finer textured soils as would be expected, Figure 6.9.

Textural Class	Normalised Porosity %	Throat Skew %	Pore Skew	Connectivity	Typical Permeability range milliDarcies	Simulated Permeability milliDarcies	Simulated Permeability after colloidal flow milliDarcies
Clay	4.03	1.52	1.5	3.2	0.0001 to 0.1	0.00427	0.00262
Sandy Clay Loam	18.03	1.2	1.3	3.3	0.1 to 1000	1.047	1.047
Sand	37.36	0.45	1.5	3.2	100 to 1000000	667	667
Compacted Sandy Clay Loam	7.74	2.04	2.8	3.9	-	0.014	

Table 6.1: Pore-Cor model output

CALCULATION SATURATED HYDRAULIC CONDUCTIVITIES

The simulated water permeabilities (saturated hydraulic conductivities) lie within the typical range for each class. This agreement is very encouraging when compared with pedo transfer functions in current use, which can be wrong by up to three orders of magnitude, and give no structural information [12]. In Chapter 2 it was shown that Pore-Cor can predict an experimental change in permeability with below-surface depth to a high degree of accuracy ($R^2 = 0.99$) [226].

CALCULATION OF HYDRODYNAMIC DISPERSION COEFFICIENT

The dispersion coefficient of the network can be calculated indirectly from the tortuosity. As mentioned in Chapter 1 tortuosity is defined as the actual random-walk distance of a particle as it passes from the top to the bottom of the unit cell, relative to the actual straight-line distance from top to bottom. 100 random walks are simulated, and the median

clay were 2.95, 5.30 and 5.90 respectively, implying solutes have a less tortuous path travelling through sands than clays.

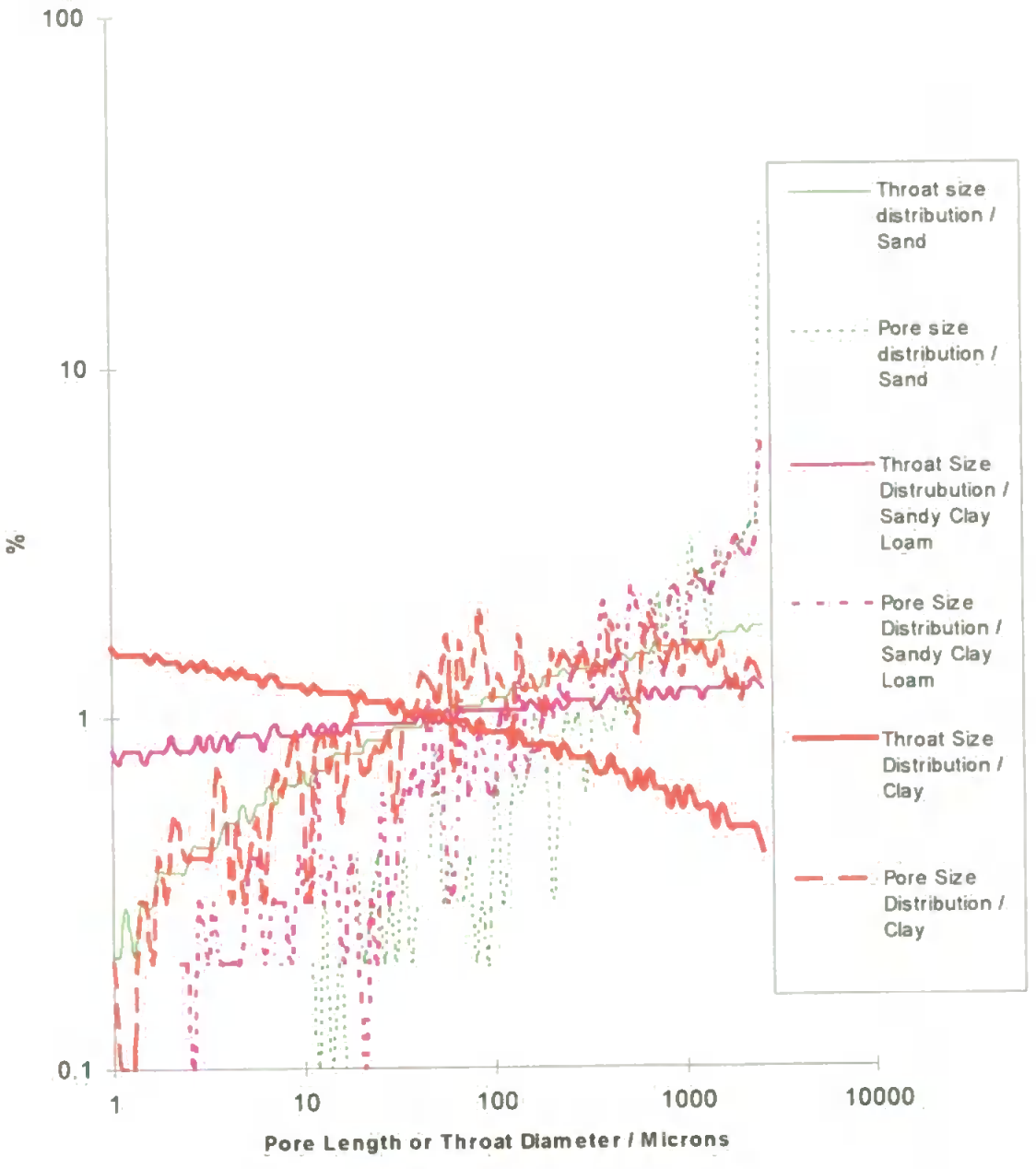

Figure 6.9: Generated pore and throat size distributions of single stochastic generations

Colloidal flow simulation is possible by blocking off all of the apertures in the network which are less than a default size [227]. When apertures < 5 microns were blocked, sand and sandy clay loam permeabilities were unaffected because of the relatively larger voids in their structures (Figure 6.9). By contrast, the permeability of the clay was approximately halved, Table 6.1.

Figure 6.10: Compacted Sandy Clay Loam. Normalised porosity 7.74 %.

In the absence of real compaction data, lognormal Kosugi parameters were adjusted to simulate a collapse of the macropore structure. As mentioned in section 1.5, the air entry values of a water retention model increase on compaction and the porosity falls. The values of ψ_0 and ψ_c were increased from by 1000 Pascals to tensions of 1518 and 1600 respectively, θ_s was decreased by 10% to 32% and the remaining parameters were left unchanged. Pore Cor was then used to fit the curve generated Pore Cor models the compaction effect by proportionally reducing the number of large pores and throats in the system as shown in Figure 6.11.

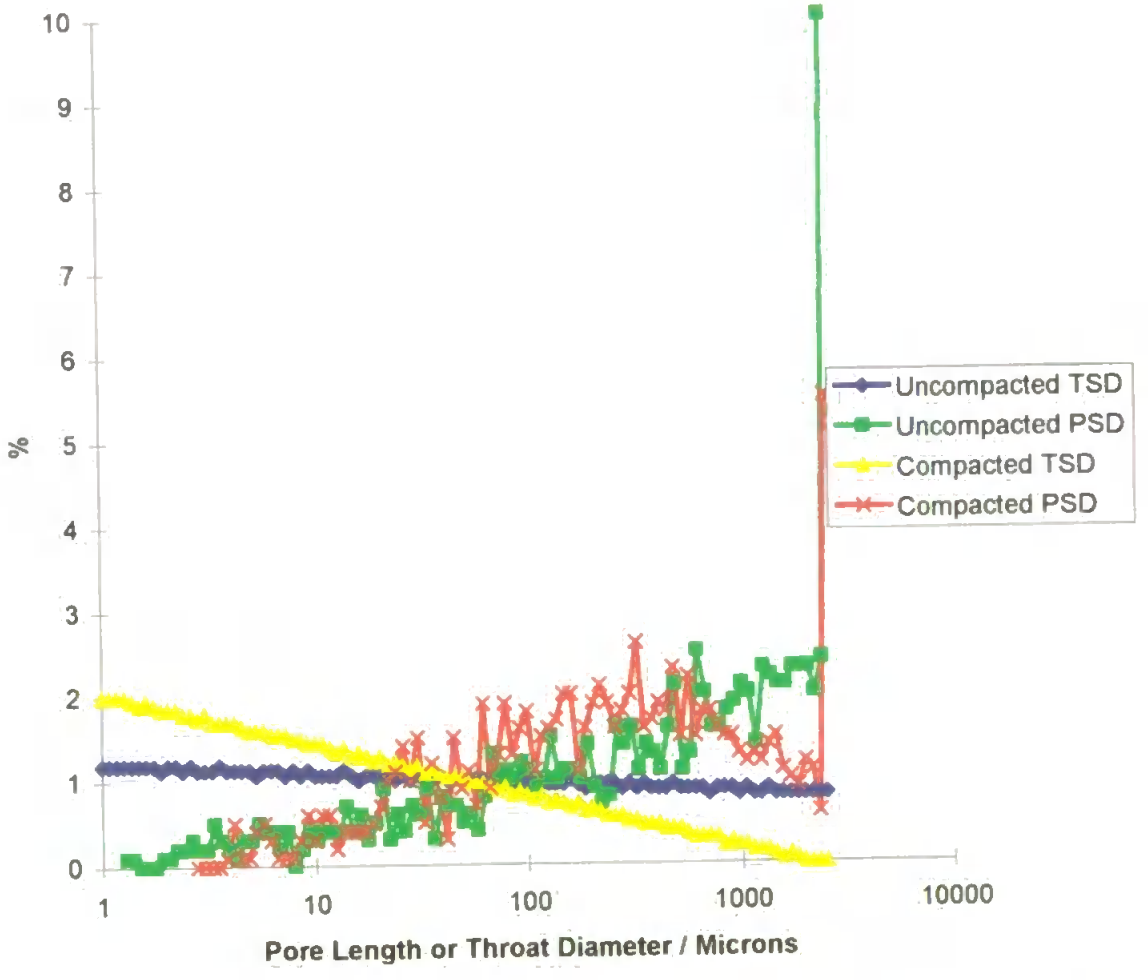

Figure 6.11: Effect of compaction on the pore and throat size distributions of a sandy clay loam.

The predicted permeability dropped from 1.047 to 0.014 milliDarcies and the tortuosity remained at 5.30. The effect of changes in porosity on permeability in the context of concurrent changes in other characteristics, can be inferred by inspection of Table 6.1. The unit cell size on compaction was unchanged due to the bulking up of pores via the pore skew parameter giving similar pore row spacings for both.

It is encouraging that the observed trends in the output of the Pore-Cor model are repeated (a lowering of permeability and no change in tortuosity.) The use water retention data makes the method more generally applicable than the one used in Chapter 5 because it can operate on intact samples.

CHAPTER 7

CONCLUSIONS AND FUTURE WORK

7.1 OVERALL CONCLUSIONS

The work carried out in this thesis has applied the Pore-Cor model to soils. The extension of the model's input data to the modelling of water retention via the use of water retention models is a major improvement and extends the model's capabilities for the first time beyond mercury porosimetry input data. The extension of the model into the modelling of water retention has two main advantages over mercury porosimetry. Firstly, intact samples can be studied and secondly the size of sample which may be used is much larger.

The transformation of the Dinic network operator from integer to real number arithmetic makes the model more suitable for porous media which have a vast range of pore sizes, which is particularly important for the prediction of the flow characteristics of soil. The model calibrated on various water retention curves reflects accurately trends in saturated hydraulic conductivity. The absolute values predicted are too small, which is a common characteristic of networks that are too small.

Image analysis of UV impregnated blocks of soil has shown that the Pore-Cor geometry is a distortion of the real experimental sample. The cause of the distortion is the restrictive nature of the Pore-Cor unit cell which inhibits the packing efficiency of the model when a wide distribution of pore sizes is used. The lack of packing efficiency is compensated by the pore skew parameter which is used to match the porosity of the sample, but this bulks up pore and therefore the network contains too many large features. The model is also

limited to 100 throat sizes which is insufficient to model the range of sizes found in real soil samples.

The development of the FI techniques for the determination of phosphorus provides a rapid (potentially field deployable) method of monitoring breakthrough curves and is a useful aid to research in itself. The DRP method with its use of wide i.d. tubing, low detection limit (2.9 μgl^{-1}), wide linear range (3-1000 μgl^{-1}) and high tolerance to Si(IV) interference (up to 10 mg l^{-1}) is ideal for the determination of RP and DRP in soil runoff and leachate waters. Further, the sample throughput of 80 samples h^{-1} makes the monitoring of rapidly occurring events straightforward. The TDP manifold described has a higher detection limit of 7 $\mu g\ l^{-1}$, which is still sufficiently sensitive for most soil analyses, and a wider linear range (7-1500 mgl^{-1}). The tolerance to Si(IV) interference was excellent (see Table 4.2). The low pH chemistry used in the TDP method overcame many of the metal-complex type interferences that were associated with earlier FI methods, making it more suitable to the analysis of soil waters. The method is sufficiently rapid (40 samples h^{-1}) to be useful in monitoring dynamic systems.

The Pore-Cor model predicted a drop in permeability on compaction, but overestimated its extent. The model was insensitive to changes in dispersivity because of the over simplicity of the tortuosity algorithm and therefore no structural interpretation of the bromide breakthrough curves was possible. The internal surface area calculation was rendered inaccurate by the model's simplified geometry and hence the change in adsorption of the phosphorus species could not be given structural interpretation. Nevertheless the Pore-Cor model makes a promising start on what is an awesomely complex problem. It is currently limited by its inherent over simplicity and will need to be modified to be made more generally useful is porous media which are as complex as soil are to be studied in more detail.

7.2 FUTURE WORK

MODIFICATION OF THE PORE-COR GEOMETRY

Clearly some of the simplifications in the Pore-Cor geometry must be removed if the model is to be useful for the prediction of more complex properties. The primary distortion of the network is caused by the inefficient packing of the Pore-Cor geometry. The only other way to for the simulation to match the experimental porosity with the current geometrical constraints is via the use of the pore skew parameter. Other geometries would also achieve this as follows:

i. the merging of neighbouring pores. This is geometrically simple, but the merged pore has an unrealistically high co-ordination number

ii. creating a fractal structure using a Pore-Cor unit cell mounted in the larger pores of an order-of-magnitude larger unit cell. This is most valid for fractal solids - papers and hygiene products are generally not fractal over a larger enough size range for this idea to be applicable

iii. using a bulged throat geometry, as shown in Figure 6.11. This has the advantage that the percolation, permeability and tortuosity characteristics of the throat are calculable (with difficulty), and an aspect ratio is introduced to reflect the nature of anisotropic samples.

These various solutions will have to be worked on mathematically and reviewed, but the most likely solution is (iii) with a partial aspect of (i). The enlargement of the unit cell would also produce more stable network solutions.

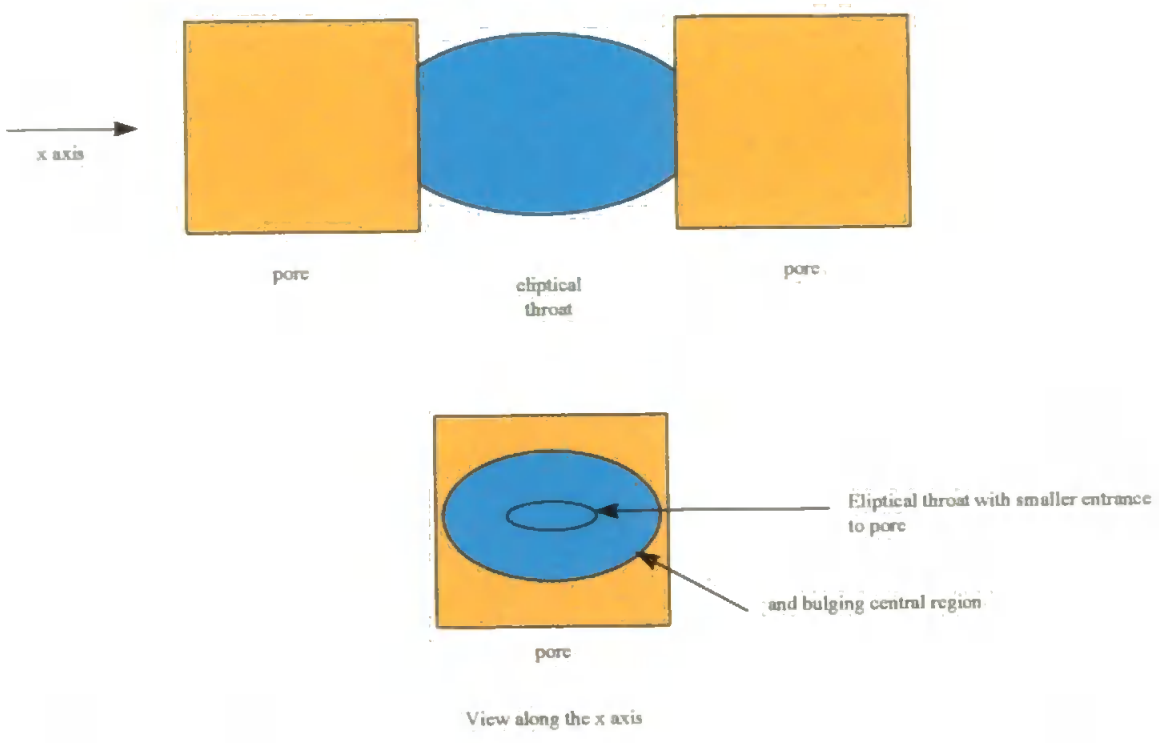

Figure 7.1: Possible modification of the Pore-Cor geometry to accommodate ellipsoid throats.1

A decrease in the distortion of the network would improve the prediction of flow characteristics and internal surface area.

When the geometry of the Pore-Cor unit cell has been modified preferential flow and adsorption network operators (with isotherms for each species) could then be incorporated to enhance the model's predictive capabilities beyond unreactive tracer movement. The network operator for reactive solutes which would be based on an improved internal surface area prediction could also include information about important clay minerals.

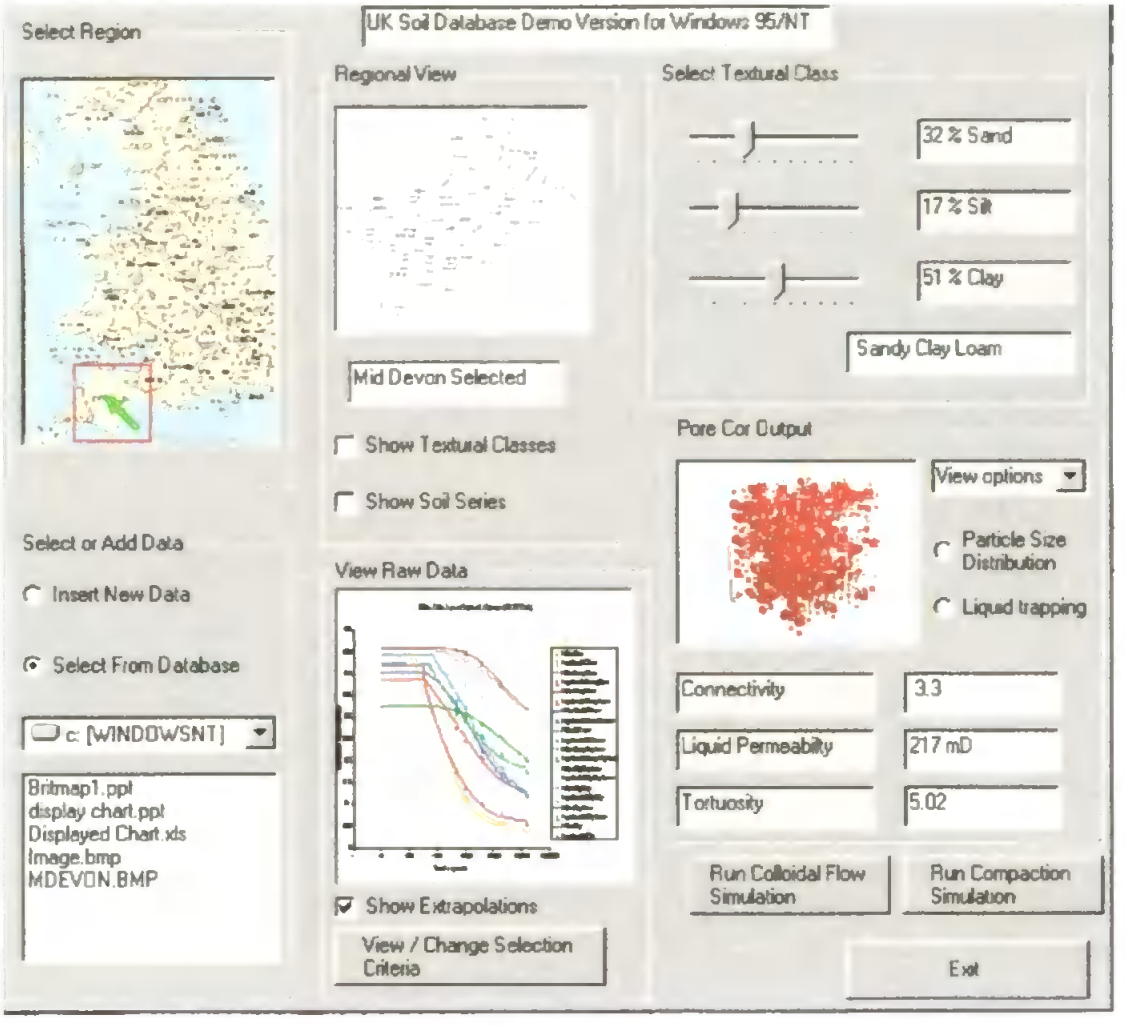

Figure 7.2 : Pilot UK soils database for use in a desktop PC or client server network.

The Pore-Cor model has been used in the pilot study in Chapter 6 to simulate a limited range of soil properties from a given database. This could be extended to form part of a national or European database engine in which soil data could be taken and interpreted with the shape testing criteria and Pore-Cor modelling. This would also open the way for the incorporation into the database of nutrient information alongside relevant interpretative tools.

This information and its readily accessible format would be a useful aid to research itself and could also form the basis for the planning of monitoring schemes. The database could be added to and any gaps in it could be augmented by input of additional analytical or soil physics data.

A pilot Visual Basic database engine has been constructed, Figure 6.12 and could in future incorporate relational database / SQL (standard query language) technology to facilitate the points made earlier.

DEVELOPMENT OF ANALYTICAL TECHNIQUES

The development of the rapid speciation technique in Chapter 4 is a useful aid to monitoring breakthrough events. Application of FI techniques to field monitoring situations is essential if real environmental phenomena are to be understood. The FI techniques described in this work could be adapted for field deployment and the data collected relayed back automatically by time domain reflectometry for incorporation into the database. Miniaturisation of the systems could be achieved via the use of microconduits which is a technology directly derived from FI [79], the use of small low power pumping units and a simple LED detector system. LED based detectors are more suitable for field deployment because they are much smaller than conventional spectrophotometers.

The chemistry of a field system has to be more user independent than is necessary in a laboratory situation. Because reagents can often not be prepared freshly every day in a field situation, the question of reagent stability must be addressed. The lifetime of a tin chloride based reagent is limited to a few days at most, even when hydrazinium sulphate is used as a stabiliser, and is therefore unsuitable for many aspects of field deployment. For field work an alternative reducing reagent would have to be found. The choice of reducing

agent also affects the λ_{max} of the molybdenum blue heteropoly acid. For example tin chloride and ascorbic acid complexes have λ_{max} values of 690 and 880 nm respectively [167], a factor which is not problematic in laboratory situations because variable wavelength spectrophotometers are readily available, but must be considered when LED detectors are used.

The development of robust (both physically and chemically) field systems for P determination is critical if the research is to be extended from laboratory experiments to dynamic natural systems.

LIST OF SYMBOLS

A	area, [L^2]
C	concentration, [ML^{-3}]
C^f	concentration in the time interval between t_j and t_{j+1}, [ML^{-3}]
C^o	original concentration of undispersed zone
c	connectivity
D	dispersion coefficient, [L^2T^{-1}]
d	tube diameter, [L]
D/v	dispersivity, [L]
$f(\psi)$	capillary distribution function, [$M^{-1}L^{-1}T^{-2}$]
$f(t)$	probability density function
$f(r)$	radial distribution function, [L^{-1}]
g	acceleration due to gravity, [MLT^{-2}]
H	height, [L]
h	tension, [MLT^{-2}]
k	permeability [LT^{-1}]
j_w	water flux [M]
k'	rate constant, [$M^nL^nT^n$]
L	length of FI tube, [L]
l	length [L]
M	mass, [M]
m	van Genuchten fitting parameter
m_j	outflow mass, [M]

n	van Genuchten fitting parameter
p	capillary pressure, [MLT^{-2}]
$P(t)$	probability density function
Q	Pumping rate, [L^3T^{-1}]
r_{max}	maximum pore radius, [L]
r_n	radius of the n^{th} pore, [L]
S	time span between injection and observation of peak height, [T]
S_e	effective saturation
T	residence time during which an FI reaction takes place [T]
t	time [T]
dV/dt	volumetric flow rate [L^3T^{-1}]
V	volume [L^3]
W	width [L]
x	depth, [L]
Z	time dependant adsorption, [M^x,L^y,T^z]

GREEK LETTERS

α	van Genuchten fitting parameter
β	contact angle
β_n	number of tubes in z direction in the Pore Cor unit cell
γ	interfacial tension, [M^3T^{-4}]
λ	Brooks and Corey fitting parameter

μ	mean
μ_{fv}	fluid viscosity, $[ML^{-4}T^{-2}]$
θ	volumetric water content, $[L^3L^{-3}]$
θ_r	residual water content, $[L^3L^{-3}]$
θ_s	saturated water content, $[L^3L^{-3}]$
σ	standard deviation
ρ_w	density of water, $[ML^{-3}]$
ψ	applied pressure, $[MLT^{-2}]$
ψ_c	air entry or bubbling pressure, $[MLT^{-2}]$
ψ_o	pressure at the mode of a lognormal capillary distribution, $[MLT^{-2}]$
Ω	network operator

ABBREVIATIONS USED

APHP	alkaline phosphatase hydrolysable phosphorus
ANOVA	analysis of variance
BAP	bioavailable phosphorus
BBSRC	biotechnology and biological sciences research council
CDE	convection-dispersion equation
DCP	dissolved condensed phosphorus
DIP	dissolved inorganic phosphorus
DLL	dynamic link library
DOP	dissolved organic phosphorus
DRN	dummy random number
DRP	dissolved reactive phosphorus
DTE	data terminal equipment
ECD	equivalent circle diameter
FI	flow injection
HMWP	high molecular weight phosphorus
LED	light emitting diode
MCP	monocalcium phosphate
NERC	Natural Environment Research Council
OLE	object linking and embedding
P	phosphorus
PP	particulate phosphorus
PDF	probability density function

PO_4-P	phosphorus as orthophosphate
PEG	polyethylene glycol
PP	particulate phosphorus
RHMWP	reactive high molecular weight phosphorus
RP	reactive phosphorus
REV	representative elementary volume
SBSR	single bead string reactor
SQL	standard query language
SSLRC	Soil Survey and Land Research Center
TDP	total dissolved phosphorus
TP	total phosphorus
TRP	total reactive phosphorus
TSP	triple super phosphate
UV	ultra violet

8.0 REFERENCES

1. Golterman, H.L. Physical Limnology. Elsevier Scientific Publishing, Amsterdam. (1975) p. 32.

2. Holtan, H., Kamp-Nielsen, L. and Stuanes, A.O. *Hydrobiologia.* **170,** (1988) p. 19.

3. Wild, A. Russell's Soil Conditions and Plant Growth. Wild, A. (Ed.) Longman Group Ltd, Harlow. (1988) p. 12.

4. White, R.E. Introduction to the Principles and Practice of Soil Science. Blackwell Scientific Publications, London. (1987) p. 192.

5. Pierrou, U. *Ecological Bulletins.* **22,** (1976) p. 75.

6. Tisdale, S.L., Nelson, W.L. and Beaton, J.D. Soil Fertililty and Fertilisers. Macmillan Publishing Company, New York. (1985) p. 227.

7. Jones III, E.D. Environmental Phosphorus Handbook. Griffith, E.J., Beeton, A., Spencer, J.M., and Mitchell, D.T. (Eds.) Wiley-Interscience, New York. (1974) p. 669.

8. Beeton, A.M. *Limnology and Oceanography.* **10,** (1965) p. 240.

9. Beeton, A.M. Changes in the environment and biota of the Great Lakes. *in Eutrophication: Causes, Consequences and Correctives.* Rolich, G.A. (Ed.) National Academy of Sciences, Washington DC. (1969) p. 150.

10. Stumm, W. and Morgan, J. Aquatic Chemistry. John Wiley and Sons, NY. (1981) p. 780.

11. Harper, D. Eutrophication of Freshwaters : principles, problems and restoration. Chapman and Hall, London. (1995) p. 164.

12. Tietje, O. and Hennings, V. *Geoderma.* **69,** (1996) p. 71.

13. Chen, C., Thomas, D.M., Green, R.E. and Wagenet, R.J. *Soil Science Society of America Journal.* **57,** (1993) p. 680.

14. Rawls, W.J. and Brakensiek, D.L. *Journal of Soil and Water Conservation.* **50,** (1995) p. 463.

15. Rawls, W.J., Brakensiek, D.L. and Logsdon, S.D. *Soil Science Society of America Journal.* **57,** (1993) p. 1193.

16. Tyler, S.W. and Wheatcraft, S.W. *Water Resources Research.* **26,** (1990) p. 1047.

17. Brooks, R.H. and Corey, A.T. *Hydrological papers. 3,Civil EngDep. ,Colo. State Univ. , Fort Collins.* (1964) p. 1.

18. Campbell, G.S. *Soil Science.* **117,** (1974) p. 311.

19. Burdine, N.T. *Petroleum Transactions AIME.* **198,** (1953) p. 71.

20. Mualem, Y. *Water Resources Research.* **12,** (1976) p. 513.

21. Chu, S.T. *Transactions of the Asae.* **37,** (1994) p. 1205.

22. Golabi, M.H., Radcliffe, D.E., Hargrove, W.L. and Tollner, E.W. *Journal of Soil and Water Conservation.* **50,** (1995) p. 205.

23. Washburn, E.W. *Proceedings of the National Academy of Science U. S. A.* **7,** (1921) p. 115.

24. Mason, G. and Morrow, N.R. *Journal of Colloid and Interface Science.* **168,** (1994) p. 130.

25. Tsakiroglou, C.D. and Payatakes, A.C. *Journal of Colloid and Interface Science.* **159,** (1993) p. 287.

26. Archie, G.E. *Bulletin of the American Association of Petroleum Geology.* **36,** (1952) p. 278.

27. Cousin, I., Levitz, P. and Bruand, A. *European Journal of Soil Science.* **47,** (1996) p. 439.

28. Garboczi, E.J. *Cement and Concrete Research.* **20,** (1990) p. 591.

29. Kosugi, K. *Water Resources Research.* **30,** (1994) p. 891.

30. van Genuchten, M.T. *Soil Science Society of America Journal.* **44,** (1980) p. 892.

31. Perrier, E., Mullon, C., Rieu, M. and Demarsily, G. *Water Resources Research.* **31,** (1996) p. 2927.

32. Celia, M.A., Reeves, P.C. and Ferrand, L.A. *Reviews of Geophysics.* **33,** (1995) p. 1049.

33. Tsakiroglou, C.D. and Payatakes, A.C. *Journal of Colloid and Interface Science.* **137,** (1990) p. 315.

34. Tsakiroglou, C.D. and Payatakes, A.C. Characterization of Porous solids II.Rodriguez-Reinoso, F. (Ed.) Elsevier Science Publishers B.V. Amsterdam. (1991) p. 169.

35. Tsakiroglou, C.D. and Payatakes, A.C. *Journal of Colloid and Interface Science.* **146,** (1992) p. 479.

36. Rajaram, H., Ferrand, L.A. and Celia, M.A. *Water Resources Research.* **33,** (1997) p. 43.

37. Lowry, M.I. and Miller, C.T. *Water Resources Research.* **31,** (1995) p. 455.

38. Matthews, G.P., Moss, A.K. and Ridgway, C.J. *Powder Technology.* **83,** (1995) p. 61.

39. Matthews, G.P., Ridgway, C.J. and Spearing, M.C. *Journal of Colloid and Interface Science.* **171,** (1995) p. 8.

40. Gane, P.A.C., Kettle, J.P., Matthews, G.P. and Ridgway, C.J. *Industrial and Engineering Chemistry Research.* **35,** (1995) p. 1753.

41. Mualem, Y. Indirect methods for estimating the hydraulic properties of unsaturated soils. Van Genuchten, M.T. (Ed.) Salinity Laboratory, Riverside, CA. (1992) p. 15.

42. Moscou, L. and Lub, S. *Powder Technology.* **29,** (1981) p. 45.

43. Haines, W.B. *Journal of Agricultural Science.* **17,** (1927) p. 264.

44. Whittaker. Operational Research on the Micro. (1984) p. 43.

45. Matthews, G.P., Moss, A.K., Spearing, M.C. and Voland, F. *Powder Technology.* **76,** (1993) p. 95.

46. Crawford, J.W., Matsui, N. and Young, I.M. *European Journal of Soil Science.* **46,** (1995) p. 369.

47. Spearing, M.C. and Matthews, G.P. *Transport In Porous Media.* **6,** (1991) p. 71.

48. Lensie, D., Elliott, L., Ingham, D.B., Clennell, B. and Knipe, R.J. *International Journal of Rock Mechanics and Mining Sciences & Geomechanics Abstracts.* **34,** (1997) p. 741.

49. Bryant, S. and Blunt, M. *Physical Review A.* **46,** (1992) p. 2004.

50. Koppi, A.J., Douglas, J.T. and Moran, C.J. *Journal of Soil Science.* **43,** (1992) p. 15.

51. Singh, P., Kanwar, R.S. and Thompson, M.L. *Soil Science Society of America Journal.* **55,** (1991) p. 1674.

52. Walker, P.J.C. and Trudgill, S.T. *Earth Surface Prossesses and Landforms.* **8,** (1983) p. 465.

53. Ghodrati, M. and Jury, W.A. *Soil Science Society of America Journal.* **54,** (1990) p. 1558.

54. Edwards, W.M., Norton, L.D. and Redmond, C.E. *Soil Science Society of America Journal.* **52,** (1988) p. 483.

55. Avery, B.W., Bascomb, C.L., Bullock, P.J., Smith, P.D. and Thomasson, A.J. Laboratory Methods. *in Technical Monograph No. 6.* Avery, B., W. and Bascomb, C., L. (Eds.) Harpenden, (1974) p. 7.

56. Murphy, C.P. Thin section preparation of Soils and Sediments. *in Soil Survey of England and Wales.* A B Academic Publishers, Berkhamsted. (1986) p. 45.

57. Ellis, M.K. Void Volume Characterization of Paper. MSc thesis. The University of Wisconsin-Milwaukee. (1993) p. 1.

58. Thompson, M.L., Singh, P., Corak, S. and Straszheim, W.E. *Geoderma.* **53,** (1992) p. 399.

59. Coster, M. and Chermant, J.L. Precis d' Analyse d'image. Preses du CNRS, Paris. (1989) p. 53.

60. Matthews, G.P. *The microReport.* (1994) p. 1.

61. Matthews, G.P. and Spearing, M.C. *Marine and Petroleum Geology.* **9,** (1992) p. 146.

62. Sallès, J., Thovert, J.F. and Adler, P.M. Transports in Reconstructed Porous Media. Studies in Surface Science and Catalysis.Rouquerol, J., Rodriguez-Reinoso, F., Sing, K.S.W. and Unger, K.K. (Eds.) Elsevier Science B.V. (1993 May 9-12) Amsterdam. (1994) p. 211.

63. Lane, A.M. *Aiche Journal.* **37,** (1991) p. 1245.

64. Hart, B.T. *unpublished.* (1997)

65. De Hann, H., De Boer, T., Kramer, T. and Moed, J., R. *Verhandlungen Internationaler Verienung fuer Theoretische und Angewante Limnologie.* **22,** (1984) p. 876.

66. Thurman, E., M. Organic Geochemistry of Natural Waters. Martinus Nijhoff, Dordrecht, NL. (1985) p. 497.

67. Stockner, J.G., Klut, M.E. and Cochlan, W.P. *Canadian Journal of Fisheries and Aquatic Sciences.* **47,** (1990) p. 16.

68. Broberg, O. and Persson, G. *Hydrobiologia.* **170,** (1988) p. 61.

69. Armstrong, D.E. Analytical Chemistry of Phosphorus Compounds. Halmann, M. (Ed.) Wiley - Interscience, NY. (1972) p. 744.

70. Robards, K., McKelvie, I.D., Benson, R.L., Worsfold, P.J. and Blundell, N. *Analytica Chimica Acta.* **287,** (1994) p. 147.

71. Morel, F.M.M. and Hering, J.G. Principles and Applications of Aquatic Chemistry. John Wiley & Sons Inc, New York. (1993) p. 588.

72. Horne, A.J. and Goldman, C.R. Limnology. McGraw-Hill, New York. (1994) p. 576.

73. Nash, D. and Murdoch, C. *Australian Journal of Soil Research.* **35,** (1997) p. 419.

74. Horn, R., Domzal, H., Slowinskajurkiewicz, A. and Vanouwerkerk, C. *Soil & Tillage Research.* **35,** (1995) p. 23.

75. Jansson, M. *Hydrobiologia.* **170,** (1988) p. 177.

76. Miller, W.E., Greene, J.C. and Shiroyama, T. The Selenastrum Capricornutum Printz Algal Assay Bottle Test - Experimental Design, Application and Data Interpretation Protocol. USEPA, Oregon. (1978) p. EPA-600/9-78-018.

77. Bostrom, B., Persson, G. and Broberg, B. *Hydrobiologia.* **170,** (1988) p. 133.

78. Broberg, O. and Pettersson, K. *Hydrobiologia.* **170,** (1988) p. 45.

79. Murphy, J. and Riley, J. P. *Analytica Chimica Acta.* **27,** (1962) p. 1.

80. Harwood, J.E. and Hattingh, W.H. Environmental Phosphorus Handbook. Griffith, E.J., Beeton, A., Spencer, J.M., and Mitchell, D.T. (Eds.) (1974) p. 289.

81. Chaimberlain, W. and Shapiro, J. *Limnology and Oceanography.* **14,** (1969) p. 961.

82. Tarapchak, S.J. *Journal Of Environmental Quality.* **12,** (1983) p. 105.

83. Dick, W.A. and Tabatabai, M.A. *Jounrnal of Environmental Quality.* **6,** (1977) p. 82.

84. Yoshimura, K., Nawtat, S. and Kura, G. *Analyst.* **115,** (1990) p. 843.

85. Sendra, J.M., Bosque, M.C. and Capitan-Valvey, L.F. *Analusis.* **18,** (1990) p. 531.

86. Lacy, N., Christian, G.D. and Ruzicka, J. *Analytical Chemistry.* **62,** (1990) p. 1482.

87. Tabata, M. and Harada, K. *Analyst.* **117,** (1992) p. 1185.

88. Downes, M.T. *Water Research.* **12,** (1978) p. 743.

89. Johnson, K.S. and Petty, R.L. *Analytical Chemistry.* **54,** (1982) p. 1185.

90. Worsfold, P.J., Clinch, J.R. and Casey, H. *Analytica Chimica Acta.* **197,** (1987) p. 43.

91. Pedersen, K.M., Kummel, M. and Soeberg, H. *Analytica Chimica Acta.* **238,** (1990) p. 191.

92. Glazier, S.A. and Arnold, M.A. *Analytical Chemistry.* **60,** (1988) p. 2540.

93. Liu, J.H., Masuda, Y., Sekido, E., Wakida, S.I. and Hiiro, K. *Analytica Chimica Acta.* **224,** (1989) p. 145.

94. Coetzee, J.F. and Gardner, C.W. *Analytical Chemistry.* **58,** (1986) p. 608.

95. Alexander, P.W. and Koopetngarm, J. *Analytica Chimica Acta.* **197,** (1987) p. 353.

96. Davey, D.E., Mulcahy, D.E. and Oconnell, G.R. *Talanta.* **37,** (1990) p. 683.

97. Pauer, J.J., Vanvliet, H.R. and Vanstaden, J.F. *Water SA.* **14,** (1988) p. 125.

98. Freeman, P.R., McKelvie, I.D., Hart, B.T. and Cardwell, T.J. *Analytica Chimica Acta.* **234,** (1990) p. 409.

99. Johnson, K.S., Petty, R.L. and Thomsen, J. Mapping Strategies in Chemical Oceanography. ACS, Washingto DC. (1985) p. 7.

100. Motomizu, S., Wakimoto, T. and Toei, K. *Talanta.* **31,** (1983) p. 235.

101. Burns, D.T., Chimpalee, N., Chimpalee, D. and Rattanariderom, S. *Analytica Chimica Acta.* **243,** (1991) p. 187.

102. Motomizu, S. and Oshima, M. *Analyst.* **112,** (1987) p. 295.

103. Susanto, J.P., Oshima, M., Motomizu, S., Mikasa, H. and Hori, Y. *Analyst.* **120,** (1995) p. 187.

104. Ormazagonzalez, F.I. and Statham, P.J. *Analytica Chimica Acta.* **244,** (1991) p. 63.

105. Fujiwara, K., Lei, W., Shimokoshi, F., Fuwa, K. and Kobayashi, T. *Analytical Chemistry.* **54,** (1982) p. 2026.

106. Nakanishi, K., Imasaka, T. and Ishibashi, N. *Analytical Chemistry.* **57,** (1985) p. 1219.

107. Fusheng, W., Zhongxiang, W. and Enjiang, T. *Analytical Letters.* **22,** (1989) p. 3081.

108. Varma, A. Handbook of Inductively Coupled Plasma Atomic Emission Spectroscopy. CRC Press, Boca Ranton, Florida. (1992) p. 380.

109. Manzoori, J.L., Miyazaki, A. and Tao, H. *Analyst.* **115,** (1990) p. 1055.

110. Jiang, S.J. and Houk, R.S. *Spectrochimica Acta Part B-Atomic Spectroscopy.* **43,** (1988) p. 405.

111. Schubert, F., Renneberg, R., Scheller, F.W. and Kirstein, L. *Analytical Chemistry.* **56,** (1984) p. 1677.

112. Durso, E.M. and Coulet, P.R. *Analytica Chimica Acta.* **239,** (1990) p. 1.

113. Fogg, A.G. and Bsebsu, N.K. *Analyst.* **107,** (1982) p. 566.

114. Harden, S.M. and Nonidez, W.K. *Analytical Chemistry.* **56,** (1984) p. 2218.

115. Matsunaga, K., Kudo, I., Yanada, M. and Hasebe, K. *Analytica Chimica Acta.* **185,** (1986) p. 355.

116. Hight, S.C., Betpera, F. and Jaselskis, B. *Talanta.* **29,** (1982) p. 721.

117. Morgan, D.K. and Danielson, N.D. *Journal of Chromatography.* **262,** (1983) p. 265.

118. Heckenberg, A.L. and Haddad, P.R. *Journal of Chromatography.* **299,** (1984) p. 301.

119. Wetzel, R.A., Anderson, C.L., Schleicher, H. and Crook, G.D. *Analytical Chemistry.* **51,** (1979) p. 1532.

120. Kaniansky, D., Zelensky, I., Hybenova, A. and Onuska, F.I. *Analytical Chemistry.* **66,** (1994) p. 4258.

121. Bondoux, G., Jandik, P. and Jones, W.R. *Journal of Chromatography.* **602,** (1992) p. 79.

122. YAO, T., Kobayashi, N. and WASA, T. *Analytica Chimica Acta.* **238,** (1990) p. 339.

123. Male, K.B. and Luong, J.H.T. *Biosensors and Bioelectronics.* **6,** (1991) p. 581.

124. Haddad, P.R. and Jackson, P.E. Ion Chromatography-Principles and Applications. Elsevier Science Publishers BV, Amsterdam. (1990) p. 776.

125. Jones, P., Stanley, R. and Barnett, N. *Analytica Chimica Acta.* **249,** (1991) p. 539.

126. Tanaka, K. and Ishizuka, T. *Water Research.* **16,** (1982) p. 719.

127. Petterson, K. *International Revue der Gestamen Hydrobiologie.* **64,** (1979) p. 585.

128. Stevens, R.J. *Water Research.* **13,** (1979) p. 763.

129. Karl, D.M. and Tien, G. *Limnology and Oceanography.* **37,** (1992) p. 105.

130. Hori, T. and Sugiyama, M. *Analyst.* **117,** (1992) p. 893.

131. Lee, T., Barg, E. and Lal, D. *Analytica Chimica Acta.* **260,** (1992) p. 113.

132. Follmi, K.B. *Chemical Geology.* **107,** (1993) p. 375.

133. Crompton, T.R. Comprehensive Water Analysis. Elsevier Applied Science, London. (1992) p. 524.

134. Solorzano, L. and Sharp, J.H. *Limnology And Oceanography.* **25,** (1980) p. 754.

135. Cembella, A.D., Anita, N.J. and taylor, F.J.R. *Water Research.* **20,** (1986) p. 1197.

136. Aoyagi, M., Yasumasa, Y. and Nishida, A. *Analytica Chimica Acta.* **214,** (1988) p. 229.

137. Hinkamp, S. and Schwedt, G. *Analytica Chimica Acta.* **236,** (1990) p. 345.

138. Benson, R.L., McKelvie, I.D., Hart, B.T. and Hamilton, I.C. *Analytica Chimica Acta.* **291,** (1994) p. 233.

139. Armstrong, F.A. and Tibbitts, S. *Journal of the Marine Biological Association of the UK.* **48,** (1968) p. 143.

140. Henriksen, A. *Analyst.* **95,** (1970) p. 601.

141. Solorzano, L. and Strickland, J.D. *Limnology and Oceanography.* **13,** (1968) p. 515.

142. McKelvie, I.D. and Hart, B.T. *Analyst.* **114,** (1989) p. 1459.

143. Ron Vaz, M.D., Edwards, M.C., Shand, A.C. and Cresser, M.S. *Talanta.* **39,** (1992) p. 1487.

144. Downes, M.T. and Paerl, H.W. *Journal of the Fisheries Research Board of Canada.* **35,** (1978) p. 1636.

145. White, E. and Payne, G. *Canadian Journal of Fisheries and Aquatic Sciences.* **37,** (1980) p. 664.

146. McKelvie, I.D., Hart, B.T., Cardwell, T.J. and Cattrall, R.W. *Talanta.* **40,** (1993) p. 1981.

147. Clarkin, C.M., Minear, R.A., Kim, S. and Elwood, J.W. *Environmental Science and Technology.* **26,** (1992) p. 199.

148. Cembella, A.D., Anita, N.J. and harrison, P.J. *CRC Critical Reviews in Microbiology.* **10,** (1984) p. 317.

149. Chrost, R., Siuda, W. and Halemejko, G.Z. *Archiv fur Hydrobiologie.* **70,** (1984) p. 1.

150. Strickland, J.D. and Solorzano, L. Some Contemporary Studies in Marine Science. Barnes, J. (Ed.) Allen and Unwin, (1966) p. 655.

151. Chrost, R.Z., Siuda, W., Albrech, D. and Overbeck, J. *Limnology And Oceanography.* **31,** (1986) p. 622.

152. Shan, Y., McKelvie, I.D. and Hart, B.T. *Analytical Chemistry.* (1997)

153. Shan, Y., McKelvie, I.D. and Hart, B.T. *Limnology And Oceanography.* **39,** (1994) p. 1993.

154. Hino, C. *Hydrobiologia.* **174,** (1989) p. 49.

155. Feuillade, M. and Dorioz, J.M. *Water Research.* **26,** (1992) p. 1195.

156. Herbes, S.E., Allen, H.E. and Mancy, K.H. *Science.* **187,** (1975) p. 432.

157. McKelvie, I.D., Hart, B.T., Cardwell, T.J. and Cattrall, R.W. *Analytica Chimica Acta.* **316,** (1995) p. 277.

158. Golterman, H.L. *Archiv fur Hydrobiologie.* **30,** (1988) p. 1.

159. Dorich, R.A., Nelson, D.W. and Sommers, L.E. *Journal Of Environmental Quality.* **14,** (1985) p. 400.

160. Engle, D.L. and Sarnelle, O. *Limnology And Oceanography.* **35,** (1990) p. 483.

161. Sharpley, A.N. *Journal Of Environmental Quality.* **22,** (1993) p. 597.

162. Nanny, M.A. and Minear, R.A. *Abstract Papers of the Chemical Society. Div. Envrion. Chem.* **205,** (1993) p. 187.

163. Ingall, E., Duchamp, J.C. and Zilm, K.W. *Abstract Papers of the Chemical Society. Div. Envrion. Chem.* **205,** (1993) p. 187.

164. Ahern, F., Eckert, J.M., Hain, S.F., Leggett, K.E.A., Payne, N.C. and Williams, K.L. *Analytica Chimica Acta.* **199,** (1987) p. 259.

165. Andrew, K.N., Blundell, N.J., Price, D. and Worsfold, P.J. *Analytical Chemistry.* **66,** (1994) p. 916A.

166. Betteridge, D. *Analytical Chemistry.* **50,** (1978) p. 832A.

167. Ruzicka, J. *Analytical Chemistry.* **55,** (1983) p. 1041A.

168. Maugh II, T.H. *Science.* **224,** (1984) p. 45.

169. Clinch, J.R., Worsfold, P.J. and Sweeting, F. *Analytica Chimica Acta.* **214,** (1988) p. 401.

170. Benson, R.L., Worsfold, P.J. and Sweeting, F. *Analytica Chimica Acta.* **238,** (1990) p. 177.

171. Dasgupta, P.K., Bellamy, H.S., Liu, H., Lopez, J.L., Loree, K., Morris, K., Peterson, K. and Mir, K.A. *Talanta.* **40,** (1993) p. 53.

172. Raper, R.L., Johnson, C.E. and Bailey, A.C. *Transactions Of The Asae.* **37,** (1994) p. 1417.

173. Assouline, S., Tavares, J. and Tessier, D. *Soil Science Society of America Journal.* **61,** (1997) p. 390.

174. Schafer, R.L., Johnson, C.E., Koolen, A.J., Gupta, S.C. and Horn, R. *Transactions Of The Asae.* **35,** (1992) p. 1761.

175. Dawidowsky, J.B. and Koolen, A.J. *Soil & Tillage Research.* **9,** (1987) p. 169.

176. Croney, D. and Coleman, J.D. *Soil Science.* **5,** (1954) p. 75.

177. Laliberte, G.E., Corey, A.T. and Brooks, R.H. *hydrological papers.* **17,** (1966)

178. Smith, R.E. and Woolhiser, D.A. *Water Resources Research.* **7,** (1971) p. 899.

179. Libardi, P.L., Reichardt, K., Jose, C., Bazza, M. and Nielsen, D.R. *Water Resources Research.* **18,** (1980) p. 177.

180.Jury, W.A. and Roth, K. Transfer Functions and Solute Movement Through Soil : theory and applications. Boston: Bitkhauser;(1990)

181. White, R.E., Dyson, J.S., Haigh, R.A., Jury, W.A. and Sposito, G. *Water Resources Research.* **22,** (1986) p. 248.

182. Jury, W.A. *Water Resources Research.* **18,** (1982) p. 363.

183. Cameron, D.R. and Klute, A. *Water Resources Research.* **13,** (1977) p. 183.

184. Nielsen, D.R., van Genuchten, M.T. and Biggar, J.W. *Water Resources Research.* **22,** (1986) p. 895.

185. Notodarmojo, S., Ho, G.E., Scott, W.D. and Davis, G.B. *Water Research.* **25,** (1991) p. 1205.

186. Ho, G.E. and Notodarmojo, S. *Water Science and Technology.* **31,** (1995) p. 83.

187. Peat, D.M.W., McKelvie, I.D., Matthews, G.P., Haygarth, P.M. and Worsfold, P.J. *Talanta.* **41,** (1997) p. 47.

188. Avery, B.E. and Bascomb, C.L. Soil Survey Laboratory Methods. *in Technical Monograph. No. 14.* Avery, B.W. and Bascomb, C.L. (Eds.) Soil Survey, (1982)

189. Holden, N.M., Dowd, J.F., Williams, A.G. and Scholefield, D. *Environmental Monitoring and Assesment.* **36,** (1995) p. 217.

190. The determination of the water retention characteristics of nine soil samples. Shardlow Laboratory, Soil Survey and Land Research Centre. Soil Survey.(1994) PLYMUNI/PLY/01/94, p.1

191. Moss, A.K. and Matthews, G.P. Computer Modelling of Pore Structure and Permeability of Outcrop and Reservoir Sandstones. Geofluids '93.Parnell, J., Ruffell, A.H. and Moles, N.R. (Eds.) (1993 May 4-7) (1993) p. 208.

192. Mathews, T.J., Matthews, G.P. and Hugget, S. *Journal of Colloid and Interface Science.* **Submitted Oct 97,** (1998)

193. Clayden, B. *in Memoirs of the Soil Survey of Great Britian.* Chaucer Press, Bungay, Suffolk. (1971) p. 46.

194. Greenbeg, A.E. *in 4500-P Phosphorus.* Greenberg, A.E. (Ed.) (1992) p. 108.

195. Kerouel, K. and Aminot, A. *Analytica Chimica Acta.* **318,** (1996) p. 385.

196. Programmer's Guide - Microsoft Visual Basic. Microsoft, (1997) p. 504.

197. Haygarth, P.M. and Jarvis, S.C. *Water Research.* **31,** (1997) p. 140.

198. Scholefield, D., Tyson, K.T., Grawood, E.A., Armstrong, A.C., Hawkins, J. and Stone, A.C. *Journal of Soil Science.* **44,** (1993) p. 601.

199. McKelvie, I.D., Hart, B.T., Cardwell, T.J. and Cattrall, R.W. *Analyst.* **114,** (1989) p. 1459.

200. Williams, K.E., Haswell, S.J., Barclay, D.A. and Preston, G. *Analyst.* **118,** (1993) p. 245.

201. Liu, H.H. and Dane, J.H. *Soil Science Society of America Journal.* **60,** (1996) p. 986.

202. House, D.A. *Chemical Reviews.* **62,** (1962) p. 185.

203. Javier, A.C., Crouch, S.R. and Malmsdadt, H.V. *Analytical Chemistry.* **40,** (1968) p. 1922.

204. Crouch, S.R. and Malmsdadt, H.V. *Analytical Chemistry.* **39,** (1967) p. 1089.

205. Rodriguez, J.B., Self, J.R. and Soltanpour, P.N. *Soil Science Society of America Journal.* **58,** (1994) p. 866.

206. Karlberg, B. and Pacey, G.E. Flow Injection Analysis - A Practical Guide. Elsevier, Amsterdam. (1989) p. 372.

207. Benson, R.L., McKelvie, I.D., Hart, B.T., Truong, Y.B. and Hamilton, I.C. *Analytica Chimica Acta.* **326,** (1996) p. 29.

208. Rabenlange, B., Bendtsen, A.B. and Jorgensen, S.S. *Communications in Soil Science and Plant Analysis.* **25,** (1994) p. 3241.

209. Ciavatta, C., Antisari, L.V. and Sequi, P. *Jounrnal Of Environmental Quality.* **19,** (1990) p. 761.

210. Frenzel, W., Titzenthaler, F. and Elbel, S. *Talanta.* **41,** (1994) p. 1965.

211. Ohishi, H. Photometric Determination of Traces of Metals. *in Chemical Analysis.* Elving, J.D. and Winefordner, J.D. (Eds.) John Wiley, New York. (1990) p. 1.

212. Ferguson, J.F. and Gavis, J. *Water Research.* **6,** (1972) p. 1259.

213. Cresser, M.S., Killham, K. and Edwards, T. Soil chemistry and its applications. *in Cambridge Environmental Chemistry Series.* Cambridge University Press, Cambridge. (1993) p. 151.

214. Kuo, S. and Jellum, E.J. *Soil Science.* **158,** (1994) p. 124.

215. Dobermann, A., Langner, H., Mutscher, H., Yang, J.E., Skogley, E.O., Adviento, M.A. and Pampolino, M.F. *Communications in Soil Science and Plant Analysis.* **25,** (1994) p. 1329.

216. Freeman, P.R., Hart, B.T. and McKelvie, I.D. *Analytica Chimica Acta.* **282,** (1993) p. 379.

217. Tisdale, S.L., Nelson, W.L. and Beaton, J.D. Soil Fertility and Fertilisers. Macmillan Publishing Company, New York. (1985) p. 201.

218. Olivier, M. *Geotechnique.* **45,** (1995) p. 363.

219. Jury, W.A., Sposito, G. and White, R.E. *Water Resources Research.* **22,** (1986) p. 243.

220. Butters, G.L., Jury, W.A. and Ernst, F.F. *Water Resources Research.* **25,** (1989) p. 1575.

221. Starr, J.L., Roo, H.C., Frink, C.R. and Parlange, J. *Soil Science Society of America Journal.* **42,** (1978) p. 386.

222. Tillman, R.W., Scotter, D.R., Clothier, B.E. and White, R.E. *Agricultural Water Management.* **20,** (1991) p. 119.

223. Rowell, D.L. Soil Science. Methods and applications. Longman, Singapore. (1994) p. 26.

224. Findlay, D.C., Colborne, D.W., Harrod, T.R., Hogan, D.V. and Staines, S.J. Soils and their use in South West England. Soil Survey, Harpenden, (1984) p. 386.

225. Hall, D., G, Reeve, M., J. and Wright, V. Soil Survey. *In Technical Monograph No.9.* Harpenden, (1977) p. 1-.

226. Peat, D.M.W., Matthews, G.P., Worsfold, P.J. and Jarvis, S. *European Journal Of Soil Science.* **submitted, Oct 97,** (1998)

227. Matthews, G.P., Ridgway, C.J. and Small, J.S. *Marine Petroleum Geology.* **13,** (1997) p. 581.

APPENDIX 1: IMAGE ANALYSIS QBASIC PROGRAMME

```
 10 REM X Y W HT BLUE YELLOW DOUBLE BORDER
 20  panel 0,0,80,79,1,14,3"WELCOME":coltext 44:coltext 33:coltext 1
 30  postext 12,14
 40  print "Place 3.5 disc in bottom drive then press space bar"
 50  g$=inkey$:if g$="" then 50
 60  test g$=" " then 70 else 50
 70  cls
 80  panel 0,0,80,79,1,14,3"SET UP":coltext 45:coltext 32:coltext 1
 90  postext 12,15
100 rem WHAT MICROSCOPE, MAG AND ILLUMINATION???????????????
110 PRINT "PLACE FUJITSU CAMERA ON OLYMPUS FLUOR' MIC X40
OBJECTIVE "
120 postext 13,21
130 PRINT "AND 3.3 EYEPIECE. FOCUS AND POSITION OBJECT "
140 postext 14,26
150 PRINT "                    "
160 postext 15,26:COLTEXT 35
170 print "WHEN READY PRESS SPACE BAR"
180 r$=inkey$:if r$="" then 180
190 TEST R$=" " THEN 200 ELSE 180
200 CLS
210 c=0:x=0:y=0
220 camera   1
230 scanner  18   3.5
240 setlamps  0    0
250 mframe 26 26 460 486
260 iframe 0 0 512 512
270 pausetext 1"AT THE BEGINNING OF EVERY SESSION YOU NEED TO
SETSHADING"
280 pausetext 2"MOVE TO A BLANK AREA AND THEN HIGHLIGHT SET
WITHMIDDLETRAKERBALL KEY"
290 PAUSETEXT 3"THEN PRESS MIDDLE KEY, THEN CONTINUE"
300 pausetext 1""
310 PAUSETEXT 3""
320 panel 0,0,80,79,1,14,3"FILE":coltext 44:coltext 33:coltext 1
330 postext 14,5
340 input "PLEASE TYPE THE NAME OF THE FILE YOU WISH TO SAVE
THISIMAGE UNDER ",N$
350 open#1 "b:"+n$+".prn"
360 postext 16,5
370 clearimages
380 CLS
390 calibrate 5, 'I'
400 pausetext 2"CHECK MAG IS X40 AND I6"
410 QMENU 'CALIBRATE'
```

```
420 riasettings 'cal_value' k
430 pausetext 1"FIND THE FIELD YOU WISH TO MEASURE"
440 qmenu 'image_setup'
450 PAUSETEXT 1""
460 PAUSETEXT 2""
470 PAUSETEXT 3""
480  panel 0,0,80,79,1,14,3"WORK":coltext 44:coltext 33:coltext 1
490 POSTEXT 12,23
500 PRINT "PLEASE WAIT I'M WORKING ON "N$ ", FIELD "C"!"
510 POSTEXT 13,28
520 PRINT "I WILL BE ABOUT ?? SECS"
530 REM
540 multiacquire 5 0 4
550 greyfill 0 1 2 1
560 greydetect 2 42 251 2 1 0
570 qmenu 'detect'
580 binclose 1 2 256 1
590 pausetext 2'MEASURE PLANE 2'
600 qmenu 'measure_field'
610 MEASFIELD 2
620 RFIELDRES A(1)
630 PRINT#1: A(1),A(5)
640 pausetext 2"
650 edgefeat 2 3
660 setftrpar "1,34,28,29,9,2,3"
670 ftrgrey 1 : measfeat 3 1 4 300000 : clraccept
680 acceptxfer 3 4
690 PAUSETEXT 2"Here are the results!"
700 qmenu 'feature_results'
710 rem transform, detect, amend, measure, display
720 rfeatnum n(1)
730 for f=0 to n(1)-1
740 rfeatres f  1 a(1)
750 RFEATRES F  9 B(1)
760 RFEATRES F 28 X(1)
770 RFEATRES F 29 Y(1)
780 RFEATRES F 34 ED(1)
790 print #1:c,n(1),K,k*k*a(1),K*B(1),K*X(1)/1000,K*Y(1)/1000,K*ED(1)
800 next f
810 d=c/4
820 d$=str$(d):d$=d$+'0'
830 row=val(mid$(d$,1,1))
840 col=4*val(mid$(d$,2,3))
850 x=col*115:y=row*121
860 if col=0 greymove 1 8
870 if col=3 then 900
880 greyshift 1 2 180 462
890 goto 910
900 greyshift 8 2 90 487
```

```
905 btoph 2 3 256 3 : sub8 2 3 5
906 wtoph 2 3 256 3 : add8 5 3 3
907 setgamma 430, -70
908 anamorph 3 4 6 10
909 greymove 4 2
910 greydetect 2 67 251 2 1 0
915 pausetext 2'DETECT RECOGNISABLE AREAS FOR MATCHING UP'
920 qmenu 'detect'
925 pausetext 2'MATCH UP YOUR TWO IMAGES'
930 display 0 1 3 2
940 qmenu 'display'
950 setblock 26 26 460 486
960 zoomblock 1 10 x y 0, -4
970 c=c+1
980 C$=STR$(C)
990 test C=16 then 1000 else 430
1000 loadimage 11 "C:\images\X4PLAN.TIG"
1005 greytoggle 10 11 5
1010 panel 0,0,80,79,1,14,3"THE END":coltext 44: coltext 33: coltext 1
1020 panel 20,5,40,12,4,14,2"COPYRIGHT":coltext 41: coltext 33: coltext 1
1030 POSTEXT 8,33
1040 PRINT "PPPPP   RRRRR"
1050 POSTEXT 9,33
1060 PRINT "P   P   R   R"
1070 POSTEXT 10,33
1080 PRINT "PPPPP   RRRRR"
1090 POSTEXT 11,33
1100 PRINT "P       RR "
1110 POSTEXT 12,33
1120 PRINT "P       R R"
1130 POSTEXT 13,33
1140 PRINT "P       R   R"
1150 panel 20,18,40,6,5,4,2""
1160 postext 19,32
1170 coltext 1:coltext 32:coltext 45
1180 print"Wasn't that fun!"
1190 postext 20,32
1200 print "That is " n$ " done"
1210 postext 21,22:COLTEXT 35
1220 print "Do you wish to do another?  y or n"
1230 a$=inkey$:if a$="" then 1230
1240 test a$='y' then 200 else 1250
1250 coltext 0
1260 close#1
1270 cls
1280 end
```